

KNOWLES, SONJA L., Ph.D., Studies on the Genotype, Phenotype, and Co-Cultures of *Aspergillus* Section *Fumigati* And the Development of New Techniques to Enhance Structure Elucidation of Fungal Metabolites. (2021)  
Directed by Dr. Nicholas H. Oberlies. 311pp.

Fungi are pathogenic to plants, humans, and animals, and secondary metabolites produced by fungi are implicated in these interactions. As part of an interdisciplinary project to identify the chemical and genomic differences between pathogenic and non-pathogenic fungi, this research identified the chemical differences among *Aspergillus* section *Fumigati*. During the research, eight fungal strains were grown under three different temperatures, and 13 different media types were evaluated for their chemical diversity. Chemical studies resulted in 30 secondary metabolites and a variety of chemometric comparisons. The characterized secondary metabolites were compared between strains using several different methodologies, including chemometrics, dereplication, and biosynthetic gene clusters. These comparisons shed light on how secondary metabolites affect pathogenicity in *Aspergillus* section *Fumigati*. Bioinformatic analysis of the genome of *Aspergillus fischeri* predicted the presence of 48 biosynthetic gene clusters, yet only 5 classes of secondary metabolites were identified by chemical characterization. Interaction-driven secondary metabolite discovery (i.e., co-culturing) was used to activate silent biosynthetic gene clusters. This methodology was utilized successfully by co-culturing *A. fischeri* and *Xylaria flabelliformis*, which produces the FDA-approved antifungal drug griseofulvin; to activate secondary metabolites not observed when the two fungi were grown in monoculture. The co-culture resulted in the characterization of a novel scaffold with cytotoxic activity.

STUDIES ON THE GENOTYPE, PHENOTYPE, AND CO-CULTURES OF  
*ASPERGILLUS* SECTION *FUMIGATI* AND THE DEVELOPMENT  
OF NEW TECHNIQUES TO ENHANCE STRUCTURE  
ELUCIDATION OF FUNGAL METABOLITES

by

Sonja L. Knowles

A Dissertation Submitted to  
the Faculty of The Graduate School at  
The University of North Carolina at Greensboro  
in Partial Fulfillment  
of the Requirements for the Degree  
Doctor of Philosophy

Greensboro  
2021

Approved by

---

Committee Chair

## APPROVAL PAGE

This dissertation written by SONJA L. KNOWLES has been approved by the following committee of the Faculty of The Graduate School at The University of North Carolina at Greensboro.

Committee Co-Chair      Dr. Nicholas H. Oberlies

Committee Members      Dr. Nadja B. Cech

Dr. Mitchell P. Croatt

Dr. Antonis Rokas

2/26/2021

---

Date of Acceptance by Committee

2/26/2021

---

Date of Final Oral Examination

## ACKNOWLEDGEMENTS

The completion of this dissertation was made possible by all the individuals who challenged, supported, and stuck with me along the way. I am tremendously fortunate to have had the opportunity to pursue this degree under the guidance of Dr. Nicholas Oberlies. I will forever be thankful for his continued support, patience, enthusiasm, and immense knowledge. I could not have imagined a better advisor and mentor for my Ph.D. studies. I would like to thank the rest of my committee: Dr. Nadja Cech, Dr. Mitchell Croatt, and Dr. Antonis Rokas for all their encouragement and insightful comments. I would like to thank Dr. Nadja Cech for her unwavering enthusiasm and our weekly writing group. I would like to thank Dr. Mitchell Croatt for always helping me with synthesis and structural stability. I would like to thank Dr. Antonis Rokas for his guidance at every stage of my research, scholarly advice, and scientific approach.

I sincerely want to thank all my fellow lab mates for their unwavering support and guidance. I especially want to thank Dr. Tamam El-Elimat for training me during my first few months in the lab and Dr. José Rivera-Chávez for training me in structure elucidation. I want to thank Mr. Tyler Graf for always guiding me and being there in my times of need and Dr. Huzefa Raja for his honest feedback, never-ending support, and for pushing me further than I knew possible. I want to give a special thank you to all the undergraduates (Mario Augustinović, Allison Wright, Christopher Roberts, Lea Shumaker, and Cameron Eller) that I have had the opportunity to work with over the past 5 years, you are all truly remarkable individuals.

I want to thank all my friends in the Department of Chemistry and Biochemistry for being there to lean on in my time of need. I want to give a special thanks to Mario Augustinović, Kristóf Cank, Gabrielle Dailey, and Allison Wright for being great friends

and always making me laugh. I especially want to thank Dr. Israa Isawi, without you this experience would not have been the same and I am truly grateful.

I want to express my gratitude to all my collaborators; this dissertation could not have been assembled without your contributions and support. I especially want to thank Dr. Matthew Mead and Mr. Jacob Steenwyk for a truly rewarding collaboration. Through their expertise, I had the opportunity to gain valuable insights into the evolution and genetics of fungi. This dissertation, in part, would not have been possible without them.

I want to thank my family and friends for all their unconditional support throughout this entire process. I want to thank my friends Maggie Smith, Ali Ladue, and Chiara Phillips for being there from the beginning and always pushing me to pursue my dreams. I want to thank my mom for her never wavering love and support.

Finally, I want to thank my biggest supporter and husband, Tom. Thank you for making the unselfish decision of leaving home and moving to a new city so that I could pursue this degree. Thank you for always being right by my side and for always believing in me.

## TABLE OF CONTENTS

	Page
LIST OF TABLES .....	vi
LIST OF FIGURES.....	ix
CHAPTER	
I. INTRODUCTION .....	1
II. CHARACTERIZING THE PATHOGENIC, GENOMIC, AND CHEMICAL TRAITS OF <i>ASPERGILLUS FISCHERI</i> , A CLOSE RELATIVE OF THE MAJOR HUMAN FUNGAL PATHOGEN <i>ASPERGILLUS FUMIGATUS</i> .....	7
III. GLIOTOXIN, A KNOWN VIRULENCE FACTOR IN THE MAJOR HUMAN PATHOGEN <i>ASPERGILLUS FUMIGATUS</i> , IS ALSO BIOSYNTHESIZED BY THE NON-PATHOGENIC RELATIVE <i>A. FISCHERI</i> .....	68
IV. VARIATION AMONG BIOSYNTHETIC GENE CLUSTERS, SECONDARY METABOLITE PROFILES, AND CARDS OF VIRULENCE ACROSS <i>ASPERGILLUS FUMIGATUS</i> AND CLOSE NONPATHOGENIC RELATIVES.....	84
V. MAPPING THE FUNGAL BATTLEFIELD: USING <i>IN SITU</i> CHEMISTRY AND DELETION MUTANTS TO MONITOR INTERSPECIFIC CHEMICAL INTERACTIONS BETWEEN FUNGI .....	135
VI. WHELDONE: CHARACTERIZATION OF A UNIQUE SCAFFOLD FROM THE CO-CULTURE OF <i>ASPERGILLUS FISCHERI</i> AND <i>XYLARIA</i> <i>FLABELLIFORMIS</i> .....	178
VII. ORTHOGONAL METHOD FOR DOUBLE BOND PLACEMENT VIA OZONE-INDUCED DISSOCIATION MASS SPECTROMETRY (OZID-MS) .....	198
VIII. OPPORTUNITIES AND LIMITATIONS FOR ASSIGNING RELATIVE CONFIGURATIONS OF ANTIBACTERIAL BISLACTONES USING GIAO NMR SHIFT CALCULATIONS .....	233
REFERENCES .....	279

## LIST OF TABLES

	Page
Table 2.1. <i>A. fischeri</i> Shows Enhanced Resistance Relative to <i>A. fumigatus</i> for Several Antifungal Drugs.....	20
Table 2.2. Secondary metabolites isolated from <i>A. fischeri</i> that have been reported from <i>A. fumigatus</i> .....	27
Table 2.3. $^1\text{H}$ (700 MHz) and $^{13}\text{C}$ (175 MHz) NMR Data in $\text{CDCl}_3$ for 14 – epi-aszonapyrone A ( <b>3</b> ) .....	43
Table 2.4. $^1\text{H}$ (700 MHz) and $^{13}\text{C}$ (175 MHz) NMR Data in $\text{CDCl}_3$ for 13-O-prenyl-fumitremorgin B ( <b>10</b> ).....	44
Table 2.5. HRESIMS Table of Compounds <b>1–10</b> .....	45
Table 4.1. Select <i>A. fumigatus</i> Secondary Metabolites Implicated in Modulating Host Biology .....	97
Table 4.2. Species and Strains Used in the Present Study .....	108
Table 4.3. A Table of Secondary Metabolites Produced by Each Species and Strain.....	118
Table 4.4. A Table Summarizing Species-Level Secondary Metabolite Production .....	119
Table 4.5. Chemical Structures, Chemical Formulas, Retention Times, UV Absorption Maxima, (+)-ESI HRMS, and (+)-ESI CID MS/MS Data of Fumigati Fungal Secondary Metabolites .....	120
Table 5.1. List of altered features in the co-culture of <i>X. cubensis</i> and <i>A. fischeri</i> analyzed by LC-MS .....	163
Table 5.2. Putative orthologs of the cytochalasin gene cluster found in <i>X. cubensis</i> and <i>A. fischeri</i> .....	165
Table 5.3. Biological replicates Area Under the Curve for Average Increase in Mycotoxins During the Co-Culture .....	166
Table 6.1. $^1\text{H}$ (700 MHz), $^{13}\text{C}$ (175 MHz), and HMBC NMR Data for <b>1</b> in $\text{CD}_3\text{OD}$ .....	182
Table 6.2. Activity of <b>1</b> Against Three Tumor Cell Lines.....	185
Table 7.1. Key considerations for performing OzID-MS analysis .....	215
Table 7.2. NMR table of ent-sartorypyrone E ( <b>1</b> ) .....	221

Table 7.3. Table of accurate masses for the OzID products of compound <b>1</b> .....	222
Table 7.4. Table of accurate masses for the OzID products of compound <b>1</b> in an extract .....	223
Table 7.5. Table of accurate masses for the OzID products of compound <b>1</b> in situ.....	224
Table 7.6. Table of accurate masses for the OzID products of compound <b>2</b> .....	225
Table 7.7. Table of accurate masses for the OzID products of compound <b>3</b> .....	225
Table 7.8. Table of accurate masses for the OzID products of compound <b>4</b> .....	226
Table 7.9. Table of accurate masses for the OzID products of compound <b>5</b> .....	226
Table 8.1. $^1\text{H}$ and $^{13}\text{C}$ NMR Data of Compound <b>1-4</b> .....	242
Table 8.2. Antimicrobial Activity of Compounds <b>1</b> , <b>4</b> , and <b>5</b> Against a Panel of Bacteria.....	244
Table 8.3. Calculated and experimental $^{13}\text{C}$ shifts (in ppm) for <b>1a-1d</b> .....	272
Table 8.4. Calculated and experimental $^1\text{H}$ shifts (in ppm) for <b>1a-1d</b> .....	272
Table 8.5. Average values of the correlation coefficients for <b>1a-1d</b> .....	273
Table 8.6. Calculated and experimental $^{13}\text{C}$ shifts (in ppm) for <b>2a-2d</b> .....	273
Table 8.7. Calculated and experimental $^1\text{H}$ shifts (in ppm) for <b>2a-2d</b> .....	274
Table 8.8. Average values of the correlation coefficients for <b>2a-2d</b> .....	274
Table 8.9. Calculated and experimental $^{13}\text{C}$ shifts (in ppm) for <b>3a-3h</b> .....	274
Table 8.10. Calculated and experimental $^1\text{H}$ shifts (in ppm) for <b>3a-3h</b> .....	275
Table 8.11. Average values of the correlation coefficients for <b>3a-3h</b> .....	275
Table 8.12. Calculated and experimental $^{13}\text{C}$ shifts (in ppm) for <b>4a-4h</b> .....	275
Table 8.13. Calculated and experimental $^1\text{H}$ shifts (in ppm) for <b>4a-4h</b> .....	276
Table 8.14. Average values of the correlation coefficients for <b>4a-4h</b> .....	276
Table 8.15. $^1\text{H}$ NMR spectrum comparison of literature acremodiol and compound <b>4</b> (acremodiol C) .....	277
Table 8.16. Calculated $[\alpha]_D$ for <b>1a</b> , <b>1d</b> , <b>2b</b> , <b>2c</b> , <b>3a/4a</b> , <b>3e/4e</b> , and <b>3g/4g</b> .....	277

Table 8.17. DP4+ Analysis .....	278
---------------------------------	-----

## LIST OF FIGURES

	Page
Figure 1. <i>A. fischeri</i> is Significantly Less Virulent than <i>A. fumigatus</i> in Multiple Murine Models of Invasive Pulmonary Aspergillosis .....	14
Figure 2. <i>A. fischeri</i> is Unable to Thrive Under Suboptimal Metabolic Conditions at 37°C.....	16
Figure 3. <i>A. fischeri</i> is More Susceptible to Multiple Host-Relevant Stresses Than <i>A. fumigatus</i> .....	18
Figure 4. Biosynthetic Gene Clusters of <i>A. fumigatus</i> and <i>A. fischeri</i> Show Substantial Evolutionary Divergence .....	22
Figure 5. Secondary Metabolite Production in <i>A. fischeri</i> .....	29
Figure 6. <i>A. fumigatus</i> Grows Slower Than <i>A. fischeri</i> in Glucose Minimal Media (GMM), but at the Same Speed as <i>A. fischeri</i> in Lung Homogenate Media .....	46
Figure 7. <i>A. fischeri</i> and <i>A. fumigatus</i> Exhibit Similar Growth Patterns at 30°C but Not at 44°C.....	47
Figure 8. The Genomes of <i>A. fumigatus</i> and <i>A. fischeri</i> are Largely Similar, but Their Secondary Metabolic Pathways are Quite Divergent.....	47
Figure 9. The Acetylaszonalenin and Gliotoxin Biosynthetic Gene Clusters in <i>A. fumigatus</i> and <i>A. fischeri</i> are Located Immediately Next to One Another.....	48
Figure 10. A Custom Chemical Analysis Protocol was Developed for Studying the Metabolites Produced by <i>A. Fischeri</i> .....	48
Figure 11. <i>A. fischeri</i> Produces Different Numbers of Metabolites, Depending on the Media it is Grown on.....	49
Figure 12. Southern Blot Confirms Construction of the $\Delta laeA$ Mutant.....	50
Figure 13. UPLC analysis of compounds <b>1-10</b> , arranged from Top to Bottom.....	51
Figure 14. $^1H$ NMR spectrum (700 MHz, Top) and $^{13}C$ NMR spectrum (175 MHz, Bottom), both in $CDCl_3$ , of sartorypyrone A ( <b>1</b> ) .....	51
Figure 15. $^1H$ NMR spectrum (700 MHz, Top) and $^{13}C$ NMR spectrum (175 MHz, Bottom), both in $CDCl_3$ , of 14-epi-aszonapyrone A ( <b>3</b> ).....	52
Figure 16. HMBC spectrum of 14-epimer of aszonapyrone A ( <b>3</b> ), $CDCl_3$ , 700 MHz.....	53

Figure 17. $^1\text{H}$ COSY spectrum of 14-epimer of aszonapyrone A ( <b>3</b> ), $\text{CDCl}_3$ , 700 MHz.....	54
Figure 18. HSQC spectrum of 14-epimer of aszonapyrone A ( <b>3</b> ), $\text{CDCl}_3$ , 700 MHz.....	55
Figure 19. NOESY spectrum of 14-epimer of aszonapyrone A ( <b>3</b> ), $\text{CDCl}_3$ , 700 MHz.....	56
Figure 20. $^1\text{H}$ NMR spectrum (400 MHz) in $\text{CDCl}_3$ , of aszonalenin ( <b>4</b> ) .....	56
Figure 21. $^1\text{H}$ NMR spectrum (500 MHz, Top) and $^{13}\text{C}$ NMR spectrum (125 MHz, Bottom), both in $\text{CDCl}_3$ , of acetylaszonalenin ( <b>5</b> ) .....	57
Figure 22. $^1\text{H}$ NMR spectrum (500 MHz, Top) and $^{13}\text{C}$ NMR spectrum (125 MHz, Bottom), both in $\text{CDCl}_3$ , of fumitremorgin A ( <b>6</b> ) .....	58
Figure 23. $^1\text{H}$ NMR spectrum (700 MHz, Top) and $^{13}\text{C}$ NMR spectrum (175 MHz, Bottom), both in $\text{CDCl}_3$ , of fumitremorgin B ( <b>7</b> ) .....	59
Figure 24. $^1\text{H}$ NMR spectrum (500 MHz, Top) and $^{13}\text{C}$ NMR spectrum (125 MHz, Bottom), both in $\text{CDCl}_3$ , of verruculogen ( <b>8</b> ).....	60
Figure 25. $^1\text{H}$ NMR spectrum (700 MHz, Top) and $^{13}\text{C}$ NMR spectrum (175 MHz, Bottom), both in $\text{CDCl}_3$ , of C-11 epimer of verruculogen TR-2 ( <b>9</b> ).....	61
Figure 26. $^1\text{H}$ NMR spectrum (700 MHz, Top) and $^{13}\text{C}$ NMR spectrum (175 MHz, Bottom), both in $\text{CDCl}_3$ , of 13-O-prenyl-fumitremorgin B ( <b>10</b> ) .....	62
Figure 27. HMBC spectrum of 13-O-prenyl-fumitremorgin B ( <b>10</b> ), $\text{CDCl}_3$ , 700 MHz.....	63
Figure 28. $^1\text{H}$ COSY spectrum of 13-O-prenyl-fumitremorgin B ( <b>10</b> ), $\text{CDCl}_3$ , 700 MHz.....	64
Figure 29. HSQC spectrum of 13-O-prenyl-fumitremorgin B ( <b>10</b> ), $\text{CDCl}_3$ , 700 MHz.....	65
Figure 30. Key COSY and HMBC data for 14-epi-azonapyrone A ( <b>3</b> ) and 13-O-prenyl-fumitremorgin B ( <b>10</b> ).....	66
Figure 31. CD Data for 13-O-fumitremorgin B ( <b>10</b> ) and fumitremorgin B ( <b>7</b> ) .....	67
Figure 32. <i>Aspergillus fischeri</i> Biosynthesizes Gliotoxin When Grown in Conditions That Induce <i>A. fumigatus</i> Gliotoxin Biosynthesis .....	70
Figure 33. Deletion of the Master Regulator <i>iaeA</i> in <i>A. fischeri</i> Does Not Alter its Virulence.....	74

Figure 34. The mass spectra of gliotoxin in <i>A. fumigatus</i> grown on CDA and blood agar at 37°C verify the biosynthesis of gliotoxin by cultures of <i>A. fumigatus</i> on both CDA and blood agar at 37°C.....	79
Figure 35. The fragmentation pattern (i.e., MS/MS data) of gliotoxin in <i>A. fumigatus</i> grown on CDA and blood agar at 37°C .....	80
Figure 36. Base peak chromatograms of the gliotoxin standard, <i>A. fumigatus</i> grown on OMA at 37°C, <i>A. fischeri</i> grown on OMA at 37°C, $\Delta$ laeA <i>A. fischeri</i> grown on CDA at 37°C, and $\Delta$ laeA <i>A. fischeri</i> grown on blood agar at 37°C .....	81
Figure 37. The mass spectra of gliotoxin in <i>A. fischeri</i> verify the biosynthesis of gliotoxin by cultures of <i>A. fischeri</i> on both CDA and blood agar at 37°C .....	82
Figure 38. The fragmentation patterns (i.e., MS/MS data) of gliotoxin in <i>A. fischeri</i> .....	83
Figure 39. Diverse Genetic Repertoire of Biosynthetic Gene Clusters and Extensive Presence and Absence Polymorphisms Between and Within Species .....	90
Figure 40. <i>Aspergillus oerlinghausenensis</i> Shares More Gene Families and Biosynthetic Gene Clusters With <i>A. fischeri</i> Than <i>A. fumigatus</i> .....	92
Figure 41. <i>A. oerlinghausenensis</i> and <i>A. fischeri</i> Have More Similar Secondary Metabolite Profiles Than <i>A. fumigatus</i> .....	95
Figure 42. Conservation in the Gliotoxin BGC Correlates with Conserved Production of Gliotoxin Analogs in <i>A. fumigatus</i> and Nonpathogenic Close Relatives .....	98
Figure 43. Conservation and Divergence in the Locus Encoding the Fumitremorgin and Intertwined Fumagillin/Pseurotin Biosynthetic Gene Clusters .....	99
Figure 44. Secondary Metabolism-Associated “Cards” of Virulence Among <i>A. fumigatus</i> and Close Relatives .....	104
Figure 45. Metrics of Genomes Assembly Quality and Number of Predicted Gene .....	124
Figure 46. A Reconstructed Evolutionary History and Timetree of <i>A. fumigatus</i> and its Closest Relatives .....	125
Figure 47. Species and Strain Heterogeneity Among BGC Cluster Presence and Absence .....	126
Figure 48. Gene Family Presence and Absence Follows a Similar Pattern to BGCs .....	127
Figure 49. Structures of Isolated Fungal Metabolites .....	128

Figure 50. Principal Component Analysis of BGC Presence and Absence and Secondary Metabolite Profiles Mirror One Another.....	130
Figure 51. Small Sequence Divergences in the Trypacidin BGC are Associated with the Production of Trypacidin or the Lack Thereof .....	131
Figure 52. An Example of the Dereplication Process Used to Identify bisdethiobis(methylthio)gliotoxin ( <b>5</b> ) in the Extract of CBS 139183 <sup>T</sup> .....	132
Figure 53. <sup>1</sup> H NMR spectrum of cyclo(L-Pro-L-Leu) ( <b>1</b> ) (400 MHz; CDCl <sub>3</sub> ).....	132
Figure 54. <sup>1</sup> H NMR spectrum of monomethylsulochrin ( <b>3</b> ) (400 MHz; CDCl <sub>3</sub> ).....	133
Figure 55. <sup>1</sup> H NMR spectrum of pseurotin A ( <b>4</b> ) (400 MHz; CDCl <sub>3</sub> ) .....	133
Figure 56. <sup>1</sup> H NMR spectrum of bisdethiobis(methylglu)gliotoxin ( <b>5</b> ) (400 MHz; CDCl <sub>3</sub> ).....	133
Figure 57. <sup>1</sup> H NMR spectrum of fumagillin ( <b>6</b> ) (400 MHz; CDCl <sub>3</sub> ) .....	134
Figure 58. <sup>1</sup> H NMR spectrum of spiro-[5H,10H-dipyrrolo[1,2-a:1',2'-d]pyrazine-2-(3H),2'-[2H]indole]-3',5,10(1'H)-trione ( <b>8</b> ) (400 MHz; CDCl <sub>3</sub> ).....	134
Figure 59. <sup>1</sup> H NMR spectrum of helvolic acid ( <b>9</b> ) (400 MHz; CDCl <sub>3</sub> ).....	134
Figure 60. The Diversity of Secondary Metabolites Isolated from the Co-Culture of Wild Type <i>Aspergillus fischeri</i> (NRRL 181) and <i>Xylaria cubensis</i> (G536) .....	140
Figure 61. The Chromatograms from the Droplet Probe Analysis of the Monocultures, as Taken at the Mycelial Edge .....	141
Figure 62. Wild Type <i>A. fischeri</i> can Form a Deadlock while $\Delta$ laeA <i>A. fischeri</i> Gets Displaced by <i>X. cubensis</i> During the Co-Culture.....	142
Figure 63. Co-Culture Produces Greater Diversity of Secondary Metabolites Over That of the Monocultures .....	143
Figure 64. Increase in Chemical Diversity in the Co-Culture Caused the Characterization of Secondary Metabolite Not Seen in Monoculture .....	144
Figure 65. Principal Component Analysis (PCA) Scores and Loadings Plots of Monoculture and Co-Culture Analysis .....	146
Figure 66. Overview of How the Secondary Metabolites Biosynthesized During the Monoculture and Co-Culture Were Analyzed.....	149
Figure 67. General Procedure for How the Droplet Probe Works.....	157
Figure 68. Wild Type and $\Delta$ laeA <i>Aspergillus fischeri</i> and <i>Xylaria cubensis</i> Grown on Petri Plates.....	166

Figure 69. Co-culture growths .....	167
Figure 70. Base peak of All Eight Spots Across the Co-Culture.....	168
Figure 71. Photodiode-Array (PDA) Detector Chromatogram of Secondary Metabolites.....	168
Figure 72. $^1\text{H}$ NMR spectrum (700 MHz, Top) and $^{13}\text{C}$ NMR spectrum (175 MHz, Bottom) both in $\text{CDCl}_3$ , of sartorypyrone A ( <b>1</b> ).....	169
Figure 73. $^1\text{H}$ NMR spectrum (400 MHz) in $\text{CDCl}_3$ , aszonalenin ( <b>2</b> ) .....	169
Figure 74. $^1\text{H}$ NMR spectrum (500 MHz, Top) and $^{13}\text{C}$ NMR spectrum (125 MHz, Bottom) both in $\text{CDCl}_3$ , of acetylaszonalenin ( <b>3</b> ).....	170
Figure 75. $^1\text{H}$ NMR spectrum (500 MHz, Top) and $^{13}\text{C}$ NMR spectrum (125 MHz, Bottom) both in $\text{CDCl}_3$ , of fumitremorgin A ( <b>4</b> ).....	171
Figure 76. $^1\text{H}$ NMR spectrum (700 MHz, Top) and $^{13}\text{C}$ NMR spectrum (175 MHz, Bottom) both in $\text{CDCl}_3$ , of fumitremorgin B ( <b>5</b> ).....	172
Figure 77. $^1\text{H}$ NMR spectrum (500 MHz, Top) and $^{13}\text{C}$ NMR spectrum (125 MHz, Bottom) both in $\text{CDCl}_3$ , of verruculogen ( <b>6</b> ) .....	173
Figure 78. $^1\text{H}$ NMR spectrum (700 MHz, Top) and $^{13}\text{C}$ NMR spectrum (175 MHz, Bottom) both in $\text{CDCl}_3$ , of C-11 epimer of verruculogen TR-2 ( <b>7</b> ) .....	174
Figure 79. $^1\text{H}$ NMR spectrum (400 MHz) in $\text{CDCl}_3$ , griseofulvin ( <b>8</b> ) .....	174
Figure 80. $^1\text{H}$ NMR spectrum (400 MHz) in $\text{CDCl}_3$ , dechlorogriseofulvin ( <b>9</b> ).....	175
Figure 81. $^1\text{H}$ NMR spectrum (400 MHz) in $\text{CDCl}_3$ , 5`-hydroxygriseofulvin ( <b>10</b> ).....	175
Figure 82. $^1\text{H}$ NMR spectrum (400 MHz) in $\text{CDCl}_3$ , dechloro-5`- hydroxygriseofulvin ( <b>11</b> ) .....	175
Figure 83. $^1\text{H}$ NMR spectrum (400 MHz, Top) and $^{13}\text{C}$ NMR spectrum (100 MHz, Bottom) both in $\text{CDCl}_3$ , of cytochalasin D ( <b>12</b> ).....	176
Figure 84. $^1\text{H}$ NMR spectrum (400 MHz) in $\text{CDCl}_3$ , cytochalasin C ( <b>14</b> ) .....	176
Figure 85. $^1\text{H}$ NMR spectrum (400 MHz) in $\text{CDCl}_3$ , zygosporin E ( <b>15</b> ).....	177
Figure 86. $^1\text{H}$ NMR spectrum (400 MHz) in $\text{CDCl}_3$ , 7-O-acetylcytochalasin B ( <b>16</b> ) .....	177
Figure 87. $^1\text{H}$ NMR spectrum (400 MHz) in $\text{CDCl}_3$ , hirsutatin A ( <b>17</b> ) .....	177
Figure 88. Wheldone ( <b>1</b> ) Was Isolated From the Co-Culture of <i>Aspergillus fischeri</i> and <i>Xylaria flabelliformis</i> .....	180
Figure 89. Comparison of wheldone abundance in junction during agar plate growth and solid media growth.....	181

Figure 90. Key COSY and HMBC correlations for <b>1</b> .....	184
Figure 91. $\Delta\delta_H$ values [ $\Delta\delta$ (in ppm) = $\delta_S - \delta_R$ ] obtained for ( <i>S</i> )- and ( <i>R</i> )-MTPA esters of wheldone ( <b>1</b> ) (1a and 1b, respectively) in pyridine- <i>d</i> <sub>5</sub> .....	185
Figure 92. LC-MS chromatogram, (+)-HRESIMS spectrum, and purity of compound <b>1</b> .....	190
Figure 93. <sup>1</sup> H (700 MHz) and <sup>13</sup> C (175 MHz) NMR data for wheldone ( <b>1</b> ) in CD <sub>3</sub> OD .....	191
Figure 94. HSQC NMR spectrum of compound <b>1</b> (700 MHz, CD <sub>3</sub> OD) .....	192
Figure 95. COSY NMR spectrum of compound <b>1</b> (700 MHz, CD <sub>3</sub> OD) .....	193
Figure 96. HMBC NMR spectrum of compound <b>1</b> (700 MHz, CD <sub>3</sub> OD) .....	194
Figure 97. NOESY NMR spectrum of compound <b>1</b> (400 MHz, CD <sub>3</sub> OD).....	195
Figure 98. Key NOESY correlations for compound <b>1</b> . The structure is presented twice, so that it is easier to see the key correlations for each face of the molecule.....	195
Figure 99. A larger version of Figure 89 Panel A .....	196
Figure 100. Data confirming the biosynthesis of <b>1</b> from a co-culture of <i>X. flabelliformis</i> vs. fungal strain MSX76272.....	197
Figure 101. Compounds <b>1-5</b> .....	202
Figure 102. In ozonolysis carbon-carbon double bonds react with ozone via a 1,3-dipolar cycloaddition.....	203
Figure 103. Key COSY and HMBC correlations for compound <b>1</b> .....	205
Figure 104. A: The OzID-MS spectrum of ent-sartorypyrone E ( <b>1</b> ) after targeted OzID fragmentation .....	207
Figure 105. The OzID-MS spectrum of <b>2</b> after targeted OzID fragmentation.....	209
Figure 106. The OzID-MS spectrum of <b>3</b> after targeted OzID fragmentation.....	210
Figure 107. The OzID-MS spectrum of <b>4</b> after targeted OzID fragmentation.....	211
Figure 108. The OzID-MS spectrum of <b>5</b> after targeted OzID fragmentation.....	212
Figure 109. The OzID-MS studies of <i>Aspergillus fischeri</i> showing the analysis of compound <b>1</b> in the context of an extract (panel A) and from in situ sampling of a Petri dish of a life culture (panel B) .....	214
Figure 110. UPLC-PDA detector chromatogram of ent-sartorypyrone E ( <b>1</b> ).....	226

Figure 111. $^1\text{H}$ NMR spectrum (700 MHz, Top) and $^{13}\text{C}$ NMR spectrum (175 MHz, Bottom) both in $\text{CDCl}_3$ , of ent-sartorypyrone E ( <b>1</b> ) .....	227
Figure 112. HSQC spectrum of ent-sartorypyrone E ( <b>1</b> ), $\text{CDCl}_3$ , 700 MHz.....	228
Figure 113. HMBC spectrum of ent-sartorypyrone E ( <b>1</b> ), $\text{CDCl}_3$ , 700 MHz .....	229
Figure 114. $^1\text{H}$ COSY spectrum of ent-sartorypyrone E ( <b>1</b> ), $\text{CDCl}_3$ , 700 MHz .....	230
Figure 115. UPLC-PDA detector chromatogram of an extract of <i>A. fischeri</i> grown on solid oatmeal media.....	230
Figure 116. $^1\text{H}$ NMR spectrum (400 MHz) in $\text{CDCl}_3$ , of sorbicillin ( <b>3</b> ) .....	231
Figure 117. $^1\text{H}$ NMR spectrum (500 MHz) in MeOD, of trichodermic acid A ( <b>4</b> ) .....	231
Figure 118. $^1\text{H}$ NMR spectrum (500 MHz) in $(\text{CD}_3)_2\text{CO}$ , of AA03390 ( <b>5</b> ).....	231
Figure 119. Schematic of the Waters Synapt G2 HDMS modified to allow ozone in the trap and transfer cells to perform OzID-MS. Adapted from Vu et al.....	232
Figure 120. Structures of compounds <b>1-5</b> .....	236
Figure 121. Key HMBC and COSY Correlations of Compounds <b>1-3</b> .....	239
Figure 122. Publications in the <i>Journal of Natural Products</i> on NMR calculations .....	251
Figure 123. LC-MS chromatograms of MSX59876 (Top) and MSX59260 (Bottom) .....	251
Figure 124. LC-MS chromatogram and (+)-HRESIMS spectrum of compound <b>1</b> .....	252
Figure 125. $^1\text{H}$ NMR spectrum (400 MHz, Top) and $^{13}\text{C}$ NMR spectrum (100 MHz, Bottom) both in $\text{CDCl}_3$ , of dihydroacremonol ( <b>1</b> ) .....	252
Figure 126. HSQC spectrum of dihydroacremonol ( <b>1</b> ), $\text{CDCl}_3$ , 400 MHz .....	253
Figure 127. HMBC spectrum of dihydroacremonol ( <b>1</b> ), $\text{CDCl}_3$ , 400 MHz .....	254
Figure 128. $^1\text{H}$ COSY spectrum of dihydroacremonol ( <b>1</b> ), $\text{CDCl}_3$ , 400 MHz .....	255
Figure 129. LC-MS chromatogram and (+)-HRESIMS spectrum of compound <b>2</b> .....	255
Figure 130. $^1\text{H}$ NMR spectrum (400 MHz, Top) and $^{13}\text{C}$ NMR spectrum (100 MHz, Bottom) both in $\text{CDCl}_3$ , of clonostachyone ( <b>2</b> ).....	256
Figure 131. HSQC spectrum of clonostachyone ( <b>2</b> ), $\text{CDCl}_3$ , 400 MHz .....	257
Figure 132. HMBC spectrum of clonostachyone ( <b>2</b> ), $\text{CDCl}_3$ , 400 MHz.....	258
Figure 133. $^1\text{H}$ COSY spectrum of clonostachyone ( <b>2</b> ), $\text{CDCl}_3$ , 400 MHz .....	259
Figure 134. LC-MS chromatogram and (+)-HRESIMS spectrum of compound <b>3</b> .....	259

Figure 135. $^1\text{H}$ NMR spectrum (700 MHz, Top) and $^{13}\text{C}$ NMR spectrum (175 MHz, Bottom) both in $\text{CDCl}_3$ , of acremodiol B ( <b>3</b> ).....	260
Figure 136. HSQC spectrum of acremodiol B ( <b>3</b> ), $\text{CDCl}_3$ , 700 MHz .....	261
Figure 137. HMBC spectrum of acremodiol B ( <b>3</b> ), $\text{CDCl}_3$ , 700 MHz.....	262
Figure 138. $^1\text{H}$ COSY spectrum of acremodiol B ( <b>3</b> ), $\text{CDCl}_3$ , 700 MHz .....	263
Figure 139. LC-MS chromatogram and (+)-HRESIMS spectrum of compound <b>4</b> .....	263
Figure 140. $^1\text{H}$ NMR spectrum (700 MHz, Top) and $^{13}\text{C}$ NMR spectrum (175 MHz, Bottom) both in $\text{CDCl}_3$ , of acremodiol C ( <b>4</b> ).....	264
Figure 141. HSQC spectrum of acremodiol C ( <b>4</b> ), $\text{CDCl}_3$ , 700 MHz.....	265
Figure 142. HMBC spectrum acremodiol C ( <b>4</b> ), $\text{CDCl}_3$ , 700 MHz .....	266
Figure 143. $^1\text{H}$ COSY spectrum of acremodiol C ( <b>4</b> ), $\text{CDCl}_3$ , 700 MHz .....	267
Figure 144. $^1\text{H}$ NMR spectrum comparison of acremodiol B ( <b>3</b> ; Top) and acremodiol C ( <b>4</b> ; Bottom), both in $\text{DMSO}-d_6$ , 300 MHz on the 400 MHz NMR.....	268
Figure 145. $^1\text{H}$ NMR spectrum comparison of acremodiol B ( <b>3</b> ; Top) and acremodiol C ( <b>4</b> ; Bottom), both in $\text{CDCl}_3$ on the 400 MHz NMR.....	269
Figure 146. Phylogeny of MSX59260 and MSX59876 .....	270
Figure 147. The structure used in GIAO NMR calculations.....	271

## CHAPTER I

### INTRODUCTION

Fungi are morphologically, phylogenetically, and chemically diverse with estimates ranging from 2 to 5 million species.<sup>1, 2</sup> They naturally grow in a broad range of environments, such as soil, rhizospheres, plants, and human fluids and tissues.<sup>3, 4</sup> This environmental diversity leads to a high chemical diversity, which fungi can biosynthetically produce and jettison into their environment.<sup>5</sup> These chemicals are known as secondary metabolites, which are small molecular weight compounds that are not necessary for growth and reproduction but are likely biosynthesized for self-protection and to gain an ecological advantage.<sup>6, 7</sup>

Fungi produce a wide range of secondary metabolites, such as mycotoxins, pigments, and antibiotics.<sup>6-8</sup> Secondary metabolite biosynthesis is encoded by biosynthetic gene clusters,<sup>9-12</sup> these gene clusters encode for several pathways, such as polyketide synthase (PKSs), non-ribosomal peptide synthases (NRPSs), as well as pathways that lead to terpenes.<sup>10, 12, 13</sup> With recent advances in the next generation sequencing of fungal genomes, secondary metabolites can now be linked to their biosynthetic gene clusters at least for those clusters which are known to produce a product(s).<sup>14-19</sup> Fungi are pathogenic to plants, humans and animals, and secondary metabolites produced by fungi are implicated in these interactions.<sup>17, 20-22</sup>

*Aspergillus fumigatus* is a common sporulating fungus found in the environment. Healthy individuals exposed to *A. fumigatus* will have little to no symptoms while people with compromised immune systems are at a greater risk of life-threatening alterations.<sup>23, 24</sup> *Aspergillus fumigatus* infections can range from mild to severe. The most severe and life threatening is invasive aspergillosis, which commonly only affects immunocompromised individuals (weakened immune systems).<sup>25</sup> *Aspergillus fumigatus* has many traits that enable it to become an invasive human pathogen, these traits are known as “cards of virulence”.<sup>26</sup> Some of these “cards of virulence” are secondary metabolites that allow *A. fumigatus* to protect itself from the host immune response, impair the host immune system, or acquire key nutrients.<sup>20, 27-33</sup> Some of the important secondary metabolites are gliotoxin which helps *A. fumigatus* evade the host immune response;<sup>34, 35</sup> fumitremorgin which inhibits the breast cancer resistance protein;<sup>36</sup> fumagillin which causes epithelial cell damage<sup>37, 38</sup> and impairs the function of neutrophils;<sup>39, 40</sup> and pseurotin which inhibits immunoglobulin E.<sup>41</sup>

In the family Aspergillaceae, section *Fumigati*, *A. fischeri* and *A. oerlinghausenensis* are perceived as the closest relative to *A. fumigatus*. Yet, *A. fischeri* and *A. oerlinghausenensis* are rarely seen to cause aspergillosis, the main divergence in their genomes is in the genes that encode for secondary metabolite biosynthesis.<sup>42</sup> For example, ~85% of the non-secondary metabolism genes are conserved between *A. fumigatus* and *A. fischeri* including 48/49 genes known to be involved in virulence.<sup>16, 22</sup> However, only 10/33 of *A. fumigatus* biosynthetic gene clusters are conserved in *A. fischeri*.<sup>16</sup> It is important to gain insights into the underlying cause of this difference in pathogenicity. Secondary metabolites gene cluster seem to be the most divergent and seem to play a key role in virulence.<sup>16</sup> Thus, it is essential to understand how chemical

diversity of secondary metabolites produced by these closely related yet diverse genotypes contributes to the evolution of a deadly pathogen.

Genome studies have shown that fungi have a rich diversity of secondary metabolite pathways, but the genes and gene clusters in these biosynthetic pathways, and their secondary metabolite products, are largely unknown.<sup>13, 43-50</sup> With so much unknown biosynthetic potential, there is a pressing need to uncover ways to turn on secondary metabolite biosynthesis in fungi, potentially uncovering new chemical diversity. Interaction-driven secondary metabolite discovery (i.e. co-culturing) has been used to activate these silent biosynthetic gene clusters.<sup>15, 51-56</sup> It works by mimicking the complex environments in which fungi naturally interact.<sup>3, 4, 29</sup> Co-culturing can cause stress for nutrients and space on both fungi, and it could accelerate the activation of unique secondary metabolites that may give a survival edge to the fungus.<sup>3, 57-61</sup> However, under standard laboratory conditions, fungi have been shown to produce only a fraction of their potential secondary metabolites,<sup>10, 18, 43, 47-49</sup> but not other silent secondary metabolites, which are hypothesized to be active in the context of ‘fighting’ with another organism. Therefore, the strategy of co-culturing two fungi in a controlled environment can be a practical application for undiscovered secondary metabolites through interspecies crosstalk.<sup>43</sup> These fungi are confined to a space with limited nutrients and territory, which will cause them to interact by mostly two ways: 1) the inhibition of one fungus, or 2) one fungus will use up all the resources, which will make them not available for the other fungus, essentially causing it to stress.<sup>62</sup> Such experimental studies shed light on the biological roles of secondary metabolites in fungi as well as increase knowledge of fungal chemical diversity.

The accurate characterization of secondary metabolites is important since they play a key role in a variety of different biological functions. Secondary metabolite characterization is primarily done through the determination of the molecular formula (mass spectrometry) and the interpretation of a suite of NMR experiments.<sup>63-68</sup> During the structure elucidation process many factors can lead to the assignment of an incorrect structure,<sup>69-71</sup> with some of the most common being double bonds<sup>72-76</sup> and a change in functional group locations.<sup>77, 78</sup> There is the need for the development of orthogonal techniques to either assign or verify the *de novo* structure elucidation of secondary metabolites. In 2008,<sup>79</sup> ozone-induced dissociation mass spectrometry (OzID-MS) was introduced into the field of lipidomics to identify the location of double bonds.<sup>80-85</sup> The mechanism of OzID-MS is based on the fundamentals of the ozonolysis reaction and takes place in the gas phase inside a mass spectrometer.<sup>86</sup> This results in a predictable cleavage pattern that accurately pinpoints the location of double bonds, which can serve as an orthogonal structure elucidation tool.<sup>79, 80, 82, 85</sup> Identification of the absolute configuration of secondary metabolites also plays a key role in biological function.<sup>87</sup> There are several traditional methods to probe the relative/absolute configuration of natural products, such as, total synthesis,<sup>88-90</sup> X-ray crystallography,<sup>91-94</sup> Mosher's ester method,<sup>95, 96</sup> Marfey's reagent,<sup>97, 98</sup> NOESY/ROSEY NMR,<sup>64</sup> and ECD (Electric Circular Dichroism).<sup>99, 100</sup> While all these methods provide accurate results, not all secondary metabolites are created equal and there is need for the development and use of new methods. GIAO NMR and optical rotation calculations have been shown to accurately provide the absolute configuration of a broad range of natural products, by calculating the <sup>1</sup>H and <sup>13</sup>C NMR data and the [α]<sub>D</sub>.<sup>101-111</sup>

This dissertation represents part of the findings of my research, which studies the secondary metabolism of Ascomycota fungi. Specific focus includes understanding the chemical difference between pathogenic and non-pathogenic fungi; co-culturing fungi to increase chemical diversity, as a source of biologically active novel scaffolds, and development of techniques to aid in the structure elucidation of secondary metabolites.

This dissertation includes chapters devoted to the isolation, characterization, chemometric analysis, and biological assessment of secondary metabolites from Ascomycota fungi for the understanding of how secondary metabolites differ between related species. So far, 9 strains have been genetically and chemically characterized, with more than 30 compounds identified from several different environmental conditions.

Chapters 2-4 presents the understanding the secondary metabolites produced by section Fumigati fungi and how they are chemically and genetically related. The optimal growth media for secondary metabolite production in *Aspergillus fischeri* (NRRL 181) was identified to be oatmeal, and ten secondary metabolites (3 new and 7 known) were characterized and compared to *A. fumigatus* secondary metabolism (Chapter 2). Gliotoxin was identified to be biosynthesized from *A. fischeri* (NRRL 181) when grown at 37°C on Czapek Dox agar and 5% blood agar (Chapter 3).

Three *A. fumigatus* strains, (Af293, CEA10, CEA17), three *A. fischeri* (NRRL 181, NRRL 4161, NRRL 4585) and one strain of *A. oerlinghausenensis* (CBS 139183) were grown at three different temperatures (23°C, 30°C, 37°C). These strains were chemically characterized and chemometrics was preformed to compare the chemical variation across section Fumigati (Chapter 4).

Chapters 5 and 6 focused on co-culturing *A. fischeri* with *Xylaria flabelliformis* (formally known as *Xylaria cubensis*) to induce secondary metabolites not seen under traditional laboratory conditions. The fungi were paired due to the antifungal ability of *X. flabelliformis* and their genetic tractability. *Aspergillus fischeri* produces a suite of mycotoxins whereas *X. flabelliformis* produces the FDA approved antifungal griseofulvin. When these fungi were paired both had to adapt to their new surrounding and this led to the activation of silent biosynthetic gene clusters. During this interspecific interaction 18 secondary metabolites were characterized. The spatial location of these metabolites during mono and co-culture was obtained to understand how these fungi chemically respond to environmental cues (Chapter 5). One novel secondary metabolite with cytotoxic activities was described (Chapter 6)

Chapters 7 and 8 focus on the development of new techniques that aid in the structure elucidation of secondary metabolites. Ozone-Induced Dissociation Mass Spectrometry (OzID-MS) was utilized for the identification of double bond placement in secondary metabolites. Four known metabolites were used as a test case to confirm the accuracy of OzID-MS on secondary metabolites. One new secondary metabolite was identified, and this method was used orthogonally to confirm the structure as a pure compound, in the context of an extract, and *in situ*. (Chapter 7). NMR and optical rotation calculations were used to determine the absolute configuration of secondary metabolites, where traditional methods were unsuccessful. These methods enabled the identification of absolute configuration of four new bioactive bislactones were characterize (Chapter 8).

CHAPTER II

CHARACTERIZING THE PATHOGENIC, GENOMIC, AND CHEMICAL TRAITS OF  
*ASPERGILLUS FISCHERI*, A CLOSE RELATIVE OF THE MAJOR HUMAN FUNGAL  
PATHOGEN *ASPERGILLUS FUMIGATUS*

Matthew E. Mead, Sonja L. Knowles, Huzefa A. Raja, Sarah R. Beattie, Caitlin H. Kowalski, Jacob L. Steenwyk, Lilian P. Silva, Jessica Chiaratto, Laure N.A. Ries, Gustavo H. Goldman, Robert A. Cramer, Nicholas H. Oberlies, and Antonis Rokas.  
*mSphere* 2019, 4, e00018-19.

*Aspergillus fischeri* is closely related to *Aspergillus fumigatus*, the major cause of invasive mold infections. Even though *A. fischeri* is commonly found in diverse environments, including hospitals, it rarely causes invasive disease. Why *A. fischeri* causes less human disease than *A. fumigatus* is unclear. A comparison of *A. fischeri* and *A. fumigatus* for pathogenic, genomic, and secondary metabolic traits revealed multiple differences in pathogenesis-related phenotypes. We observed that *A. fischeri* NRRL 181 is less virulent than *A. fumigatus* strain CEA10 in multiple animal models of disease, grows slower in low oxygen environments, and is more sensitive to oxidative stress. Strikingly, the observed differences for some traits are of the same order of magnitude as those previously reported between *A. fumigatus* strains. In contrast, similar to what has previously been reported, the two species exhibit high genomic similarity; ~90% of the *A. fumigatus* proteome is conserved in *A. fischeri*, including 48/49 genes known to be involved in *A. fumigatus* virulence. However, only 10/33 *A. fumigatus* biosynthetic gene clusters (BGCs) likely involved in secondary metabolite production are conserved in *A. fischeri* and only 13/48 *A. fischeri* BGCs are conserved in *A. fumigatus*.

Detailed chemical characterization of *A. fischeri* cultures grown on multiple substrates identified multiple secondary metabolites, including two new compounds and one never before isolated as a natural product. Additionally, an *A. fischeri* deletion mutant of laeA, a master regulator of secondary metabolism, produced fewer secondary metabolites and in lower quantities, suggesting that regulation of secondary metabolism is at least partially conserved. These results suggest that the non-pathogenic *A. fischeri* possesses many of the genes important for *A. fumigatus* pathogenicity but is divergent with respect to its ability to thrive under host-relevant conditions and its secondary metabolism.

*Aspergillus fumigatus* is the primary cause of aspergillosis, a devastating ensemble of diseases associated with severe morbidity and mortality worldwide. *A. fischeri* is a close relative of *A. fumigatus*, but is not generally observed to cause human disease. To gain insights into the underlying causes of this remarkable difference in pathogenicity, we compared two representative strains (one from each species) for a range of pathogenesis-relevant biological and chemical characteristics. We found that disease progression in multiple *A. fischeri* mouse models was slower and caused less mortality than *A. fumigatus*. Remarkably, the observed differences between *A. fischeri* and *A. fumigatus* strains examined here closely resembled those previously described for two commonly studied *A. fumigatus* strains, AF293 and CEA10. *A. fischeri* and *A. fumigatus* exhibited different growth profiles when placed in a range of stress-inducing conditions encountered during infection, such as low levels of oxygen and the presence of chemicals that induce the production of reactive oxygen species. We also found that the vast majority of *A. fumigatus* genes known to be involved in virulence are conserved in *A. fischeri*, whereas the two species differ significantly in their secondary metabolic

pathways. These similarities and differences that we report here are the first step toward understanding the evolutionary origin of a major fungal pathogen.

Aspergillosis is a major cause of human morbidity and mortality, resulting in over 200,000 life-threatening infections each year worldwide, and is primarily caused by the filamentous fungus *Aspergillus fumigatus*.<sup>112</sup> Multiple virulence traits related to Invasive Aspergillosis (IA) are known for *A. fumigatus*, including growth at human body temperature and in low oxygen conditions, the ability to acquire micronutrients such as iron and zinc in limiting environments, and the production of a diverse set of secondary metabolites.<sup>112</sup>

Growth at human body temperature is a key trait for the survival of *A. fumigatus* inside mammalian hosts and may have arisen through adaptation to the warm temperatures present in decaying compost piles, one of the organism's ecological niches.<sup>113-115</sup> The primary route of *A. fumigatus* colonization and infection is through the lung, where oxygen levels have been observed to be as low as 2/3 of atmospheric pressure during infection. A successful response to this hypoxic environment is required for fungal pathogenesis.<sup>116, 117</sup> Moreover, *A. fumigatus* produces a diverse set of small, bioactive molecules, known as secondary metabolites, which are biosynthesized in pathways that are often encoded by Biosynthetic Gene Clusters (BGCs).<sup>10</sup> Some of these secondary metabolites and their regulators have been shown to contribute to disease in mouse models.<sup>11, 18, 20</sup> Furthermore, a master regulator of secondary metabolism, *IaeA*, is required for full virulence in IA mouse model studies.<sup>118, 119</sup>

Species closely related to *A. fumigatus* are also capable of causing disease, but they are rarely observed in the clinic.<sup>112, 120-122</sup> For example, *A. fischeri* is the closest evolutionary relative to *A. fumigatus* for which a genome has been sequenced,<sup>123, 124</sup> but

it is rarely reported to cause human disease.<sup>112</sup> Recent evolutionary genomic analyses suggest that *A. fischeri* and *A. fumigatus* last shared a common ancestor approximately 4 million years ago (95% credible interval: 2 – 7 million years ago).<sup>124</sup> Why *A. fischeri*-mediated disease is less common than *A. fumigatus*-mediated disease remains an open question. Non-mutually exclusive possibilities include differences in ecological abundance, lack of species-level diagnosis of disease-causing strains in the clinic, and innate differences in pathogenicity and virulence between the two species.

Previous studies have suggested that the difference in the frequencies with which the two species cause disease is unlikely to be solely due to ecological factors, as both can be isolated from a variety of locales, including soils, fruits, and hospitals.<sup>125-127</sup> For example, approximately 2% of the fungi isolated from the respiratory intensive care unit at Beijing Hospital were *A. fischeri* compared to approximately 23% of fungal species identified as *A. fumigatus*.<sup>127</sup> While *A. fischeri* is easily isolated from a variety of environments, only a few cases of human infections have been reported.<sup>128-131</sup> Furthermore, numerous recent epidemiological studies from multiple countries that used state-of-the-art molecular typing methods were able to identify several rarely isolated pathogenic species closely related to *A. fumigatus*, such as *A. lentulus* and *A. udagawae*, as the source of 10-15% of human infections but did not identify *A. fischeri* in any patient sample.<sup>120, 121, 132-134</sup>

If ecological factors and lack of precision in species identification do not convincingly explain why *A. fischeri* is non-pathogenic and *A. fumigatus* is pathogenic, other factors must be responsible. An initial genomic comparison between strains of *A. fumigatus*, *A. fischeri*, as well as the more distantly related *Aspergillus clavatus* identified 818 genes that were *A. fumigatus*-specific.<sup>123</sup> These genes were enriched for functions

associated with carbohydrate transport and catabolism, secondary metabolite biosynthesis, and detoxification,<sup>123</sup> raising the possibility that the observed differences in pathogenicity observed between *A. fischeri* and *A. fumigatus* have a molecular basis.

To gain further insight into why *A. fischeri*-mediated disease is less abundant than *A. fumigatus*-mediated disease, we took a multi-pronged approach to investigate phenotypic, genomic, and chemical differences between *A. fischeri* strain NRRL 181 and *A. fumigatus* strain CEA10. We observed that while *A. fischeri* is able to cause fatal disease in multiple animal models, its disease progression and response to multiple host-relevant stresses is markedly reduced when compared to *A. fumigatus* CEA10. We also found that while the two organisms' genomes are in general very similar, the sets of secondary metabolite pathways in each of them exhibit a surprisingly low level of overlap. Examination of the secondary metabolite profile of *A. fischeri* identified both previously isolated as well as novel compounds. Finally, construction of a mutant *A. fischeri* strain that lacked the *laeA* gene, a master regulator of secondary metabolism, and examination of its chemical profile suggested that LaeA-mediated regulation of secondary metabolism in *A. fischeri* closely resembles that of *A. fumigatus*. These results begin to reveal the molecular differences between *A. fischeri* and *A. fumigatus* related to fungal pathogenesis and suggest that a functional evolutionary genomic comparison between pathogenic and non-pathogenic species closely related to *A. fumigatus* harbors great promise for generating insights into the evolution of fungal disease.

## Results

**A. fischeri is Less Virulent Than A. fumigatus in Multiple Animal Models of Invasive Pulmonary Aspergillosis (IPA).** In contrast to *A. fumigatus*-mediated disease, only a handful of cases of invasive fungal infections have been reported to be caused by *A. fischeri*.<sup>128-131</sup> Given this contrast, we utilized two immunologically distinct murine IPA models to assess differences in pathogenicity and virulence between the two species. In a leukopenic murine model, *A. fischeri* NRRL 181 was significantly less virulent than *A. fumigatus* CEA10, in a dose dependent manner (Figure 1A). Using an inoculum of  $1 \times 10^5$  conidia, *A. fischeri* was completely attenuated in virulence, with 100% murine survival by day 15 post-fungal challenge. In contrast, inoculation with *A. fumigatus* resulted in 100% murine mortality by day 15 (Figure 1A). Using a higher dose ( $2 \times 10^6$ ) of conidia, both strains caused 90% mortality by day 14; however, the disease progression was markedly different. 80% of mice inoculated with *A. fumigatus* succumbed to infection by day 4, whereas in mice inoculated with *A. fischeri*, mortality started occurring on day 5, and then one or two mice succumbed each day until day 14 (Figure 1A). Thus, despite the similar overall mortality at higher fungal challenge doses, *A. fischeri* is substantially less virulent than *A. fumigatus* in a leukopenic murine IPA model.

To better understand what is happening *in vivo* during disease progression with *A. fischeri* NRRL 181 and *A. fumigatus* CEA10, we performed histological analyses on lungs from the leukopenic model 3 days post inoculation. Histological sections were stained with Gomori methenamine silver (GMS) to visualize fungal burden and with hematoxylin and eosin (H&E) stain to visualize host related pathology (Figure 1C). Leukopenic mice inoculated with *A. fumigatus* had an overall greater number of fungal lesions per animal than mice inoculated with *A. fischeri*. These *A. fumigatus* lesions

contained a greater amount of fungus, which coincided with increased tissue necrosis surrounding the lesions. There was also a greater number of *A. fumigatus* lesions with fungi invading from the larger airways into the lung parenchyma. Meanwhile, the *A. fischeri* lesions were largely maintained within the larger airways. A striking difference between the lesions caused by the two species was in the appearance of the hyphae of the two species, where *A. fischeri* filaments were much shorter than those of *A. fumigatus*. We hypothesize that in the leukopenic mouse, *A. fischeri* is unable to grow as well as *A. fumigatus*, resulting in smaller and fewer fungal lesions, shorter fungal filaments, and attenuation of virulence.

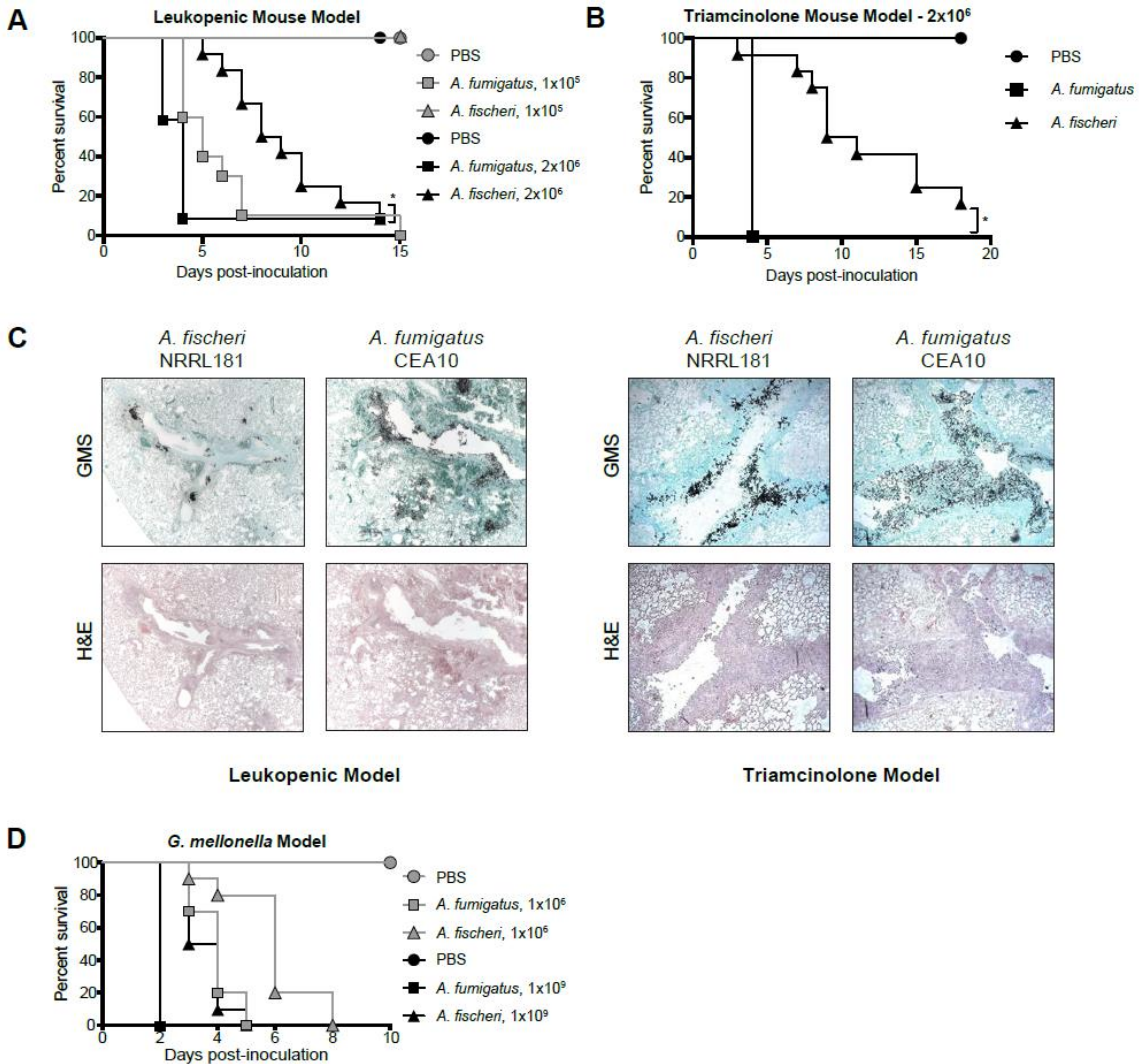


**Figure 1.** *A. fischeri* is Significantly Less Virulent than *A. fumigatus* in Multiple Murine Models of Invasive Pulmonary Aspergillosis. A) Cumulative survival of mice inoculated with 1x10<sup>5</sup> (gray) or 2x10<sup>6</sup> (black) conidia in a leukopenic model of IPA. For the 1x10<sup>5</sup> inoculations, 10 mice were infected per group and for the 2x10<sup>6</sup> inoculations, 12 mice were infected per group. For each PBS control, 4 mice were inoculated. \*p=0.0098 by Log-Rank test, p=0.0002 by Gehan-Breslow-Wilcoxon test. B) Cumulative survival of mice inoculated with 2x10<sup>6</sup> conidia in a steroid model of IPA. n=12/group, 4/PBS. \*p=<0.0001 by Log-Rank and Gehan-Breslow-Wilcoxon tests. C) Histological sections from 3 days post inoculation in a leukopenic (left) and steroid (right) model of IPA stained with H&E and GMS. Images were acquired at 100x. D) Cumulative survival of *G. mellonella* larvae inoculated with 1x10<sup>6</sup> (gray) or 1x10<sup>9</sup> (black) conidia. 10 larvae were used per condition in all assays. Survival curves for *A. fischeri* and *A. fumigatus* were significantly different (p<0.003) in both Log-Rank and Gehan-Breslow-Wilcoxon tests for both inoculums.

As the patient population at risk for IA continues to change and grow,<sup>135</sup> we next tested a non-leukopenic, triamcinolone (steroid)-induced immune suppression model and observed a significant reduction in virulence of *A. fischeri* compared to *A. fumigatus* ( $p<0.0001$  by Log-Rank and Gehan-Breslow-Wilcoxon tests). All mice inoculated with *A. fumigatus* succumbed to infection by day 4; however, similar to the leukopenic model, mice inoculated with *A. fischeri* had significantly slower disease progression as monitored by Kaplan-Meier analyses (Figure 1B).

Histological analyses were also carried out on lungs from the steroid model 3 days post fungal inoculation (Figure 2C). Overall, mice inoculated with *A. fischeri* in the steroid model had similar numbers of fungal lesions as those inoculated with *A. fumigatus*, but the lesions caused by the two species were phenotypically distinct (Figure 1C). In larger terminal bronchioles infected with *A. fumigatus*, there was greater fungal growth per lesion, and the growth was observed throughout the bronchiole itself, extending well into the lumen. These lesions were accompanied by substantial granulocytic inflammation and obstructed the airways surrounding the hyphae (Figure 1C). In the lesions containing *A. fischeri*, the fungal growth was contained to the epithelial lining of the bronchioles. This pattern of growth was accompanied by inflammation at the airway epithelia, leaving the airway lumen largely unobstructed (Figure 1C). The lack of airway obstruction during *A. fischeri* infection and reduced inflammation may contribute to the reduced virulence compared to *A. fumigatus* in this murine model.

Although the distribution of the fungal lesions varied, there was still significant fungal growth in the steroid immunosuppressed mice infected with *A. fischeri*, suggesting that *A. fischeri* is capable of growing within the immune compromised murine

host. Indeed, we tested the growth rate of *A. fischeri* and *A. fumigatus* in lung homogenate as a proxy for growth capability within the nutrient environment of the host and observed no difference between the two strains (Figure 6). These experiments show that in multiple models of fungal disease, *A. fischeri* is less virulent than *A. fumigatus* even though it is able to grow within the immune compromised murine lung.

We observed similar pathogenicity and virulence results when using the *Galleria mellonella* insect larvae model of aspergillosis (Figure 1D). Both low ( $1 \times 10^6$  conidia) and high ( $1 \times 10^9$  conidia) inoculum experiments showed significant differences between the disease progression of *A. fischeri* (slower) and *A. fumigatus* (faster) in this insect model of fungal pathogenicity.

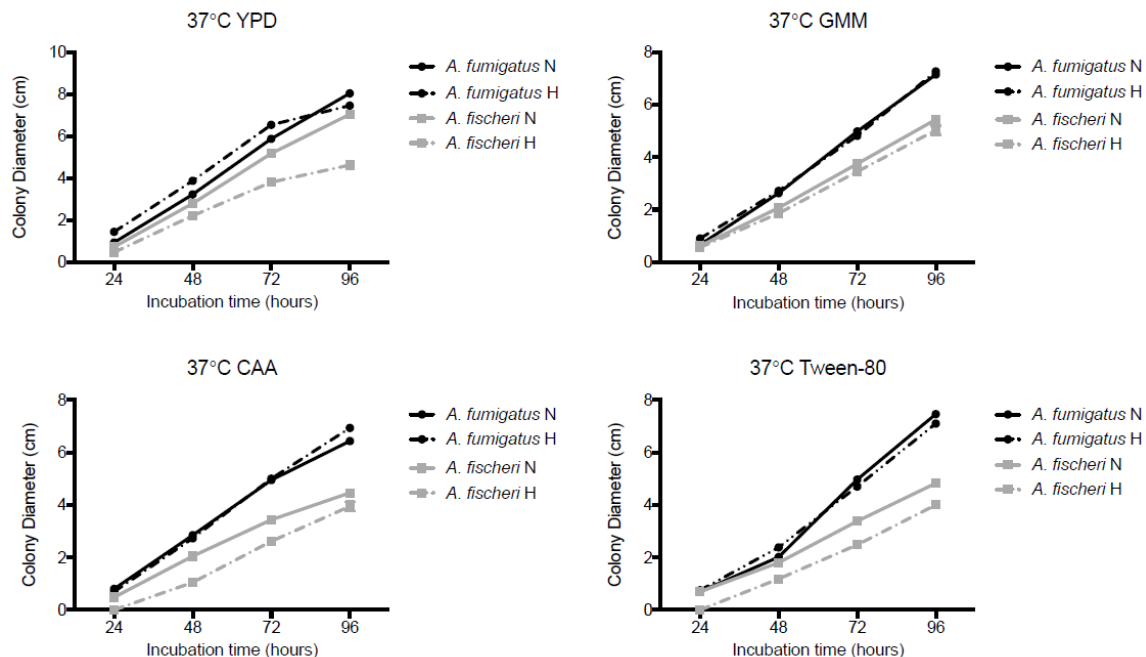


**Figure 2.** *A. fischeri* is Unable to Thrive Under Suboptimal Metabolic Conditions at 37°C.  $1 \times 10^3$  conidia were point inoculated on each plate, then plates were incubated at 37°C in normoxia (N; ~21% oxygen, 5%CO<sub>2</sub>) or hypoxia (H; 0.2% O<sub>2</sub>, 5%CO<sub>2</sub>); colony diameter was measured every 24 hours. Mean and SEM of triplicates. CAA – Casamino acids; GMM – glucose minimal media.

### **When Compared to *A. fumigatus*, *A. fischeri* Differs in its Response to**

**Several Host-Relevant Stresses.** Our *in vivo* experiments suggested that the lower virulence of *A. fischeri* is not the result of an inability to grow within the host *per se*. Therefore, we hypothesized that *A. fischeri* is unable to mitigate stresses encountered in the host as effectively as its close evolutionary relative, *A. fumigatus*. Nutrient fluctuation is a stress encountered *in vivo* during *A. fumigatus* infection,<sup>136</sup> and to assess differences in metabolic plasticity between the two species, we measured the two organisms' growth on media supplemented with glucose, fatty acids (Tween-80), or casamino acids. Because low oxygen tension is a significant stress encountered during infection,<sup>116</sup> and recently, fitness in low oxygen has been correlated to virulence of *A. fumigatus*,<sup>137</sup> we measured growth of both species at 37°C in both normoxic (ambient air) and hypoxia-inducing (0.2% O<sub>2</sub>, 5% CO<sub>2</sub>) conditions. In normoxia with glucose, fatty acids (Tween-80), or casamino acids supplied as the carbon source, radial growth of *A. fischeri* was reduced when compared to *A. fumigatus* (Figure 2). However, on rich media both organisms grew equally well (Figure 2). We also observed a slower growth rate of *A. fischeri* compared to *A. fumigatus* in the first 16 hours of culture in liquid media supplied with glucose at 37°C. At 30°C, *A. fischeri* grew the same as, or better than, *A. fumigatus* except on Tween-80 where *A. fumigatus* had a slight advantage (Figure 7). Also, *A. fischeri* grew substantially worse than *A. fumigatus* when grown at 44°C (Figure 7), a temperature rarely observed in the patient but easily observed in compost piles. To determine relative fitness in hypoxic liquid environments, we measured the ratio of biomass in liquid culture in ambient air (normoxia) versus hypoxic (0.2% O<sub>2</sub>, 5%CO<sub>2</sub>) conditions. *A. fischeri* showed significantly lower fitness in hypoxic conditions, with about an 8.5-fold lower biomass than *A. fumigatus* (Figure 3A). These data suggest that *A.*

*fischeri* is less fit than *A. fumigatus* at 37°C and in low oxygen conditions, both of which have been shown to impact fungal virulence.

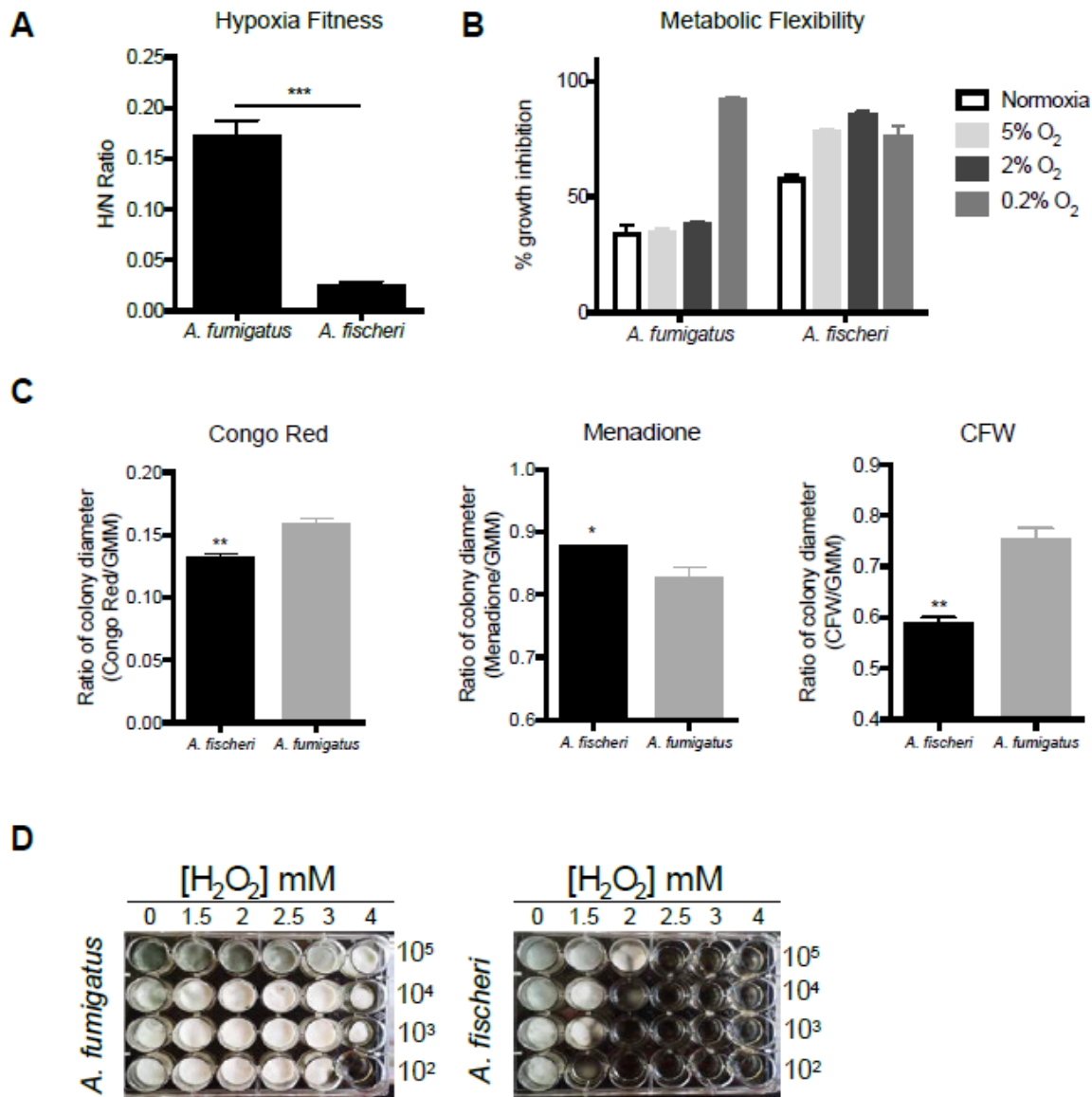


**Figure 3.** *A. fischeri* is More Susceptible to Multiple Host-Relevant Stresses Than *A. fumigatus*. A) Fitness ratio of *A. fumigatus* or *A. fischeri* during hypoxic vs normoxic growth (measured as the dry weight of cultures). Data represent mean and SEM of biological triplicates; \*\*\*p=0.0006 by Student's t-test. B) Growth inhibition of strains grown on 1% lactate minimal media with 0.1% 2-deoxyglucose (2-DG) under a range of low oxygen conditions. C) *A. fumigatus* and *A. fischeri* were grown in the presence of the

cell wall perturbing agent Congo Red (0.5mg/mL), the oxidative stressor Menadione (20  $\mu$ M), or the chitin perturbing agent Calcofluor White (CFW, 25 $\mu$ g/mL). Plates were grown for 96 hours at 37°C and 5% CO<sub>2</sub>. For all plates except Congo Red and its GMM control, 1x10<sup>3</sup> spores were plated. For Congo Red and the control GMM plate 1x10<sup>5</sup> spores were plated. Student's t-test was performed where \*: p<0.05, \*\*: p<0.01. D) Strains were grown for 48 h at 37°C in liquid complete medium supplemented with increasing concentrations of hydrogen peroxide.

Metabolic flexibility, or the ability for an organism to utilize multiple carbon sources simultaneously, has been suggested to provide a fitness advantage to *Candida albicans* during *in vivo* growth.<sup>138</sup> Metabolic flexibility can be characterized using the glucose analog, 2-deoxyglucose (2-DG), in combination with an alternative carbon source available *in vivo*, such as lactate. 2-DG triggers carbon catabolite repression, which shuts down alternative carbon utilization pathways. However, in *C. albicans* this shut down is delayed and growth occurs on lactate with 2-DG.<sup>138, 139</sup> We tested the metabolic flexibility of both *A. fumigatus* and *A. fischeri* and observed that while both species can grow in the presence of 2-DG on lactate, the growth inhibition of *A. fischeri* is higher (~60%) than that of *A. fumigatus* (~35%; Figure 3B). Even under low oxygen conditions (5% and 2%), *A. fumigatus* maintains this metabolic flexibility except under extremely low oxygen conditions (0.2%), whereas *A. fischeri* shows even greater inhibition at all oxygen tensions of 5% or below. These data suggest that while both species exhibit some level of metabolic flexibility, *A. fumigatus* appears more metabolically flexible under a wider range of conditions than *A. fischeri*.

Next, we measured the susceptibility of *A. fischeri* to oxidative stress, cell wall stress, and antifungal drugs as they are stresses that are encountered during infection and treatment.<sup>140</sup> Interestingly, we observed that *A. fischeri* is more resistant to the intracellular oxidative stress agent menadione than *A. fumigatus* but more susceptible to the external oxidative stress agent hydrogen peroxide (Figure 3CD). As the *in vivo* levels

of inflammation caused by the two species appeared different, we indirectly tested for differences in cell wall pathogen-associated molecular patterns using the cell wall perturbing agents Congo Red and Calcofluor White. *A. fumigatus* was significantly more resistant to both agents than *A. fischeri* (Figure 3C), suggesting differences in the response to cell wall stress or in the composition and organization of the cell wall between the two species. These differences are likely important for host immune cell recognition and interaction, which in turn influences pathology and disease outcome.

Lastly, *A. fischeri* showed enhanced resistance relative to *A. fumigatus* for three of the four antifungal drugs tested (Table 2.1), consistent with previous experiments.<sup>42</sup> Overall, our phenotypic data show that the response of *A. fischeri* to host-related stresses and antifungals is substantially different from that of *A. fumigatus*. Furthermore, our results suggest that increased growth capability of *A. fumigatus* in low oxygen and in high temperatures are two important attributes that likely contribute to its pathogenic potential compared to *A. fischeri*.

**Table 2.1.** *A. fischeri* Shows Enhanced Resistance Relative to *A. fumigatus* for Several Antifungal Drugs

<u>Strain</u>	<u>Posaconazole [µg/ml]</u>	<u>Voriconazole [µg/ml]</u>	<u>Itraconazole [µg/ml]</u>	<u>Caspofungin [µg/ml]</u>
<i>A. fumigatus</i>	0.7	0.8	5	0.09
<i>A. fischeri</i>	2.4	> 4	> 24	0.06

**The Proteomes of *A. fumigatus* and *A. fischeri* are Highly Similar, but Their Secondary Metabolic Pathways Show Substantial Divergence.** The large differences in virulence and virulence-related traits we observed between *A. fumigatus* and *A. fischeri* led us to investigate the genotypic differences that could be responsible. To

describe the genomic similarities and differences between *A. fumigatus* and *A. fischeri*, we determined how many orthologous proteins and how many species-specific proteins were present in each genome using a Reciprocal Best BLAST Hit approach.<sup>141</sup> We identified 8,737 proteins as being shared between the two species (Figure 8), representing 88% and 84% of the *A. fumigatus* and *A. fischeri* proteomes, respectively, and 1,684 *A. fischeri*-specific proteins (16% of its proteome) and 1,189 *A. fumigatus*-specific proteins (12% of its proteome). These results are similar to what had previously been reported in an early analysis of the *A. fischeri* genome.<sup>123</sup>

To narrow our search for genes that are absent in *A. fischeri* but are important for *A. fumigatus* disease, we compiled a list of 49 *A. fumigatus* genes considered to be involved in virulence (Table 2.3) based on two previously published articles<sup>142, 143</sup> and extensive literature searches of our own. We observed that all but one of these virulence-associated genes were also present in *A. fischeri*, a surprising finding considering the substantial differences observed between the two species in our animal models of infection. The virulence-associated gene not present in *A. fischeri* is *pesL* ([Afu6g12050](#)), a non-ribosomal peptide synthase that is essential for the synthesis of the secondary metabolite fumigaclavine C and required for virulence in the *Galleria* model of *A. fumigatus* infection.<sup>144</sup>

Since the only previously described *A. fumigatus* virulence-associated gene not present in the *A. fischeri* genome (i.e. *pesL*) is involved in secondary metabolism and a previous study suggested that secondary metabolism is not conserved between these two species,<sup>145</sup> we investigated the differences between the repertoire of secondary metabolic pathways present in *A. fumigatus* and *A. fischeri*. Using the program antiSMASH,<sup>146</sup> we identified 598 genes distributed amongst 33 BGCs in *A. fumigatus*

(Table 2.4) and 786 genes spread out over 48 BGCs in *A. fischeri* (Table 2.5). Of these 598 *A. fumigatus* genes, 407 (68%) had an orthologous gene that was part of an *A. fischeri* BGC. This level of conservation of BGC genes (68%) is much lower than the amount of conservation observed for the rest of the proteome (88%), illustrating the rapid rate at which fungal metabolic pathways evolve.<sup>147, 148</sup>

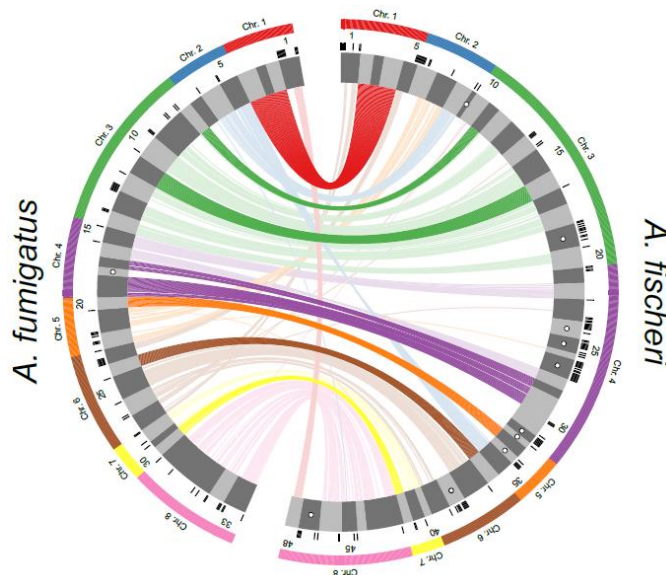


**Figure 4.** Biosynthetic Gene Clusters (BGCs) of *A. fumigatus* and *A. fischeri* Show Substantial Evolutionary Divergence. Predicted BGCs are shown in the inner track, are alternatively colored dark and light gray, and their size is proportional to the number of genes in them. Black ticks on the exterior of the cluster track indicate genes that possess an ortholog in the other species but are not in a BGC in the second species. White dots indicate species-specific clusters. Solid bars on the exterior correspond to the chromosome on which the BGCs below them reside. Genes are connected to their orthologs in the other species with dark lines if >90% of the BGC genes in *A. fumigatus* are conserved in the same BGC in *A. fischeri*. Lighter lines connect all other orthologs that are present in both species' sets of BGCs. Image was made using Circos version 0.69-4.<sup>149</sup>

We next directly compared the BGCs of the two organisms. An *A. fumigatus* BGC was considered conserved in *A. fischeri* if  $\geq 90\%$  of its genes were also present in an *A. fischeri* BGC and vice versa. We found that only 10 / 33 *A. fumigatus* BGCs are

conserved in *A. fischeri* and only 13 / 48 *A. fischeri* BGCs are conserved in *A. fumigatus* (Figure 4), a finding consistent with previous results<sup>145</sup> and the low conservation of individual secondary metabolic genes between the two species. While only 10 *A. fumigatus* BGCs were conserved in *A. fischeri*, many other BGCs contained one or more orthologs of genes in *A. fischeri* BGCs.

Only one BGC (Cluster 18) was completely *A. fumigatus*-specific. Interestingly, our previous examination of the genomes of 66 *A. fumigatus* strains showed that this BGC was a “jumping cluster”, as it was found to be present in only 5 strains and to reside in three distinct genomic locations.<sup>148</sup> Conversely, there are 10 *A. fischeri*-specific BGCs that do not have orthologs in BGCs in *A. fumigatus*. One of these BGCs is responsible for making helvolic acid [a gene cluster known to be absent from the *A. fumigatus* strain CEA10 but present in strain Af293],<sup>148</sup> but the other 9 have not been biochemically connected to any metabolite.

All the genes required for the production of the mycotoxin gliotoxin are located in a BGC in *A. fischeri* (Figure 9), and are in fact similar to their *A. fumigatus* orthologs,<sup>150</sup> even though *A. fischeri* is not known to produce this mycotoxin.<sup>151</sup> Both the gliotoxin and acetylaszonalenin BGCs are adjacent to one another in the *A. fischeri* genome (Figure 9). In *A. fumigatus*, the gliotoxin BGC is immediately next to what appears to be a truncated version of the acetylaszonalenin BGC that lacks portions of the nonribosomal peptide synthase and acetyltransferase genes as well as the entire indole prenyltransferase gene required for acetylaszonalenin production. The close proximity of these two BGCs is noteworthy, as it is similar to previously reported “super clusters” in *A. fumigatus* and *A. fumigatus*-related strains.<sup>152</sup> These super clusters have been

hypothesized to be “evolutionary laboratories” that may give rise to new compounds and pathways.<sup>148</sup>

### **Isolation and Characterization of Three New Compounds from *A. fischeri*.**

The relatively low level of conservation of BGCs we observed between *A. fumigatus* and *A. fischeri* led us to characterize the secondary metabolites produced by *A. fischeri* (Figure 10).<sup>96, 153-156</sup> The one strain-many compounds (OSMAC) approach was used to alter the secondary metabolites being biosynthesized in order to produce a diverse set of molecules.<sup>157-160</sup> Depending on the media on which it was grown, *A. fischeri* produced as few as 4 (Yeast Extract Soy Peptone Dextrose Agar - YESD) or as many as 10 compounds (Oatmeal Agar – OMA) (Figure 11). These results showed that culture media influences the biosynthesis of secondary metabolites in *A. fischeri*, a phenomenon observed in many other fungi.<sup>158, 161</sup>

To characterize the peaks of interest we observed when *A. fischeri* was grown on OMA, we increased the size of our fungal cultures; doing so yielded seven previously isolated compounds (sartorypyrone A (**1**), aszonalenin (**4**), acetylaszonalenin (**5**), fumitremorgin A (**6**), fumitremorgin B (**7**), verruculogen (**8**), and the C-11 epimer of verruculogen TR2 (**9**)) and three newly biosynthesized secondary metabolites (sartorypyrone E (**2**), 14-epi-aszonapyrone A (**3**), and 13-O-fumitremorgin B (**10**)). Two of the secondary metabolites were new compounds (**2** and **3**) and one was a new natural product (**10**) (Figure 5B). The structures for all 10 compounds were determined using a set of spectroscopic (1 and 2D NMR) and spectrometric techniques (HRMS). Our data for sartorypyrone A (**1**),<sup>162</sup> aszonalenin (**4**),<sup>163, 164</sup> acetylaszonalenin (**5**),<sup>162, 165</sup> fumitremorgin A (**6**),<sup>166, 167</sup> fumitremorgin B (**7**),<sup>19, 168, 169</sup> verruculogen (**8**),<sup>170, 171</sup> and the C-11 epimer of verruculogen TR2 (**9**)<sup>171</sup> correlated well with literature values (Figures 13,

14, 20-25). The structures of 14-*epi*-aszonapyrone A (**3**), and 13-O-prenyl fumitremorgin B (**10**) were fully characterized in this study; the structure elucidation of sartorypyrone E (**2**) is ongoing and will be reported in detail in a forthcoming manuscript.

The structures of compounds **1 - 10** were determined using a set of spectroscopic (1 and 2D NMR) and spectrometric techniques (HRMS), where the data for sartorypyrone A (**1**)<sup>162</sup>, aszonalenin (**4**)<sup>163, 164</sup>, acetylaszonalenin (**5**)<sup>162, 165</sup>, fumitremorgin A (**6**)<sup>166, 167</sup>, fumitremorgin B (**7**)<sup>19, 168, 169</sup>, verruculogen (**8**)<sup>170, 171</sup>, and 11-epimer of verruculogen TR-2 (**9**)<sup>171</sup>, compared favorably to the literature.

14 – *epi*-aszonapyrone A (**3**) (3.2mg) was obtained as a white solid. Its formula was C<sub>28</sub>H<sub>40</sub>O<sub>5</sub> based on the HRESIMS data, indicating nine degrees of unsaturation. Analysis of the <sup>1</sup>H and <sup>13</sup>C NMR data indicated the structure to be a cyclic diterpenoid, with a di-substituted fully-unsaturated δ-lactone. The <sup>1</sup>H and <sup>13</sup>C data were similar to those of aszonapyrone A <sup>162</sup>. Whereas there are slight differences around the C-14 chiral center, the <sup>1</sup>H shifts for C-14, C-15, and C-26 were shifted. However, the 1D and 2D NMR (Figure 30) data confirmed the planar structure to be the same as aszonapyrone A, this could indicate the inversion of the stereocenter. Through Nuclear Overhauser Effects Spectroscopy (NOESY) there were no correlations between the <sup>1</sup>Hs on C-14 and C-15 with those at C-25. Although the lack of correlations does not confirm the switch in stereochemistry, this combined with the 1D NMR shifts and 2D correlations, leads the absolute configuration of 14 – *epi*-aszonapyrone A at the C-14 position to be the S configuration (Figures 15-19).

13-O-prenyl-fumitremorgin B (**10**) (1.22mg) was obtained as a white solid. Its formula was C<sub>32</sub>H<sub>41</sub>N<sub>3</sub>O<sub>5</sub>, on the basis of the HRESIMS, indicating 14 degrees of unsaturation. Analysis of the <sup>1</sup>H, <sup>13</sup>C NMR, and CD data indicated the structure to be

similar to that of the fumitremorgin class of secondary metabolites<sup>19, 166-169</sup>. The chemical shifts of the similarities between fumitremorgin A<sup>167</sup> and B<sup>169</sup> are conserved in **10**, other than the loss of the peroxide ring from fumitremorgin A, and the addition of a prenyl group in fumitremorgin B. The <sup>1</sup>H and <sup>13</sup>C data of 13-O-prenyl-fumitremorgin B was highly similar to that of fumitremorgin B other than the addition of the prenylated O at position 13. The Heteronuclear Multiple Bond Correlation spectroscopy (HMBC) correlations (Figure 30) of H<sub>2</sub>-31 to C-13 and H<sub>1</sub>-13 to C-31 connected the prenyl group to C-13 (Figures 26-29). In 2012, the activity of the gene *ftmPT3* from the gene cluster that produces the fumitremorgin-type alkaloids was explored<sup>19</sup>. It was expressed in *E. coli* and assayed with fumitremorgin B and the desired product was 13-O-prenyl-fumitremorgin B. This proved that *ftmPT3* prenylates the hydroxyl at the C-13; however, this secondary metabolite has never been isolated naturally. Only the <sup>1</sup>H NMR was obtained, and the assignment was based on previously isolated analogues; however, it has for the first time been isolated naturally from *A. fischeri*. The absolute configuration of compound **10** was determined by Circular Dichroism (CD) (Figure 31) and found to be identical to fumitremorgin B.

Since four secondary metabolites (**5-8**) from *A. fischeri* had also been reported from *A. fumigatus* (Table 2.2), we hypothesized that the mechanisms *A. fischeri* employs to regulate its secondary metabolism would also be similar to those used by *A. fumigatus*. To test this hypothesis, we constructed a deletion mutant of *laeA* in *A. fischeri* (Figure 12). LaeA is a master regulator of secondary metabolism in *A. fumigatus* and a variety of other fungi (67-69). Both the wild type and  $\Delta laeA$  strains of *A. fischeri* were subjected to LC-MS analysis. The chromatographic profile of  $\Delta laeA$  showed mass data that corresponded to sartorypyrone A (**1**), sartorypyrone E (**2**), 14-epi-aszonapyrone A

(**3**), aszonalenin (**4**), acetylaszonalenin (**5**), fumitremorgin A (**6**), verruculogen (**8**), and the C-11 epimer of verruculogen TR2 (**9**). However, the relative abundance of compounds present was very low compared to the wild type (Figure 5C). Fumitremorgin B (**7**) and 13-O-prenyl-fumitremorgin B (**10**) were not produced by the  $\Delta laeA$  mutant at all.

**Table 2.2.** Secondary metabolites isolated from *A. fischeri* that have been reported from *A. fumigatus*

<u>Secondary Metabolites</u>	<u><i>A. fischeri</i></u>	<u><i>A. fumigatus</i></u>
sartorypyrone A ( <b>1</b> )	+	-
sartorypyrone E ( <b>2</b> )	+	-
14-epi-aszonapyrone A ( <b>3</b> )	+	-
aszonalenin ( <b>4</b> )	+	-
acetylaszonalenin ( <b>5</b> )	+	+
fumitremorgin A ( <b>6</b> )	+	+
fumitremorgin B ( <b>7</b> )	+	+
verruculogen ( <b>8</b> )	+	+
C-11 epimer of verruculogen TR2 ( <b>9</b> )	+	-
13-O-fumitremorgin B ( <b>10</b> )	+	-

## Discussion

*A. fumigatus* is a major human fungal pathogen, yet its close relative *A. fischeri* is rarely an agent of human disease. A number of traits that contribute to the virulence of *A. fumigatus* have been characterized, but their distribution and potential role in *A. fischeri*-mediated disease is largely unknown. In this study, we thoroughly characterized *A. fischeri* (strain NRRL 181) and compared it to *A. fumigatus* (strain CEA10) for multiple disease-relevant biological and chemical differences. Our data shows that *A. fischeri* can grow in a mammalian host but is much less fit and causes a disease progression quite different than that observed during *A. fumigatus* infections (Figures 1 and 2). Future studies will be needed to determine if these differences between *A. fischeri* NRRL 181 and *A. fumigatus* CEA10 are conserved across a range of *A. fischeri* and *A. fumigatus* isolates.

Further investigations revealed that secondary metabolic genes are much less conserved than genes in the rest of the genome (Figure 8), and a chemical analysis of *A. fischeri* resulted in the identification of both previously identified and new compounds (Figure 5). While the BGCs producing secondary metabolites in *A. fischeri* and *A. fumigatus* appear to be quite different, our data suggest that a master regulator of secondary metabolism in *A. fumigatus* (*iaeA*) possesses a similar role in *A. fischeri* (Figure 5C). This is consistent with previous observations that the global regulation of secondary metabolism is conserved but that the underlying BGCs are not, suggesting that the regulatory circuit involved in *Aspergillus* secondary metabolism has undergone extensive regulatory rewiring.<sup>147</sup> Our analyses are the first to infer the occurrence of regulatory circuit rewiring in *A. fischeri* and are among the first gene knockout studies of this organism.<sup>172</sup>

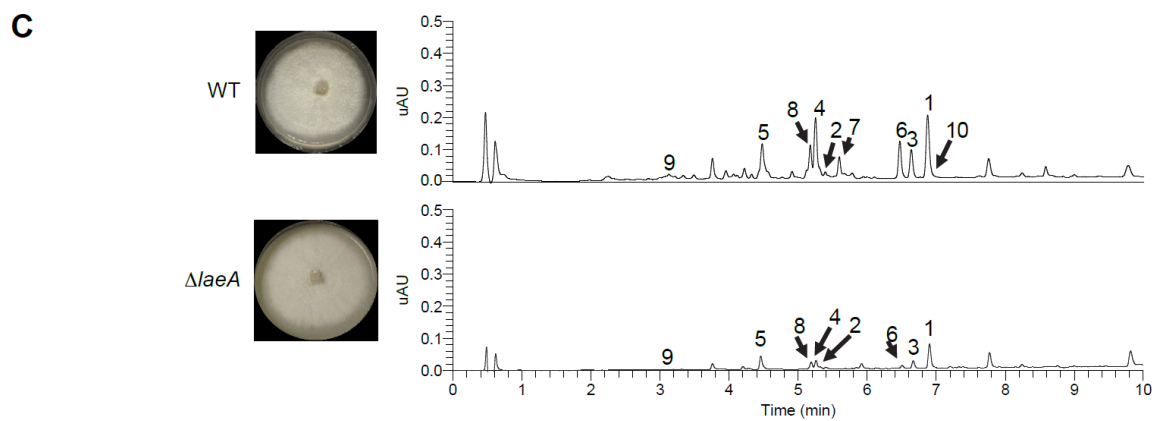
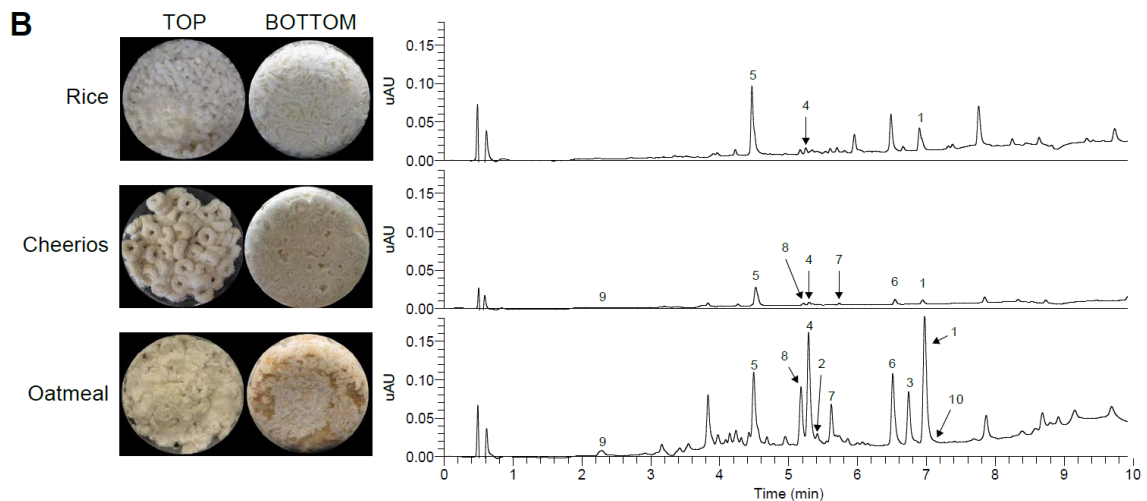
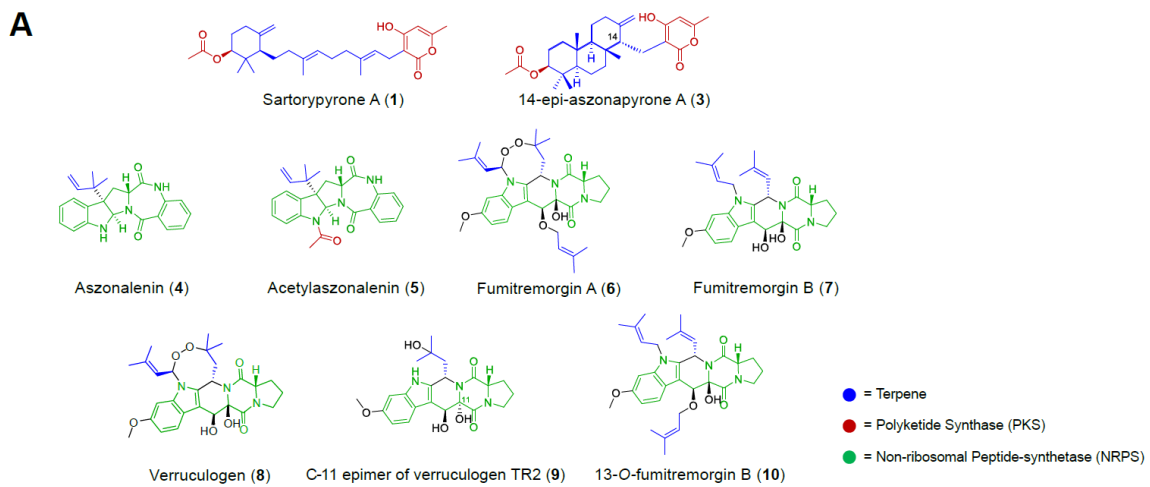


**Figure 5.** Secondary Metabolite Production in *A. fischeri*. A) Compounds isolated from *A. fischeri*: **(1)** sartorypyrone A, **(2)** sartorypyrone E, **(3)** 14-epimer aszonapyrone A, **(4)** aszonalenin, **(5)** acetylzaszonalenin, **(6)** fumitremorgin A, **(7)** fumitremorgin B, **(8)** verruculogen, **(9)** C-11 epimer verruculogen TR2, and **(10)** 13-O-prenyl-fumitremorgin B. The color coding indicates which putative class the molecule belongs to; e.g., terpenes, PKS, or NRPS. B) Top, *Aspergillus fischeri* was initially grown on rice for two weeks and then extracted using methods outlined in Figure S5. The rice culture yielded compounds **1**, **4**, and **5**. Middle, *A. fischeri* was grown on multigrain Cheerios for two weeks, which yielded compounds **1** and **4-9**. Bottom, *A. fischeri* on Quaker oatmeal for two weeks. All compounds that were previously isolated in rice and multigrain cheerios cultures in addition to three new compounds (**2**, **3**, and **10**) were found in the oatmeal culture. All pictures depict fungi growing in 250 mL Erlenmeyer flasks; left panel indicates top view, while the right panel shows bottom view. All chromatographic profiles have been normalized to the highest  $\mu$ AU value. C) *A. fischeri* WT and  $\Delta$ laeA were grown on solid breakfast oatmeal for two weeks and extracted using organic solvents as indicated previously. The crude de-sugared and de-fatted extracts were run using UPLC-MS at a concentration of 2 mg/mL with 5  $\mu$ L being injected for analysis. The chromatographic profiles were normalized to the highest  $\mu$ AU value. Mass spec analysis indicated the presence of secondary metabolites **1-10** within the wild type, and only **1-6**, **8**, and **9** were seen in the  $\Delta$ laeA mutant. All pictures show *A. fischeri* grown on oatmeal agar in Petri plates.

In order to cause disease, a microbe must be able to respond to the set of diverse and stressful environments presented by its host. Based on our data, *A. fischeri* strain NRRL 181 is unable to respond to many of these stresses as well as *A. fumigatus* CEA10 (Figures 2-3). We hypothesize that this inability to thrive under stress contributes to the varying disease progressions observed during our animal model experiments (Figure 1). Some or all of the genetic determinants responsible for this discrepancy in stress response and virulence could reside in the ~1,200 *A. fumigatus*-specific genes we identified (Figure 8); alternatively, some of the ~1,700 *A. fischeri*-specific genes we identified may inadvertently facilitate control of *A. fischeri* in a mammalian host. An additional explanation for the discrepancy in stress response is that *A. fumigatus* has evolved more efficient regulatory circuits than *A. fischeri* that allow it to cope with more stringent conditions that are observed in the host.

Even though more than 10% of the genes in each species lack an ortholog in the other species, only ~2% (1/49) of previously identified genetic determinants of virulence in *A. fumigatus* are not conserved in *A. fischeri* (Table 2.3). This result, and our observation that many of the pathways of secondary metabolism are quite different between *A. fischeri* and *A. fumigatus*, support a multifactorial model of *A. fumigatus* virulence<sup>24, 173, 174</sup> and suggest a need to investigate virulence on multiple levels of biological complexity. In order to cause disease in a host, *A. fumigatus* (and other species closely related to it) must adhere and germinate in the lung,<sup>24</sup> survive inherently stressful conditions presented by host environments (ex. severe lack of metals and oxygen),<sup>116, 175, 176</sup> and modulate or endure actions of the host immune system.<sup>177</sup> Given the diversity of these activities, it is unlikely that single genes or pathways will be responsible for the totality of *A. fumigatus*-derived disease, even though many genes in the genome have not yet been characterized for their role in pathogenicity. We hypothesize that multiple pathways (including those involved in secondary metabolism) have changed during the evolution of *A. fischeri* and *A. fumigatus*, resulting in their differing ability to cause disease.

As mentioned, an important caveat to our experiments is that we only analyzed a single, representative strain from each species, and further studies are needed to determine how typical these observed trait and genomic differences are across multiple strains from each species. Several recent studies have identified a wide variety of differences between *A. fumigatus* strains, which have in turn been shown to contribute to physiological differences, including but not limited to secondary metabolism and virulence.<sup>24, 137, 146, 174</sup> While the genome of only one isolate of *A. fischeri* has so far been sequenced<sup>123</sup> and the organism has only been reported to cause human disease a few

times,<sup>128-131</sup> it would be of great interest to compare patient-derived and environment-derived isolates at the genomic, phenotypic, and chemical levels. Although it appears that clinical and environmental isolates do not stem from separate lineages in *A. fumigatus*,<sup>178</sup> whether this is also the case for largely non-pathogenic species, such as *A. fischeri*, or for rarely isolated pathogenic species, such as *A. lentulus* or *A. udagawae*, remains largely unknown.

Our mouse infection studies revealed that *A. fischeri* strain NRRL 181 was less virulent than *A. fumigatus* strain CEA10 in both leukopenic and steroid-induced immune suppression models of disease. The difference in disease outcome in the steroid model closely matches what was observed in comparisons of two *A. fumigatus* strains, CEA10 and Af293.<sup>137</sup> It is intriguing that the difference between pathogenic (*A. fumigatus* CEA10) and non-pathogenic (*A. fischeri* NRRL 181) species in disease outcomes in this model is similar to that between two clinically derived pathogenic strains (*A. fumigatus* CEA10 and Af293). Interestingly, Kowalski et al. did not observe any statistically significant difference in disease progression between CEA10 and Af293 in the leukopenic model, whereas we found that *A. fischeri* is less virulent in this second murine model of disease (Figure 1). These strain-, species-, and infection model-specific differences in disease outcomes are consistent with our hypothesis that *A. fumigatus* virulence is a complex genetic trait and highlight the need for further studies using wider sets of strains, species, and virulence-related traits.

*A. fumigatus* and *A. fischeri* are members of *Aspergillus* section *Fumigati*, a clade that includes multiple closely related species, some of which are pathogens (e.g., *A. fumigatus*, *A. lentulus*, and *A. udagawae*) and some of which are considered non-pathogens (e.g., *A. fischeri*, *A. aureolus*, and *A. turcosus*).<sup>112, 151, 179, 180</sup> The ability to

cause disease in humans appears to have either arisen or been lost (or both) multiple times independently during the evolution of this lineage, as pathogenic species are spread throughout the phylogeny.<sup>124, 181</sup> A broader, phylogenetically-informed comparison of pathogenic and non-pathogenic species in section *Fumigati* would provide far greater resolution in identifying (or dismissing) factors and pathways that may contribute or prevent the ability of these organisms to cause disease. Also, leveraging the diversity of section *Fumigati* would give researchers a better understanding of the nature and evolution of human fungal pathogenesis as the appreciation for the health burden caused by fungi increases.<sup>182</sup>

## **Materials and Methods**

**Strains and Growth Media.** *A. fischeri* strain NRRL 181 was acquired from the ARS Culture Collection (NRRL). *A. fumigatus* strain CEA10 (CBS 144.89) was obtained from the Westerdijk Fungal Biodiversity Institute (CBS). All strains were grown on glucose minimal media (GMM) from conidial glycerol stocks stored at -80°C. All strains were grown in the presence of white light at 37°C. Conidia were collected in 0.01% Tween-80 and enumerated with a hemocytometer.

**Murine Virulence Studies.** For the chemotherapeutic (leukopenic) murine model, outbred CD-1 female mice (Charles River Laboratories, Raleigh, NC, USA), 6-8 weeks old, were immunosuppressed with intraperitoneal (i.p.) injections of 150 mg/kg cyclophosphamide (Baxter Healthcare Corporation, Deerfield, IL, USA) 48 hours before and 72 hours after fungal inoculation, along with subcutaneous (s.c.) injections of 40 mg/kg Kenalog-10 (triamcinolone acetonide, Bristol-Myer Squibb, Princeton, NJ, USA) 24 hours before and 6 days after fungal inoculation. For the murine triamcinolone model

outbred CD-1 female mice, 6-8 weeks old, were treated with 40 mg/kg Kenalog-10 by s.c. injection 24 hours prior to fungal inoculation.

Unless otherwise noted, conidial suspensions of  $2 \times 10^6$  conidia were prepared in 40  $\mu\text{L}$  sterile PBS and administered to mice intranasally while under isoflourine anesthesia. Mock mice were given 40  $\mu\text{L}$  PBS. Mice were monitored three times a day for signs of disease for 14 or 18 days post-inoculation. Survival was plotted on Kaplan-Meir curves and statistical significance between curves was determined using Mantel-Cox Log-Rank and Gehan Breslow-Wilcoxon tests. Mice were housed in autoclaved cages at 4 mice per cage with HEPA filtered air and autoclaved food and water available at libitum.

**Galleria mellonella Virulence Studies.** *G. mellonella* larvae were obtained by breeding adult moths.<sup>183</sup> *G. mellonella* larvae of a similar size were selected (approximately 275–330 mg) and kept without food in glass containers (Petri dishes) at 37°C in darkness for 24 h prior to use. *A. fumigatus* and *A. fischeri* conidia were obtained by growing on YAG media for 2 days. The conidia were harvested in PBS and filtered through Miracloth (Calbiochem). The concentration of conidia was estimated by using a hemocytometer and were resuspended at a concentration of  $2.0 \times 10^8$  conidia/ml. The viability of the conidia was determined by incubating on YAG media at 37°C for 48 hours. Inoculum (5  $\mu\text{l}$ ) of conidia from both strains were used to investigate the virulence of *A. fumigatus* and *A. fischeri* against *G. mellonella*. Ten *G. mellonella* in the final (sixth) instar larval stage of development were used per condition in all assays. The control group was the larvae inoculated with 5  $\mu\text{l}$  of PBS to observe the killing due to physical trauma. The inoculation was performed by using a Hamilton syringe (7000.5KH) and injecting 5  $\mu\text{l}$  into the haemocel of each larva via the last left proleg. After, the larvae

were incubated in a glass container (Petri dishes) at 37°C in the dark. Larval killing was scored daily. Larvae were considered dead by presenting the absence of movement in response to touch.

**Histopathology.** Outbred CD-1 mice, 6-8 weeks old, were immunosuppressed and intranasally inoculated with  $2 \times 10^6$  conidia as described above for the chemotherapeutic and corticosteroid murine models. Mice were sacrificed 72 hours post inoculation. Lungs were perfused with 10% buffered formalin phosphate before removal, then stored in 10% buffered formalin phosphate until embedding. Paraffin embedded sections were stained with haematoxylin and eosin (H&E) and Gömöri methenamine silver (GMS). Slides were analyzed microscopically with a Zeiss Axioplan 2 imaging microscope (Carl Zeiss Microimaging, Inc. Thornwood, NY, USA) fitted with a Qimaging RETIGA-SRV Fast 1394 RGB camera. Analysis was performed in Phylum Live 4 imaging software.

**Ethics Statement.** We carried out our mouse studies in strict accordance with the recommendations in the Guide for the Care and Use of Laboratory Animals of the National Research Council (Council, 1996). The mouse experimental protocol was approved by the Institutional Animal Care and Use Committee (IACUC) at Dartmouth College (Federal-Wide Assurance Number: A3259-01).

**Growth Assays.** Radial growth was quantified by point inoculation of  $1 \times 10^3$  conidia in 2 µL on indicated media; plates were incubated at 37°C in normoxia (~21% O<sub>2</sub>, 5% CO<sub>2</sub>) or hypoxia (0.2% O<sub>2</sub>, 5% CO<sub>2</sub>). Colony diameter was measured every 24 hours for 4 days and reported as the average of three biological replicates per strain.

For 2-DG experiments,  $1 \times 10^3$  conidia in 2 µL were spotted on 1% lactate minimal media with or without 0.1% 2-deoxyglucose (2-DG; Sigma, D8375). Plates were

incubated for 3 days at 37°C in normoxia or hypoxia with 5% CO<sub>2</sub>. Percent inhibition was calculated by dividing radial growth on 2-DG plates by the average radial growth of biological triplicates on plates without 2-DG.

Fungal biomass was quantified by measuring the dry weight of fungal tissue from 5x10<sup>7</sup> conidia grown in 100 mL liquid GMM shaking at 200 rpm for 48 hours in normoxia (~21% O<sub>2</sub>) and hypoxia (0.2% O<sub>2</sub>, 5% CO<sub>2</sub>). Liquid biomass is reported as the average of three biological replicates per strain. Hypoxic conditions were maintained using an INVIVO<sub>2</sub> 400 Hypoxia Workstation (Ruskinn Technology Limited, Bridgend, UK) with a gas regulator and 94.8% N<sub>2</sub>.

Liquid growth curves were performed with conidia adjusted to 2x10<sup>4</sup> conidia in 20 μL 0.01% Tween-80 in 96-well dishes, then 180 μL of media (GMM or lung homogenate) was added to each well. Plates were incubated at 37°C for 7 hours, then Abs<sub>405</sub> measurements were taken every 10 minutes for the first 16 hours of growth with continued incubation at 37°C. Lung homogenate media was prepared as follows: lungs were harvested from healthy CD-1 female mice (20-24 g) and homogenized through a 100 μM cell strainer in 2 mL PBS/lung. Homogenate was diluted 1:4 in sterile PBS, spun down to remove cells, then filter sterilized through 22 μM PVDF filters.

**Cell Wall and Oxidative Stresses.** Congo Red (0.5 mg/mL), Menadione (20 μM), or calcofluor white (CFW, 25 μg/mL) were added to GMM plates. 1x10<sup>3</sup> conidia (Calcofluor white and Menadione) or 1x10<sup>5</sup> conidia (Congo Red) were point inoculated and plates were incubated for 96 hours at 37°C with 5% CO<sub>2</sub>.

**Orthology Determination and Analyses.** Genomes for *A. fumigatus* CEA10 and *A. fischeri* NRRL 181 were downloaded from NCBI (Accession numbers of GCA\_000150145.1 and GCF\_000149645.1, respectively). To identify putative

orthologous genes between *A. fischeri* and *A. fumigatus*, a reciprocal best BLAST hit (RBBH) approach was used. We blasted the proteome of *A. fischeri* to *A. fumigatus* and vice versa using an e-value cutoff of  $10^{-3}$  and then filtered for RBBHs according to bitscore.<sup>184</sup> A pair of genes from each species was considered orthologous if their best blast hit was to each other. Species-specific and orthologous protein sets were visualized using version 3.0.0 of eulerAPE.<sup>185</sup>

**Biosynthetic Gene Cluster (BGC) Prediction and Analyses.** Version 4.2.0 of antiSMASH<sup>146</sup> was used with its default settings to identify BGCs. Orthologous cluster genes were identified using our RBBH results and visualized using version 0.69 of Circos.<sup>149</sup> Chromosomes were identified for *A. fischeri* NRRL1 and *A. fumigatus* CEA10 using NUCMER<sup>186</sup> and chromosomal sequences from *A. fumigatus* strain AF293 from NCBI (Accession number GCA\_000002655.1). Syntenic clusters were visualized using easyfig version 2.2.2.<sup>187</sup>

**Secondary Metabolite Extraction and Identification.** Secondary metabolites were extracted from *A. fischeri* using techniques well established in the Natural Products literature.<sup>188, 189</sup> This was done by adding a 1:1 mixture of CHCl<sub>3</sub>:CH<sub>3</sub>OH and left to shake overnight. The resulting slurry was partitioned twice, first with a 4:1:5 CHCl<sub>3</sub>:CH<sub>3</sub>OH:H<sub>2</sub>O solution, with the organic layer drawn off and evaporated to dryness *in vacuo*, and secondly, reconstituting 1:1:2 CH<sub>3</sub>CN:CH<sub>3</sub>OH:hexanes, where the organic layer was drawn off and evaporated to dryness. The extract then underwent chromatographic separation (flash chromatography and HPLC) using varied gradient systems.

**Growth on Petri Dish.** *Aspergillus fischeri* strain NRRL 181 was maintained in the laboratory on potato dextrose agar (PDA; Difco). For the chemical analysis of *A.*

*fischeri* in Petri dishes different types of media, such as (1) synthetic, and (2) semi-synthetic were made. Some media were prepared with antibiotics (Streptomycin and Penicillin G (ab); 250 mg added in 1L after media sterilization); Potato Dextrose Agar + ab + Balsa wood (PDA + Balsa; Difco), PDA + ab (Difco), PDA and cheerios (Difco and General Mills), Oatmeal Agar (OMA; Difco), Sabouraud Agar (SDA; Difco), Peptone Yeast Glucose Agar (PYG; 1.25 g soy peptone, 1.25 g yeast extract, 5 g D-glucose, 1 L H<sub>2</sub>O), Czapek Yeast Agar (CYA; 50 g Czapek mixture, 5 g yeast extract, 1 L H<sub>2</sub>O), and Yeast Extract Soy Peptone Dextrose Agar (YESD; 20 g soy peptone, 20 g dextrose, 5 g yeast extract, 1 L H<sub>2</sub>O). A small piece of agar plug (~0.5 cm<sup>2</sup>) from a fresh culture grown on potato dextrose agar was cut from the leading edge of 2-week old colony from *A. fischeri* and was used to inoculate eight different types of agar media, respectively. The Petri plates were then incubated at room temperature until the cultures showed formation of conidia (sporulation), which would indicate completion of initial growth phase (~2 weeks), thus corresponding to the production of secondary metabolites.

#### **Growth on Solid-State Fermentation for Isolation and Structural**

**Elucidation of Secondary Metabolites.** *Aspergillus fischeri* was grown on three different types of solid-state fermentation media, rice <sup>96, 153-156</sup>, multigrain cheerios <sup>190</sup>, and oatmeal. To initiate growth on grain or cereal based media, we first prepared a seed culture of the fungus. As outlined above a small square of agar along with the fungal mycelium was cut out aseptically from the leading edge of a 2-week old culture growing on potato dextrose agar media and transferred to a sterile falcon tube with 10 ml of YESD liquid media for seed culture. The liquid YESD cultures were grown for three days on an orbital shaker (100 rpm) at room temperature, and then they were used to

inoculate three different types of solid fermentation media, which was prepared as outlined below.

Solid-state fermentation using rice [(1:1 commercial white rice (variety: Calrose Botan; 5 g) and (variety: Sona Masoori; 5 g)] was prepared by adding 10 g rice into a 250 mL Erlenmeyer flask with 20 mL of DI-H<sub>2</sub>O, then autoclaved at 221 °C for 30 min. Cheerios breakfast cereal (multigrain variety) was prepared using 7g of cheerios (enough to cover the bottom surface area of a 250 mL Erlenmeyer flask) and autoclaved at 221 °C for 30 min, without any DI-H<sub>2</sub>O. Finally, Oatmeal cereal media (Old fashioned breakfast Quaker oats) was made by adding 10 g oatmeal to a 250 mL Erlenmeyer flask with 15-17 mL of DI-H<sub>2</sub>O, then autoclaved at 221 °C for 30 min. All fermentation cultures were incubated statically at room temperature for 14 days before chemical analysis.

For chemical analysis, cultures of *A. fischeri* were not grown on liquid media because previous studies in our laboratory suggested that solid media yield a larger quantity of secondary metabolites.<sup>159</sup>

**Solid Media Extraction.** To each of the solid fermentation cultures of *Aspergillus fischeri*, 60 mL of 1:1 CHCl<sub>3</sub>-CH<sub>3</sub>OH were added, and the cultures were chopped using a spatula and left to shake overnight (~ 16 hrs.). The resulting slurries were vacuum filtered, and to the filtrate was added 90 mL of CHCl<sub>3</sub> and 150 mL of DI H<sub>2</sub>O. This 4:1:5 CHCl<sub>3</sub>:CH<sub>3</sub>OH:H<sub>2</sub>O solution was partitioned in a separatory funnel, and the organic layer was drawn off and evaporated to dryness *in vacuo*. This sample was then reconstituted with 100 mL 1:1 CH<sub>3</sub>CN : CH<sub>3</sub>OH and 100 mL of hexanes and partitioned. The defatted organic layer was evaporated to dryness.

**Isolation.** The defatted extract was then dissolved in CHCl<sub>3</sub>, absorbed onto celite 545 (Acros Organics, celite 545), and fractioned by normal phase flash chromatography

using a gradient of hexane-CHCl<sub>3</sub>-CH<sub>3</sub>OH at an 18 mL/min flow rate and 90.0 column volumes over 24.0 min to produce five fractions. Fraction 1 was purified further via preparative HPLC using a gradient system 20:80 to 100:0 of CH<sub>3</sub>CN-H<sub>2</sub>O with 0.1% formic acid over 30 min at a flow rate of 16.9 mL/min to yield seven subfractions. Subfractions 1, 2, 3, 4, 5, and 6 yielded compounds **8** (0.85 mg), **4** (0.82 mg), **7**(0.51 mg), **6** (1.13 mg), **1** (2.88 mg), and **3** (3.20 mg), which eluted at approximately 6.9, 7.7, 8.9, 13.2, 17.0, and 24.4 min, respectively. Fraction 3 was purified further via preparative HPLC using the same gradient system to yield ten subfractions. Subfractions 2, 3, 4, and 5 yielded compounds **10** (1.20 mg), **9** (1.73 mg), **2** (1.17 mg), and **5** (3.2 mg), which eluted at approximately 8.2, 9.3, 17.2, and 24.4 min respectively.

**Agar Plate Extraction.** Each agar plate culture of *A. fischeri* was chopped thoroughly and added to a scintillation vial, then 10 mL of 1:1 CHCl<sub>3</sub>-CH<sub>3</sub>OH were added. The cultures were shaken vigorously on a vortex for a few minutes, and then let to sit for four hours. The cultures were then filtered, and the supernatant was collected. The supernatant was then subjected to LC-MS analysis.

**General Experimental Procedures.** Optical rotation data were obtained using a Rudolph Research Autopol III polarimeter (Rudolph Research Analytical). UV was carried out on a Varian Cary 100 Bio UV-vis spectrophotometer (Varian Inc.) Circular Dichroism (CD) was carried out on an Olis DSM 17 ECD spectrophotometer (Olis, Inc.) The NMR data were collected using either a JEOL ECS-400 spectrometer, which was equipped with a JEOL normal geometry broadband Royal probe, and a 24-slot autosampler, and operated at 400 MHz for <sup>1</sup>H and 100 MHz for <sup>13</sup>C, or a JEOL ECA-500 spectrometer operating at 500 MHz for <sup>1</sup>H and 125 MHz for <sup>13</sup>C (Both from JEOL USA, Inc.), or an Agilent 700 MHz spectrometer (Agilent Technologies), equipped with a

cryoprobe, operating at 700 MHz for <sup>1</sup>H and 175 MHz for <sup>13</sup>C. HRMS experiments utilized either a Thermo LTQ Orbitrap XL mass spectrometer or a Thermo QExactive Plus (Thermo Fisher Scientific); both were equipped with an electrospray ionization source. A Waters Acuity UPLC (Waters Corp.) was utilized for both mass spectrometers, using a BEH C<sub>18</sub> column (1.7 µm; 50 mm x 2.1 mm) set to a column temperature of 40°C and a flow rate of 0.3 mL/min. The mobile phase consisted of a linear gradient of CH<sub>3</sub>CN-H<sub>2</sub>O (acidified with 0.1% formic acid), starting at 15% CH<sub>3</sub>CN and increasing linearly to 100% CH<sub>3</sub>CN over 8 min, with a 1.5 min hold before returning to the starting condition. The HPLC separations were performed with an Atlantis T3 C<sub>18</sub> semi-preparative (5 µm; 10 x 250 mm) and preparative (5 µm; 19 x 250 mm) columns, at a flow rate of 4.6 mL/min and 16.9 mL/min, respectively, with a Varian Prostar HPLC system equipped with a Prostar 210 pumps and a Prostar 335 photodiode array detector (PDA), with the collection and analysis of data using Galaxie Chromatography Workstation software. Flash chromatography was performed on a Teledyne ISCO Combiflash Rf 200 and monitored by both ELSD and PDA detectors.

**Construction of the *A. fischeri* ΔlaeA Mutant.** The gene replacement cassettes were constructed by “*in vivo*” recombination in *S. cerevisiae* as previously described.<sup>191, 192</sup> Approximately 2.0 kb from the 5'-UTR and 3'-UTR flanking regions of the targeted ORF were selected for primer design. The primers pRS NF010750 5'fw (5'-GTAACGCCAGGGTTTCCCAGTCACGACGCAGTCTAACGCTGGGCCCTCC-3') and pRS NF010750 3'rv (5'-GCGGTTAACAAATTCTCTGGAAACAGCTACGGCGTTGACGGCACAC-3') contained a short homologous sequence to the Multicloning site (MCS) of the plasmid pRS426. Both the 5'- and 3'-UTR fragments were PCR-amplified from *A. fischeri*

genomic DNA (gDNA). The *prtA* gene, conferring resistance to pyrithiamine, which was placed within the cassette as a dominant marker, was amplified from the pPRT1 plasmid by using the primers *prtA* NF010750 5'rv (5'-  
GTAATCAATTGCCCGTCTGTCAGATCCAGGTCGAGGAGGTCCAATCGG-3') and *prtA* NF010750 3'fw (5'-  
CGGCTCATCGTCACCCCATGATAGCCGAGATCAATCTGCATCC-3'). The deletion cassette was generated by transforming each fragment along with the plasmid pRS426, cut with *Bam*HI/*Eco*RI, into the *S. cerevisiae* strain SC94721 using the lithium acetate method.<sup>193</sup> The DNA from the transformants was extracted by the method described by Goldman et al..<sup>194</sup> The cassette was PCR-amplified from these plasmids utilizing TaKaRa Ex Taq™ DNA Polymerase (Clontech Takara Bio) and used for *A. fischeri* transformation according to the protocol described by Malavazi and Goldman.<sup>192</sup> Southern blot and PCR analyses were used to demonstrate that the cassette had integrated homologously at the targeted *A. fischeri* locus. Genomic DNA from *A. fischeri* was extracted by grinding frozen mycelia in liquid nitrogen and then gDNA was extracted as previously described.<sup>192</sup> Standard techniques for manipulation of DNA were carried out as described.<sup>195</sup> For Southern blot analysis, restricted chromosomal DNA fragments were separated on 1% agarose gel and blotted onto Hybond N<sup>+</sup> nylon membranes (GE Healthcare). Probes were labeled using [ $\alpha$ -<sup>32</sup>P]dCTP using the Random Primers DNA Labeling System (Life Technologies). Labeled membranes were exposed to X-ray films, which were scanned for image processing. Southern blot and PCR schemes are shown in Figure 12.

**Secondary Metabolite Information.** Compound 3 (14 – epi-aszonapyrone A): white solid;  $[\alpha]_D^{20} = +43$  (c 0.1, MeOH); UV (MeOH)  $\lambda_{\text{max}}$  ( $\log \epsilon$ ) 293 (3.16), 221 (3.00)

nm;  $^1\text{H}$  and  $^{13}\text{C}$  NMR data, see Table 2.3; HRESIMS  $[\text{M} + \text{H}]^+$  457.2941 (calculated for  $\text{C}_{28}\text{H}_{41}\text{O}_5$ , 457.2948).

Compound **10** (13-O-prenyl-fumitremorgin B): white solid;  $[\alpha]_D^{20} = +19$  ( $c$  0.09, MeOH); UV (MeOH)  $\lambda_{\text{max}}$  ( $\log \epsilon$ ) 293 (2.99), 277 (3.01), 232 (3.26) nm;  $^1\text{H}$  and  $^{13}\text{C}$  NMR data, see Table 2.4; HRESIMS  $[\text{M} + \text{H}]^+$  548.3103 (calculated for  $\text{C}_{32}\text{H}_{42}\text{N}_3\text{O}_5$ , 548.3118).

### Supplementary Data

**Table 2.3.**  $^1\text{H}$  (700 MHz) and  $^{13}\text{C}$  (175 MHz) NMR Data in  $\text{CDCl}_3$  for 14 – epi-aszonapyrone A (**3**).

Position	$\delta_{\text{H}}$	$\delta_{\text{C}}$	Mult ( $J$ in Hz)
1	1.03, 1.69	38.3	m
2	1.35, 1.62	23.8	m
3	4.49	81.1	dd (11.7, 4.7)
4		37.9	
5	0.91	55.5	dd (12.3, 2.2)
6	1.43, 1.63	18.8	m
7	1.32, 2.04	40.3	m
8		40.8	
9	1.08	60.0	m
10		37.6	
11	1.68	23.7	m
12	1.99	38.3	td (12.8, 5.0)
	2.39		ddd (12.5, 3.7, 2.2)
13		151.4	
14	2.15	55.9	m
15	2.48	18.6	dd (15.2, 9.2)
	2.72		dd (15.5, 2.4)
16		103.5	
17		166.1	
19		160.0	
20	5.80	100.8	s
21		165.0	

22	0.85	16.6	s
23	0.84	28.1	s
24	0.83	16.4	s
25	0.75	15.1	s
26	4.87, 4.98	106.8	s
27	2.16	19.8	s
1'		171.3	
2'	2.05	21.5	s

**Table 2.4.**  $^1\text{H}$  (700 MHz) and  $^{13}\text{C}$  (175 MHz) NMR Data in  $\text{CDCl}_3$  for 13-O-prenyl-fumitremorgin B (**10**).

Position	$\delta_{\text{H}}$	$\delta_{\text{C}}$	Mult ( $J$ in Hz)
2		131.3	
3	6.05	48.1	dd (10.1, 1.0)
5		171.6	
6	4.63	59.1	dd (9.6, 7.4)
7	2.15	28.9	m
	2.42		dtd (13.3, 6.9, 2.4)
8	2.03	23.2	m
9	3.61	45.8	m
11		166.5	
12		84.5	
13	5.57	73.1	d (0.9)
14		105.2	
15		120.5	
16	7.65	120.6	dd (8.7, 0.5)
17	6.80	109.3	dd (8.7, 2.3)
18		156.1	
19	6.69	94.2	d (2.3)
20		138.2	
21	4.53	41.9	m
22	5.02	120.5	m
23		134.7	
24	1.84	18.4	d (1.2)
25	1.68	25.7	d (1.5)
26	4.66	123.8	m

27		135.1	
28	1.96	18.5	d (1.3)
29	1.61	25.8	d (1.3)
30	3.85	55.9	s
31	4.74	69.5	dd (11.1, 7.0)
	5.03		m
32	5.60	121.2	tt (6.9, 1.4)
33		137.3	
34	1.81	18.6	m
35	1.81	26.0	m
12 - OH	4.42		s

**Table 2.5.** HRESIMS Table of Compounds **1-10**

Compound Name and Molecular Formula	Measured Value	Calculated Value	Ionization	Accuracy
sartorypyrone A ( <b>1</b> ) $C_{28}H_{40}O_5$	457.2940	457.2949	[M+H] <sup>+</sup>	-1.9
14-epi-aszonapyrone A ( <b>3</b> ) $C_{28}H_{40}O_5$	457.2941	457.2949	[M+H] <sup>+</sup>	-1.6
azonalenin ( <b>4</b> ) $C_{23}H_{23}N_3O_2$	374.1856	374.1863	[M+H] <sup>+</sup>	-1.9
acetylaszonalenin ( <b>5</b> ) $C_{25}H_{25}N_3O_3$	416.1961	416.1969	[M+H] <sup>+</sup>	-1.8
fumitremorgin A ( <b>6</b> ) $C_{32}H_{41}N_3O_7$	580.3001	580.3017	[M+H] <sup>+</sup>	-2.8
fumitremorgin B ( <b>7</b> ) $C_{27}H_{33}N_3O_5$	480.2482	480.2493	[M+H] <sup>+</sup>	-2.3
verruculogen ( <b>8</b> ) $C_{27}H_{33}N_3O_7$	512.2386	512.2391	[M+H] <sup>+</sup>	-1.0
C-11 epimer of verruculogen TR-2 ( <b>9</b> ) $C_{22}H_{27}N_3O_6$	430.1961	430.1973	[M+H] <sup>+</sup>	-2.7
13-O-prenyl-fumitremorgin B ( <b>10</b> ) $C_{32}H_{41}N_3O_5$	548.3103	548.3119	[M+H] <sup>+</sup>	-2.9

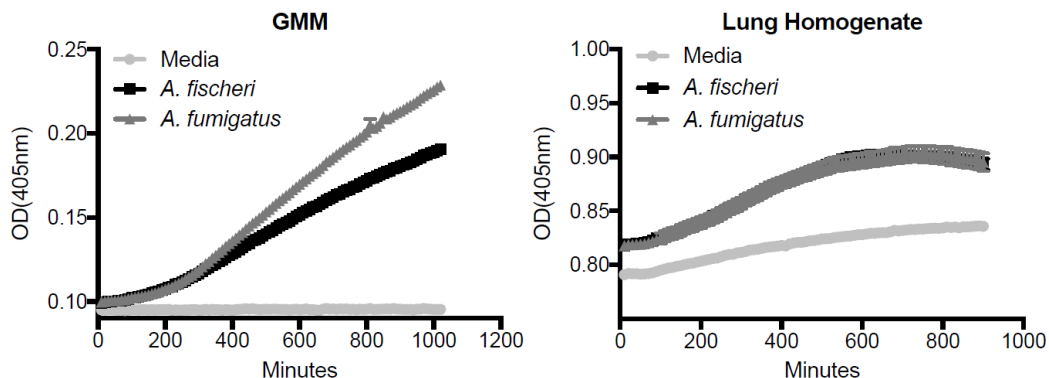


**Figure 6.** *A. fumigatus* Grows Slower Than *A. fischeri* in Glucose Minimal Media (GMM), but at the Same Speed as *A. fischeri* in Lung Homogenate Media. *A. fumigatus* CEA10 or *A. fischeri* NRRL181 were cultured in flat-bottom 96 well plates at  $2 \times 10^4$  conidia per well. Conidia were added in a 20  $\mu\text{L}$  of 0.01% Tween-80 and media was carefully pipetted over the inoculum into each well. Lung homogenate was generated according to (29). Plates were incubated for 7 hours at 37°C before measurements at 405 nm were taken every 10 min. Mean and SEM of eight technical replicates; data is representative of three biological replicates.

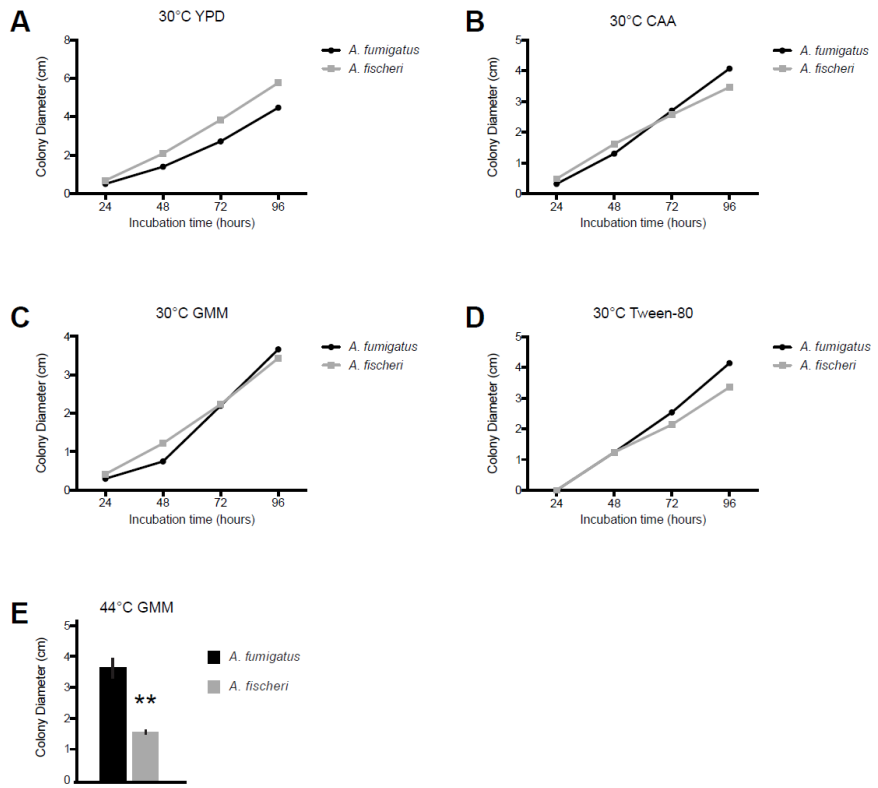


**Figure 7.** *A. fischeri* and *A. fumigatus* Exhibit Similar Growth Patterns at 30°C but Not at 44°C. A-D)  $1 \times 10^3$  conidia were point inoculated on each plate, plates were then incubated at 30°C in normoxia (~21% oxygen, 5%CO<sub>2</sub>); colony diameter was measured every 24 hours. Mean and SEM of triplicates. Tween-80 – 1% Tween-80 provided as sole carbon source; CAA – Casamino acids; GMM – glucose minimal media. E) Error bars indicate standard deviations between biological duplicates (\*\*P-value < 0.005 in a paired, equal variance Student t-test).

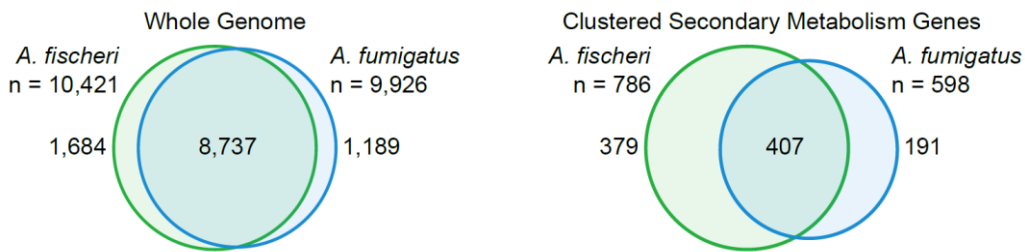


**Figure 8.** The Genomes of *A. fumigatus* and *A. fischeri* are Largely Similar, but Their Secondary Metabolic Pathways are Quite Divergent. Left, Venn diagram showing the sets of *A. fischeri*-specific proteins, shared orthologous proteins, and *A. fumigatus*-specific proteins encoded in each genome. Numbers below each species name indicate the total number of proteins encoded in that genome. Right, Venn diagram showing the

sets of *A. fischeri*-specific BGC proteins, shared BGC proteins, and *A. fumigatus*-specific BGC proteins. Numbers below each species name indicate the total number of BGC proteins encoded in that genome. In each diagram, circles are proportional to the number of proteins they contain.

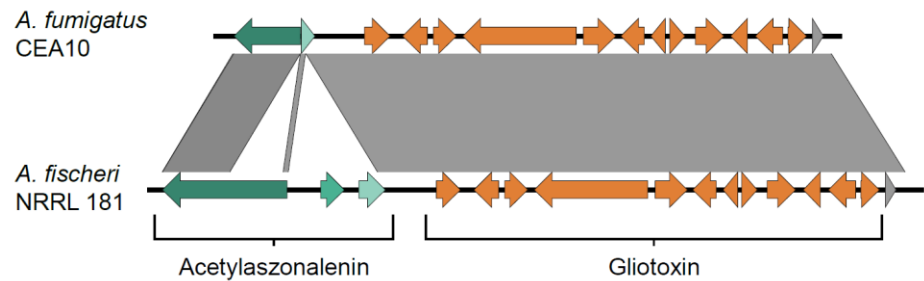


**Figure 9.** The Acetylaszonalenin and Gliotoxin Biosynthetic Gene Clusters in *A. fumigatus* and *A. fischeri* are Located Immediately Next to One Another. The portions of Clusters 37 and 25 from *A. fischeri* and *A. fumigatus*, respectively, that are known to contain the previously characterized acetylaszonalenin<sup>196</sup> and gliotoxin<sup>150</sup> BGCs is shown. Genes colored in shades of green are involved in the acetylaszonalenin biosynthetic pathway. Dark green, *anaPS* (nonribosomal peptide synthase). Light green, *anaAT* (acetyltransferase). Green, *anaPT* (prenyltransferase). Orange, gliotoxin biosynthetic genes. Gray arrow, syntenic gene in both species not involved in gliotoxin synthesis. Sequences that are similar to one another (based on blastn scores) are marked by gray parallelograms. Image was made using EasyFig version 2.2.2.<sup>187</sup>

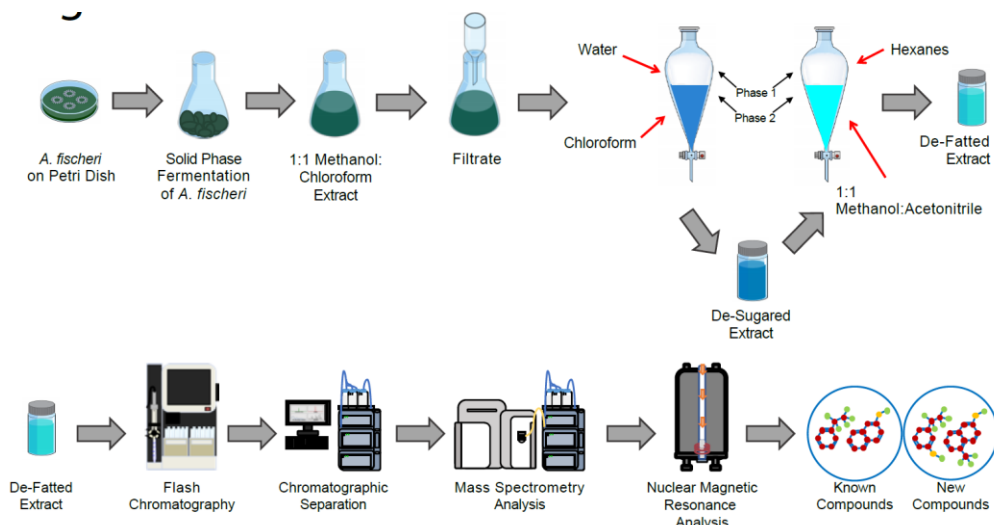


**Figure 10.** A Custom Chemical Analysis Protocol was Developed for Studying the Metabolites Produced by *A. fischeri*. Approximately 60 mL of 1:1 CH<sub>3</sub>OH:CH<sub>3</sub>Cl was added to cultures of *Aspergillus fischeri* grown on solid-state fermentation for two weeks. The cultures were then chopped thoroughly with a large scalpel and shaken for 16 hours

using an orbital shaker. The liquid culture was then vacuum filtered and concentrated using 90 mL CH<sub>3</sub>Cl and 150 mL water and transferred into a separatory funnel. The organic (bottom) layer was drawn off and evaporated to dryness. The dried, de-sugared extract was reconstituted in 100 mL of 1:1 CH<sub>3</sub>OH:CH<sub>3</sub>CN and 100 mL of hexane. The biphasic solution was shaken vigorously and transferred to a separatory funnel. The CH<sub>3</sub>OH:CH<sub>3</sub>CN layer was evaporated to dryness under vacuum, producing a de-fatted extract. The extract was then subdivided into several peaks or fractions using flash chromatography. The subfractions were further separated using HPLC until pure compounds were isolated. The pure compounds were subjected to UPLC-MS analysis to establish the molecular formula and fragmentation patterns. Finally, pure compounds were identified using both NMR analysis as well as information from UPLC-MS data.

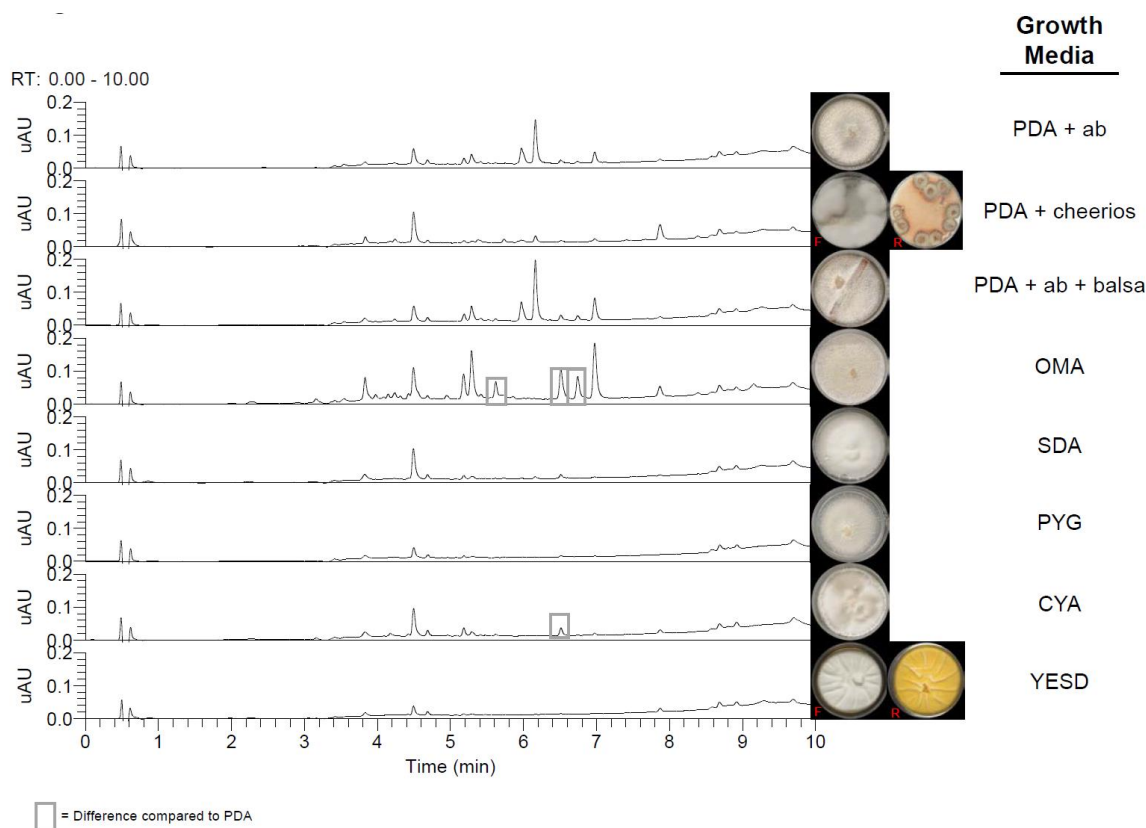


**Figure 11. A. Fischeri** Produces Different Numbers of Metabolites, Depending on the Media it is Grown on. Base peak chromatograms as measured by LC-MS, illustrating how the chemistry profiles varied based on growth conditions. PDA + ab was used as the chemical control to observe the differences in the secondary metabolites, due to it being the media that *A. Fischeri* is stored. There were overall no chemical differences observed between the different variations of PDA media. Each peak (which indicates different chemical entities) was observed in the three PDA variations, albeit at fluctuating intensities. SDA, PYG, and YESD produced the majority of the peaks observed in PDA, but it also lacked some observed peaks, indicating that these growth conditions were not

chemically favored. CYA produced the majority of the peaks, as well as an additional peak that was observed at a much lower intensity in PDA. However, this peak was similarly observed in OMA. OMA produced similar peaks to those observed in PDA, but with higher intensity. Due to this, OMA was selected to further study. The gray boxes indicate differences in the observed peaks compared to PDA.

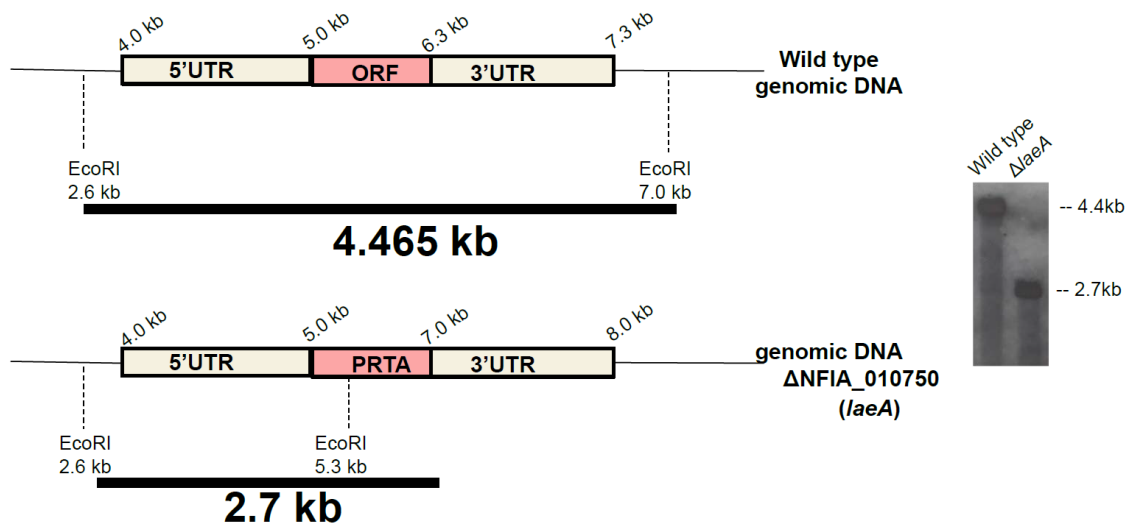


**Figure 12.** Southern Blot Confirms Construction of the  $\Delta$ iaeA Mutant. A 1kb probe recognizes a single DNA band (~4.4kb) in the wild type strain and a single DNA band (~2.7kb) in the  $\Delta$ iaeA mutant.

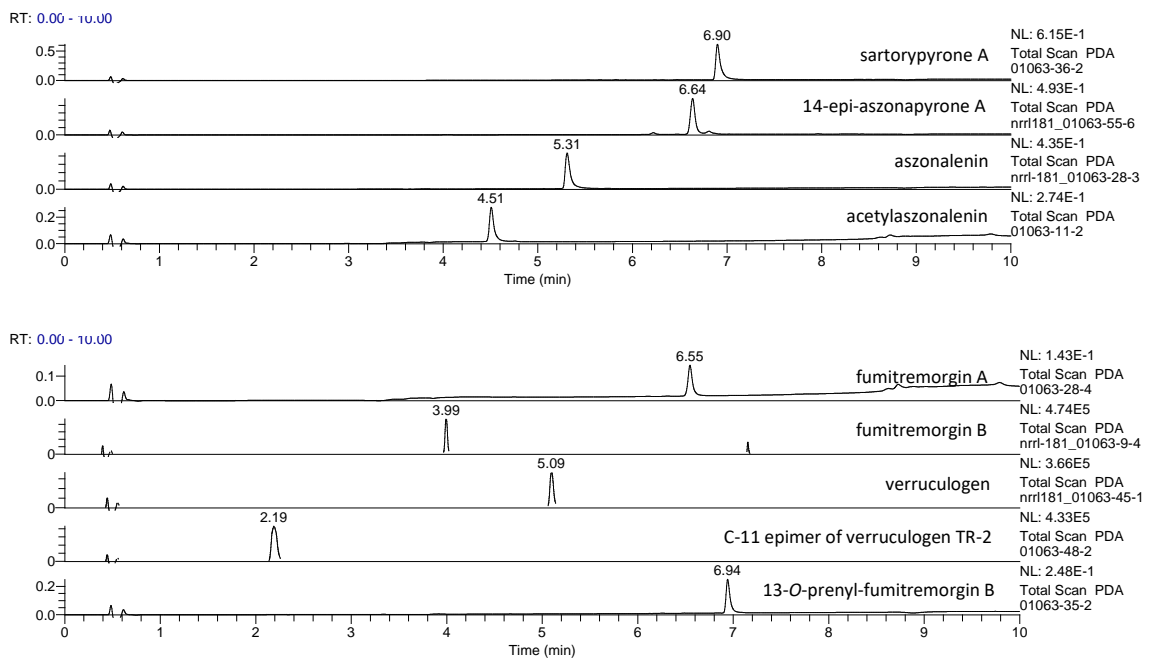


**Figure 13.** UPLC analysis of compounds **1-10**, arranged from Top to Bottom.

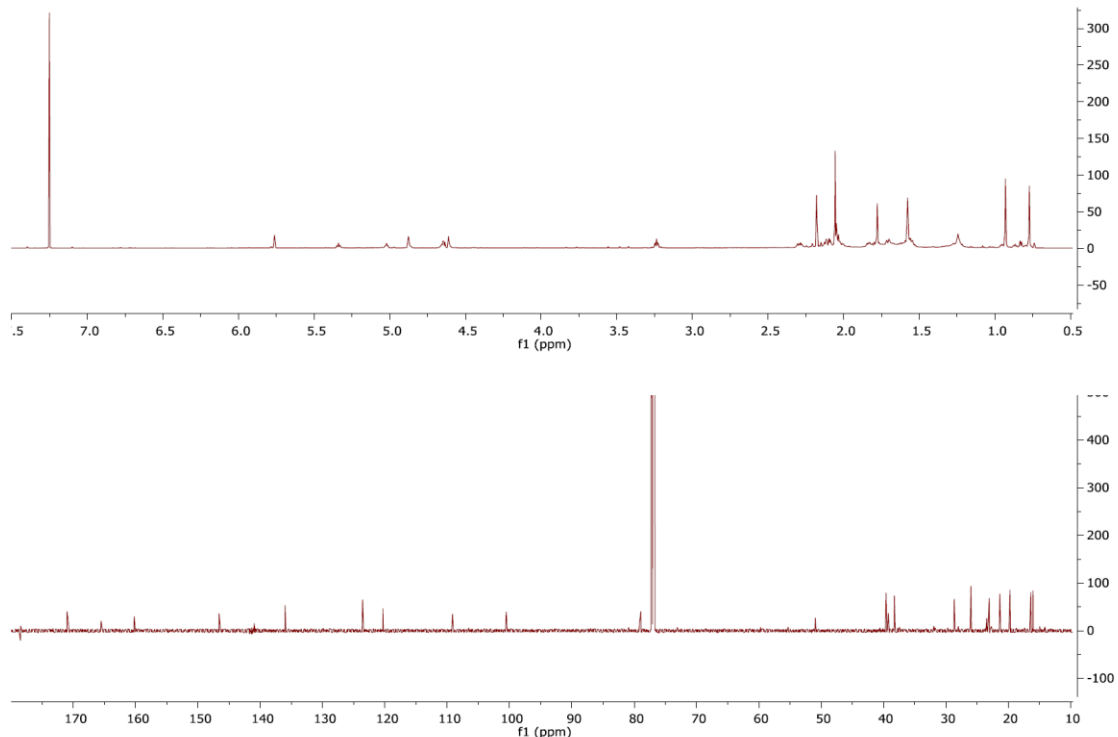


**Figure 14.**  $^1\text{H}$  NMR spectrum (700 MHz, Top) and  $^{13}\text{C}$  NMR spectrum (175 MHz, Bottom), both in  $\text{CDCl}_3$ , of sartorypyrone A (**1**)

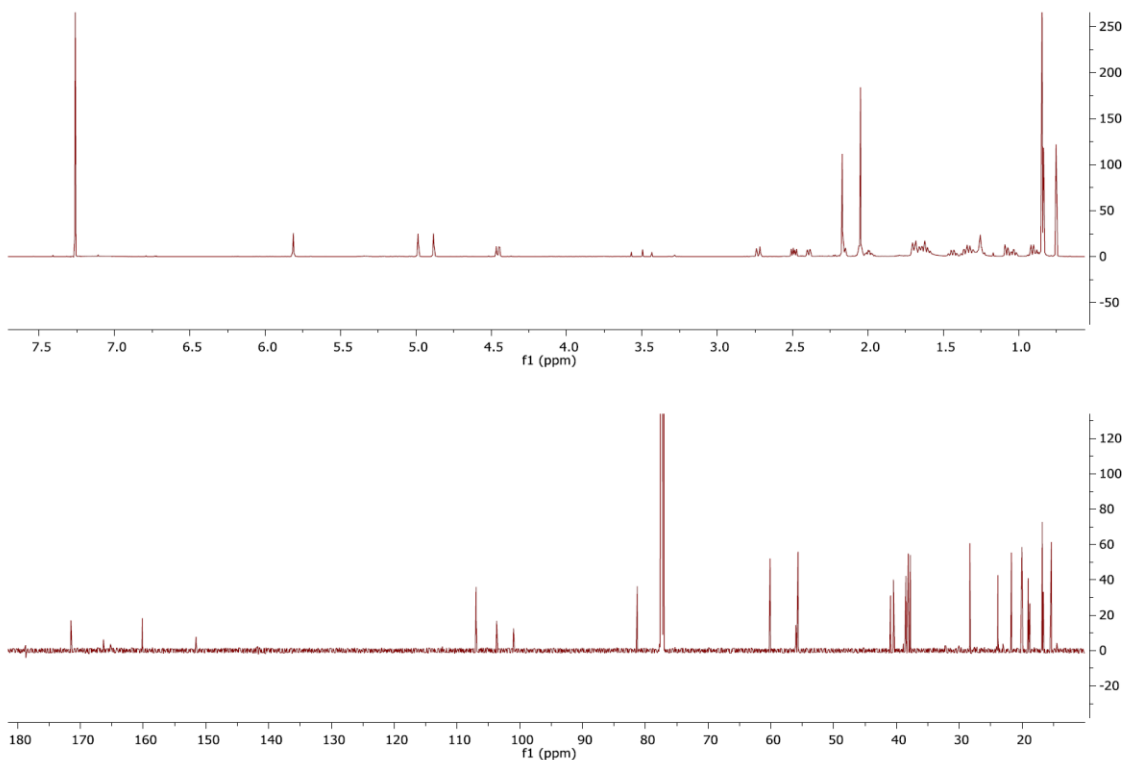


**Figure 15.**  $^1\text{H}$  NMR spectrum (700 MHz, Top) and  $^{13}\text{C}$  NMR spectrum (175 MHz, Bottom), both in  $\text{CDCl}_3$ , of 14-epi-aszonapyrone A (**3**)

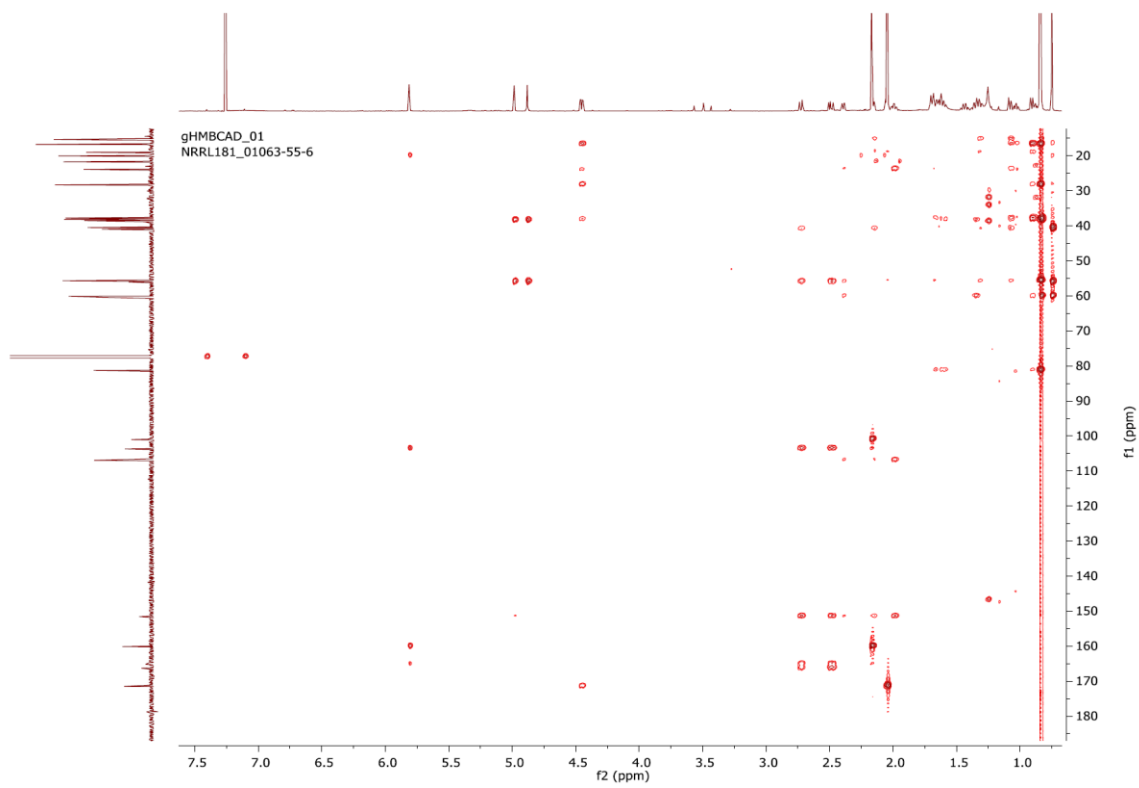


**Figure 16.** HMBC spectrum of 14-epimer of aszonapyrone A (**3**),  $\text{CDCl}_3$ , 700 MHz

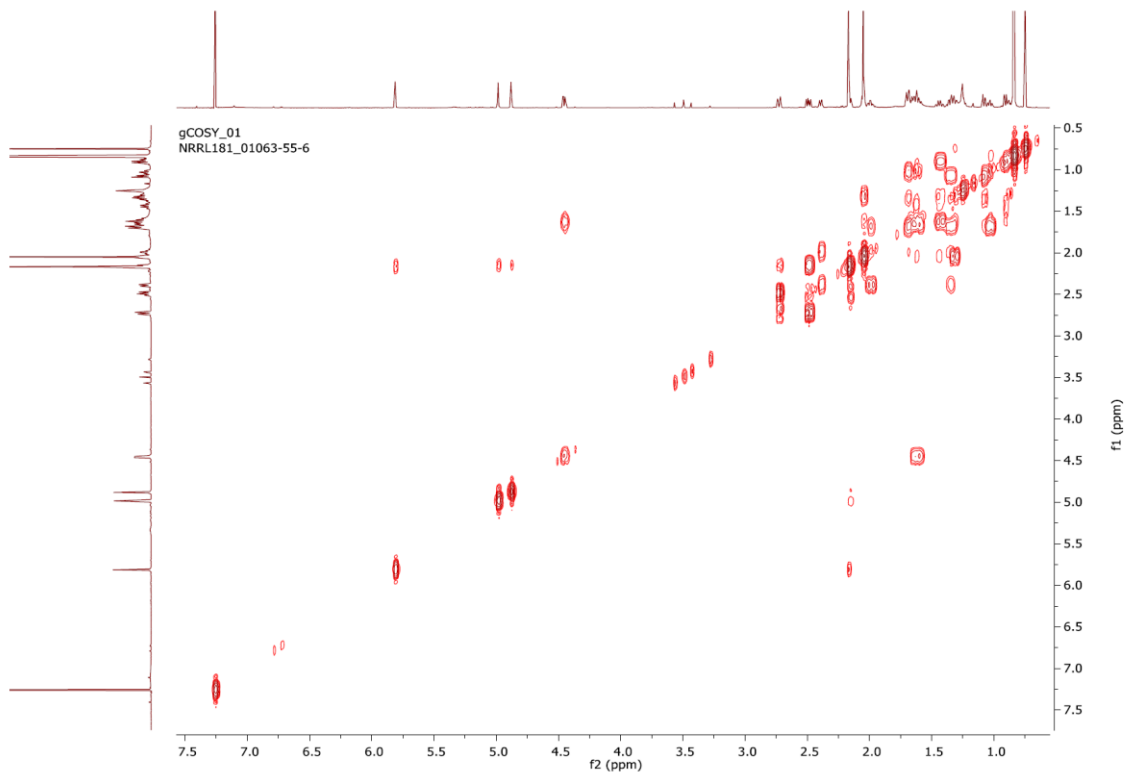


**Figure 17.** <sup>1</sup>H COSY spectrum of 14-epimer of aszonapyrone A (**3**), CDCl<sub>3</sub>, 700 MHz

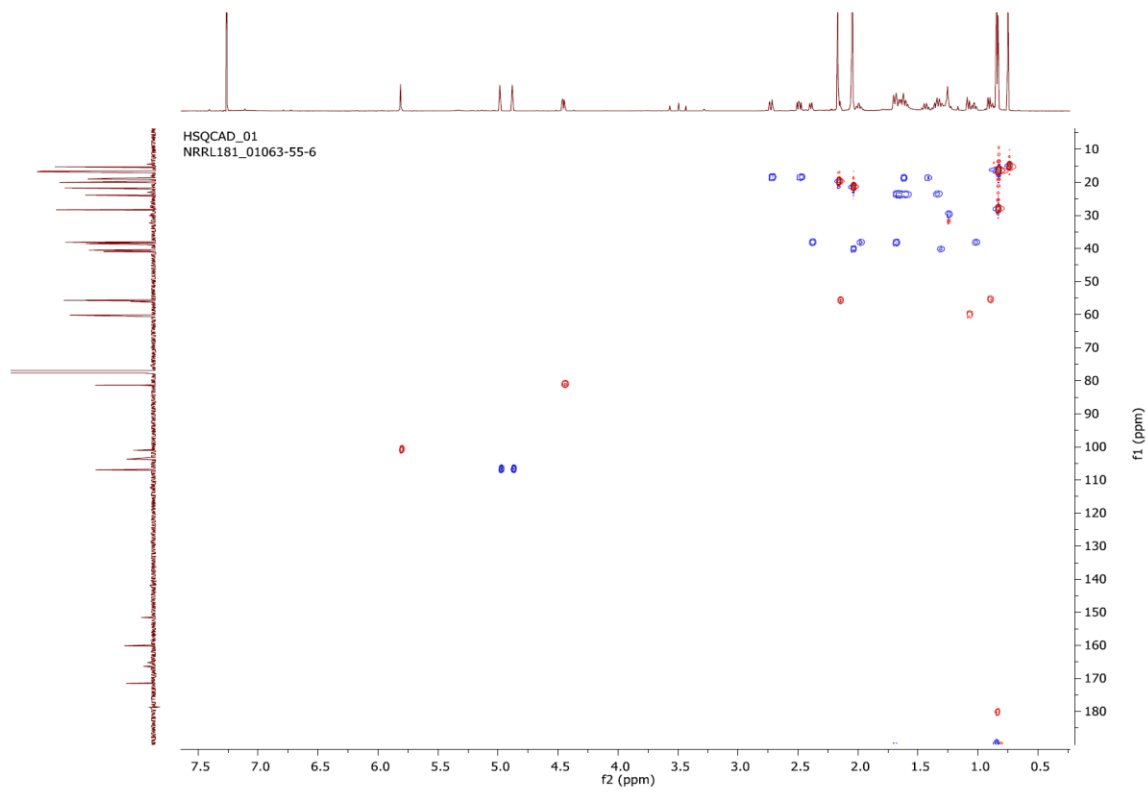


**Figure 18.** HSQC spectrum of 14-epimer of aszonapyrone A (**3**), CDCl<sub>3</sub>, 700 MHz

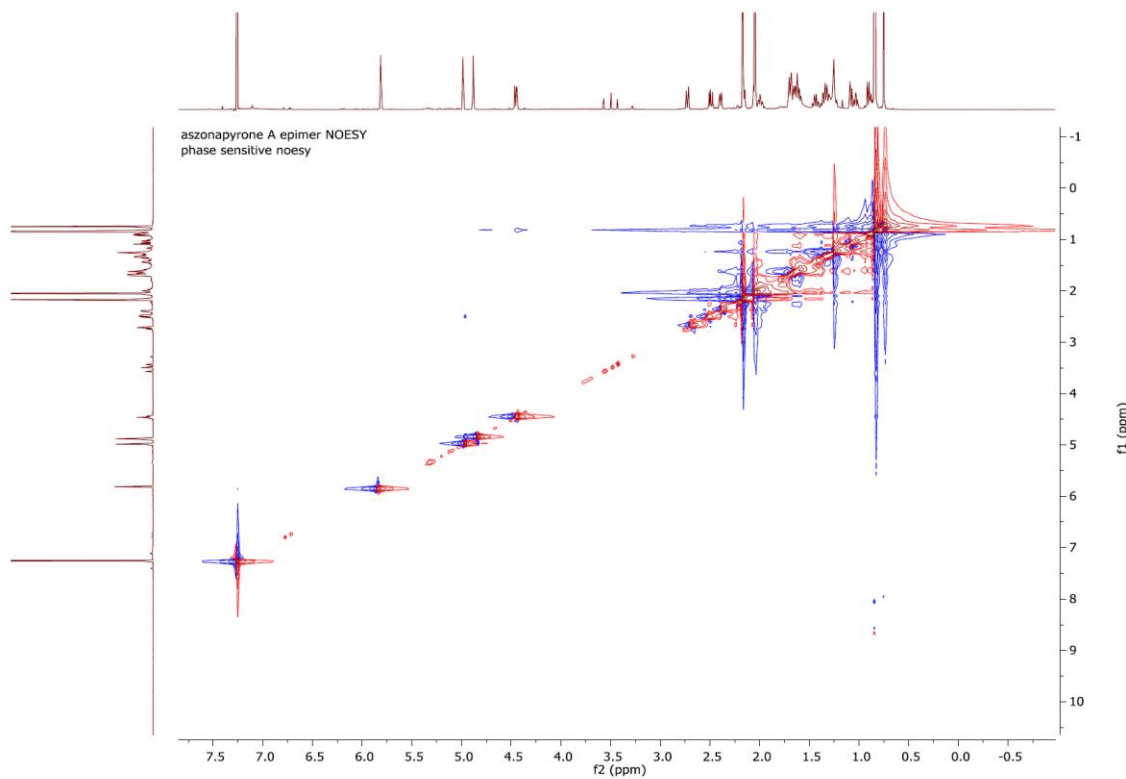


**Figure 19.** NOESY spectrum of 14-epimer of aszonapyrone A (**3**),  $\text{CDCl}_3$ , 700 MHz

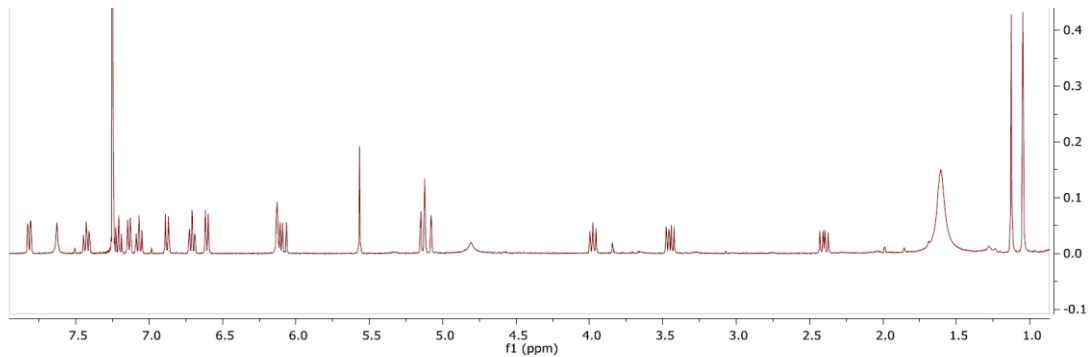


**Figure 20.**  $^1\text{H}$  NMR spectrum (400 MHz) in  $\text{CDCl}_3$ , of aszonalenin (**4**)

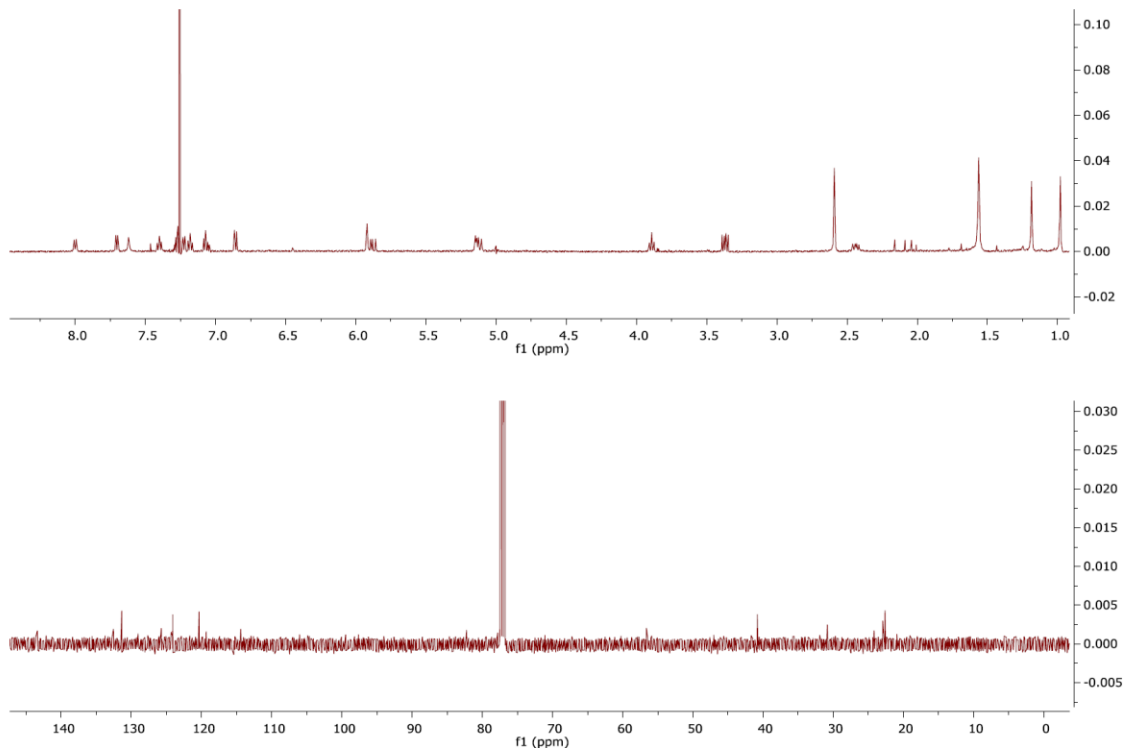


**Figure 21.**  $^1\text{H}$  NMR spectrum (500 MHz, Top) and  $^{13}\text{C}$  NMR spectrum (125 MHz, Bottom), both in  $\text{CDCl}_3$ , of acetylaszonalenin (5)

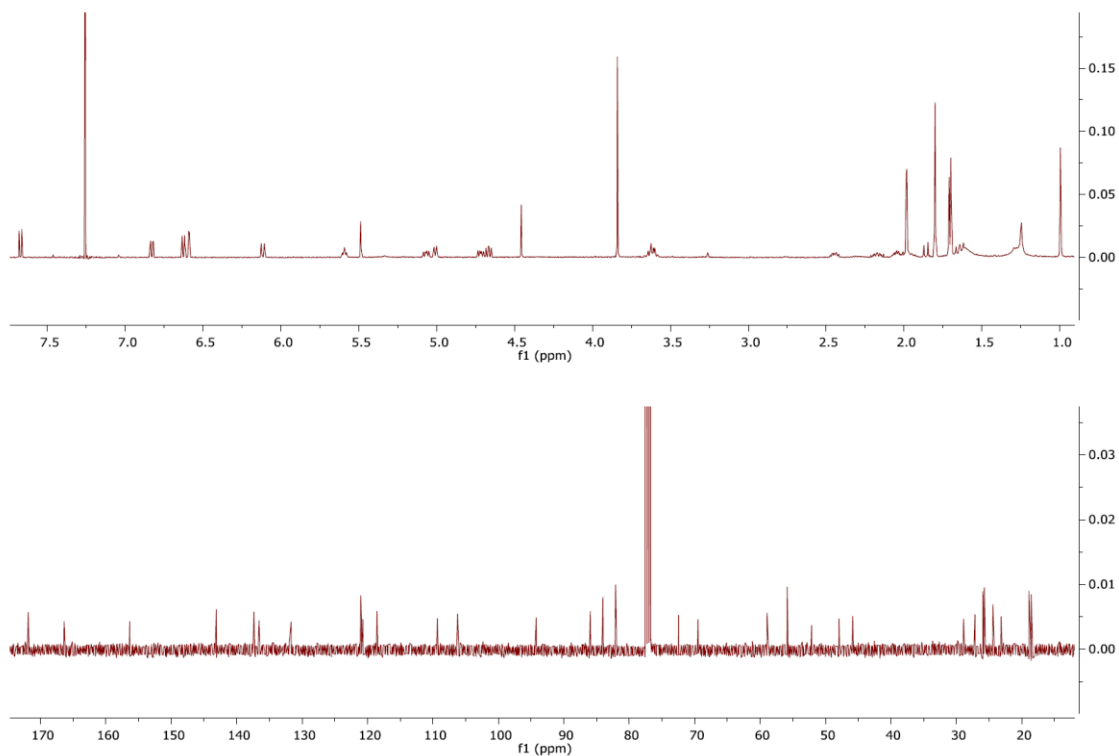


**Figure 22.**  $^1\text{H}$  NMR spectrum (500 MHz, Top) and  $^{13}\text{C}$  NMR spectrum (125 MHz, Bottom), both in  $\text{CDCl}_3$ , of fumitremorgin A (**6**)

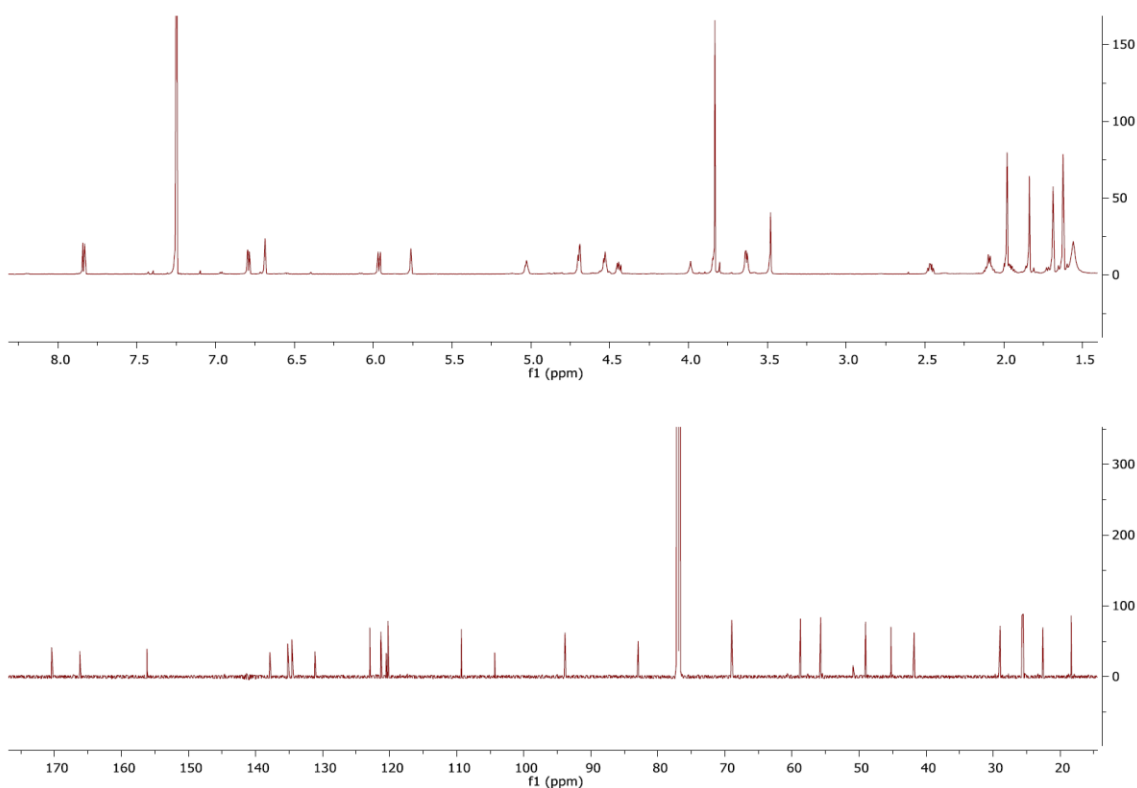


**Figure 23.** <sup>1</sup>H NMR spectrum (700 MHz, Top) and <sup>13</sup>C NMR spectrum (175 MHz, Bottom), both in CDCl<sub>3</sub>, of fumitremorgin B (**7**)

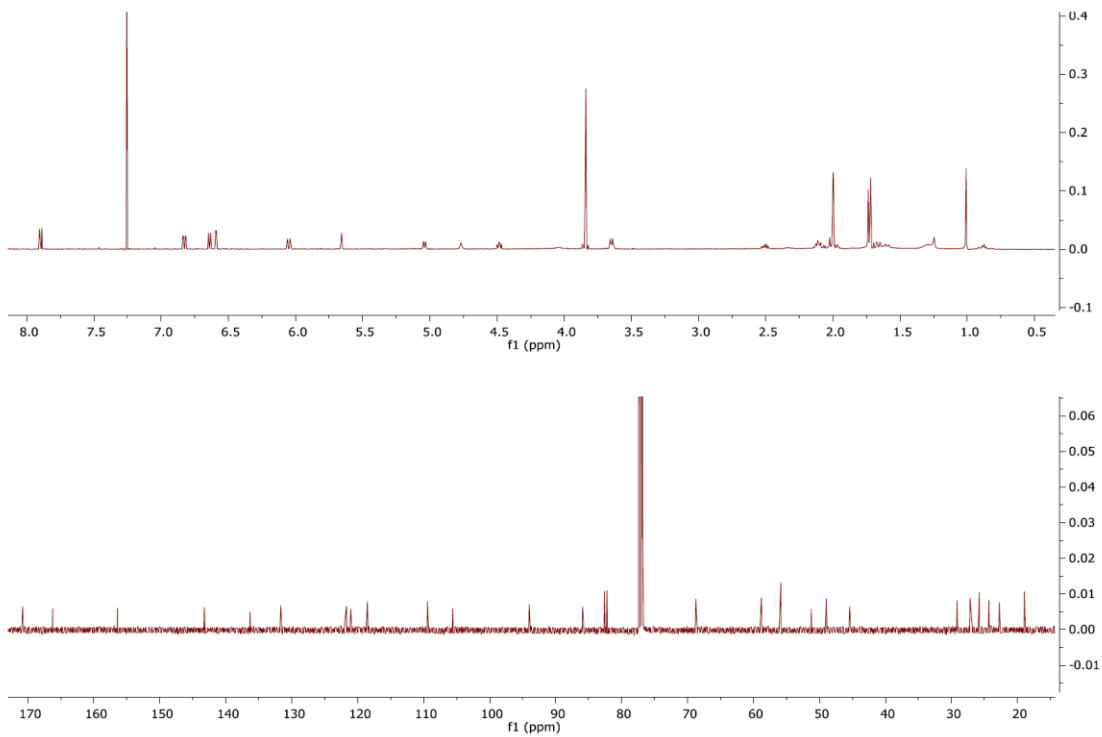


**Figure 24.**  $^1\text{H}$  NMR spectrum (500 MHz, Top) and  $^{13}\text{C}$  NMR spectrum (125 MHz, Bottom), both in  $\text{CDCl}_3$ , of verruculogen (**8**)

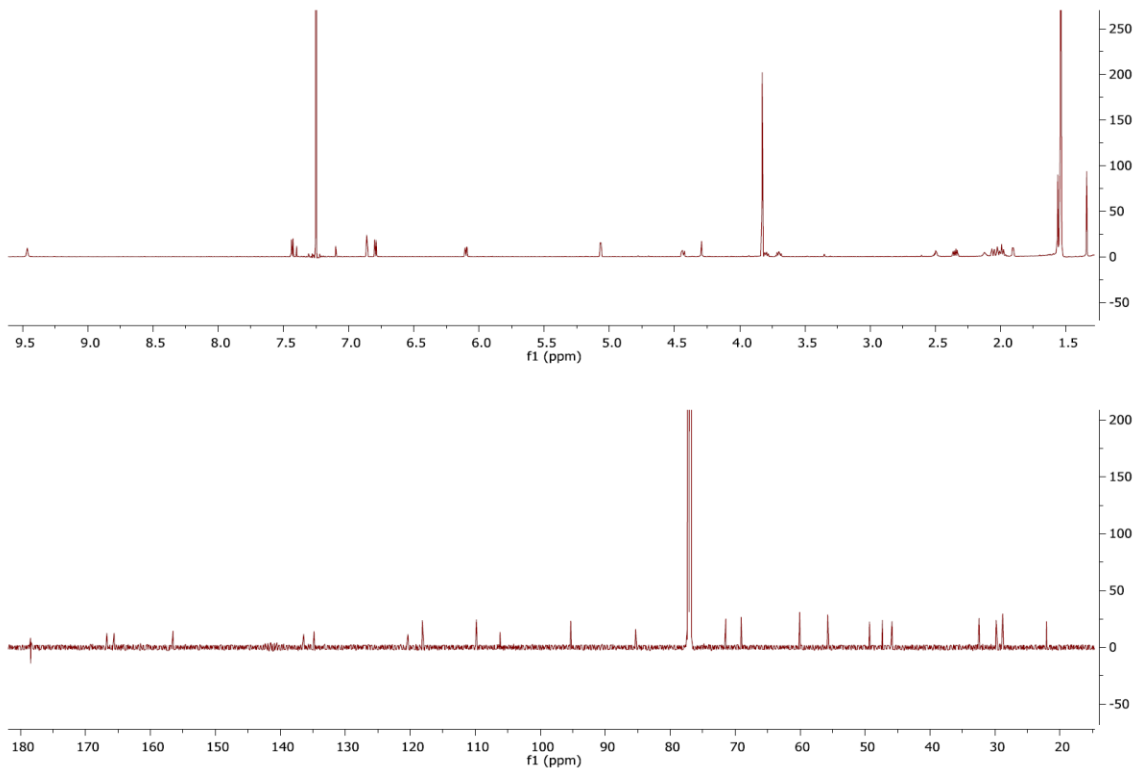


**Figure 25.**  $^1\text{H}$  NMR spectrum (700 MHz, Top) and  $^{13}\text{C}$  NMR spectrum (175 MHz, Bottom), both in  $\text{CDCl}_3$ , of C-11 epimer of verruculogen TR-2 (**9**)

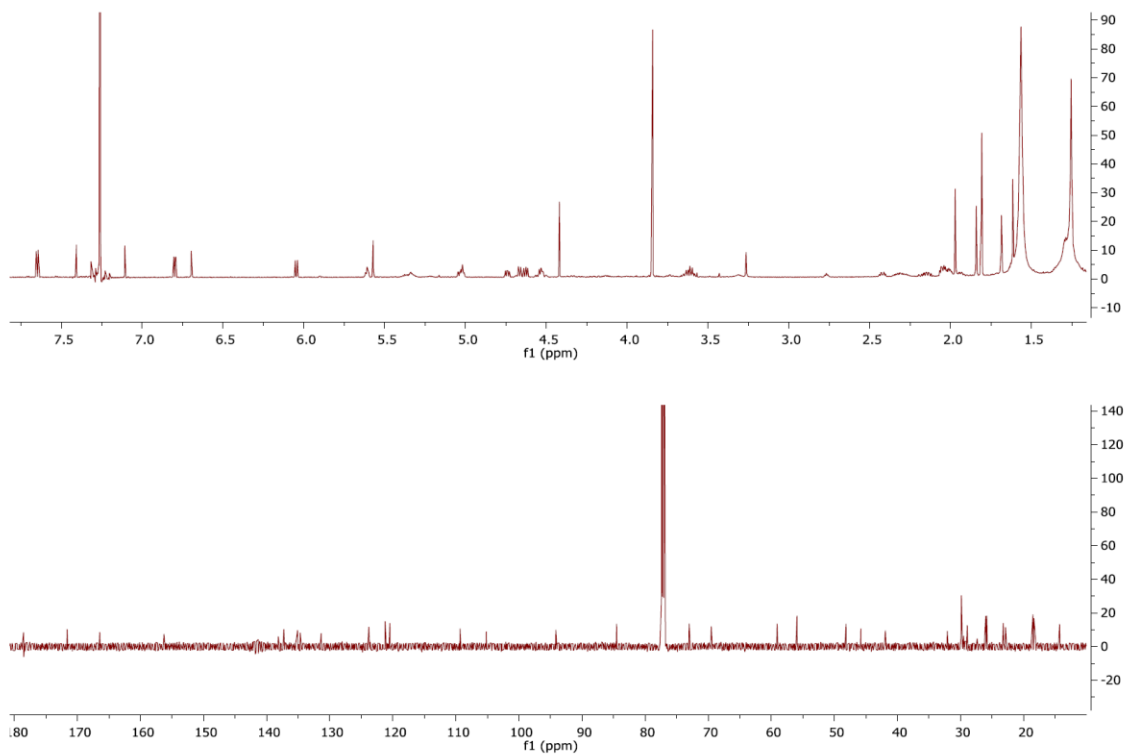


**Figure 26.** <sup>1</sup>H NMR spectrum (700 MHz, Top) and <sup>13</sup>C NMR spectrum (175 MHz, Bottom), both in CDCl<sub>3</sub>, of 13-O-prenyl-fumitremorgin B (**10**)

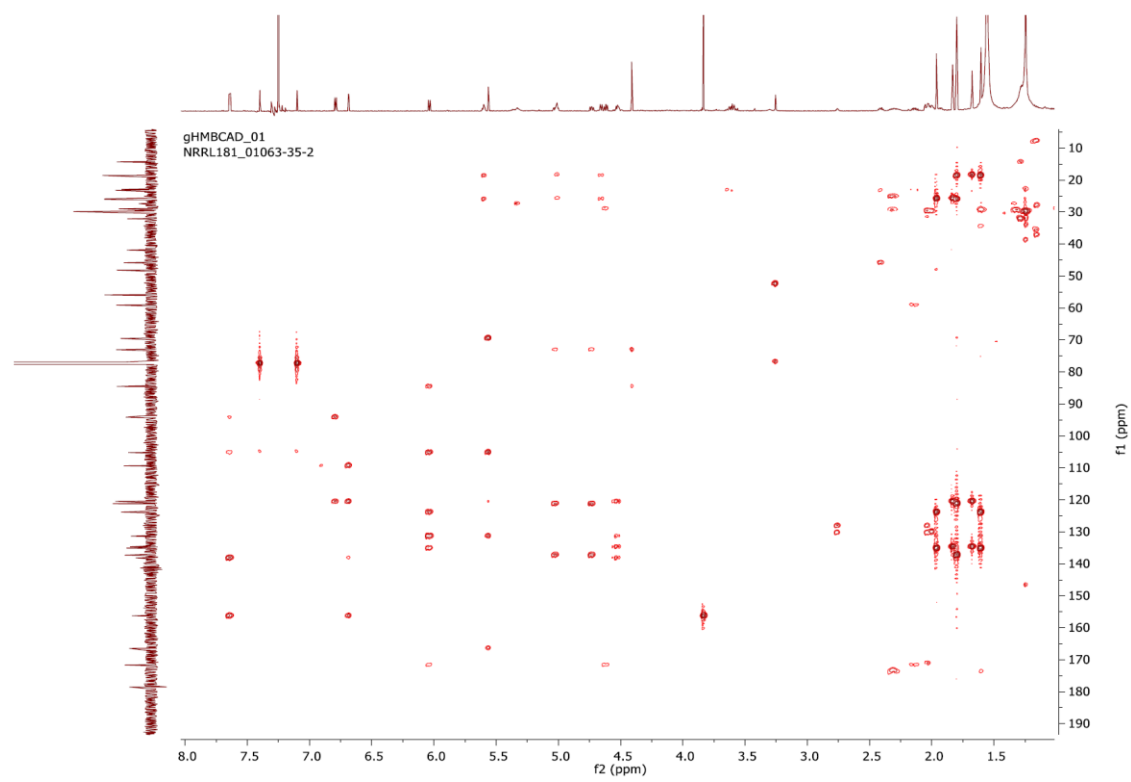


**Figure 27.** HMBC spectrum of 13-O-prenyl-fumitremorgin B (**10**),  $\text{CDCl}_3$ , 700 MHz

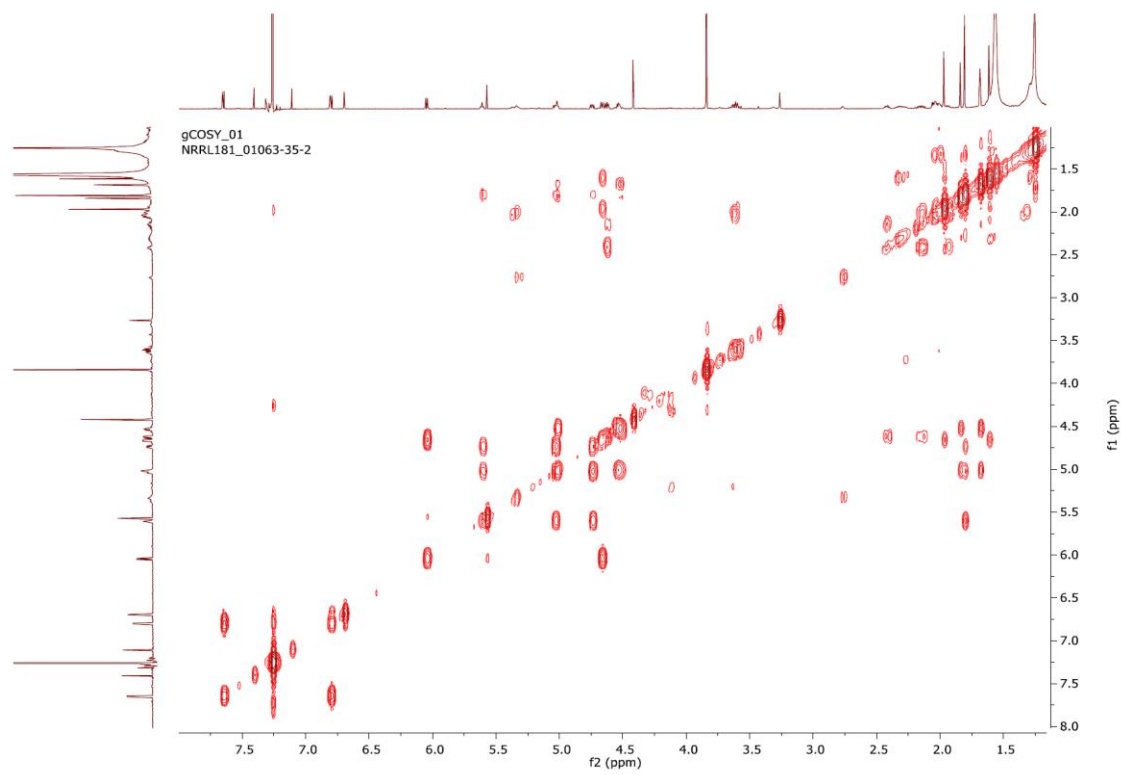


**Figure 28.** <sup>1</sup>H COSY spectrum of 13-O-prenyl-fumitremorgin B (**10**), CDCl<sub>3</sub>, 700 MHz

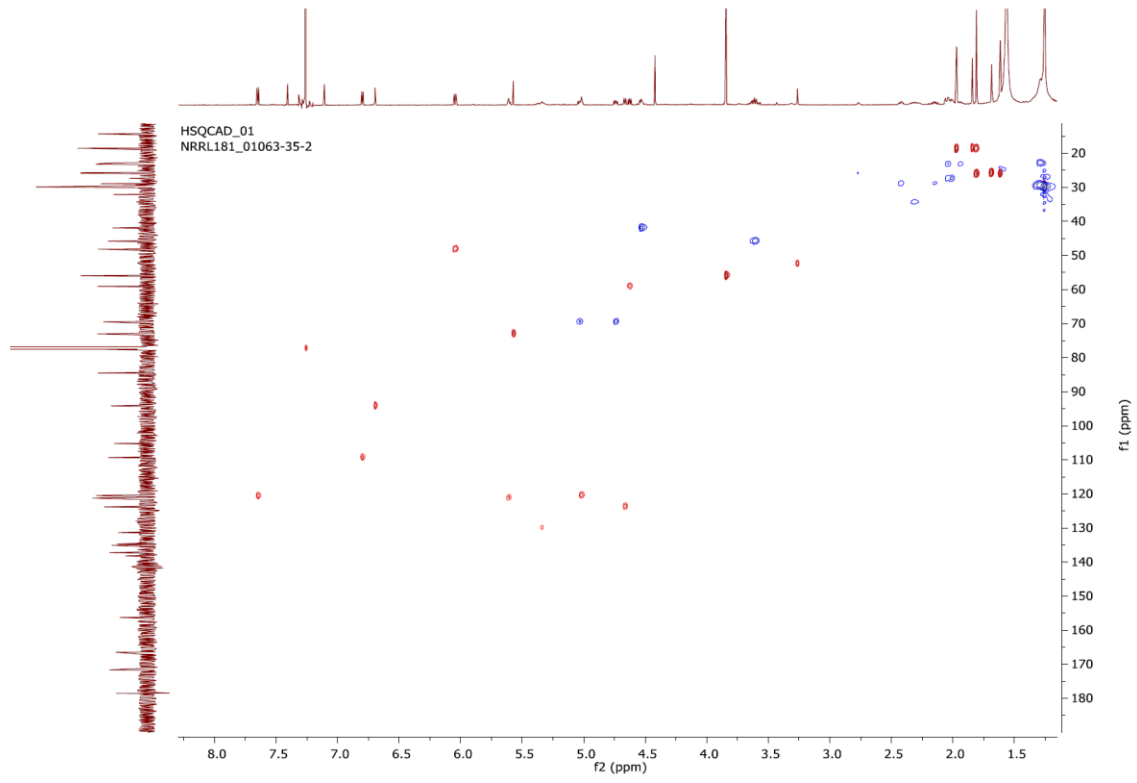


**Figure 29.** HSQC spectrum of 13-O-prenyl-fumitremorgin B (**10**),  $\text{CDCl}_3$ , 700 MHz

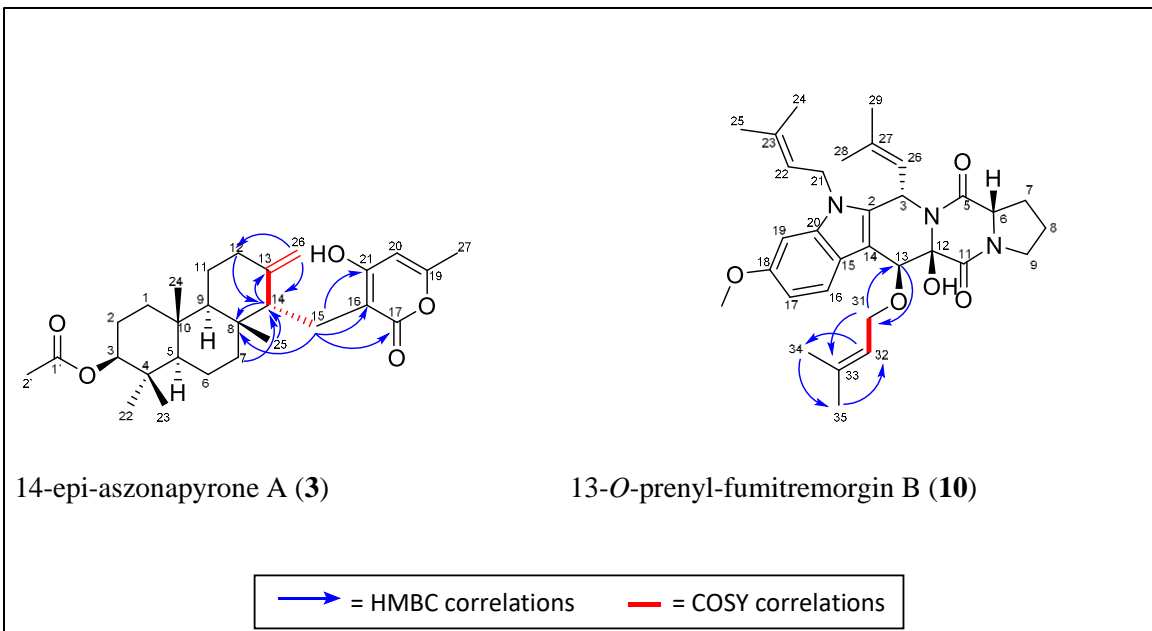


**Figure 30.** Key COSY and HMBC data for 14-epi-aszonapyrone A (**3**) and 13-O-prenyl-fumitremorgin B (**10**)

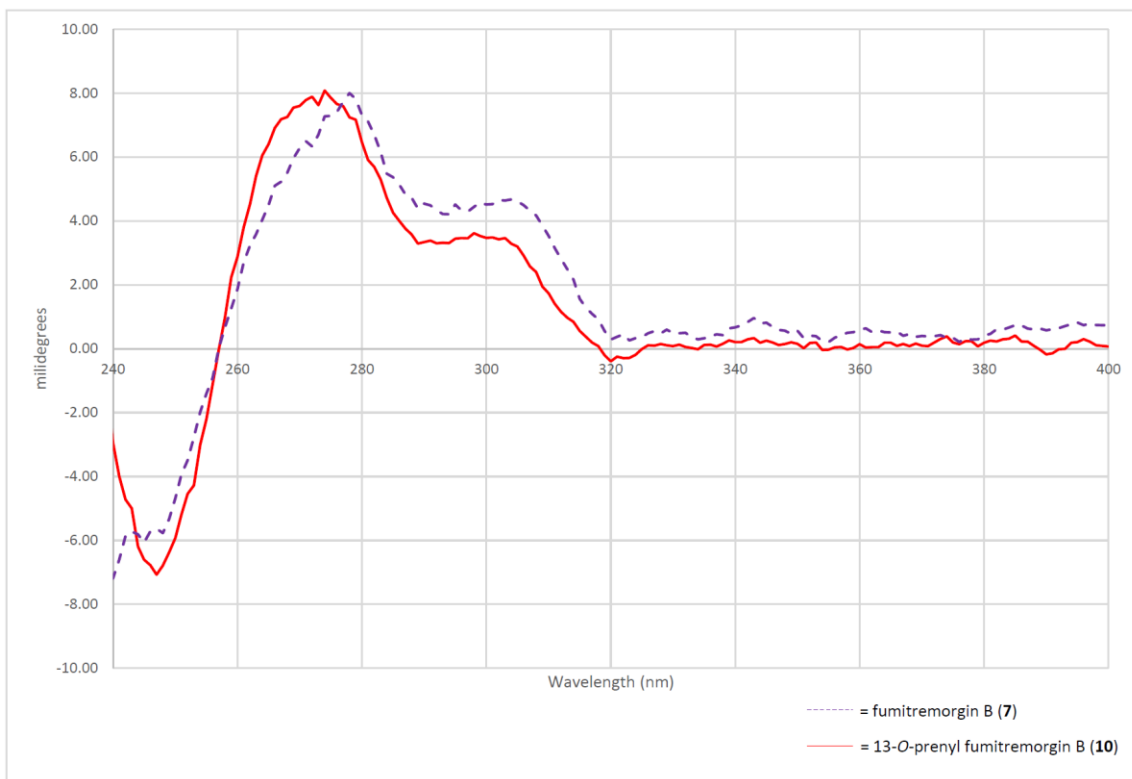


**Figure 31.** CD Data for 13-O-fumitremorgin B (**10**) and fumitremorgin B (**7**)

## CHAPTER III

### GLIOTOXIN, A KNOWN VIRULENCE FACTOR IN THE MAJOR HUMAN PATHOGEN *ASPERGILLUS FUMIGATUS*, IS ALSO BIOSYNTHESIZED BY THE NON- PATHOGENIC RELATIVE *A. Fischeri*

Sonja L. Knowles, Matthew E. Mead, Lilia Pereira Silva, Huzefa A. Raja, Jacob L. Steenwyk, Gustavo H. Goldman, Antonis Rokas, and Nicholas H. Oberlies. *mBio* 2020, 11.

*Aspergillus fumigatus* is a major opportunistic human pathogen. Multiple traits contribute to *A. fumigatus* pathogenicity, including its ability to produce specific secondary metabolites, such as gliotoxin. Gliotoxin is known to inhibit the host immune response, and genetic mutants that inactivate gliotoxin biosynthesis (or secondary metabolism in general) attenuate *A. fumigatus* virulence. The genome of *A. Fischeri*, a very close non-pathogenic relative of *A. fumigatus*, contains a biosynthetic gene cluster that exhibits high sequence similarity to the *A. fumigatus* gliotoxin cluster. However, *A. Fischeri* is not known to produce gliotoxin. To gain further insight into the similarities and differences between the major pathogen *A. fumigatus* and the non-pathogen *A. Fischeri*, we examined whether *A. Fischeri* strain NRRL 181 biosynthesizes gliotoxin and whether its production, and of secondary metabolites more generally, influence its virulence profile. We found that *A. Fischeri* biosynthesizes gliotoxin in the same conditions as *A. fumigatus*. However, whereas loss of *laeA*, a master regulator of secondary metabolite production, including gliotoxin, has been previously shown to reduce the virulence of

*A. fumigatus*, we found that *laeA* loss (and loss of secondary metabolite production) in *A. Fischeri* does not influence its virulence. These results suggest that LaeA-regulated secondary metabolites are virulence factors in the genomic and phenotypic background of the major pathogen *A. fumigatus* but are much less important in the background of the non-pathogen *A. Fischeri*. We submit that understanding the observed spectrum of pathogenicity across closely related pathogenic and non-pathogenic *Aspergillus* species will require detailed characterization of their biological, chemical, and genomic similarities and differences.

*Aspergillus fumigatus* is a major opportunistic fungal pathogen of humans but most of its close relatives are non-pathogenic. Why is that so? This important, yet largely unanswered, question can be addressed by examining how *A. fumigatus* and its non-pathogenic close relatives are similar or different with respect to virulence-associated traits. We investigated whether *Aspergillus fischeri*, a non-pathogenic close relative of *A. fumigatus*, can produce gliotoxin, a mycotoxin known to contribute to *A. fumigatus* virulence. We discovered that the non-pathogenic *A. Fischeri* produces gliotoxin under the same conditions as the major pathogen *A. fumigatus*. However, we also discovered that, in contrast to what has been previously observed in *A. fumigatus*, loss of secondary metabolite production in *A. Fischeri* does not alter its virulence. Our results are consistent with the “cards of virulence” model of opportunistic fungal disease, where the ability to cause disease stems from the combination (“hand”) of individual virulence factors (“cards”), but not from individual factors *per se*.

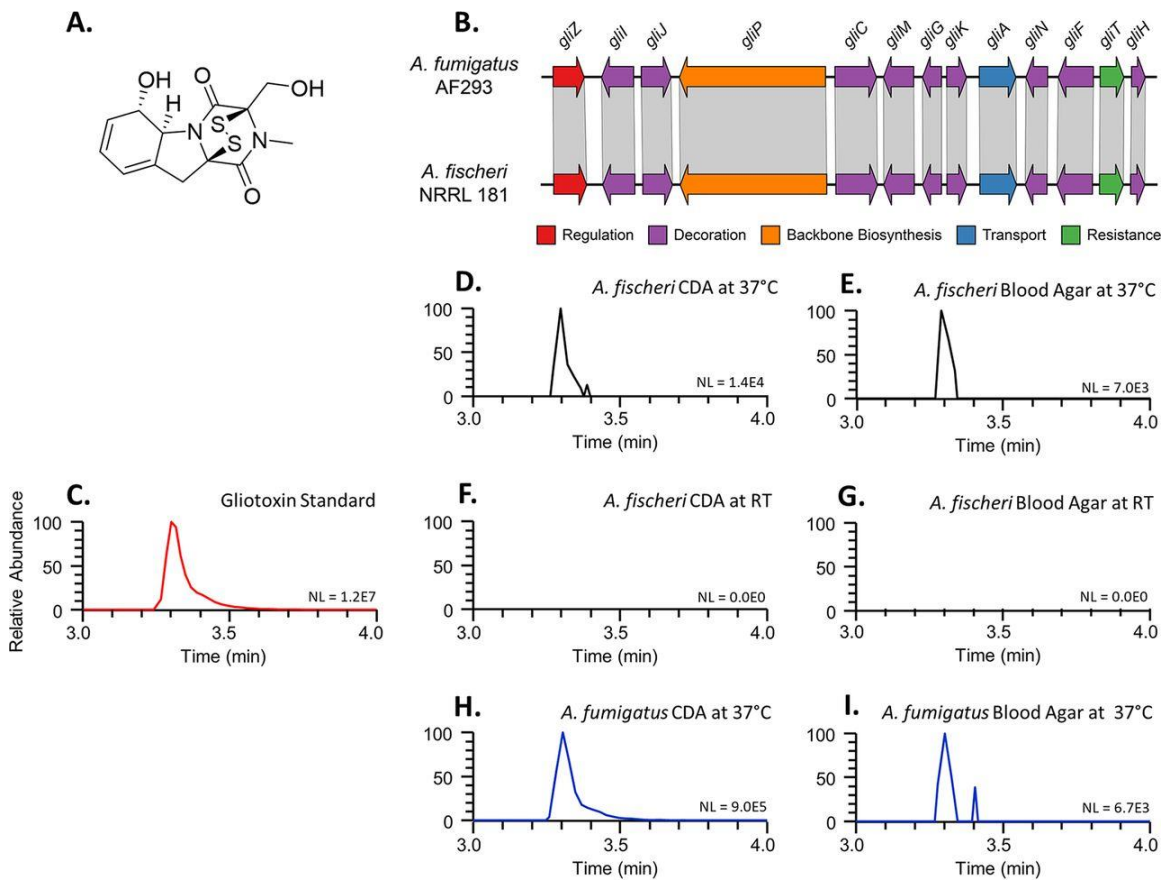


**Figure 32.** *Aspergillus fischeri* Biosynthesizes Gliotoxin When Grown in Conditions That Induce *A. fumigatus* Gliotoxin Biosynthesis. A. Chemical structure of gliotoxin. B. The genome of the non-pathogenic species *A. Fischeri* strain NRRL 181<sup>16, 123</sup> contains a biosynthetic gene cluster homologous to the gliotoxin cluster in the major pathogen *A. fumigatus* strain Af293.<sup>150, 197, 198</sup> Arrows indicate genes and the direction in which they are transcribed. Red – regulation, Purple – decoration, Orange – backbone biosynthesis, Blue – transport, Green – resistance. Homologous genes are connected by gray parallelograms. C – I. Chromatograms demonstrating the biosynthesis of gliotoxin in *A. Fischeri* when grown on Czaapek-Dox Agar (CDA) or blood agar at 37°C. Each sample (dried organic extract in MeOH at a concentration of 0.2 mg/mL) was analyzed by UHPLC-HRESIMS, and the data are presented as extracted ion chromatograms (XIC) using the protonated mass of gliotoxin ( $C_{13}H_{15}N_2O_4S_2$ ;  $[M+H]^+$  = 327.0473) and a window of  $\pm 5.0$  ppm. C. Analysis of the gliotoxin standard (in MeOH at a concentration of 0.01 mg/mL). D. *A. fumigatus* grown on CDA at 37°C. E. *A. fumigatus* grown on blood agar at 37°C. F. *A. Fischeri* grown on CDA incubated at 37°C. G. *A. Fischeri* grown on blood agar incubated at 37°C. H. *A. Fischeri* grown on CDA at room temperature (RT). I. *A. Fischeri* grown on blood agar at RT. The retention time (3.30 min) and accurate mass ( $327.0473 \pm 5.0$  ppm) data confirm the biosynthesis of gliotoxin by *A. Fischeri* in panels F and G. NL: Normalization Level (i.e., base peak intensity; the larger the NL value the better the signal to noise ratio).

*Aspergillus fumigatus* is a major fungal pathogen responsible for hundreds of thousands of infections and deaths each year.<sup>199, 200</sup> Several secondary metabolites biosynthesized by *A. fumigatus* have been shown to be required for disease.<sup>27</sup> For example, gliotoxin (Figure 32A), a secondary metabolite that belongs to the epipolythiodioxopiperazine (ETP) class of mycotoxins,<sup>150, 197, 198</sup> can be detected in the sera of patients with invasive aspergillosis<sup>201</sup> and is known to inhibit the host immune response.<sup>27</sup> When the *gliP* gene, which encodes the essential non-ribosomal peptide synthetase of the gliotoxin biosynthetic gene cluster, is deleted from *A. fumigatus*, the mutant strain does not biosynthesize gliotoxin and exhibits attenuated virulence in a non-neutropenic murine model of aspergillosis.<sup>34, 35, 202</sup> Similarly, deletion of *iaeA*, a positive regulator of several *A. fumigatus* secondary metabolites, including gliotoxin, also reduces virulence.<sup>119, 203</sup> These results suggest that gliotoxin, as well as other secondary metabolites, contribute to *A. fumigatus* virulence.<sup>27</sup>

Even though *A. fumigatus* is a major pathogen, its closest relatives are non-pathogenic.<sup>16, 181, 204</sup> For example, the closely related species *Aspergillus fischeri* has been identified as the cause of only a handful of clinical cases<sup>129, 131</sup> and is not considered pathogenic. Detailed comparisons of virulence in diverse murine and invertebrate models of fungal disease have shown that *A. Fischeri* is much less virulent than *A. fumigatus*.<sup>16</sup> It is important to emphasize here that in diverse animal models of aspergillosis, especially when high inocula of spores are administered, non-pathogens can sometimes cause disease, as we have observed in previous experiments with *A. Fischeri*; however, in all such cases non-pathogens exhibit lower levels of virulence than pathogens.<sup>16</sup>

Despite their significant differences in ability to cause fungal disease, a recent examination of known genetic contributors to virulence revealed that nearly all genes known to contribute to *A. fumigatus* disease are also present in *A. Fischeri*.<sup>16</sup> For example, both species appear to contain *iaeA*, and deletion of the *iaeA* gene in either species is known to reduce biosynthesis of secondary metabolites,<sup>16, 205</sup> suggesting that the gene's function is conserved. Similarly, both species appear to contain intact gliotoxin biosynthetic gene clusters (Figure 32B); however, gliotoxin production has been shown in *A. fumigatus* and a few other closely related species,<sup>151</sup> but not in *A. Fischeri*.<sup>16</sup>

<sup>151</sup> These data raise two questions: Is *A. Fischeri* capable of biosynthesizing gliotoxin? And if it is, how does production of gliotoxin, and secondary metabolites more generally, influence its virulence profile?

## Results

***A. Fischeri*, a Non-Pathogenic Relative of the Major Pathogen *A. fumigatus*, Can Also Biosynthesize Gliotoxin.** To test whether *A. Fischeri* biosynthesizes gliotoxin, we examined the chemical profile of a standard of gliotoxin and extracts of *A. fumigatus* strain Af293, and *A. Fischeri* strain NRRL 181 via UHPLC–HRESIMS (ultra-high-performance liquid chromatography–high-resolution electrospray ionization mass spectrometry). We collected three sets of data, specifically chromatographic retention time, high resolution mass spectrometry data, and tandem mass spectrometry fragmentation patterns. Analysis of a gliotoxin standard (Figure 32C) showed that it elutes at 3.30 min, with an accurate mass of 327.0464 Da (2.8 ppm) and has key fragments of 263.1 Da and 245.1 Da, in accord with values reported in the literature.<sup>206</sup>

We next analyzed *A. fumigatus* strain Af293, which we used as a positive control, since it is known to biosynthesize gliotoxin.<sup>151</sup> When *A. fumigatus* was grown on Czapek-

Dox Agar (CDA) at 37°C (Figure 32D), a peak with the same retention time (3.30 min), HRESIMS spectrum, MS/MS spectrum, and accurate mass of 327.0463 (3.1ppm) was noted (Figures 34 and 35). We also detected gliotoxin production, albeit in lower abundance, when we cultured *A. fumigatus* on 5% blood agar at 37°C (Figure 32E). In contrast, we did not observe gliotoxin production when we grew *A. fumigatus* on oatmeal agar at 37°C (Figure 36).

To test whether *A. Fischeri* biosynthesized gliotoxin, we grew strain NRRL 181 on the same media and temperature conditions as *A. fumigatus*. When *A. Fischeri* was grown on CDA at 37°C, we observed a peak with the same retention time (Figure 32F), HRESIMS spectrum (Figure 37), and MS/MS spectrum as that of *A. fumigatus* (Figure 38), indicating gliotoxin biosynthesis in *A. Fischeri*. Similarly, we detected gliotoxin production in lower abundance when we grew *A. Fischeri* on 5% blood agar at 37°C (Figure 32G). In contrast, we did not observe gliotoxin production when we grew *A. Fischeri* on CDA or on 5% blood agar at room temperature (Figures 32H and 32I, respectively) or on oatmeal agar at 37°C (Figure 36). These results demonstrate that: a) the non-pathogen *A. Fischeri* biosynthesizes similar quantities of gliotoxin in the same conditions that induce gliotoxin biosynthesis in the major pathogen *A. fumigatus*, and b) similar to what has been previously observed in *A. fumigatus*,<sup>207, 208</sup> both growth medium and temperature influence gliotoxin biosynthesis in *A. Fischeri*.

***IaeA*, a Master Regulator of Secondary Metabolism and *A. fumigatus* Virulence Factor, is Not a Virulence Factor in *A. Fischeri*.** To test whether the regulation of secondary metabolite production contributes to the virulence profile of *A. Fischeri*, we deleted the endogenous copy of *IaeA* from *A. Fischeri* and infected larvae of the moth *Galleria mellonella*, a well-established invertebrate model of fungal disease,<sup>183</sup>

with the resulting mutant strain. The use of *G. mellonella* larvae is an appropriate model for our study for two reasons. First, because our previous work revealed consistent virulence profile differences between wild-type (WT) strains of *A. Fischeri* and *A. fumigatus* in two difference murine models and in *G. mellonella* moth larvae<sup>16</sup>. Second, because infection of *G. mellonella* larvae with *A. fumigatus* is known to induce gliotoxin biosynthesis.<sup>209</sup> We infected asexual spores (conidia) at two different concentrations and compared the survival curves between the  $\Delta/\text{iaeA}$  and the WT strain of *A. Fischeri* (Figure 33). At both concentrations, our experiments showed that moth larval survival was not significantly different between the  $\Delta/\text{iaeA}$  and the WT strains.

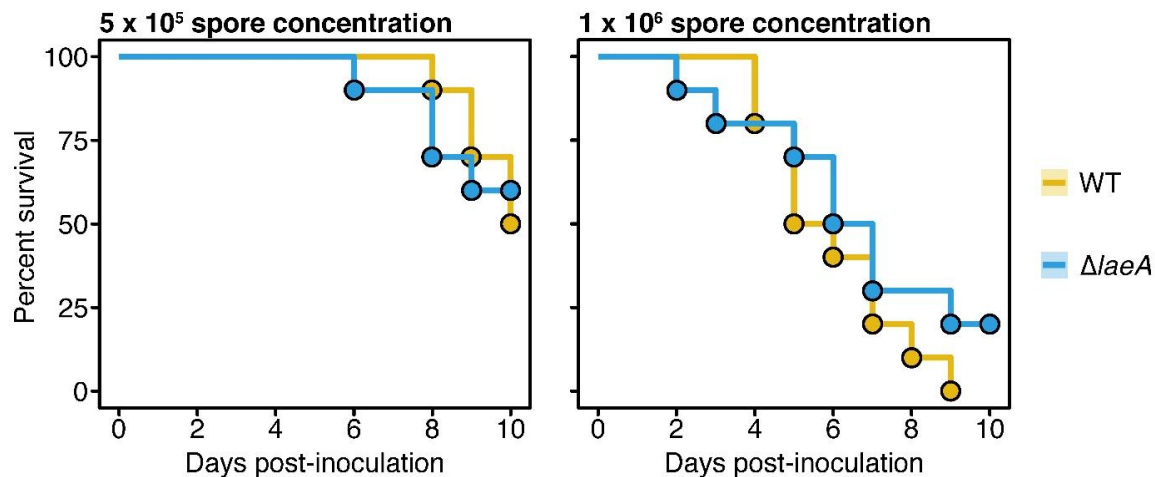


**Figure 33.** Deletion of the Master Regulator *iaeA* in *A. Fischeri* Does Not Alter its Virulence. Cumulative survival of moth (*Galleria mellonella*) larvae inoculated with  $5 \times 10^5$  (left) or  $1 \times 10^6$  (right) asexual spores or conidia of either the  $\Delta/\text{iaeA}$  mutant or the wild-type (WT) *A. Fischeri* NRRL 181 strain. Comparisons of moth cumulative survival when infected with either  $\Delta/\text{iaeA}$  or WT strain revealed no statistically significant differences at spore concentrations of  $5 \times 10^5$  (left) or  $1 \times 10^6$  (right) ( $p$ -value = 0.91 and 0.30, respectively; log-rank test). For the inoculations, ten moths were infected per group.

Importantly, the  $\Delta laeA$  strain of *A. Fischeri* NRRL 181 is known to exhibit reduced production of secondary metabolites in diverse conditions in a manner consistent with the gene's role as a master regulator of secondary metabolism.<sup>16</sup> To confirm that the  $\Delta laeA$  strain does not produce gliotoxin, we analyzed it using the same chemical methods that showed production of gliotoxin in the WT strain following growth on CDA or 5% blood agar at 37°C. In contrast to the WT strain (Figures 32F and 32G), we did not observe gliotoxin production in the  $\Delta laeA$  strain (Figure 36). Whereas loss of *laeA* and secondary metabolite – including gliotoxin – production has been previously shown to reduce the virulence of the major pathogen *A. fumigatus*,<sup>119, 203</sup> our results suggest that loss of *laeA* and secondary metabolite production<sup>16</sup> in *A. Fischeri* does not influence its virulence.

In contrast to the attenuation of *A. fumigatus* virulence observed in the  $\Delta laeA$ <sup>119,</sup><sup>203</sup> and  $\Delta gliP$ <sup>34, 35, 202</sup> strains, deletion or overexpression of *gliZ*, the transcriptional regulator of the gliotoxin biosynthetic cluster, does not alter the virulence of *A. fumigatus*.<sup>210</sup> Dissecting the effect of gliotoxin in *A. Fischeri* virulence through the construction of  $\Delta gliZ$  and  $\Delta gliP$  mutants in multiple animal models would be an interesting follow-up experiment, especially given that *A. fumigatus*  $\Delta laeA$  strains have been previously shown to produce a lower, but considerable, amount of gliotoxin *in vivo* during murine infection.<sup>210</sup> However, given that deletion of *laeA* does not alter *A. Fischeri* virulence (Figure 33), the expectation would be that specific inactivation of the gliotoxin biosynthetic gene cluster would not alter the virulence profile of *A. Fischeri*.

## **Materials and Methods**

**Fungal Strains.** *Aspergillus fischeri* strain NRRL 181 was obtained from ARS Culture Collection (NRRL).<sup>16</sup> *A. fumigatus* strain Af293 was also utilized as a positive control.<sup>211</sup>

**Growth Conditions.** All strains were maintained on potato dextrose agar (PDA; Difco). To establish individual cultures, an agar square along with fungal mycelium was cut out aseptically from the leading edge of the culture and transferred onto blood agar (tryptic soy agar with 5% sheep's blood; Hardy Diagnostics), Czapek-Dox agar (CDA; Difco), or oatmeal agar (OMA; Difco). All cultures at 37°C were maintained in an incubator (VWR International) in the dark over four days. All cultures at room temperature (RT; ~22°C) were kept for two weeks under 12h light/dark cycles. *A. Fischeri* was grown on CDA (RT and 37°C), blood agar (RT and 37°C), and OMA (37°C). *A. fumigatus* was grown on CDA (37°C), blood agar (37°C), and OMA (37°C).

**Extraction.** To evaluate the biosynthesis of gliotoxin in these fungal strains, cultures were extracted with organic solvents and analyzed by mass spectrometry (see below). The agar plates were extracted by spraying the fungal mycelium with MeOH, chopping it with a spatula, and transferring the contents to a scintillation vial. Acetone (~15 ml) was then added to the scintillation vial, and the resulting slurry was vortexed vigorously for approximately 3 min before steeping for 4 h at RT. Subsequently, the mixture was filtered and the resulting extract was dried under a stream of nitrogen gas.

**UHPLC-HRESIMS Analysis.** High-resolution electrospray ionization mass spectrometry (HRESIMS) experiments utilized a Thermo LTQ Orbitrap XL mass spectrometer (Thermo Fisher Scientific), equipped with an electrospray ionization source. This was coupled to an Acquity ultra-high-performance liquid chromatography

(UHPLC) system (Waters Corp.), using a flow rate of 0.3 ml/min and a BEH C<sub>18</sub> column (2.1 mm x 50 mm, 1.7 µm) that was operated at 40°C. The mobile phase consisted of CH<sub>3</sub>CN–H<sub>2</sub>O (Fischer Optima LC-MS grade; both acidified with 0.1% formic acid). The gradient began at 15% CH<sub>3</sub>CN and increased linearly to 100% CH<sub>3</sub>CN over 8 mins, where it was held for 1.5 mins before returning to starting conditions to re-equilibrate.

Extracts were analyzed in the positive ion mode, scanning over a mass range of *m/z* 100 to 2,000 at a resolving power of 30,000. The spray voltage, source capillary, and tube lens voltages were set to 4.0 kV, 20 V, and 100 V, respectively, with a nitrogen sheath gas set to 30 arb and capillary temperature at 300°C. The fragmentation patterns (i.e., MS/MS data) were obtained by using an inclusion list containing the mass of gliotoxin ([M+H]<sup>+</sup> = 327.047 *m/z*), with an isolation window of 2 Da and collision energy of 35%. The extracts and gliotoxin standard (Cayman Chemical Company) were prepared at a concentration of 0.2 mg/ml and 0.01 mg/ml, respectfully; both were dissolved in MeOH with an injection volume of 3 µl. To eliminate the possibility for sample carryover, two blanks (MeOH) were injected between every sample injection and the gliotoxin standard was analyzed at the end of the run.

**Virulence Studies Using an Invertebrate Model of Fungal Disease (*Galleria mellonella*).** These experiments were performed as previously described.<sup>16</sup> Briefly, larvae of the moth *G. mellonella* were obtained by breeding adult moths<sup>183</sup> and selecting larvae that were similar in size (~275–330 mg). Prior to use, all larvae were kept for 24 hours in glass petri dishes in darkness at 37°C. Asexual spores (conidia) of Δ<sub>laeA</sub> mutant or the wild-type (WT) *A. Fischeri* were obtained by growing the organism on a yeast extract-agar-glucose (YAG) medium for 2 days. Conidia were harvested in PBS and filtered through Miracloth (Calbiochem). Conidial concentration was estimated using

a hemocytometer and conidial viability was assessed through incubation on YAG medium at 37°C for 48 h.

For infection assays, ten *G. mellonella* larvae in the final (sixth) instar larval stage of development were used per condition. Each larva in the test group was infected with a 5 µl inoculum of conidia from the  $\Delta/\text{iaeA}$  mutant of *A. Fischeri* (at either a  $5 \times 10^5$  spores / µl or a  $1 \times 10^6$  spores / µl concentration), whereas each larva in the control group was inoculated with the same concentration of the WT strain of *A. Fischeri*. All inoculations were done using a Hamilton syringe (7000.5KH). All injections were performed at the hemocoel of each larva via the last left proleg. Following inoculation, all larvae were incubated in glass petri dishes in darkness at 37°C. Larval killing was scored daily. Larvae were considered dead by if they did not move in response to touch.

## Conclusion

In this study, we show for the first time that *A. Fischeri* – when grown in conditions known to induce gliotoxin production in *A. fumigatus* – can biosynthesize gliotoxin (Figure 32). Furthermore, we show that an *A. Fischeri* mutant that lacks a master regulatory gene of secondary metabolism (*iaeA*) does not alter the pathogenic potential of *A. Fischeri* (Figure 33). Thus, it appears that secondary metabolites are virulence factors in the genomic and phenotypic background of the pathogen *A. fumigatus* but that they are much less important for virulence in the genomic background of the non-pathogen *A. Fischeri*. These results provide support for the “cards of virulence” model of opportunistic fungal disease<sup>212</sup>, where the ability to cause disease stems from the combination (“hand”) of individual virulence factors (“cards”). We hypothesize that while *A. Fischeri* possesses the “cards” for gliotoxin production and

secondary metabolism regulation, its cumulative “hand” is thankfully not a winner when it comes to causing disease.

## Supplementary Data

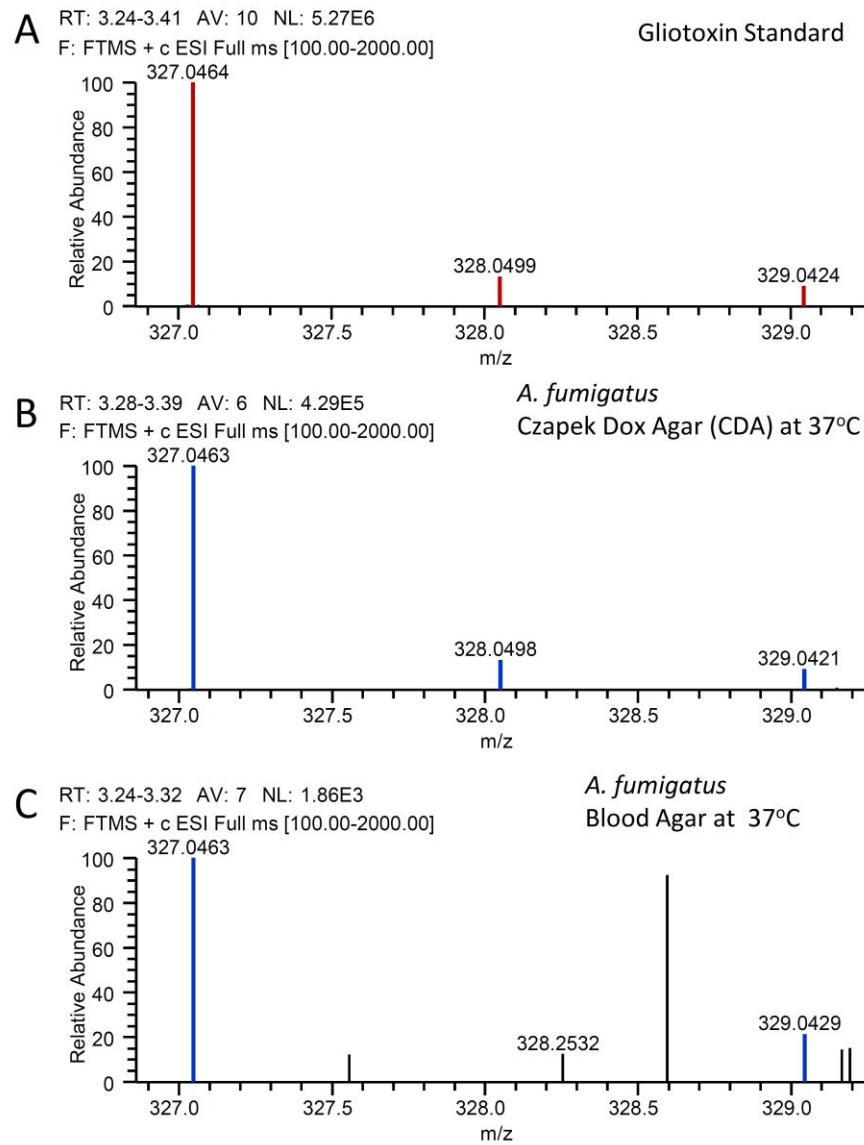


**Figure 34.** The mass spectra of gliotoxin in *A. fumigatus* grown on CDA and blood agar at 37°C verify the biosynthesis of gliotoxin by cultures of *A. fumigatus* on both CDA and blood agar at 37°C. Data are presented as mass to charge ratios ( $m/z$ ). A. The isotopic pattern of the standard gliotoxin. B. The isotopic pattern of gliotoxin observed in *A.*

*fumigatus* grown on CDA at 37°C. C. The isotopic pattern of gliotoxin observed in *A. fumigatus* grown on blood agar at 37°C.

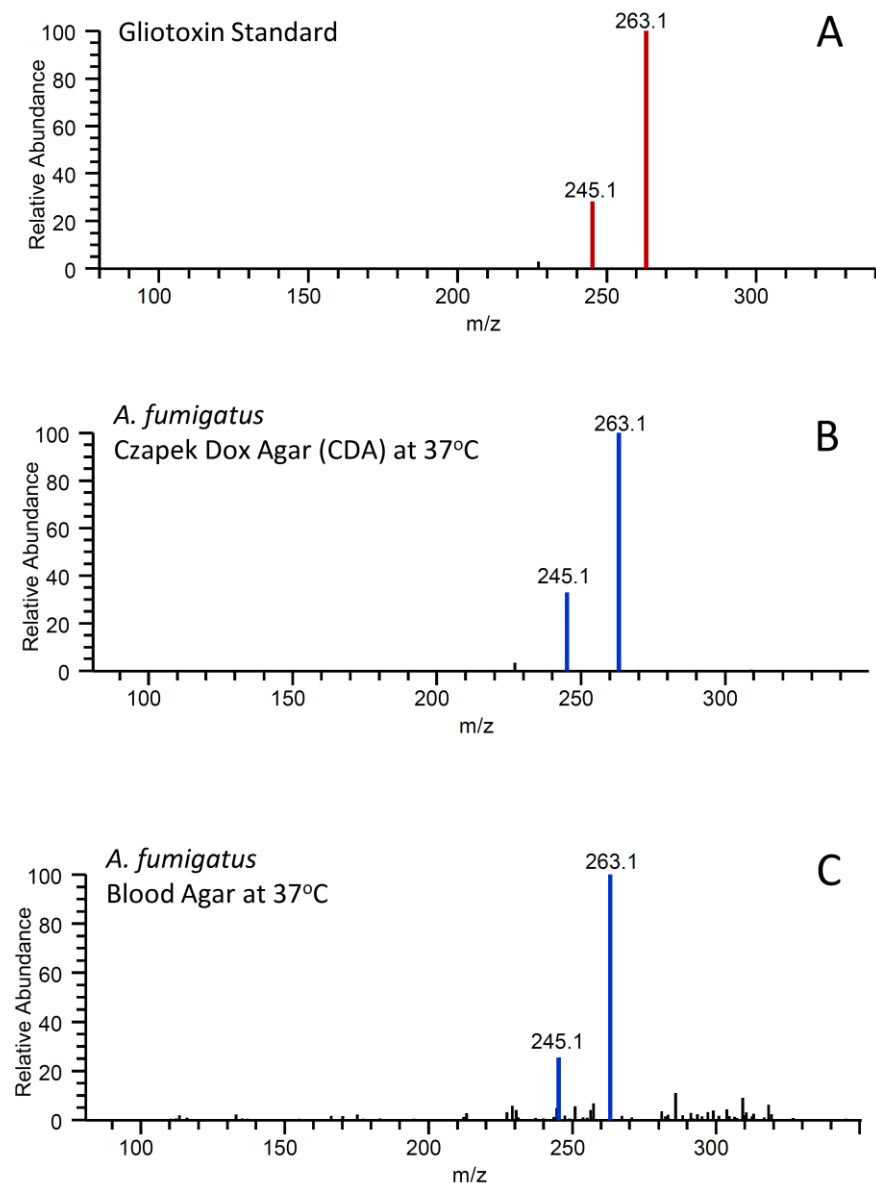


**Figure 35.** The fragmentation pattern (i.e., MS/MS data) of gliotoxin in *A. fumigatus* grown on CDA and blood agar at 37°C verify the biosynthesis of gliotoxin in both the CDA and blood agar growths of *A. fumigatus* at 37°C. A. The fragmentation pattern of the gliotoxin standard (263.1 and 245.1). B. The fragmentation pattern of gliotoxin observed in *A. fumigatus* grown on CDA incubated at 37°C. C. The fragmentation pattern of gliotoxin observed in *A. fumigatus* grown on blood agar incubated at 37°C.

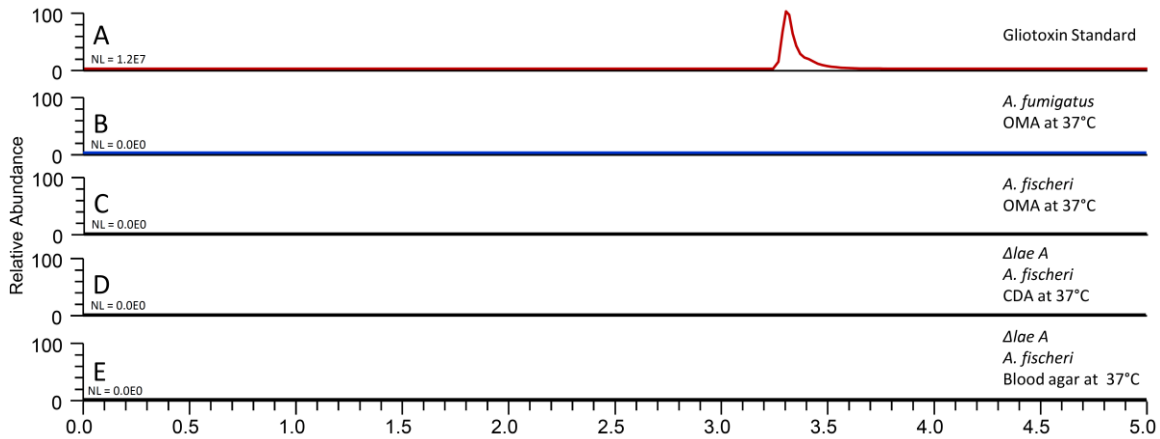


**Figure 36.** Base peak chromatograms of the gliotoxin standard, *A. fumigatus* grown on OMA at 37°C, *A. Fischeri* grown on OMA at 37°C,  $\Delta lae\ A$  *A. Fischeri* grown on CDA at 37°C, and  $\Delta lae\ A$  *A. Fischeri* grown on blood agar at 37°C show that some media do not induce gliotoxin biosynthesis. Additionally, a negative control was analyzed (Panel C), to confirm that the observation of gliotoxin biosynthesis (Figure 32) was genuine and not simply due to system carryover. Each sample (0.2 mg/mL) was analyzed by UHPLC-HRESIMS, and the data are presented as extracted ion chromatograms (XIC) using the protonated mass of gliotoxin ( $C_{13}H_{15}N_2O_4S_2$ ;  $[M+H]^+ = 327.0473$ ) and a window of  $\pm 5.0$  ppm. A. Analysis of the gliotoxin standard (0.01 mg/mL). B. *A. fumigatus* grown on OMA incubated at 37°C. C. *A. Fischeri* grown on OMA incubated at 37°C. D.  $\Delta lae\ A$  *A. Fischeri* grown on CDA incubated at 37°C. E.  $\Delta lae\ A$  *A. Fischeri* grown on blood agar incubated at 37°C.

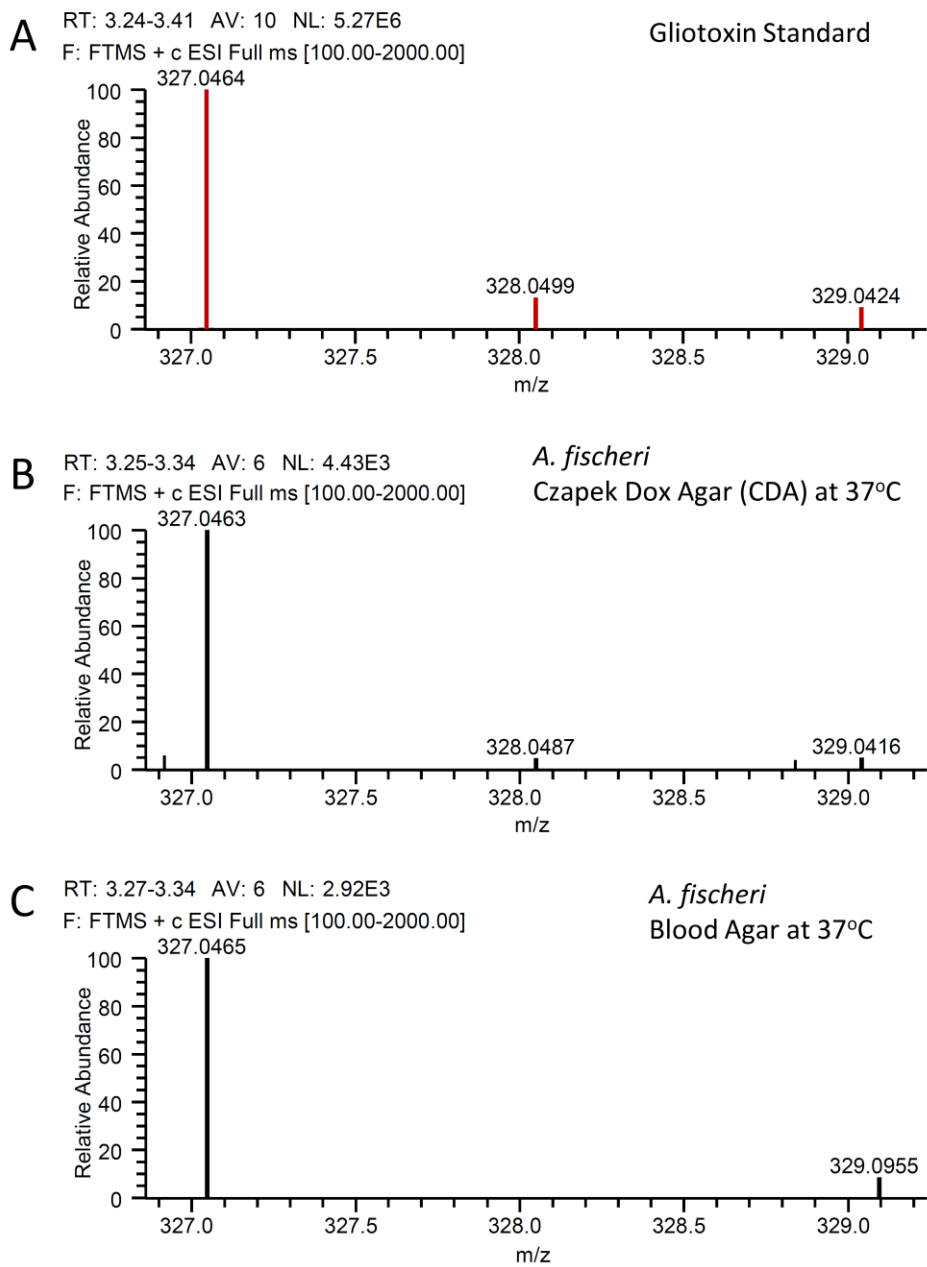


**Figure 37.** The mass spectra of gliotoxin in *A. Fischeri* verify the biosynthesis of gliotoxin by cultures of *A. Fischeri* on both CDA and blood agar at 37°C. The data are presented as mass to charge ratios ( $m/z$ ). A. The isotopic pattern of the standard gliotoxin. B. Isotopic pattern of gliotoxin observed in *A. Fischeri* grown on CDA at 37°C. C. Isotopic pattern of gliotoxin observed in *A. Fischeri* grown on blood agar at 37°C.

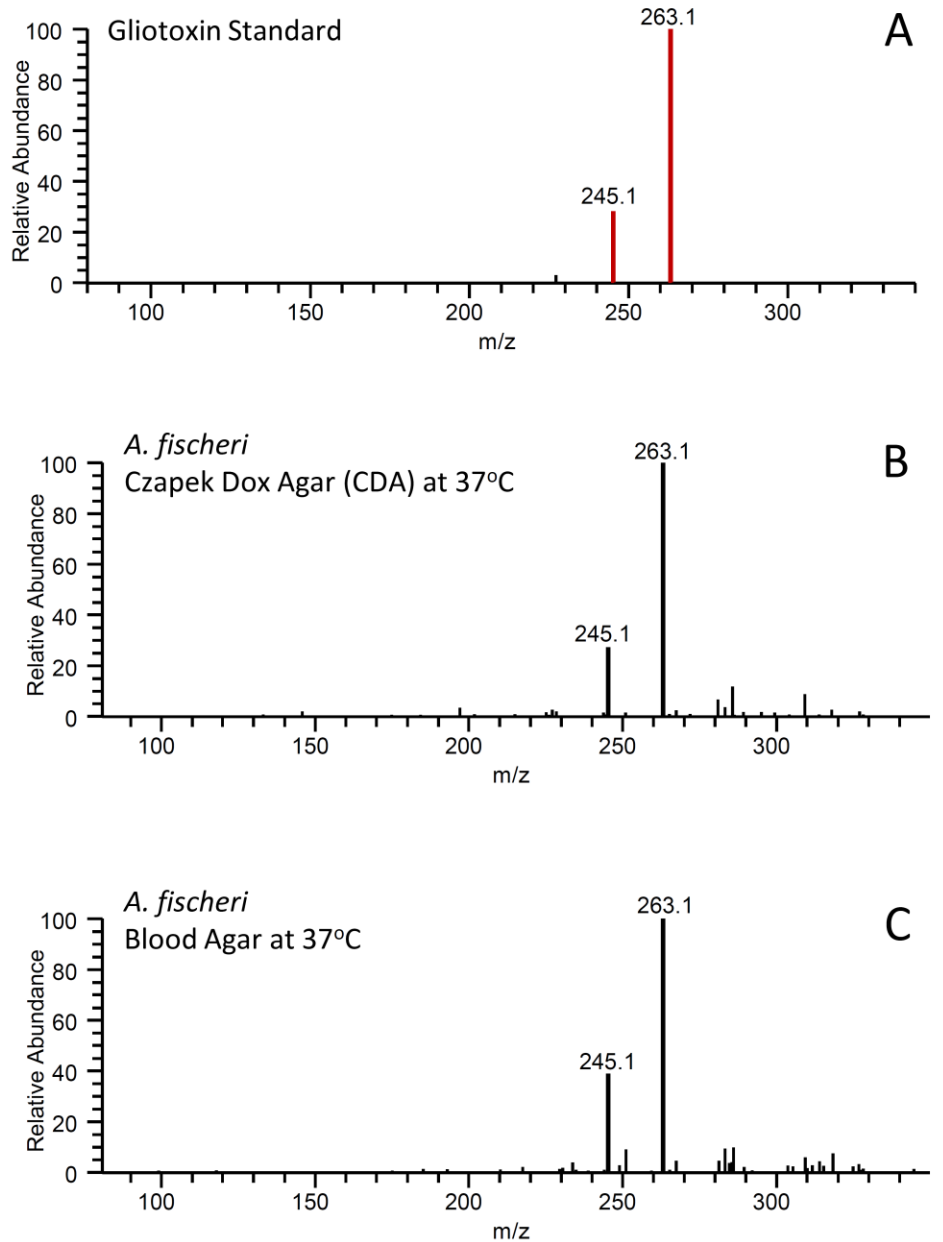


**Figure 38.** The fragmentation patterns (i.e., MS/MS data) of gliotoxin in *A. Fischeri* further verify the biosynthesis of gliotoxin by cultures of *A. Fischeri* in both the CDA and blood agar at 37°C. A. Fragmentation pattern of the gliotoxin standard (263.1 and 245.1). B. Fragmentation pattern of gliotoxin observed in *A. Fischeri* grown on CDA incubated at 37°C. C. Fragmentation pattern of gliotoxin observed in *A. Fischeri* grown on blood agar incubated at 37°C.

CHAPTER IV

VARIATION AMONG BIOSYNTHETIC GENE CLUSTERS, SECONDARY  
METABOLITE PROFILES, AND CARDS OF VIRULENCE ACROSS *ASPERGILLUS*  
*FUMIGATUS* AND CLOSE NONPATHOGENIC RELATIVES

Jacob L. Steenwyk, Sonja L. Knowles, Matthew E. Mead, Huzefa A. Raja, Christopher D. Roberts, Oliver Bader, Jos Houbraken, Gustavo H. Goldman, Nicholas H. Oberlies, Antonis Rokas. *Genetics* 2020, 216, 481-497.

*Aspergillus fumigatus* is a major human pathogen. In contrast, *Aspergillus fischeri* and the recently described *Aspergillus oerlinghausenensis*, the two species most closely related to *A. fumigatus*, are not known to be pathogenic. Some of the genetic determinants of virulence (or “cards of virulence”) that *A. fumigatus* possesses are secondary metabolites that impair the host immune system, protect from host immune cell attacks, or acquire key nutrients. To examine whether secondary metabolism-associated cards of virulence vary between these species, we conducted extensive genomic and secondary metabolite profiling analyses of multiple *A. fumigatus*, one *A. oerlinghausenensis*, and multiple *A. fischeri* strains. We identified two cards of virulence (gliotoxin and fumitremorgin) shared by all three species and three cards of virulence (trypacidin, pseurotin, and fumagillin) that are variable. For example, we found that all species and strains examined biosynthesized gliotoxin, which is known to contribute to virulence, consistent with the conservation of the gliotoxin biosynthetic gene cluster (BGC) across genomes. For other secondary metabolites, such as fumitremorgin, a modulator of host biology, we found that all species produced the metabolite but that there was strain heterogeneity in its production within species. Finally, species differed in

their biosynthesis of fumagillin and pseurotin, both contributors to host tissue damage during invasive aspergillosis. *A. fumigatus* biosynthesized fumagillin and pseurotin, while *A. oerlinghausenensis* biosynthesized fumagillin and *A. fischeri* biosynthesized neither. These biochemical differences were reflected in sequence divergence of the intertwined fumagillin/pseurotin BGCs across genomes. These results delineate the similarities and differences in secondary metabolism-associated cards of virulence between a major fungal pathogen and its nonpathogenic closest relatives, shedding light onto the genetic and phenotypic changes associated with the evolution of fungal pathogenicity.

Fungal diseases impose a clinical, economic, and social burden on humans.<sup>213-215</sup> Fungi from the genus *Aspergillus* are responsible for a considerable fraction of this burden, accounting for more than 250,000 infections annually with high mortality rates.<sup>199</sup> *Aspergillus* infections often result in pulmonary and invasive diseases that are collectively termed aspergillosis. Among *Aspergillus* species, *Aspergillus fumigatus* is the primary etiological agent of aspergillosis.<sup>23</sup>

Even though *A. fumigatus* is a major pathogen, its closest relatives are not considered pathogenic.<sup>16, 216, 217</sup> Numerous studies have identified genetic determinants that contribute to *A. fumigatus* pathogenicity, such as the organism's ability to grow well at higher temperatures and in hypoxic conditions.<sup>113, 142, 218, 219</sup> Genetic determinants that contribute to pathogenicity could be conceived as analogous to individual "cards" of a "hand" (set of cards) in a card game – that is, individual determinants are typically insufficient to cause disease but can collectively do so.<sup>26</sup>

*Aspergillus fumigatus* biosynthesizes a cadre of secondary metabolites and several metabolites could be conceived as "cards" of virulence because of their involvement in impairing the host immune system, protecting the fungus from host

immune cell attacks, or acquiring key nutrients.<sup>20, 27-33</sup> For example, the secondary metabolite gliotoxin has been shown in *A. fumigatus* to inhibit the host immune response.<sup>34, 35</sup> Other secondary metabolites implicated in virulence include: fumitremorgin, which inhibits the activity of the breast cancer resistance protein;<sup>36</sup> verruculogen, which modulates the electrophysical properties of human nasal epithelial cells;<sup>220</sup> trypacidin, which is cytotoxic to lung cells and inhibits phagocytosis;<sup>221, 222</sup> pseurotin, which inhibits immunoglobulin E;<sup>41</sup> and fumagillin which causes epithelial cell damage<sup>37</sup> and impairs the function of neutrophils.<sup>39, 40</sup>

By extension, the metabolic pathways responsible for the biosynthesis of secondary metabolites could also be conceived as components of these secondary metabolism-associated “cards” of virulence. Genes in these pathways are typically organized in contiguous sets termed biosynthetic gene clusters (BGCs).<sup>10</sup> BGCs are known to evolve rapidly, and their composition can differ substantially across species and strains.<sup>11, 12, 143, 147, 148, 223-225</sup> For example, even though *A. fumigatus* contains 33 BGCs and *A. fischeri* contains 48 BGCs, only 10 of those BGCs appear to be shared between the two species.<sup>16</sup> Interestingly, one of the BGCs that is conserved between *A. fumigatus* and *A. fischeri* is the gliotoxin BGC and both species have been shown to biosynthesize the secondary metabolite, albeit at different amounts.<sup>226</sup> These results suggest that the gliotoxin “card” is part of a winning “hand” that facilitates virulence only in the background of the major pathogen *A. fumigatus* and not in that of the nonpathogen *A. fischeri*.<sup>226</sup>

To date, such comparisons of BGCs and secondary metabolite profiles among *A. fumigatus* and closely related nonpathogenic species have been few and restricted to single strains.<sup>16, 226</sup> However, genetic and phenotypic heterogeneity among strains of a

single species is an important consideration when studying *Aspergillus* pathogenicity.<sup>33</sup>  
<sup>137, 227-233</sup> Examination of multiple strains of *A. fumigatus* and close relatives—including the recently described closest known relative of *A. fumigatus*, *A. oerlinghausenensis*, whose virulence has yet to be examined but which is not thought to be a human pathogen<sup>42</sup> and has never been associated with human infections—will increase our understanding of the *A. fumigatus* secondary metabolism-associated “cards” of virulence.

To gain insight into the genomic and chemical similarities and differences in secondary metabolism among *A. fumigatus* and nonpathogenic close relatives, we characterized variation in BGCs and secondary metabolites produced by *A. fumigatus* and nonpathogenic close relatives. To do so, we first sequenced and assembled *A. oerlinghausenensis* CBS 139183<sup>T</sup> as well as *A. fischeri* strains NRRL 4585 and NRRL 4161 and analyzed them together with four *A. fumigatus* and three additional *A. fischeri* publicly available genomes. We also characterized the secondary metabolite profiles of three *A. fumigatus*, one *A. oerlinghausenensis*, and three *A. fischeri* strains. We observed both variation and conservation among species- and strain-level BGCs and secondary metabolites. We found that the biosynthesis of the secondary metabolites gliotoxin and fumitremorgin, which are both known to interact with mammalian cells,<sup>27, 36, 234, 235</sup> as well as their BGCs, were conserved among pathogenic and nonpathogenic strains. Interestingly, we found only *A. fischeri* strains, but not *A. fumigatus* strains, biosynthesized verruculogen, which changes the electrophysical properties of human nasal epithelial cells.<sup>220</sup> Similarly, we found that both *A. fumigatus* and *A. oerlinghausenensis* biosynthesized fumagillin and trypacidin, whose effects include broad suppression of the immune response system and lung cell damage,<sup>39-41, 221</sup> but *A.*

*fischeri* did not. Taken together, these results reveal that nonpathogenic close relatives of *A. fumigatus* also produce some, but not all, of the secondary metabolism-associated cards of virulence known in *A. fumigatus*. Further investigation of the similarities and differences among *A. fumigatus* and close nonpathogenic relatives may provide additional insight into the “hand of cards” that enabled *A. fumigatus* to evolve into a deadly pathogen.

## Results

**Conservation and Diversity of Biosynthetic Gene Clusters Within and Between Species.** We sequenced and assembled *A. oerlinghausensis* CBS 139183<sup>T</sup> and *A. fischeri* strains NRRL 4585 and NRRL 4161. Together with publicly available genomes, we analyzed 10 *Aspergillus* genomes (five *A. fischeri* strains; four *A. fumigatus* strains; one *A. oerlinghausensis* strain; see Methods). We found that the newly added genomes were of similar quality to other publicly available draft genomes (average percent presence of BUSCO genes:  $98.80 \pm 0.10\%$ ; average N50: 451,294.67  $\pm$  9,696.11; Figure 45). We predicted that *A. oerlinghausensis* CBS 139183<sup>T</sup>, *A. fischeri* NRRL 4585, and *A. fischeri* NRRL 4161 have 10,044, 11,152 and 10,940 genes, respectively, numbers similar to publicly available genomes. Lastly, we inferred the evolutionary history of the 10 *Aspergillus* genomes using a concatenated matrix of 3,041 genes (5,602,272 sites) and recapitulated species-level relationships as previously reported (Houbraken *et al.* 2016). Relaxed molecular clock analyses suggested that *A. oerlinghausensis* CBS 139183<sup>T</sup> diverged from *A. fumigatus* approximately 3.9 (6.4 – 1.3) million years ago and that *A. oerlinghausensis* and *A. fumigatus* split from *A. fischeri* approximately 4.5 (6.8 – 1.7) million years ago (Figures 39A and 46).

Examination of the total number of predicted BGCs revealed that *A. fischeri* has the largest BGC count. Among *A. fumigatus*, *A. oerlinghausenensis*, and *A. fischeri*, we predicted an average of  $35.75 \pm 2.22$ , 40,  $50.80 \pm 2.17$  BGCs, respectively, and found they spanned diverse biosynthetic classes (e.g., polyketides, non-ribosomal peptides, terpenes, etc.) (Figure 39B). Network-based clustering of BGCs into cluster families (or groups of homologous BGCs) resulted in qualitatively similar networks when we used moderate similarity thresholds (or edge cut-off values; Figure 47A). Using a (moderate) similarity threshold of 0.5, we inferred 88 cluster families of putatively homologous BGCs (Figure 39C).

Examination of BGCs revealed extensive presence and absence polymorphisms within and between species. We identified 17 BGCs that were present in all 10 *Aspergillus* genomes including the hexadehydroasteochrome (HAS) BGC (cluster family 311 or CF311), the neosartoricin BGC (CF61), and other putative BGCs likely encoding unknown products (Figure 47B). In contrast, we identified 18 BGCs found in single strains, which likely encode unknown products. Between species, similar patterns of broadly present and species-specific BGCs were observed. For example, we identified 18 BGCs that were present in at least one strain across all species; in contrast, *A. fumigatus*, *A. oerlinghausenensis*, and *A. fischeri* had 16, 8, and 27 BGCs present in at least one strain but absent from the other species, respectively. These results suggest each species has a largely distinct repertoire of BGCs.

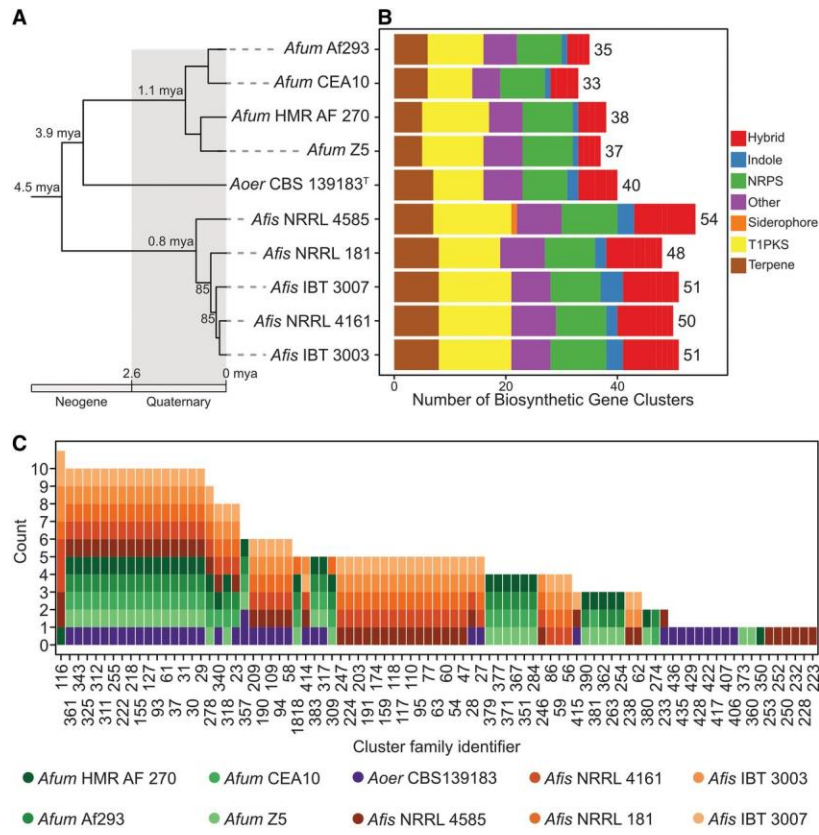


**Figure 39.** Diverse Genetic Repertoire of Biosynthetic Gene Clusters and Extensive Presence and Absence Polymorphisms Between and Within Species. (A) Genome-scale phylogenomic analysis confirms *A. oerlinghausenensis* is the closest relative to *A. fumigatus*. Relaxed molecular clock analyses suggest *A. fumigatus*, *A. oerlinghausenensis*, and *A. fischeri* diverged from one another during the Neogene geological period. Bipartition support is depicted for internodes that did not have full support. (B) *A. fumigatus* harbors the lowest number of BGCs compared to its two closest relatives. (C) Network-based clustering of BGCs into cluster families reveal extensive cluster presence and absence polymorphisms between species and strains. Cluster family identifiers are depicted on the x-axis; the number of strains represented in a cluster family are shown on the y-axis; the colors refer to a single strain from each species. Genus and species names are written using the following abbreviations: *Afum*: *A. fumigatus*; *Aoer*: *A. oerlinghausenensis*; *Afis*: *A. fischeri*. Classes of BGCs are written using the following abbreviations: NRPS: nonribosomal peptide synthetase; T1PKS: type I polyketide synthase; Hybrid: a combination of multiple BGC classes.

Examination of shared BGCs across species revealed *A. oerlinghausenensis* CBS139183<sup>T</sup> and *A. fischeri* shared more BGCs with each other than either did with *A. fumigatus*. Surprisingly, we found ten homologous BGCs between *A. oerlinghausenensis*

CBS 139183<sup>T</sup> and *A. fischeri* but only three homologous BGCs shared between *A. fumigatus* and *A. oerlinghausensis* CBS 139183<sup>T</sup> (Figures 40A and 47C) even though *A. oerlinghausensis* is more closely related to *A. fumigatus* than to *A. fischeri* (Figure 39A). BGCs shared by *A. oerlinghausensis* CBS 139183<sup>T</sup> and *A. fischeri* were uncharacterized while BGCs present in both *A. fumigatus* and *A. oerlinghausensis* CBS 139183<sup>T</sup> included those that encode fumigaclavine and fumagillin/pseurotin. Lastly, to associate each BGC with a secondary metabolite in *A. fumigatus* Af293, we cross referenced our list with a publicly available one.<sup>148</sup> Importantly, all known *A. fumigatus* Af293 BGCs were represented in our analyses.

At the level of gene families, there were few species-specific gene families in *A. oerlinghausensis* (Figure 40B). *A. oerlinghausensis* CBS 139183<sup>T</sup> has only eight species-specific gene families, whereas *A. fischeri* and *A. fumigatus* have 1,487 and 548 species-specific gene families, respectively. Examination of the best BLAST hits of the eight species-specific gene families suggest that most are hypothetical or uncharacterized fungal genes. To determine if the eight *A. oerlinghausensis* CBS 139183<sup>T</sup> specific gene families were an artifact of using a single representative strain, we conducted an additional ortholog clustering analysis using a single strain of *A. fischeri* (NRRL 181), a single strain of *A. fumigatus* (Af293), or a single strain of each species (CBS 139183, NRRL 181, Af293). When using a single strain of *A. fischeri* or *A. fumigatus*, there were 23 or six gene families unique to each species, respectively. Therefore, the low number of *A. oerlinghausensis*-specific gene families likely stems from our use of the genome of a single strain.

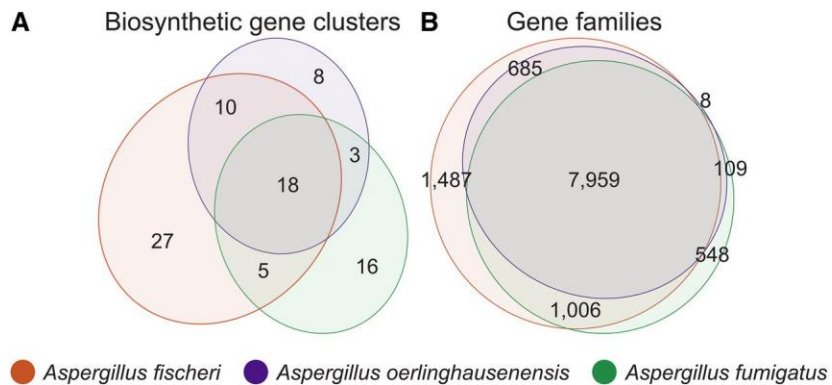


**Figure 40.** *Aspergillus oerlinghausensis* Shares More Gene Families and BGCs With *A. fischeri* Than *A. fumigatus*. (A) Euler diagram showing species-level shared BGCs. (B) Euler diagram showing species-level shared gene families. In both diagrams, *A. oerlinghausensis* shares more gene families or BGCs with *A. fischeri* than *A. fumigatus* despite a closer evolutionary relationship. The Euler diagrams show the results for the species-level comparisons, which may be influenced by the unequal numbers of strains used for the three species; strain-level comparisons of BGCs and gene families can be found in Figures 39C and 48, respectively.

Despite a closer evolutionary relationship between *A. oerlinghausensis* and *A. fumigatus*, we found *A. oerlinghausensis* shares more gene families with *A. fischeri* than with *A. fumigatus* (685 and 109, respectively) suggestive of extensive gene loss in the *A. fumigatus* stem lineage. Lastly, we observed strain heterogeneity in gene family presence and absence within both *A. fumigatus* and *A. fischeri* (Figure 48). For example, the largest intersection that does not include all *A. fischeri* strains is 493 gene families, which were found in all but one strain, NRRL 181. For *A. fumigatus*, the largest intersection that does not include all strains is 233 gene families, which were shared by strains Af293 and CEA10.

**Within and Between Species Variation in Secondary Metabolite Profiles of *A. fumigatus* and its Closest Relatives.** To gain insight into variation in secondary metabolite profiles within and between species, we profiled *A. fumigatus* strains Af293, CEA10, and CEA17 (a *pyrG1/URA3* derivative of CEA10), *A. fischeri* strains NRRL 181,

NRRL 4585, and NRRL 4161, and *A. oerlinghausenensis* CBS 139183<sup>T</sup> for secondary metabolites. Specifically, we used three different procedures, including the isolation and structure elucidation of metabolites, where possible, followed by two different metabolite profiling procedures that use mass spectrometry techniques. Altogether, we isolated and characterized 19 secondary metabolites; seven from *A. fumigatus*, two from *A. oerlinghausenensis*, and ten from *A. fischeri* (Figure 49). These products encompassed a wide diversity of secondary metabolite classes, such as those derived from polyketide synthases, non-ribosomal peptide-synthetases, terpene synthases and mixed biosynthesis enzymes.

To characterize the secondary metabolites biosynthesized that were not produced in high enough quantity for structural identification through traditional isolation methods, we employed “derePLICATION” mass spectrometry protocols specific to natural products research on all tested strains at both 30°C and 37°C (Figure 52).<sup>188, 236-238</sup> We found that most secondary metabolites were present across strains of the same species (Table 4.3 and Table 4.4); for example, monomethylsulochrin was isolated from *A. fumigatus* Af293, but through metabolite profiling, its spectral features were noted also in *A. fumigatus* strains CEA10 and CEA17. We identified metabolites that were biosynthesized by only one species; for example, pseurotin A was solely present in *A. fumigatus* strains. Finally, we found several secondary metabolites that were biosynthesized across species, such as fumagillin, which was biosynthesized by *A. fumigatus* and *A. oerlinghausenensis*, and fumitremorgin B, which was biosynthesized by strains of both *A. oerlinghausenensis* and *A. fischeri*. Together, these analyses suggest that closely related *Aspergillus* species and strains exhibit variation both within as well as between species in the secondary metabolites produced.

To further facilitate comparisons of secondary metabolite profiles within and between species, we used the 1,920 features (i.e., unique  $m/z$  – retention time pairs) that were identified from all strains at all temperatures (Figure 41A), to perform hierarchical clustering (Figure 41B) and Principal Components Analysis (PCA) (Figure 50). Hierarchical clustering at 37°C and 30°C indicated the chromatogram of *A. oerlinghausenensis* CBS 139183<sup>T</sup> is more similar to the chromatogram of *A. fischeri* than to that of *A. fumigatus*. PCA results were broadly consistent with the clustering results, but suggested that *A. oerlinghausenensis* was just as similar to *A. fischeri* strains as it was to *A. fumigatus* strains. This difference likely stems from the fact that hierarchical clustering is a total-evidence approach whereas PCA captures most but not all variance in the data (e.g., the two principal components in Figures 50B and 50C capture 84.6% of the total variance). PCA analysis revealed greater variation in secondary metabolite production at 30°C compared to 37°C (Figure 50), suggesting there is a more varied response in how BGCs are being utilized at 30°C. PCA at both 37°C and 30°C showed that variation between *A. oerlinghausenensis* CBS 139183<sup>T</sup> and *A. fischeri* strains was largely captured along the second principal component; in contrast, the differences between *A. oerlinghausenensis* CBS 139183<sup>T</sup> and *A. fumigatus* strains are captured along the first principal component (Figure 50D-E). Taken together, these results suggest that the three *A. fischeri* strains and *A. oerlinghausenensis* were the most chemically similar to each other.

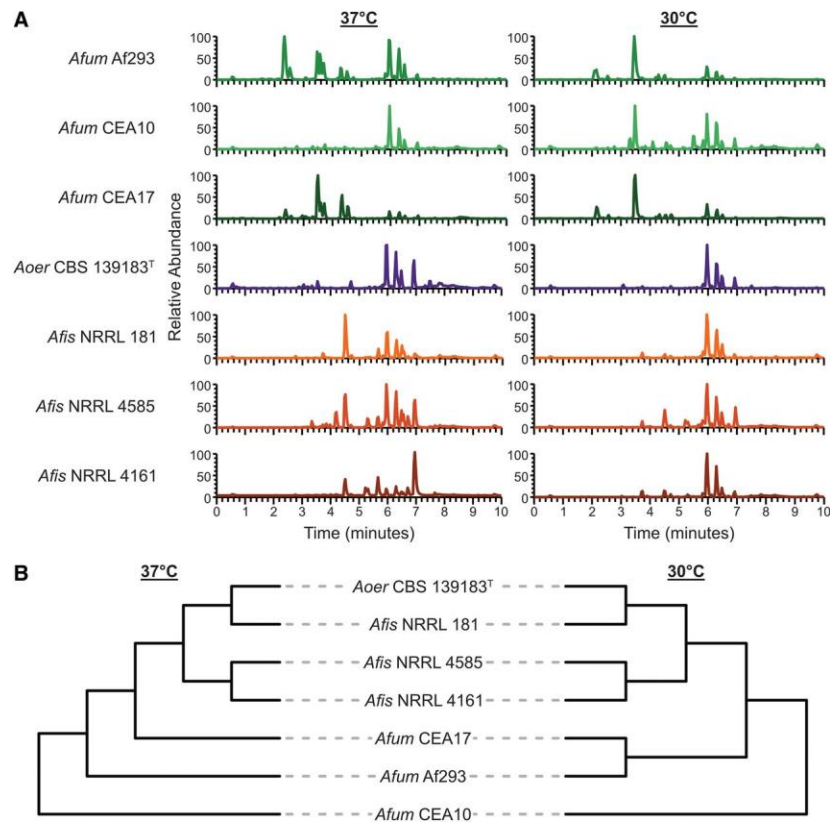


**Figure 41.** *A. oerlinghausenensis* and *A. fischeri* Have More Similar Secondary Metabolite Profiles Than *A. fumigatus*. (A) UPLC-MS chromatograms of secondary metabolite profiles of *A. fumigatus* and its closest relatives, *A. oerlinghausenensis* and *A. fischeri* at 37°C and 30°C (left and right, respectively). (B) Hierarchical clustering of chromatograms (1,920 total features) reveals *A. oerlinghausenensis* clusters with *A. fischeri* and not its closest relative, *A. fumigatus* at 37°C and 30°C (left and right, respectively).

In summary, even though *A. oerlinghausenensis* is phylogenetically more closely related to *A. fumigatus* than to *A. fischeri* (Figure 39A), our chemical analyses suggest that the secondary metabolite profile of *A. oerlinghausenensis* is more similar to the profile of *A. fischeri* than it is to the profile of *A. fumigatus* (Figures 41B and 50B-E). The similarity of secondary metabolite profiles of *A. oerlinghausenensis* and *A. fischeri* is consistent with our finding that the genome of *A. oerlinghausenensis* shares higher numbers of BGCs and gene families with *A. fischeri* than with *A. fumigatus* (Figure 40).

The broad clustering patterns in secondary metabolite-based plots (Figure 50B-E) are less robust than, but consistent with, those of BGC-based plots (Figure 50A), suggesting that the observed similarities in the secondary metabolism-associated genotypes of *A. oerlinghausenensis* and *A. fischeri* are likely reflected in their chemotypes.

### **Conservation and Divergence Among Biosynthetic Gene Clusters**

**Implicated in *A. fumigatus* Pathogenicity.** Secondary metabolites are known to play a role in *A. fumigatus* virulence.<sup>27</sup> We therefore conducted a focused examination of specific *A. fumigatus* BGCs and secondary metabolites that have been previously implicated in the organism's ability to cause human disease (Table 4.1). We found varying degrees of conservation and divergence that were associated with the absence or presence of a secondary metabolite. Among conserved BGCs that were also associated with conserved secondary metabolite production, we highlight the mycotoxins gliotoxin and fumitremorgin. Interestingly, we note that only *A. fischeri* strains synthesized verruculogen, a secondary metabolite that is implicated in human disease and is encoded by the fumitremorgin BGC.<sup>220, 239</sup> Among BGCs that exhibited varying degrees of sequence divergence and divergence in their production of the corresponding secondary metabolites, we highlight those associated with the production of the trypacidin and fumagillin/pseurotin secondary metabolites. We found that nonpathogenic close relatives of *A. fumigatus* produced some but not all mycotoxins, which provides novel insight into the unique cocktail of secondary metabolites biosynthesized by *A. fumigatus*.

**Table 4.1.** Select *A. fumigatus* Secondary Metabolites Implicated in Modulating Host Biology

Function	Evidence of biosynthetic gene cluster / secondary metabolite							
	<i>A. fumigatus</i>			<i>A. oerlinghausenensis</i>	<i>A. fischeri</i>			
	Af 293	CEA 10	CEA 17	CBS 139183 <sup>T</sup>	NRRL 181	NRRL 4585	NRRL 4161	
Gliotoxin	Inhibits host immune response <sup>34</sup>	+/-	+/-	+/-	+/-	+/-	+/-	+/-
Fumitremorgin	Inhibits the breast cancer resistance protein <sup>36</sup>	+/-	+/-	+/-	+/-	+/-	+/-	+/-
Verruculogen	Changes electrophysiological properties of human nasal epithelial cells <sup>220</sup>	+/-	+/-	+/-	+/-	+/-	+/-	+/-
Trypacidin	Damages lung cell tissues <sup>221</sup>	+/-	+/-	+/-	+/-	+/-	-/-	-/-
Pseurotin	Inhibits immunoglobulin E <sup>41</sup>	+/-	+/-	+/-	+/-	-/-	-/-	-/-
Fumagillin	Inhibits neutrophil function <sup>39, 40</sup>	+/-	+/-	+/-	+/-	-/-	-/-	-/-

A list of select secondary metabolites implicated in human disease and their functional role are described here. All secondary metabolites listed or analogs thereof were identified during secondary metabolite profiling. Plus (+) and minus (-) signs indicate the presence or absence of the BGC and secondary metabolite, respectively. For example, +/+ indicates both BGC presence and evidence of secondary metabolite production, whereas +/- indicates BGC presence but no evidence of secondary metabolite production. '+/+' cells are colored orange; '-/-' cells are colored blue; '+/-' and '-/+' cells are colored green.

**Gliotoxin.** Gliotoxin is a highly toxic compound and known virulence factor in *A. fumigatus*.<sup>34</sup> Nearly identical BGCs encoding gliotoxin are present in all pathogenic (*A. fumigatus*) and nonpathogenic (*A. oerlinghausensis* and *A. fischeri*) strains examined (Figure 42). Additionally, we found that all examined strains synthesized bisdethiobis(methylthio)gliotoxin a derivative from dithiogliotoxin, involved in the down-regulation of gliotoxin biosynthesis,<sup>240</sup> one of the main mechanisms of gliotoxin resistance in *A. fumigatus*.<sup>239</sup>

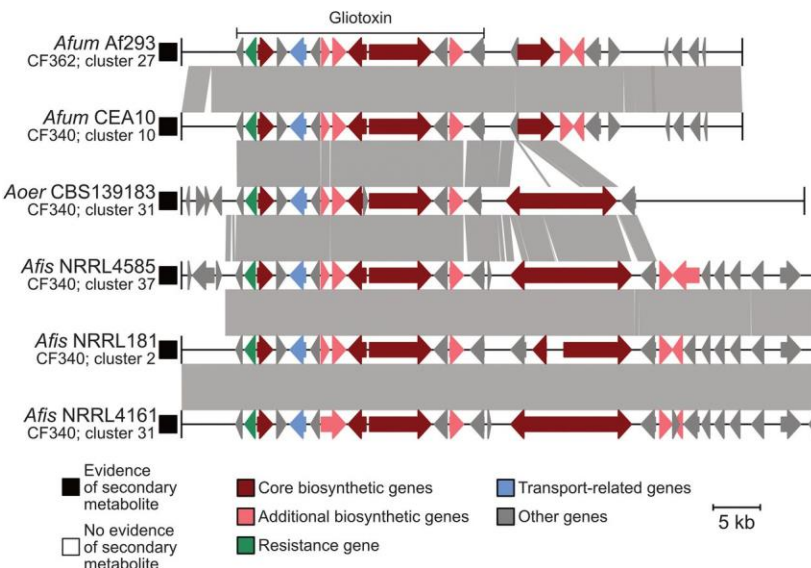


**Figure 42.** Conservation in the Gliotoxin BGC Correlates with Conserved Production of Gliotoxin Analogs in *A. fumigatus* and Nonpathogenic Close Relatives. Microsynteny analysis reveals a high degree of conservation in the BGC encoding gliotoxin across all isolates. The known gliotoxin gene cluster boundary is indicated above the *A. fumigatus* Af293 BGC. Black and white squares correspond to evidence or absence of evidence of secondary metabolite production, respectively. Genes are drawn as arrows with orientation indicated by the direction of the arrow. Gene function is indicated by gene color. Grey boxes between gene clusters indicate BLAST-based similarity of nucleotide sequences defined as being at least 100 bp in length, share at least 30% sequence similarity, and have an expectation value threshold of 0.01. Genus and species names are written using the following abbreviations: *Afum*: *A. fumigatus*; *Aoer*: *A. oerlinghausensis*; *Afis*: *A. fischeri*. Below each genus and species abbreviation is the cluster family each BGC belongs to and their cluster number.

**Fumitremorgin and Verruculogen.** Similarly, there is a high degree of conservation in the BGC that encodes fumitremorgin across all strains (Figure 43). Fumitremorgins have known antifungal activity, are lethal to brine shrimp, and are implicated in inhibiting mammalian proteins responsible for resistance to anticancer drugs in mammalian cells.<sup>27</sup> We found that conservation in the fumitremorgin BGC is associated with the production of fumitremorgins in all isolates examined. The fumitremorgin BGC is also responsible for the production of verruculogen, which is implicated to aid in *A. fumigatus* pathogenicity by changing the electrophysical properties of human nasal epithelial cells.<sup>220</sup> Interestingly, we found that only *A. fischeri* strains produced verruculogen under the conditions we analyzed.

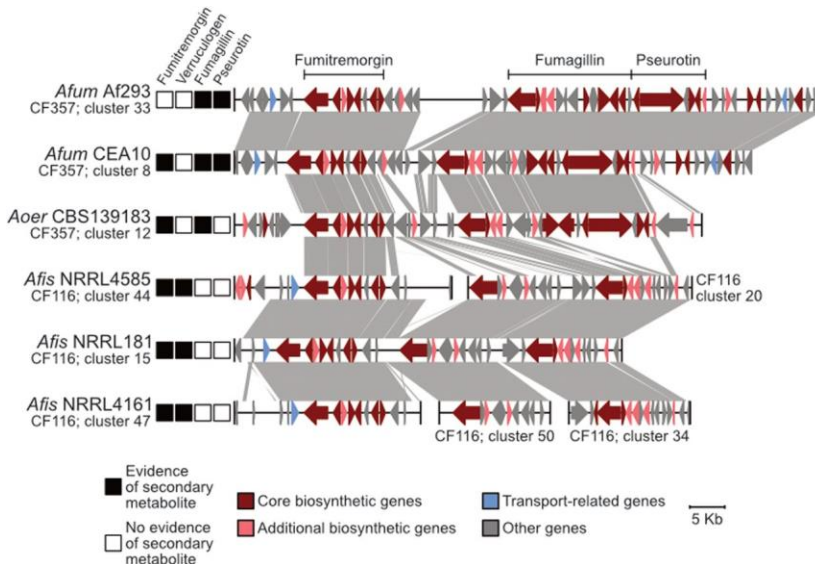


**Figure 43.** Conservation and Divergence in the Locus Encoding the Fumitremorgin and Intertwined Fumagillin/Pseurotin BGCs. Microsynteny analysis reveals conservation in the fumitremorgin BGC across all isolates. Interestingly, only *A. fischeri* strains synthesize verruculogen, a secondary metabolite also biosynthesized by the fumitremorgin BGC. In contrast, the intertwined fumagillin/pseurotin BGCs are conserved between *A. fumigatus* and *A. oerlinghausenensis* but divergent in *A. fischeri*. BGC conservation and divergence is associated with the presence and absence of a secondary metabolite, respectively. The hysame convention used in Figure 42 is used to depict evidence of a secondary metabolite, represent genes and broad gene function,

BGC sequence similarity, genus and species abbreviations, and BGC cluster families and cluster numbers

**Trypacidin.** Examination of the trypacidin BGC, which encodes a spore-borne and cytotoxic secondary metabolite, revealed a conserved cluster found in four pathogenic and nonpathogenic strains: *A. fumigatus* Af293, *A. fumigatus* CEA10, *A. oerlinghausenensis* CBS 139183<sup>T</sup>, and *A. fischeri* NRRL 181 (Figure 51). Furthermore, we found that three of these four isolates (except *A. fischeri* NRRL 181) biosynthesized a trypacidin analog, monomethylsulochrin. Examination of the microsynteny of the trypacidin BGC revealed that it was conserved across all four genomes with the exception *A. fischeri* NRRL I81, which lacked a RING (Really Interesting New Gene) finger gene. Interestingly, RING finger proteins can mediate gene transcription.<sup>241</sup> We confirmed the absence of the RING finger protein by performing a sequence similarity search with the *A. fumigatus* Af293 RING finger protein (AFUA\_4G14620; EAL89333.1) against the *A. fischeri* NRRL 181 genome. In the homologous locus in *A. fischeri*, we found no significant BLAST hit for the first 23 nucleotides of the RING finger gene suggestive of pseudogenization. Taken together, we hypothesize that presence/absence polymorphisms or a small degree of sequence divergence between otherwise homologous BGCs may be responsible for the presence or absence of a toxic secondary metabolite in *A. fischeri* NRRL 181. Furthermore, inter- and intra-species patterns of trypacidin presence and absence highlight the importance of strain heterogeneity when examining BGCs.

**Fumagillin/pseurotin.** Examination of the intertwined fumagillin/pseurotin BGCs revealed that fumagillin has undergone substantial sequence divergence and that pseurotin is absent from strains of *A. fischeri*. The fumagillin/pseurotin BGCs are under

the same regulatory control<sup>152</sup> and biosynthesize secondary metabolites that cause cellular damage during host infection (fumagillin)<sup>38</sup> and inhibit immunoglobulin E production (pseurotin)<sup>41</sup>. Microsynteny of the fumagillin BGC reveals high sequence conservation between *A. fumigatus* and *A. oerlinghausensis*; however, sequence divergence was observed between *A. oerlinghausensis* and *A. fischeri* (Figure 43). Accordingly, fumagillin production was only observed in *A. fumigatus* and *A. oerlinghausensis* and not in *A. fischeri*. Similarly, the pseurotin BGC is conserved between *A. fumigatus* and *A. oerlinghausensis*. Rather than sequence divergence, no sequence similarity was observed in the region of the pseurotin cluster in *A. fischeri*, which may be due to an indel event. Accordingly, no pseurotin production was observed among *A. fischeri* strains. Despite sequence conservation between *A. fumigatus* and *A. oerlinghausensis*, no evidence of pseurotin biosynthesis was observed in *A. oerlinghausensis*, which suggests regulatory decoupling of the intertwined fumagillin/pseurotin BGC. Alternatively, the genes downstream of the *A. fumigatus* pseurotin BGC, which are absent from the *A. oerlinghausensis* locus, may contribute to BGC production and could explain the lack of pseurotin production in *A. oerlinghausensis*. Altogether, these results show a striking correlation between sequence divergence and the production (or absence) of secondary metabolites implicated in human disease among *A. fumigatus* and nonpathogenic closest relatives.

## Discussion

*Aspergillus fumigatus* is a major fungal pathogen nested within a clade (known as section *Fumigati*) of at least 60 other species, the vast majority of which are nonpathogenic.<sup>216, 217</sup> Currently, it is thought that the ability to cause human disease evolved multiple times among species in section *Fumigati*.<sup>217</sup> Secondary metabolites

contribute to the success of the major human pathogen *A. fumigatus* in the host environment<sup>27</sup> and can therefore be thought of as “cards” of virulence.<sup>26, 226</sup> However, whether the closest relatives of *A. fumigatus*, *A. oerlinghausensis* and *A. fischeri*, both of which are nonpathogenic, biosynthesize secondary metabolites implicated in the ability of *A. fumigatus* to cause human disease remained largely unknown. By examining genomic and chemical variation between and within *A. fumigatus* and its closest nonpathogenic relatives, we identified both conservation and divergence (including within species heterogeneity) in BGCs and secondary metabolite profiles (Figures 39-43, 47, and 49-51; Tables 4.1, 4.3, and 4.4). Examples of conserved BGCs and secondary metabolites include the major virulence factor, gliotoxin (Figure 42), as well as several others (Figures 43 and 51; Tables 4.1, 4.3, and 4.4); examples of BGC and secondary metabolite heterogeneity or divergence include pseurotin, fumagillin, and several others (Figure 43; Tables 4.1, 4.3, and 4.4). Lastly, we found that the fumitremorgin BGC, which biosynthesizes fumitremorgin in all three species, is also associated with verruculogen biosynthesis in *A. fischeri* strains (Figure 43).

One of the surprising findings of our study was that although *A. oerlinghausensis* and *A. fumigatus* are evolutionarily more closely related to each other than to *A. fischeri* (Figure 39), *A. oerlinghausensis* and *A. fischeri* appear to be more similar to each other than to *A. fumigatus* in BGC composition, gene family content, and secondary metabolite profiles. The power of pathogen-nonpathogen comparative genomics is best utilized when examining closely related species.<sup>16, 123, 217, 242, 243</sup> Genomes from additional strains from the closest known nonpathogenic relatives of *A. fumigatus*, including from the closest species relative *A. oerlinghausensis*, *A.*

*fischeri*, and other nonpathogenic species in section *Fumigati* will be key for understanding the evolution of *A. fumigatus* pathogenicity.

Our finding that *A. oerlinghausensis* and *A. fischeri* shares more gene families and BGCs with each other than they do with *A. fumigatus* (Figures 39C, 40, 47, and 48) suggests that the evolutionary trajectory of the *A. fumigatus* ancestor was marked by gene loss. We hypothesize that there were two rounds of gene family and BGC loss in the *A. fumigatus* stem lineage: (1) gene families and BGCs were lost in the common ancestor of *A. fumigatus* and *A. oerlinghausensis* and (2) additional losses occurred in the *A. fumigatus* ancestor. In addition to losses, we note that 548 gene families and 16 BGCs are unique to *A. fumigatus*, which may have resulted from genetic innovation (e.g., *de novo* gene formation) or unique gene family and BGC retention (Figure 40). In line with the larger number of shared BGCs between *A. oerlinghausensis* and *A. fischeri*, we found their secondary metabolite profiles were also more similar (Figures 41, 50). Notably, the evolutionary rate of the internal branch leading to the *A. fumigatus* common ancestor is much higher than those in the rest of the branches in our genome-scale phylogeny (Figure 46B), suggesting that the observed gene loss and gene gain / retention events specific to *A. fumigatus* may be part of a wider set of evolutionary changes in the *A. fumigatus* genome. Analyses with a greater number of strains and species will help further test the validity of this hypothesis. More broadly, these results suggest that comparisons of the pathogen *A. fumigatus* against either the non-pathogen *A. oerlinghausensis* (this manuscript) or the non-pathogen *A. fischeri*<sup>16, 226</sup> (and this manuscript) will both be instructive in understanding the evolution of *A. fumigatus* pathogenicity.

When studying *Aspergillus* pathogenicity, it is important to consider any genetic and phenotypic heterogeneity between strains of a single species.<sup>32, 33, 137, 227-233</sup> Our finding of strain heterogeneity among gene families, BGCs, and secondary metabolites in *A. fumigatus* and *A. fischeri* (Figures 39-41, 47, 48, and 50) suggests considerable strain-level diversity in each species. For example, we found secondary metabolite profile strain heterogeneity was greater in *A. fumigatus* than *A. fischeri* (Figure 50B-E). These results suggest that strain-specific secondary metabolite profiles may play a role in variation of pathogenicity among *A. fumigatus* strains. In support of this hypothesis, differential secondary metabolite production has been associated with differences in virulence among isolates of *A. fumigatus*.<sup>33</sup> More broadly, our finding supports the hypothesis that strain-level diversity is an important parameter when studying pathogenicity.<sup>33, 137, 227-233</sup>

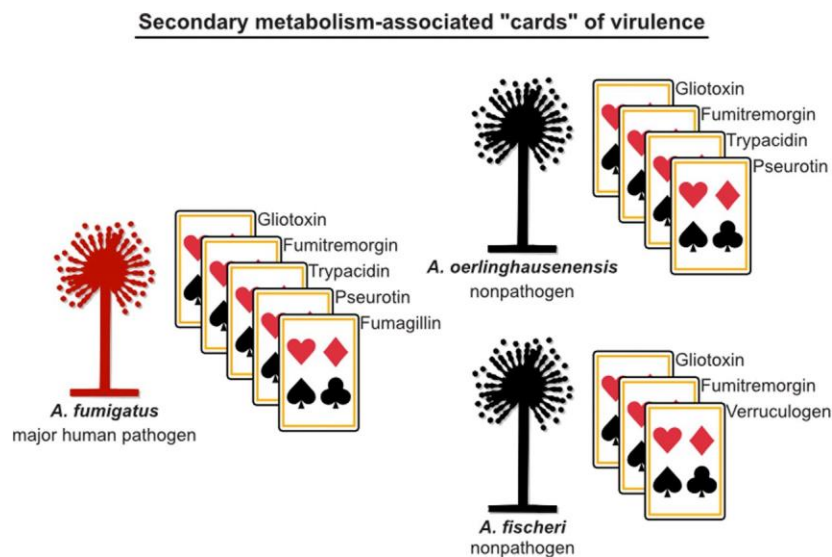


**Figure 44.** Secondary Metabolism-Associated “Cards” of Virulence Among *A. fumigatus* and Close Relatives. Secondary metabolites contribute to the “hand of cards” that enable *A. fumigatus* to cause disease. Here, we show that the nonpathogenic closest relatives of *A. fumigatus* possess a subset of the *A. fumigatus* secondary metabolism-associated cards of virulence. We hypothesize that the unique combination of cards of *A. fumigatus* contributes to its pathogenicity and that the cards in *A. oerlinghausenensis*

and *A. fischeri* (perhaps in combination with other non-secondary-metabolism-associated cards, such as thermotolerance) are insufficient to cause disease. Pathogenic and nonpathogenic species are shown in red and black, respectively. Cartoons of *Aspergillus* species were obtained from WikiMedia Commons (source: M. Piepenbring) and modified in accordance with the Creative Commons Attribution-Share Alike 3.0 Unported license (<https://creativecommons.org/licenses/by-sa/3.0/deed.en>).

Secondary metabolites contribute to *A. fumigatus* virulence through diverse processes including suppressing the human immune system and damaging tissues (Table 4.1). Interestingly, we found that the nonpathogens *A. oerlinghausenensis* and *A. fischeri* produced several secondary metabolites implicated in the ability of *A. fumigatus* to cause human disease, such as gliotoxin, trypacidin, verruculogen, and others (Figures 42, 43, and 51; Tables 4.1 and 4.5). Importantly, our work positively identified secondary metabolites for many structural classes implicated in a previous taxonomic study (Samson *et al.* 2007). These results suggest that several of the secondary metabolism-associated cards of virulence present in *A. fumigatus* are conserved in closely related nonpathogens (summarized in Figure 44) as well as in closely related pathogenic species, such as *A. novofumigatus*.<sup>143</sup> Interestingly, disrupting the ability of *A. fumigatus* to biosynthesize gliotoxin attenuates but does not abolish virulence,<sup>34, 174, 228</sup> whereas disruption of the ability of *A. fischeri* NRRL 181 to biosynthesize secondary metabolites, including gliotoxin, does not appear to influence virulence.<sup>226</sup> Our findings, together with previous studies, support the hypothesis that individual secondary metabolites are “cards” of virulence in a larger “hand” that *A. fumigatus* possesses.

## Materials and Methods

**Strain Acquisition, DNA Extraction, and Sequencing.** Two strains of *Aspergillus fischeri* (NRRL 4161 and NRRL 4585) were acquired from the Northern Regional Research Laboratory (NRRL) at the National Center for Agricultural Utilization

Research in Peoria, Illinois, while one strain of *Aspergillus oerlinghausenensis* (CBS 139183<sup>T</sup>) was acquired from the Westerdijk Fungal Biodiversity Institute, Utrecht, The Netherlands. These strains were grown in 50 ml of liquid yeast extract soy peptone dextrose (YESD) medium. After approximately seven days of growth on an orbital shaker (100 rpm) at room temperature, the mycelium was harvested by filtering the liquid media through a Corning®, 150 ml bottle top, 0.22µm sterile filter and washed with autoclaved distilled water. All subsequent steps of DNA extraction from the mycelium were performed following protocols outlined previously.<sup>14</sup> The genomic DNA from these three strains was sequenced using a NovaSeq S4 at the Vanderbilt Technologies for Advanced Genomes facility (Nashville, Tennessee, US) using paired-end sequencing (150 bp) strategy with the Illumina TruSeq library kit.

**Genome Assembly, Quality Assessment, and Annotation.** To assemble and annotate the three newly sequenced genomes, we first quality-trimmed raw sequence reads using Trimmomatic, v0.36<sup>244</sup> using parameters described elsewhere (ILLUMINACLIP:TruSeq3-PE.fa:2:30:10, leading:10, trailing:10, slidingwindow:4:20, minlen:50).<sup>245</sup> The resulting paired and unpaired quality-trimmed reads were used as input to the SPAdes, v3.11.1,<sup>246</sup> genome assembly algorithm with the ‘careful’ parameter and the ‘cov-cutoff’ set to ‘auto’.

We evaluated the quality of our newly assembled genomes, using metrics based on continuity of assembly and gene-content completeness. To evaluate genome assemblies by scaffold size, we calculated the N50 of each assembly (or the shortest contig among the longest contigs that account for 50% of the genome assembly’s length).<sup>247</sup> To determine gene-content completeness, we implemented the BUSCO, v2.0.1,<sup>248</sup> pipeline using the ‘genome’ mode. In this mode, the BUSCO pipeline

examines assembly contigs for the presence of near-universally single copy orthologous genes (hereafter referred to as BUSCO genes) using a predetermined database of orthologous genes from the OrthoDB, v9.<sup>249</sup> We used the OrthoDB database for Pezizomycotina (3,156 BUSCO genes). Each BUSCO gene is determined to be present in a single copy, as duplicate sequences, fragmented, or missing. Our analyses indicate the newly sequenced and assembled genomes have high gene-content completeness and assembly continuity (average percent presence of BUSCO genes:  $98.80 \pm 0.10\%$ ; average N50:  $451,294.67 \pm 9,696.11$ ; Figure 45). These metrics suggest these genomes are suitable for comparative genomic analyses.

To predict gene boundaries in the three newly sequenced genomes, we used the MAKER, v2.31.10, pipeline<sup>250</sup> which, creates consensus predictions from the collective evidence of multiple *ab initio* gene prediction software. Specifically, we created consensus predictions from SNAP, v2006-07-28 (Korf 2004), and AUGUSTUS, v3.3.2,<sup>251</sup> after training each algorithm individually on each genome. To do so, we first ran MAKER using protein evidence clues from five different publicly available annotations of *Aspergillus* fungi from section *Fumigati*. Specifically, we used protein homology clues from *A. fischeri* NRRL 181 (GenBank accession: GCA\_000149645.2), *A. fumigatus* Af293 (GenBank accession: GCA\_000002655.1), *Aspergillus lentulus* IFM 54703 (GenBank accession: GCA\_001445615.1), *Aspergillus novofumigatus* IBT 16806 (GenBank accession: GCA\_002847465.1), and *Aspergillus udagawae* IFM 46973 (GenBank accession: GCA\_001078395.1). The resulting gene predictions were used to train SNAP. MAKER was then rerun using the resulting training results. Using the SNAP trained gene predictions, we trained AUGUSTUS. A final set of gene boundary

predictions were obtained by rerunning MAKER with the training results from both SNAP and AUGUSTUS.

**Table 4.2.** Species and Strains Used in the Present Study.

Genus and species	Strain	Environmental /Clinical	Genomic analysis	Secondary metabolite profiling	Reference
<i>Aspergillus oerlinghausenensis</i>	CBS 139183 <sup>T</sup>	Environmental	+	+	This study
<i>Aspergillus fischeri</i>	NRRL 4585	Environmental	+	+	This study
<i>Aspergillus fischeri</i>	NRRL 4161	Unknown	+	+	This study
<i>Aspergillus fischeri</i>	NRRL 181	Environmental	+	+	(Fedorova et al. 2008) 123
<i>Aspergillus fischeri</i>	IBT 3007	Environmental	+	-	(Zhao et al. 2019) <sup>252</sup>
<i>Aspergillus fischeri</i>	IBT 3003	Environmental	+	-	(Zhao et al. 2019) <sup>252</sup>
<i>Aspergillus fumigatus</i>	Af293	Clinical	+	+	(Nierman et al. 2005) <sup>211</sup>
<i>Aspergillus fumigatus</i>	CEA10 / CEA17	Clinical	+	+	(Fedorova et al. 2008) 123
<i>Aspergillus fumigatus</i>	HMR AF 270	Clinical	+	-	BioSample: SAMN07177 964
<i>Aspergillus fumigatus</i>	Z5	Environmental	+	-	(Miao et al. 2015) <sup>253</sup>

‘+’ and ‘-’ indicate if BGCs and secondary metabolite profiling was conducted on a particular strain. More specifically ‘+’ indicates the strain was analyzed whereas ‘-’ indicates that the strain was not analyzed.

To supplement our data set of newly sequenced genomes, we obtained publicly available ones. Specifically, we obtained genomes and annotations for *A. fumigatus* Af293 (GenBank accession: GCA\_000002655.1), *A. fumigatus* CEA10 (strain synonym: CBS 144.89 / FGSC A1163; GenBank accession: GCA\_000150145.1), *A. fumigatus* HMR AF 270 GenBank accession: GCA\_002234955.1), *A. fumigatus* Z5 (GenBank accession: GCA\_001029325.1), *A. fischeri* NRRL 181 (GenBank accession: GCA\_000149645.2). We also obtained assemblies of the recently published *A. fischeri* genomes for strains IBT 3003 and IBT 3007<sup>252</sup> which, lacked annotations. We annotated the genome of each strain individually using MAKER with the SNAP and AUGUSTUS training results from a close relative of both strains, *A. fischeri* NRRL 4161. Altogether, our final data set contained a total of ten genome from three species: four *A. fumigatus* strains, one *A. oerlinghausenensis* strain, and five *A. fischeri* strains (Table 4.2).

### **Maximum Likelihood Phylogenetics and Bayesian Estimation of Divergence**

**Times.** To reconstruct the evolutionary history among the ten *Aspergillus* genomes, we implemented a recently developed pipeline,<sup>216</sup> which relies on the concatenation-approach to phylogenomics<sup>254</sup> and has been successfully used in reconstructing species-level relationships among *Aspergillus* and *Penicillium* fungi.<sup>216, 255</sup> The first step in the pipeline is to identify single copy orthologous genes in the genomes of interest which, are ultimately concatenated into a larger phylogenomic data matrix. To identify single copy BUSCO genes across all ten *Aspergillus* genomes, we used the BUSCO pipeline with the Pezizomycotina database as described above. We identified 3,041 BUSCO genes present at a single copy in all ten *Aspergillus* genomes and created multi-FASTA files for each BUSCO gene that contained the protein sequences for all ten taxa. The protein sequences of each BUSCO gene were individually aligned using Mafft,

v7.4.02,<sup>256</sup> with the same parameters as described elsewhere.<sup>216</sup> Nucleotide sequences were then mapped onto the protein sequence alignments using a custom Python, v3.5.2 (<https://www.python.org/>), script with BioPython, v1.7.<sup>257</sup> The resulting codon-based alignments were trimmed using trimAl, v1.2.rev59,<sup>258</sup> with the ‘gappyout’ parameter. The resulting trimmed nucleotide alignments were concatenated into a single matrix of 5,602,272 sites and was used as input into IQ-TREE, v1.6.11.<sup>259</sup> The best-fitting model of substitutions for the entire matrix was determined using Bayesian information criterion values.<sup>260</sup> The best-fitting model was a general time-reversible model with empirical base frequencies that allowed for a proportion of invariable sites and a discrete Gamma model with four rate categories (GTR+I+F+G4).<sup>261-264</sup> To evaluate bipartition support, we used 5,000 ultrafast bootstrap approximations.<sup>265</sup>

To estimate divergence times among the ten *Aspergillus* genomes, we used the concatenated data matrix and the resulting maximum likelihood phylogeny from the previous steps as input to Bayesian approach implemented in MCMCTree from the PAML package, v4.9d.<sup>266</sup> First, we estimated the substitution rate across the data matrix using a “GTR+G” model of substitutions (model = 7), a strict clock model, and the maximum likelihood phylogeny rooted on the clade of *A. fischeri* strains. We imposed a root age of 3.69 million years ago according to results from recent divergence time estimates of the split between *A. fischeri* and *A. fumigatus*.<sup>216</sup> We estimated the substitution rate to be 0.005 substitutions per one million years. Next, the likelihood of the alignment was approximated using a gradient and Hessian matrix. To do so, we used previously established time constraints for the split between *A. fischeri* and *A. fumigatus* (1.85 to 6.74 million years ago).<sup>216</sup> Lastly, we used the resulting gradient and Hessian matrix, the rooted maximum likelihood phylogeny, and the concatenated data

matrix to estimate divergence times using a relaxed molecular clock (model = 2). We specified the substitution rate prior based on the estimated substitution rate (rgene\_gamma = 1 186.63). The ‘sigma2\_gamma’ and ‘finetune’ parameters were set to ‘1 4.5’ and ‘1’, respectively. To collect a high-quality posterior probability distribution, we ran a total of 5.1 million iterations during MCMC analysis which, is 510 times greater than the minimum recommendations.<sup>267</sup> Our sampling strategy across the 5.1 million iterations was to discard the first 100,000 results followed by collecting a sample every 500<sup>th</sup> iteration until a total of 10,000 samples were collected.

**Identification of Gene Families and Analyses of Putative Biosynthetic Gene Clusters.** To identify gene families across the ten *Aspergillus* genomes, we used a Markov clustering approach. Specifically, we used OrthoFinder, v2.3.8.<sup>268</sup> OrthoFinder first conducts a blast all-vs-all using the protein sequences of all ten *Aspergillus* genomes and NCBI’s Blast+, v2.3.0,<sup>269</sup> software. After normalizing blast bit scores, genes are clustered into discrete orthogroups using a Markov clustering approach. We clustered genes using an inflation parameter of 1.5. The resulting orthogroups were used proxies for gene families.

To identify putative biosynthetic gene clusters (BGCs), we used the gene boundaries predictions from the MAKER software as input into antiSMASH, v4.1.0 (Weber *et al.* 2015). To identify homologous BGCs across the ten *Aspergillus* genomes, we used the software BiG-SCAPE, v20181005.<sup>270</sup> Based on the Jaccard Index of domain types, sequence similarity among domains, and domain adjacency, BiG-SCAPE calculates a similarity metric between pairwise combinations of clusters where smaller values indicate greater BGC similarity. BiG-SCAPE’s similarity metric can then be used as an edge-length in network analyses of cluster similarity. We evaluated networks using

an edge-length cutoff from 0.1-0.9 with a step of 0.1 (Figure 47). We found networks with an edge-length cutoff of 0.4-0.6 to be similar and based further analyses on a cutoff of 0.5. Because BiG-SCAPE inexplicably split the gliotoxin BGC of the *A. fumigatus* Af293 strain into two cluster families even though the BGC was highly similar to the gliotoxin BGCs of all other strains, we supplemented BiG-SCAPE's approach to identifying homologous BGCs with visualize inspection of microsyteny and blast-based analyses using NCBI's BLAST+, v2.3.0<sup>269</sup> for BGCs of interest. Similar sequences in microsynteny analyses were defined as at least 100 bp in length, at least 30 percent similarity, and an expectation value threshold of 0.01. Lastly, to determine if any BGCs have been previously linked to secondary metabolites, we cross referenced BGCs and BGC families with those found in the MIBiG database<sup>239</sup> as well as previously published *A. fumigatus* BGCs. BGCs not associated with secondary metabolites were considered to likely encode for unknown compounds.

#### **Identification and characterization of secondary metabolite production**

**General Experimental Procedures.** The <sup>1</sup>H NMR data were collected using a JOEL ECS-400 spectrometer, which was equipped with a JOEL normal geometry broadband Royal probe, and a 24-slot autosampler, and operated at 400 MHz. HRESIMS experiments utilized either a Thermo LTQ Orbitrap XL mass spectrometer or a Thermo Q Exactive Plus (Thermo Fisher Scientific); both were equipped with an electrospray ionization source. A Waters Acquity UPLC (Waters Corp.) was utilized for both mass spectrometers, using a BEH C<sub>18</sub> column (1.7 μm; 50 mm x 2.1 mm) set to a temperature of 40°C and a flow rate of 0.3 ml/min. The mobile phase consisted of a linear gradient of CH<sub>3</sub>CN-H<sub>2</sub>O (both acidified with 0.1% formic acid), starting at 15% CH<sub>3</sub>CN and increasing linearly to 100% CH<sub>3</sub>CN over 8 min, with a 1.5 min hold before

returning to the starting condition. The HPLC separations were performed with Atlantis T3 C<sub>18</sub> semi-preparative (5 µm; 10 x 250 mm) and preparative (5 µm; 19 x 250 mm) columns, at a flow rate of 4.6 ml/min and 16.9 ml/min, respectively, with a Varian Prostar HPLC system equipped with a Prostar 210 pumps and a Prostar 335 photodiode array detector (PDA), with the collection and analysis of data using Galaxie Chromatography Workstation software. Flash chromatography was performed on a Teledyne ISCO Combiflash Rf 200 and monitored by both ELSD and PDA detectors.

**Chemical Characterization.** To identify the secondary metabolites that were biosynthesized by *A. fumigatus*, *A. oerlinghausensis*, and *A. fischeri*, these strains were grown as large-scale fermentations to isolate and characterize the secondary metabolites. To inoculate oatmeal cereal media (Old fashioned breakfast Quaker oats), agar plugs from fungal stains grown on potato dextrose agar; difco (PDA) were excised from the edge of the Petri dish culture and transferred to separate liquid seed media that contained 10 ml YESD broth (2% soy peptone, 2% dextrose, and 1% yeast extract; 5 g of yeast extract, 10 g of soy peptone, and 10 g of D-glucose in 500 ml of deionized H<sub>2</sub>O) and allowed to grow at 23°C with agitation at 100 rpm for three days. The YESD seed cultures of the fungi were subsequently used to inoculate solid-state oatmeal fermentation cultures, which were either grown at room temperature (approximately 23°C under 12h light/dark cycles for 14 days), 30°C, or 37°C; all growths at the latter two temperatures were carried out in an incubator (VWR International) in the dark over four days. The oatmeal cultures were prepared in 250 ml Erlenmeyer flasks that contained 10 g of autoclaved oatmeal (10 g of oatmeal with 17 ml of deionized H<sub>2</sub>O and sterilized for 15–20 minutes at 121°C). For all fungal strains three flasks of oatmeal cultures were grown at all three temperatures, except for *A. oerlinghausensis* (CBS 139183<sup>T</sup>) at

room temperature and *A. fumigatus* (Af293) at 37°C. For CBS 139183<sup>T</sup>, the fungal cultures were grown in four flasks, while for Af293 eight flasks were grown in total. The growths of these two strains were performed differently from the rest because larger amounts of extract were required in order to perform detailed chemical characterization.

The cultures were extracted by adding 60 ml of (1:1) MeOH-CHCl<sub>3</sub> to each 250 ml flask, chopping thoroughly with a spatula, and shaking overnight (~ 16 h) at ~ 100 rpm at room temperature. The culture was filtered *in vacuo*, and 90 ml CHCl<sub>3</sub> and 150 ml H<sub>2</sub>O were added to the filtrate. The mixture was stirred for 30 min and then transferred to a separatory funnel. The organic layer (CHCl<sub>3</sub>) was drawn off and evaporated to dryness *in vacuo*. The dried organic layer was reconstituted in 100 ml of (1:1) MeOH-CH<sub>3</sub>CN and 100 ml of hexanes, transferred to a separatory funnel, and shaken vigorously. The defatted organic layer (MeOH-CH<sub>3</sub>CN) was evaporated to dryness *in vacuo*.

To isolate compounds, the defatted extract was dissolved in CHCl<sub>3</sub>, absorbed onto Celite 545 (Acros Organics), and fractioned by normal phase flash chromatography using a gradient of hexane-CHCl<sub>3</sub>-MeOH. *Aspergillus fischeri* strain NRRL 181 was chemically characterized previously.<sup>16, 271</sup> *A. fumigatus* strain Af293, grown at 37°C, was subjected to a 12g column at a flow rate of 30 ml/min and 61.0 column volumes, which yielded four fractions. Fraction 2 was further purified via preparative HPLC using a gradient system of 30:70 to 100:0 of CH<sub>3</sub>CN-H<sub>2</sub>O with 0.1% formic acid over 40 min at a flow rate of 16.9 ml/min to yield six subfractions. Subfractions 1, 2 and 5, yielded cyclo(L-Pro-L-Leu)<sup>272</sup> (0.89 mg), cyclo(L-Pro-L-Phe)<sup>273</sup> (0.71 mg), and monomethylsulochrin<sup>274</sup> (2.04 mg), which eluted at approximately 5.7, 6.3, and 10.7 min, respectively. Fraction 3 was further purified via preparative HPLC using a gradient system of 40:60 to 65:35 of CH<sub>3</sub>CN-H<sub>2</sub>O with 0.1% formic acid over 30 min at a flow rate

of 16.9 ml/min to yield four subfractions. Subfractions 1 and 2 yielded pseurotin A<sup>275</sup> (12.50 mg) and bisdethiobis(methylthio)gliotoxin<sup>169</sup> (13.99 mg), which eluted at approximately 7.5 and 8.0 min, respectively.

*A. fumigatus* strain CEA10, grown at 37°C, was subjected to a 4g column at a flow rate of 18 ml/min and 90.0 column volumes, which yielded five fractions. Fraction 1 was purified via preparative HPLC using a gradient system of 50:50 to 100:0 of CH<sub>3</sub>CN-H<sub>2</sub>O with 0.1% formic acid over 45 min at a flow rate of 16.9 ml/min to yield eight subfractions. Subfraction 1, yielded fumagillin<sup>276</sup> (1.69 mg), which eluted at approximately 18.5 min. Fraction 2 was purified via semi-preparative HPLC using a gradient system of 35:65 to 80:20 of CH<sub>3</sub>CN-H<sub>2</sub>O with 0.1% formic acid over 30 min at a flow rate of 4.6 ml/min to yield 10 subfractions. Subfraction 5 yielded fumitremorgin C<sup>277</sup> (0.25 mg), which eluted at approximately 15.5 min. Fraction 3 was purified via preparative HPLC using a gradient system of 40:60 to 100:0 of CH<sub>3</sub>CN-H<sub>2</sub>O with 0.1% formic acid over 30 min at a flow rate of 16.9 ml/min to yield nine subfractions. Subfraction 2 yielded pseurotin A (1.64 mg), which eluted at approximately 7.3 min.

*Aspergillus oerlinghausenensis* strain CBS 139183<sup>T</sup>, grown at RT, was subjected to a 4g column at a flow rate of 18 ml/min and 90 column volumes, which yielded 4 fractions. Fraction 3 was further purified via preparative HPLC using a gradient system of 35:65 to 70:30 of CH<sub>3</sub>CN-H<sub>2</sub>O with 0.1% formic acid over 40 min at a flow rate of 16.9 ml/min to yield 11 subfractions. Subfractions 3 and 10 yielded spiro [5H,10H-dipyrrrolo[1,2-a:1',2'-d]pyrazine-2-(3H),2'-[2H]indole]-3',5,10(1'H)-trione<sup>278</sup> (0.64 mg) and helvolic acid<sup>279</sup> (1.03 mg), which eluted at approximately 11.5 and 39.3 min, respectively. (NMR data Figures 53-59).

**Metabolite Profiling by Mass Spectrometry.** The metabolite profiling by mass spectrometry, also known as dereplication, was performed as stated previously.<sup>188</sup> Briefly, ultraperformance liquid chromatography-photodiode array-electrospray ionization high resolution tandem mass spectrometry (UPLC-PDA-HRMS-MS/MS) was utilized to monitor for secondary metabolites across all strains (Af293, CEA10, CEA17, CBS 139183<sup>T</sup>, NRRL 181, NRRL 4161, and NRRL 4585). Utilizing positive-ionization mode, ACD MS Manager with add-in software IntelliXtract (Advanced Chemistry Development, Inc.; Toronto, Canada) was used for the primary analysis of the UPLC-MS chromatograms. The data from 19 secondary metabolites are provided in Table 4.5, which for each secondary metabolite lists: molecular formula, retention time, UV-absorption maxima, high-resolution full-scan mass spectra, and MS-MS data (top 10 most intense peaks).

**Metabolomics Analyses.** Principal component analysis (PCA) analysis was performed on the UPLC-MS data. Untargeted UPLC-MS datasets for each sample were individually aligned, filtered, and analyzed using MZmine 2.20 software (<https://sourceforge.net/projects/mzmine/>).<sup>280</sup> Peak detection was achieved using the following parameters, *A. fumigatus* at (Af293, CEA10, and CEA17): noise level (absolute value),  $1 \times 10^6$ ; minimum peak duration, 0.05 min; *m/z* variation tolerance, 0.05; and *m/z* intensity variation, 20%; *A. fischeri* (NRRL 181, NRRL 4161, and NRRL 4585): noise level (absolute value),  $1 \times 10^6$ ; minimum peak duration, 0.05 min; *m/z* variation tolerance, 0.05; and *m/z* intensity variation, 20%; and all strains (Af293, CEA10, CEA17, CBS 139183<sup>T</sup>, NRRL 181, NRRL 4161, and NRRL 4585): noise level (absolute value),  $7 \times 10^5$ ; minimum peak duration, 0.05 min; *m/z* variation tolerance, 0.05; and *m/z* intensity variation, 20%. Peak list filtering and retention time alignment algorithms were used to

refine peak detection. The join algorithm integrated all sample profiles into a data matrix using the following parameters: *m/z* and retention time balance set at 10.0 each, *m/z* tolerance set at 0.001, and RT tolerance set at 0.5 mins. The resulting data matrix was exported to Excel (Microsoft) for analysis as a set of *m/z* – retention time pairs with individual peak areas detected in triplicate analyses. Samples that did not possess detectable quantities of a given marker ion were assigned a peak area of zero to maintain the same number of variables for all sample sets. Ions that did not elute between 2 and 8 minutes and/or had an *m/z* ratio less than 200 or greater than 800 Da were removed from analysis. Relative standard deviation was used to understand the quantity of variance between the technical replicate injections, which may differ slightly based on instrument variance. A cutoff of 1.0 was used at any given *m/z* – retention time pair across the technical replicate injections of one biological replicate, and if the variance was greater than the cutoff, it was assigned a peak area of zero. Final chemometric analysis, data filtering<sup>281</sup> and PCA was conducted using Sirius, v10.0 (Pattern Recognition Systems AS),<sup>282</sup> and dendograms were created with Python. The PCA scores plots were generated using data from either the three individual biological replicates or the averaged biological replicates of the fermentations. Each biological replicate was plotted using averaged peak areas obtained across four replicate injections (technical replicates).

**Data Availability.** Sequence reads and associated genome assemblies generated in this project are available in NCBI's GenBank database under the BioProject PRJNA577646. Additional descriptions of the genomes including predicted gene boundaries are available through figshare  
<https://doi.org/10.6084/m9.figshare.12055503>). The figshare repository is also populated

with other data generated from genomic analysis. Among genomic analyses, we provide information about predicted BGCs, results associated with network-based clustering of BGCs into cluster families, phylogenomic data matrices, and trees.

## Supplementary Data

**Table 4.3.** A Table of Secondary Metabolites Produced by Each Species and Strain. '+' (orange) and '-' (blue) indicate evidence and no evidence of secondary metabolite biosynthesis, respectively.

Secondary Metabolites Detected	Chemical Analogs	<i>A. fumigatus</i>			<i>A. oerlingha usenensis</i>	<i>A. Fischeri</i>		
		Af 293	CEA 10	CEA 17	CBS 139183	NRRL 181	NRRL 4161	NRRL 4585
cyclo (L-Pro-L-Leu)		+	+	-	+	+	+	+
cyclo (L-Pro-L-Phe)FMDA		+	+	-	+	+	+	+
Monomethylsulochrin	Trypacidin	+	+	+	+	-	-	-
Pseurotin A		+	+	+	-	-	-	-
Bisdethiobis(methylthio)gliotoxin	Gliotoxin	+	+	+	+	+	+	+
Fumagillin		+	+	+	+	-	-	-
Sartorypyrone A		+	+	-	+	+	+	+
Sartorypyrone E		-	-	-	-	+	+	+
14-epi-aszonapyrone A		-	+	-	-	+	+	+
Aszonalenin		-	-	-	-	+	+	+
Acetylaszonalenin		-	-	-	-	+	+	+
Spiro[5H,10H-dipyrrolo[1,2-a:1',2'-d]pyrazine-2-(3H),2'-[2H]indole]-		-	-	-	+	-	-	-

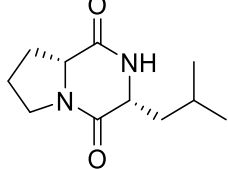
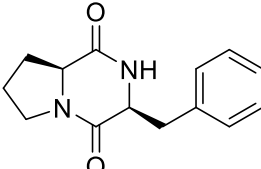
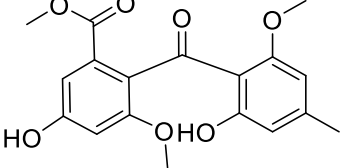
3',5,10(1'H)-trione									
Helvolic Acid	-	-	-	-	+	-	-	-	-
Fumitremorgin A	-	-	-	-	-	+	+	+	+
Fumitremorgin B	-	-	-	-	+	+	+	+	+
13-O-prenyl-fumitremorgin B	-	-	-	-	-	+	+	+	+
Fumitremorgin C	-	+	-	-	+	-	-	-	-
Verruculogen	-	-	-	-	-	+	+	+	+

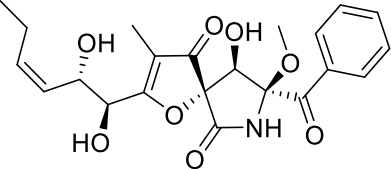
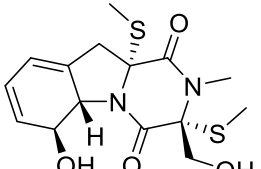
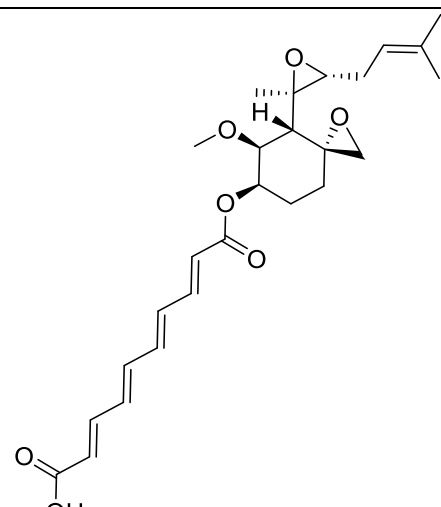
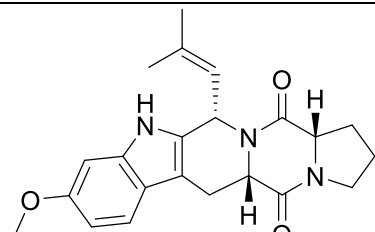
**Table 4.4.** A Table Summarizing Species-Level Secondary Metabolite Production

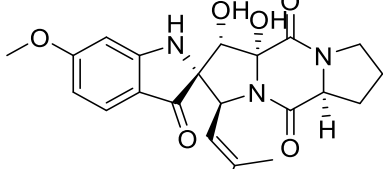
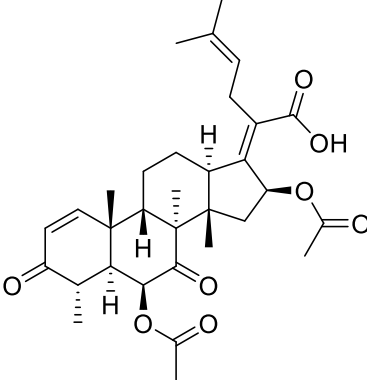
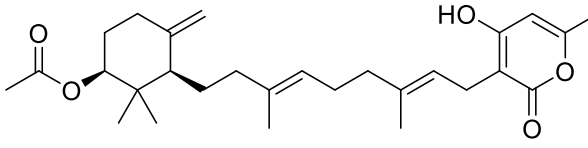
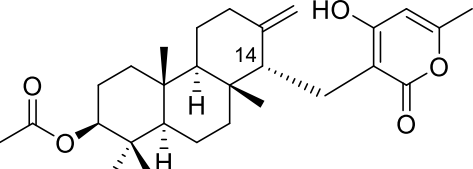
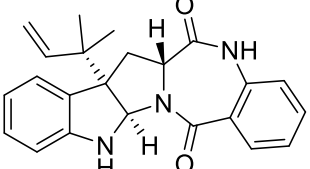
Secondary Metabolite Detected	Chemical Analogs	<i>A. fumigatus</i>	<i>A. oerlinghausenensis</i>	<i>A. fischeri</i>
cyclo (L-Pro-L-Leu)		+	+	+
cyclo (L-Pro-L-Phe)		+	+	+
Monomethylsulochrin	Trypacidin	+	+	-
Pseurotin A		+	-	-
Bisdethiobis(methylthio) gliotoxin	Gliotoxin	+	+	+
Fumagillin		+	+	-
Sartorypyrone A		+	+	+
Sartorypyrone E		-	-	+
14-epi-aszonapyrone A		+	-	+
Aszonalenin		-	-	+
Acetylaszonalenin		-	-	+
Spiro [5H,10H-dipyrrolo[1,2-a:1',2'-d]pyrazine-2-(3H),2'-[2H]indole]-3',5,10(1'H)-trione		-	+	-
Helvolic Acid		-	+	-

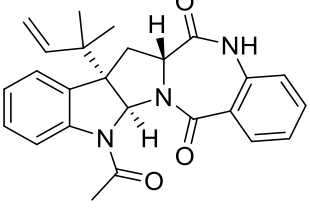
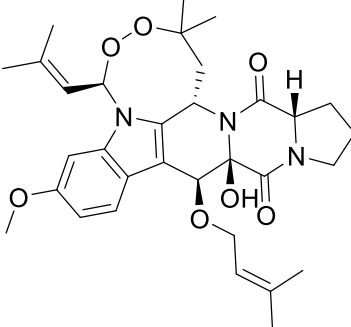
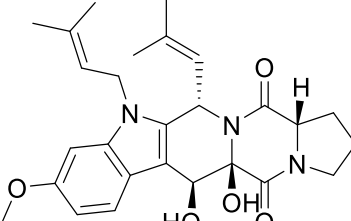
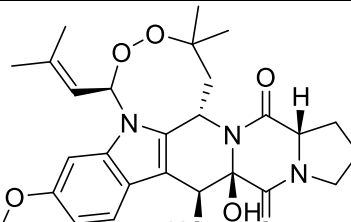
Fumitremorgin A		-	-	+
Fumitremorgin B		-	+	+
13-O-prenyl-fumitremorgin B		-	-	+
Fumitremorgin C		+	+	-
Verruculogen		-	-	+
11-epimer of verruculogen TR2		-	-	+

**Table 4.5.** Chemical Structures, Chemical Formulas, Retention Times, UV Absorption Maxima, (+)-ESI HRMS, and (+)-ESI CID MS/MS Data of Fumigati Fungal Secondary Metabolites.

Chemical Structure and Chemical formula	Rt (min)	UV (nm)	Positive Ionization Mode <sup>a</sup>	
			[M+H] <sup>+</sup>	MS/MS
 Cyclo (L-Pro-L-Leu) (1) $C_{11}H_{18}N_2O_2$	1.85	193	211.1437 (-1.92)	211.07, 183.05 85.93, 69.87 194.04, 138.04 155.12, 126.95
 Cyclo (L-Pro-L-Phe) (2) $C_{14}H_{16}N_2O_2$	2.29	193 210	245.1281 (-1.45)	119.96, 217.12 245.10, 69.93 200.06, 172.04 130.98, 228.17, 154.04
 Monomethylsulochrin (3) $C_{18}H_{18}O_7$	4.52	195 221 284	347.1122 (-0.95)	208.98, 164.97 315.26, 150.00 121.71, 282.95 319.34, 303.17

 <p>Pseorotin A (<b>4</b>)  <math>C_{22}H_{25}NO_8</math></p>	3.33	195, 256, 280	432.1647 (-1.37)	316.06, 329.19 330.22, 333.96 312.32, 319.53 245.35, 272.37
 <p>Bisdethiobis(methylthio)gliotoxin (<b>5</b>)  <math>C_{15}H_{20}N_2O_4S_2</math></p>	3.38	202, 265	357.0934 (-0.91)	308.97, 243.09 290.95, 215.047 261.07, 233.15 273.19, 192.07
 <p>Fumagillin (<b>6</b>)  <math>C_{26}H_{34}O_7</math></p>	5.53	221 320 336 352	459.2369 (-3.99)	427.10, 233.11 215.09, 176.97 441.16, 265.14 187.13, 247.16
 <p>Fumitremorgin C (<b>7</b>)  <math>C_{22}H_{25}N_3O_3</math></p>	4.06	211 223 271 297	380.1962 (-1.76)	226.06, 324.13 266.13, 352.23 214.11, 255.15 296.16, 282.21

 <p>spiro [5H,10H-dipyrrolo[1,2-a:1',2'-d]pyrazine-2-(3H),2'-[2H]indole]-3',5,10(1'H)-trione (<b>8</b>)  <math>C_{22}H_{25}N_3O_6</math></p>	3.58	195 221 249 289 391	428.1807 (-2.13) 410.1704 [M+H-H <sub>2</sub> O] <sup>+</sup> (-1.58)	392.18, 364.17 230.05, 382.22 313.11, 295.10 297.16, 228.10
 <p>Helvolic Acid (<b>9</b>)  <math>C_{33}H_{44}O_8</math></p>	5.67	195 228	591.2913 [M+Na] <sup>+</sup> (-2.60)	ND
 <p>Sartorypyrone A (<b>10</b>)  <math>C_{28}H_{40}O_5</math></p>	6.99	197 211 293	457.2940 (-1.86)	397.28, 259.23 247.22, 139.08 275.27, 207.18 181.09, 289.28
 <p>14-epi-azonapyrone A (<b>12</b>)  <math>C_{28}H_{40}O_5</math></p>	6.80	199 223 293	457.2936 (-2.72)	259.22, 397.30 257.27, 271.28 139.00, 231.24 163.18, 189.19
 <p>Aszonalenin (<b>13</b>)  <math>C_{23}H_{23}N_3O_2</math></p>	5.31	197 235 293	374.1856 (-1.88)	198.14, 306.24 318.24, 238.23 290.30, 275.16 357.28, 200.13

 <p><b>Acetylaszonalenin (14)</b>  <math>C_{25}H_{25}N_3O_3</math></p>	4.51	197 250 285 319	416.1961 (-1.85)	348.20, 306.20 374.24, 318.22 198.18, 360.26 330.29, 290.23
 <p><b>Fumitremorgin A (15)</b>  <math>C_{32}H_{41}N_3O_7</math></p>	6.57	196 233 276 294	580.2991 (-4.53)	494.07, 438.26 496.26, 352.20 478.28, 510.18 266.17, 562.17
 <p><b>Fumitremorgin B (16)</b>  <math>C_{27}H_{33}N_3O_5</math></p>	5.74	225, 277 297	480.2475 (-3.74)	242.22, 298.23, 356.26, 424.25 462.28, 412.20 396.35, 338.09
 <p><b>Verruculogen (18)</b>  <math>C_{27}H_{33}N_3O_7</math></p>	5.17	197 235 274 295	494.2267 $[M+H-H_2O]^+$ (-3.77)	352.25, 313.22 410.17, 295.20 364.28, 382.18 392.24, 240.18

<sup>a</sup>Mass spectrometry data are reported as m/z values with the difference in ppm between the measured and the calculated data given in parentheses.

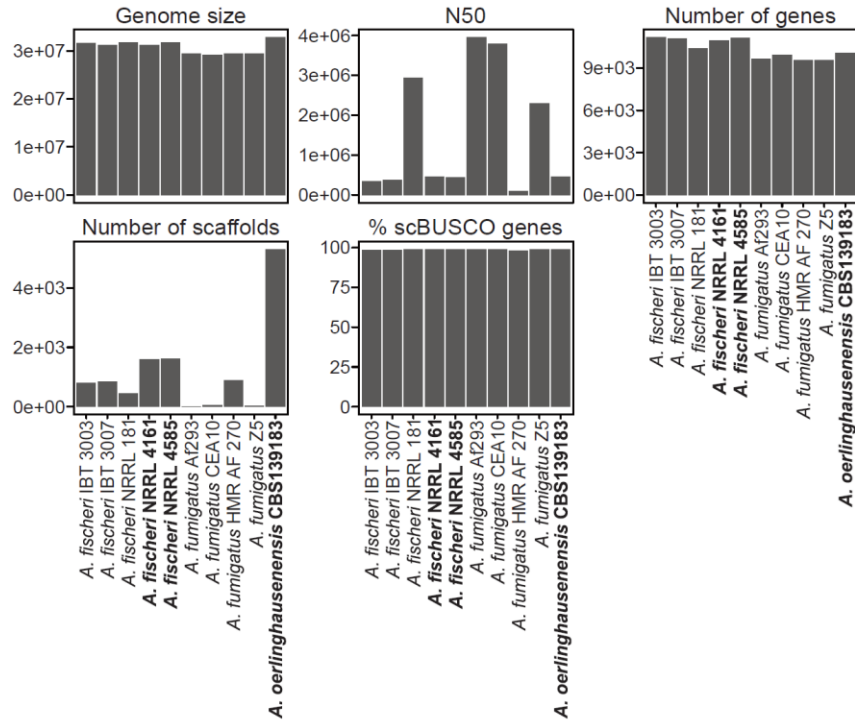


**Figure 45.** Metrics of Genomes Assembly Quality and Number of Predicted Gene. Genome size, N50, number of genes, number of scaffolds and percent single copy BUSCO genes (scBUSCO) are depicted here. Examination of metrics reveal genomes are of sufficient quality for comparative genomics purposes. Of concern, we noted *A. oerlinghausensis* CBS 139183<sup>T</sup> was assembled into 5,300 contigs; however, we evaluated the assembly's N50 value and gene content completeness (461,327 base pairs and 98.90% BUSCO genes present in single copy, respectively) and found the *A. oerlinghausensis* genome is suitable for comparative genomic analyses. Strains in bold font are genomes sequenced in this study.

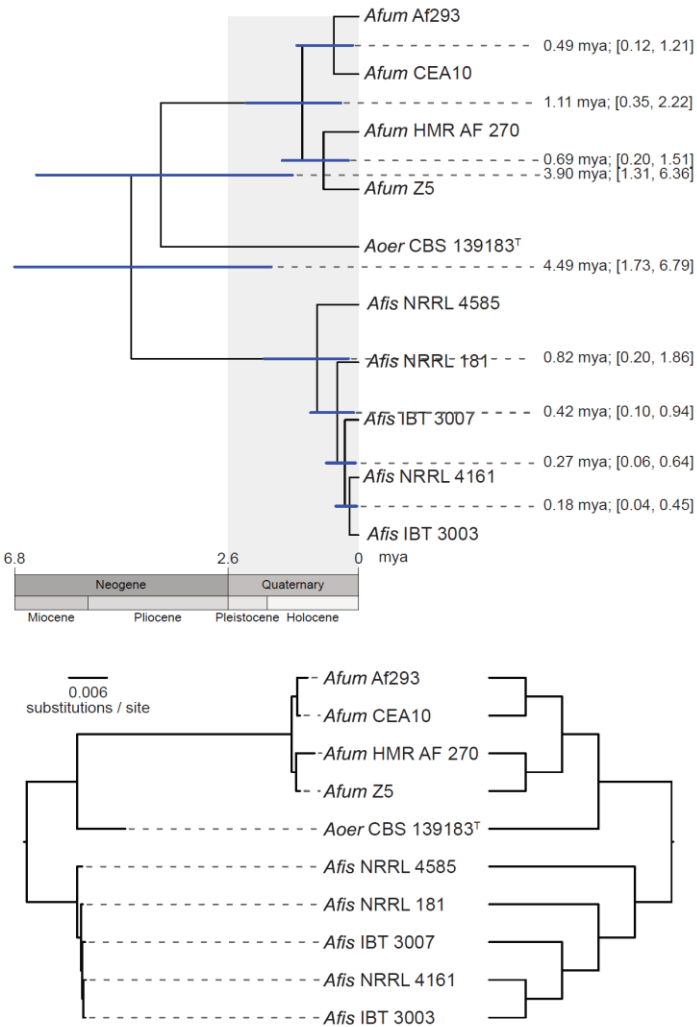


**Figure 46.** A Reconstructed Evolutionary History and Timetree of *A. fumigatus* and its Closest Relatives. (top) Divergence times were estimated using a concatenated matrix of 3,041 genes (5,602,272 sites). Blue bars at each node correspond to the 95% divergence time confidence interval. Divergence times and confidence intervals for each internode are shown on the right side of the figure. (bottom) A phylogeny where branch lengths represent substitutions per site rather than geologic time. A cladogram is drawn to the right of the phylogeny to clarify divergences where branch lengths are short (e.g., among strains of *A. fischeri*).

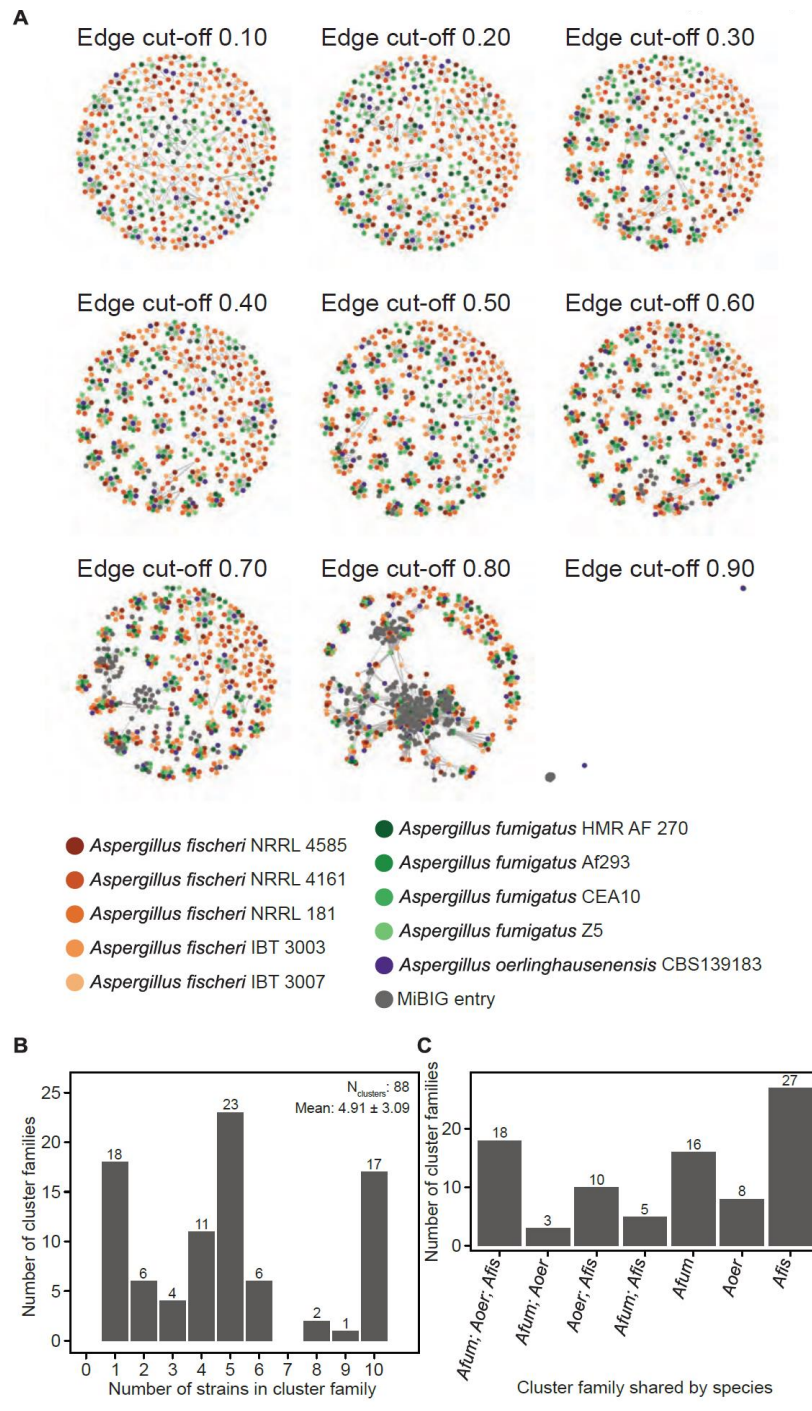


**Figure 47.** Species and Strain Heterogeneity Among BGC Cluster Presence and Absence. (A) Networks using edge cut-offs ranging from 0.1-0.9 with a step of 0.1 were evaluated. Networks from 0.4 to 0.6 were qualitatively similar. Thus, we used cluster families inferred from the network using an edge cut-off of 0.5. (B) Examination of the number of strains in each cluster family reveal a wide variation. For example, all 10

genomes are represented in 17 cluster families; in contrast, 18 cluster families have only one BGC. (C) Species occupancy among cluster families reveal *A. fischeri* has the largest number of unique BGCs followed by *A. fumigatus* and *A. oerlinghausenensis*.

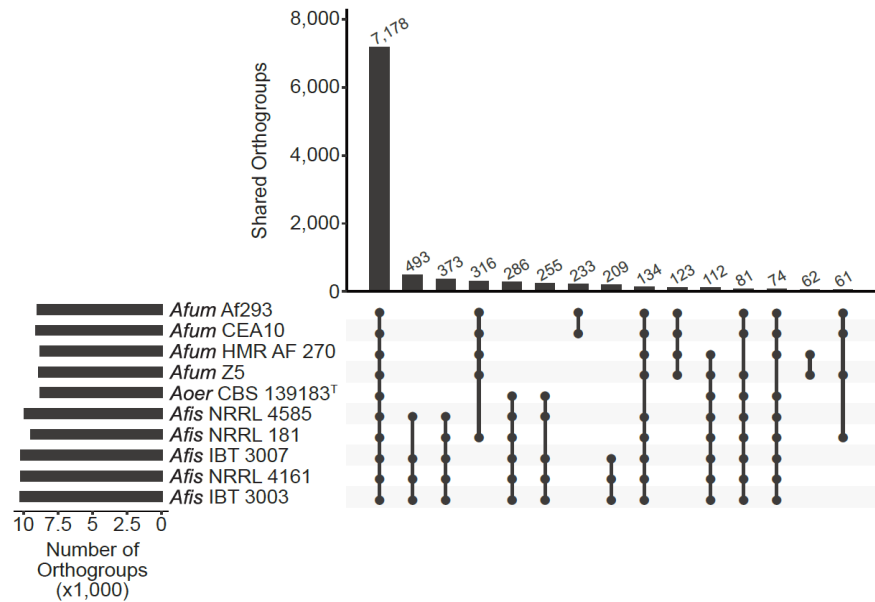
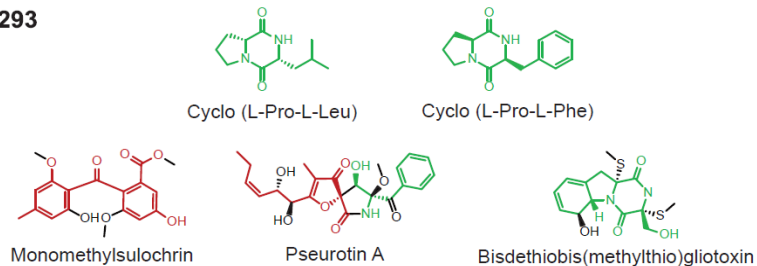
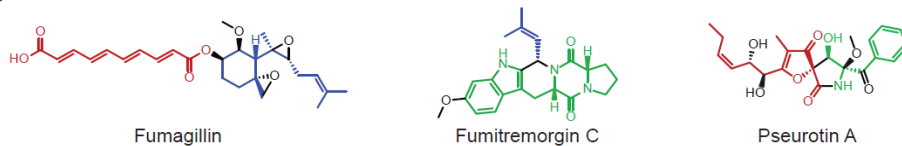


**Figure 48.** Gene Family Presence and Absence Follows a Similar Pattern to BGCs. Orthogroups were used as proxies for gene families. A strain-level UpSet plot for gene family presence and absence patterns reveals heterogeneity among strains.

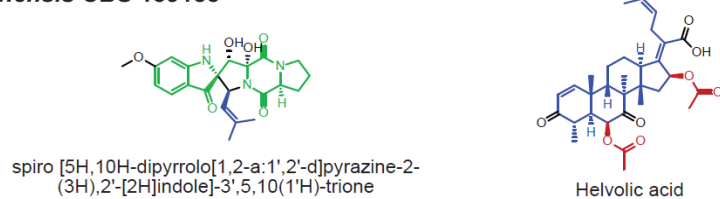
***A. fumigatus* Af293**



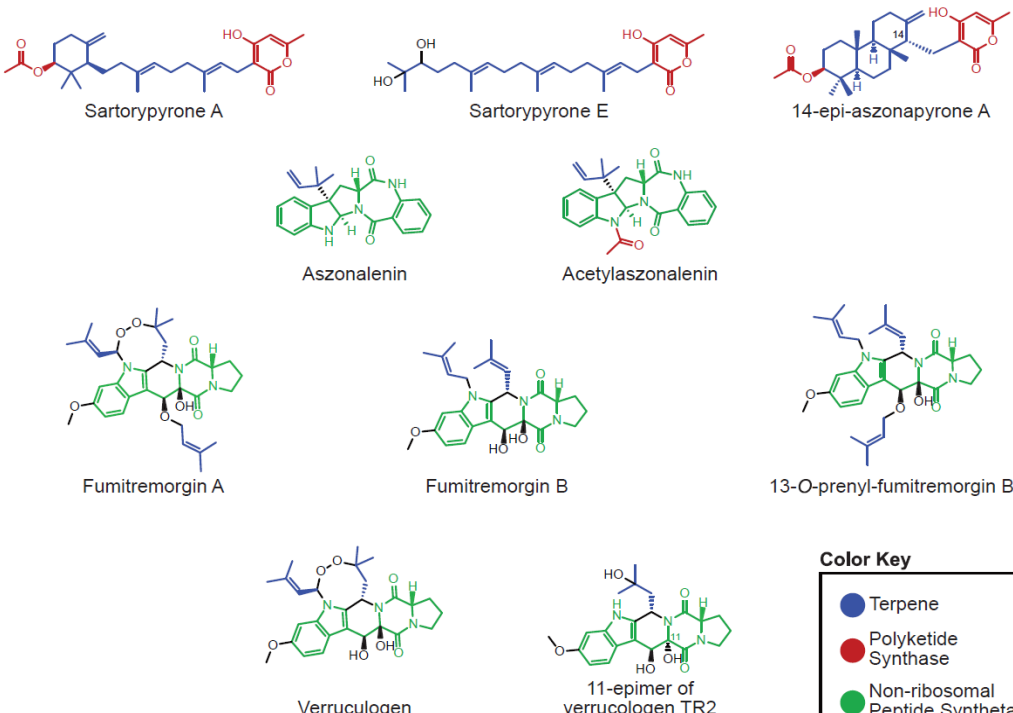
***A. fumigatus* CEA10**



***A. oerlinghausenensis* CBS 139183<sup>T</sup>**



***A. fischeri* strains NRRL 181, NRRL 4585, NRRL 4161**



**Color Key**

- Terpene
- Polyketide
- Synthase
- Non-ribosomal Peptide Synthetase

**Figure 49.** Structures of Isolated Fungal Metabolites. Secondary metabolites produced in sufficient quantity were isolated for structural determination. The structures of compounds are correlated to each strain from where they were isolated. Structural moieties biosynthesized by terpene synthases, polyketide synthases, and non-ribosomal peptide synthetases are colored blue, red, and green, respectively.

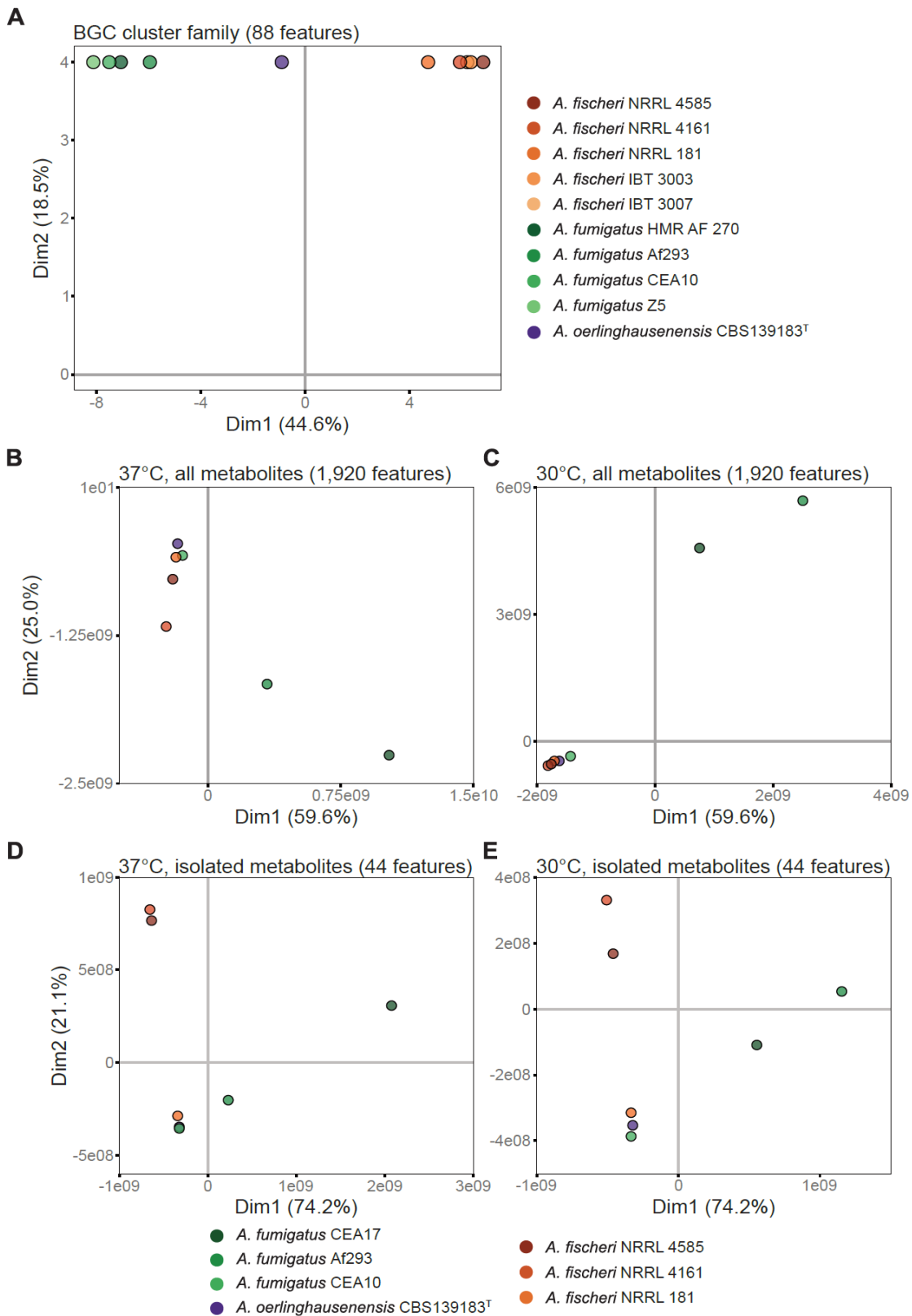


**Figure 50.** Principal Component Analysis of BGC Presence and Absence and Secondary Metabolite Profiles Mirror One Another. (A) Principal component analysis of BGC presence and absence reveal that each species is distinct from the other. Furthermore, *A. oerlinghausenensis* is between *A. fischeri* and *A. fumigatus*. (B, C) Broadly, similar patterns of species relationships in principal component space are observed among all metabolites produced at 37°C and 30°C. (D, E) Similar results were observed for isolatable metabolites.

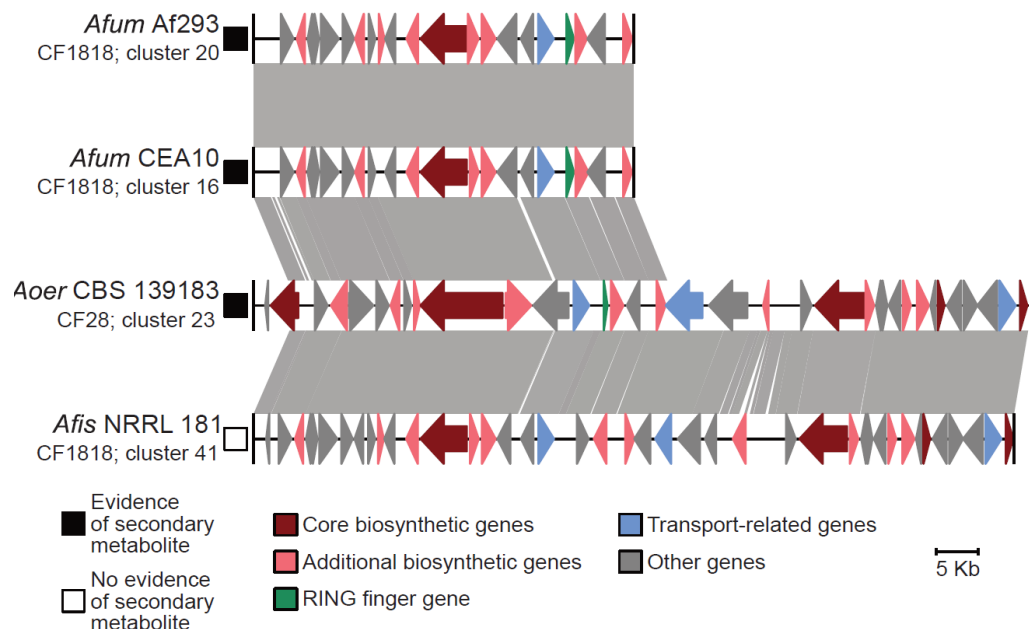


**Figure 51.** Small Sequence Divergences in the Trypacidin BGC are Associated with the Production of Trypacidin or the Lack Thereof. The trypacidin BGC is found in *A. fumigatus* strains Af293 and CEA10, *A. oerlinghausenensis* CBS 139183<sup>T</sup>, and *A. fischeri* NRRL 181. Evidence of trypacidin biosynthesis is found in all isolates with the exception of *A. fischeri* NRRL 181. The absence of trypacidin biosynthesis is associated with the absence of a RING finger gene in *A. fischeri* NRRL 181. Black and white squares correspond to evidence or no evidence of secondary metabolite production, respectively. Grey boxes connecting BGCs represent BLAST-based similarity of nucleotide sequences defined as being at least 100 bp in length, share at least 30% sequence similarity, and have an expectation value threshold of 0.01. Genus and species names are written using the following abbreviations: *Afum*: *A. fumigatus*; *Aoer*: *A. oerlinghausenensis*; *Afis*: *A. fischeri*.

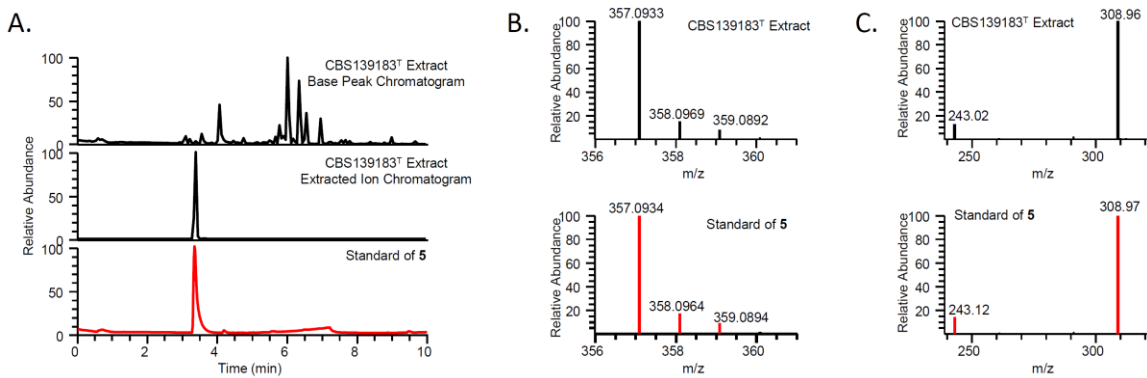


**Figure 52.** Panels A-C demonstrate an example of the dereplication process used to identify bisdethiobis(methylthio)gliotoxin (**5**) in the extract of CBS 139183<sup>T</sup>. Panel A shows the base peak chromatogram of an extract of CBS 139183<sup>T</sup> (top), the extracted ion chromatogram of the same extract using the m/z value for compound **5** (middle) and the retention time for a standard of compound **5** (bottom). This demonstrates a retention time match between the standard and the peak in the extracted ion chromatogram. Panel B demonstrates a match between the isotopic ratios and the accurate mass for the peak highlighted in Panel A for the extracted ion chromatogram (middle) and compound **5** (bottom). Panel C demonstrates a match between the fragmentation patterns of the peak in the base peak chromatogram (top) and a standard of **5** (bottom). In summation, these data confirm the presence of **5** in CBS139183<sup>T</sup> grown on oatmeal at 37°C. A similar process was used for all of the compounds that were identified via dereplication in this manuscript (i.e. Tables 4.5-4.7).

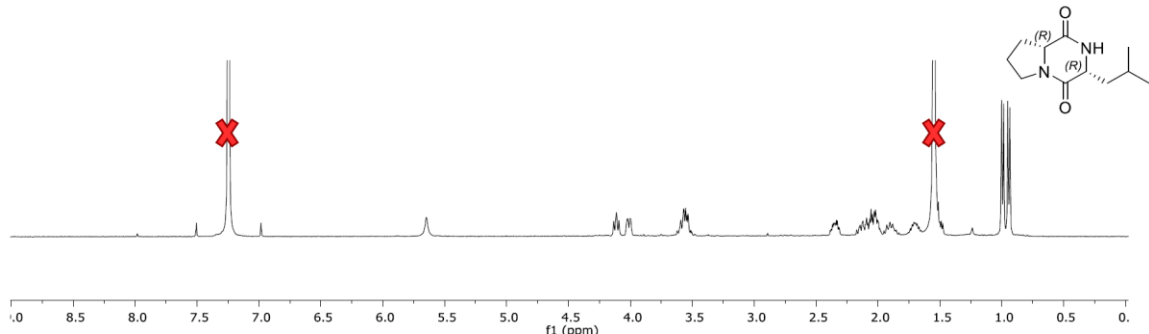


**Figure 53.** <sup>1</sup>H NMR spectrum of cyclo(L-Pro-L-Leu) (**1**) (400 MHz; CDCl<sub>3</sub>).

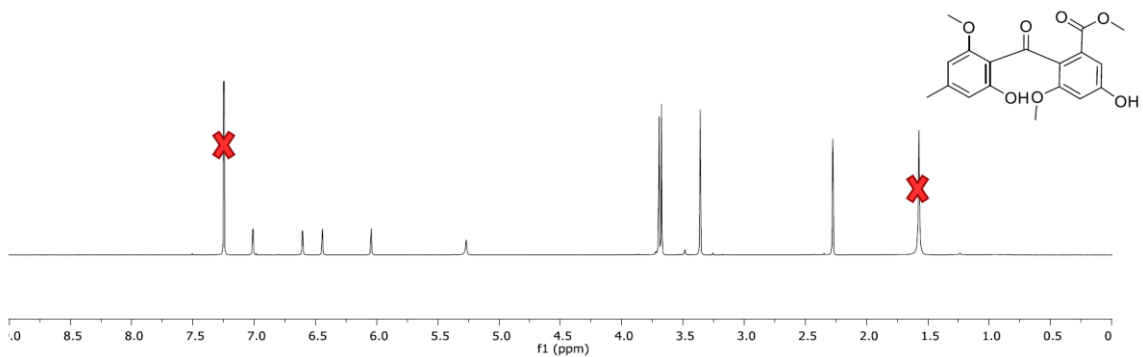


**Figure 54.**  $^1\text{H}$  NMR spectrum of monomethylsulochrin (3) (400 MHz;  $\text{CDCl}_3$ ).

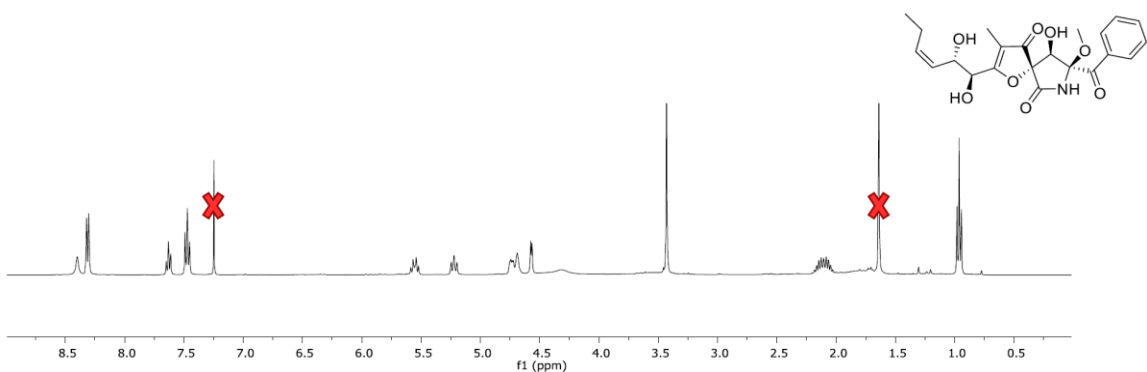


**Figure 55.**  $^1\text{H}$  NMR spectrum of pseurotin A (4) (400 MHz;  $\text{CDCl}_3$ ).

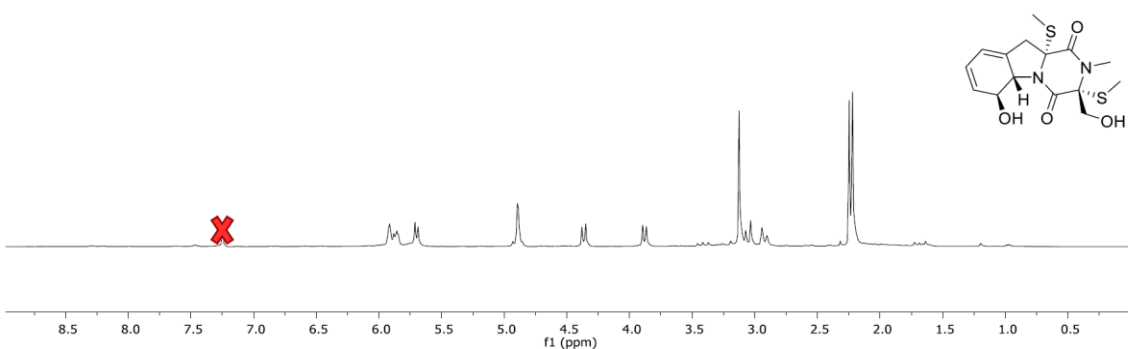


**Figure 56.**  $^1\text{H}$  NMR spectrum of bisdethiobis(methylglio)gliotoxin (5) (400 MHz;  $\text{CDCl}_3$ ).

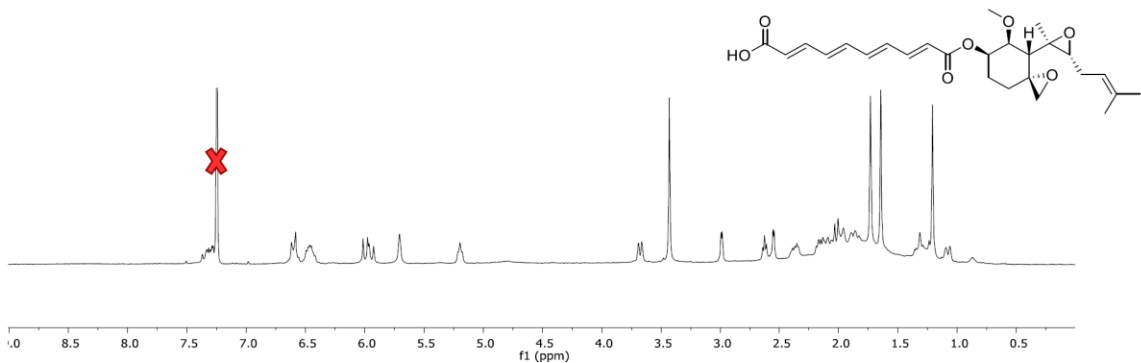


**Figure 57.** <sup>1</sup>H NMR spectrum of fumagillin (6) (400 MHz; CDCl<sub>3</sub>).

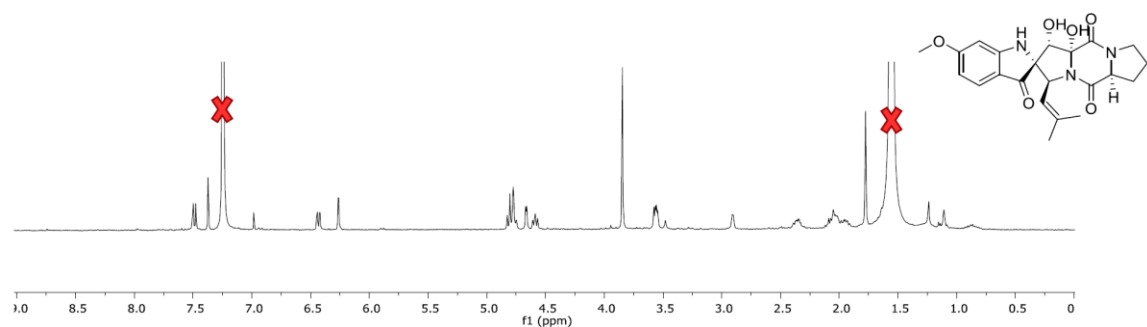


**Figure 58.** <sup>1</sup>H NMR spectrum of spiro-[5H,10H-dipyrrolo[1,2-a:1',2'-d]pyrazine-2-(3H),2'-(2H]indole]-3',5,10(1'H)-trione (8) (400 MHz; CDCl<sub>3</sub>).

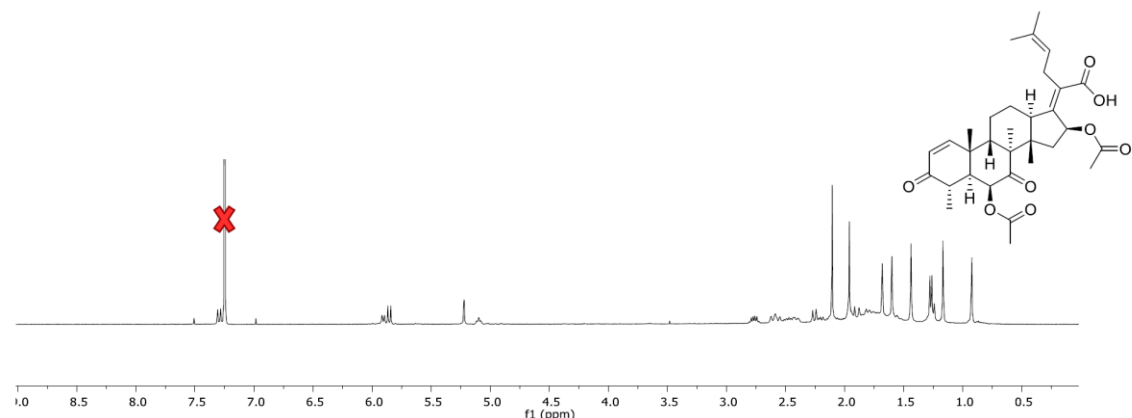


**Figure 59.** <sup>1</sup>H NMR spectrum of helvolic acid (9) (400 MHz; CDCl<sub>3</sub>).

CHAPTER V

MAPPING THE FUNGAL BATTLEFIELD: USING *IN SITU* CHEMISTRY AND  
DELETION MUTANTS TO MONITOR INTERSPECIFIC CHEMICAL INTERACTIONS  
BETWEEN FUNGI

Sonja L. Knowles, Huzefa A. Raja, Allison J. Wright, Ann Marie L. Lee, Lindsay K. Caesar, Nadja B. Cech, Matthew E. Mead, Jacob L. Steenwyk, Laure N. A. Ries, Gustavo H. Goldman, Antonis Rokas, Nicholas H. Oberlies. *Front. Microbiol.* 2019, 10, 285.

Fungi grow in competitive environments, and to cope, they have evolved strategies, such as the ability to produce a wide range of secondary metabolites. This begs two related questions. First, how do secondary metabolites influence fungal ecology and interspecific interactions? Second, can these interspecific interactions provide a way to “see” how fungi respond, chemically, within a competitive environment? To evaluate these, and to gain insight into the secondary metabolic arsenal fungi possess, we co-cultured *Aspergillus fischeri*, a genetically tractable fungus that produces a suite of mycotoxins, with *Xylaria cubensis*, a fungus that produces the fungistatic compound and FDA-approved drug, griseofulvin. To monitor and characterize fungal chemistry *in situ*, we used the droplet-liquid microjunction-surface sampling probe (droplet probe). The droplet probe makes a microextraction at defined locations on the surface of the co-culture, followed by analysis of the secondary metabolite profile via liquid chromatography-mass spectrometry. Using this, we mapped and compared the spatial profiles of secondary metabolites from both fungi in monoculture versus co-culture. *X. cubensis* predominantly biosynthesized griseofulvin and dechlorogriseofulvin

in monoculture. In contrast, under co-culture conditions a deadlock was formed between the two fungi, and *X. cubensis* biosynthesized the same two secondary metabolites, along with dechloro-5`-hydroxygriseofulvin and 5`-hydroxygriseofulvin, all of which have fungistatic properties, as well as mycotoxins like cytochalasin D and cytochalasin C. In contrast, in co-culture, *A. fischeri* increased the production of the mycotoxins fumitremorgin B and verruculogen, but otherwise remained unchanged relative to its monoculture. To evaluate that secondary metabolites play an important role in defense and territory establishment, we co-cultured *A. fischeri* lacking the master regulator of secondary metabolism *iaeA* with *X. cubensis*. We found that the reduced secondary metabolite biosynthesis of the  $\Delta iaeA$  strain of *A. fischeri* eliminated the organism's ability to compete in co-culture and led to its displacement by *X. cubensis*. These results demonstrate the potential of *in situ* chemical analysis and deletion mutant approaches for shedding light on the ecological roles of secondary metabolites and how they influence fungal ecological strategies; co-culturing may also stimulate the biosynthesis of secondary metabolites that are not produced in monoculture in the laboratory.

Fungi naturally grow in competitive environments, such as soil, plants, and animal tissues.<sup>3</sup> They have evolved a diversity of ecological strategies to combat their competitors, which include rapid growth, stress recovery, and the use and negation of inhibitors.<sup>29</sup> Interaction-driven secondary metabolite discovery (i.e. co-culturing) can exploit the ability of fungi to produce secondary metabolites that have evolved to combat various competitors. Co-culturing experiments often activate the biosynthesis of defense secondary metabolites, allowing one to "see" how fungi respond, chemically, within a competitive environment.<sup>57, 58</sup> They also provide a window to understanding fungal ecology and the ecological relevance of secondary metabolites.

Previous studies have shown that fungal genomes have a rich diversity of biosynthetic gene clusters,<sup>9, 11, 283, 284</sup> and that fungi have the potential to produce numerous chemically diverse secondary metabolites; however, a large proportion of biosynthetic gene clusters are silent under traditional laboratory culture conditions.<sup>18, 43, 47-49, 284</sup> One possibility is that only a fraction of the potential secondary metabolites are produced, likely due to fungal domestication as a result of repeated culturing at optimal media conditions. Another possibility is that the stressors that elicit the expression of certain secondary metabolites are not present.<sup>17, 284</sup>

Co-culturing is a promising approach for activating regulatory mechanisms that result in the biosynthesis of otherwise silenced secondary metabolites for targeted interaction discovery.<sup>60</sup> For example, when *Trichophyton rubrum* and *Bionectria ochroleuca* were co-cultured, there was an activation of silent biosynthetic gene clusters, as evidenced by a new secondary metabolite that was only present in the zone separating the two fungi.<sup>285</sup> It has also been shown that co-culturing two fungi can increase the quantity of certain secondary metabolites that were previously being biosynthesized.<sup>17, 62, 286</sup> A potential reason for these activations is interspecific interactions. These interactions can cause chemical cues to be exuded to the environment between two or more species competing for nutrition and space that could result in the activation of biosynthetic gene clusters.<sup>56, 287, 288</sup>

Over the last decade numerous mass spectrometry tools have been utilized to study microbial interactions *in situ* to obtain a holistic understanding of the chemical interactions between two competing microbes.<sup>289-291</sup> Most studies have explored bacterial-bacterial interactions and fungal-bacterial interactions *in situ* in a Petri plate,<sup>290-</sup><sup>293</sup> but there are a few studies that have explored the mapping and characterization of

fungal-fungal interactions *in situ*.<sup>289, 294-296</sup> One of the main issues that precludes *in situ* studies on fungi is the uneven morphology (heterogeneous topography) of fungal mycelia, which is not easily amenable to *in situ* ionization techniques without modifying the culture.<sup>3, 289, 297, 298</sup> The problem of uneven topology can be overcome by using the droplet–liquid microjunction–surface sampling probe (droplet probe).<sup>299, 300</sup> Importantly, mapping the chemical entities of fungi as they compete *in situ* can address chemical ecology questions, such as where (spatially) and when (temporally) the compounds are biosynthesized, and such data are typically lost in previous studies on co-culturing fungi through the use of a traditional chemical extraction processes.<sup>288, 301, 302</sup>

A connection has been established in the literature between the production of secondary metabolites produced by fungi and their role in ecological chemical interactions.<sup>303, 304</sup> It is well known that *laeA* (loss of *aflR* expression, with *aflR* being the regulatory gene for aflatoxin biosynthesis) is a global regulator and controls both fungal growth and development and is responsible for over 50% of secondary metabolites produced in *Aspergillus* as well as other genera.<sup>305, 306</sup> It has been reported that deletion mutants *laeA* are less pathogenic.<sup>305</sup> However, what is not known is what would happen if a *laeA* mutant of *Aspergillus fischeri* were grown in co-culture with a competing fungus. In other words, by monitoring the chemical interaction between fungi *in situ*, could a wild type and *laeA* mutant of *Aspergillus fischeri* co-cultured with another fungus help answer the role of secondary metabolites for defense? We hypothesized, based on the large body of previous literature, that since *laeA* is integral to both growth and development as well as production of secondary metabolites,<sup>305</sup> a  $\Delta/\text{laeA}$  mutant would be unable to battle with other fungi. Thus, as the chemical arsenal of the  $\Delta/\text{laeA}$  mutant is affected, this in turn would affect its ability to occupy space and survive. Such experimental studies

would help shed light on the biological roles of secondary metabolites in fungi and provide experimental evidence for the ecological role of secondary metabolites in fungi *in situ*.

In this study, we evaluated the co-culturing of two fungi, *Aspergillus fischeri* and *Xylaria cubensis*, *in situ* and observed distinct chemical profile changes resulting from the interspecific interactions between them. *X. cubensis* commonly occurs as an endophyte (endosymbiotic) and decomposer (saprobic)<sup>9</sup> and biosynthesizes the fungistatic secondary metabolite griseofulvin, an FDA-approved drug.<sup>289, 307</sup> Fungistatic denotes that it inhibits fungal growth, rather than kills competing fungi, and we hypothesized, therefore, that the resulting stress in a co-culture environment would allow us to examine how secondary metabolite production changes when the two species interact.

*Aspergillus fischeri* was chosen due to its genetic tractability and its evolutionary relatedness with *A. fumigatus*, the human pathogen.<sup>16, 308, 309</sup> It also has its own metabolite weaponry in the form of mycotoxins.<sup>16</sup> The secondary metabolites of *Aspergilli*, including *A. fischeri*, are largely controlled by the master regulator protein *IaeA*.<sup>16, 205, 306, 310, 311</sup> A deletion strain of *A. fischeri* where *IaeA* was knocked out ( $\Delta IaeA$ ) was co-cultured with *X. cubensis*. Concomitant with reduction of the biosynthesis of secondary metabolites, *A. fischeri* lost its competitive advantage, and *X. cubensis* was able to out compete it, as compared to the co-culture with wild type *A. fischeri*.

## Results

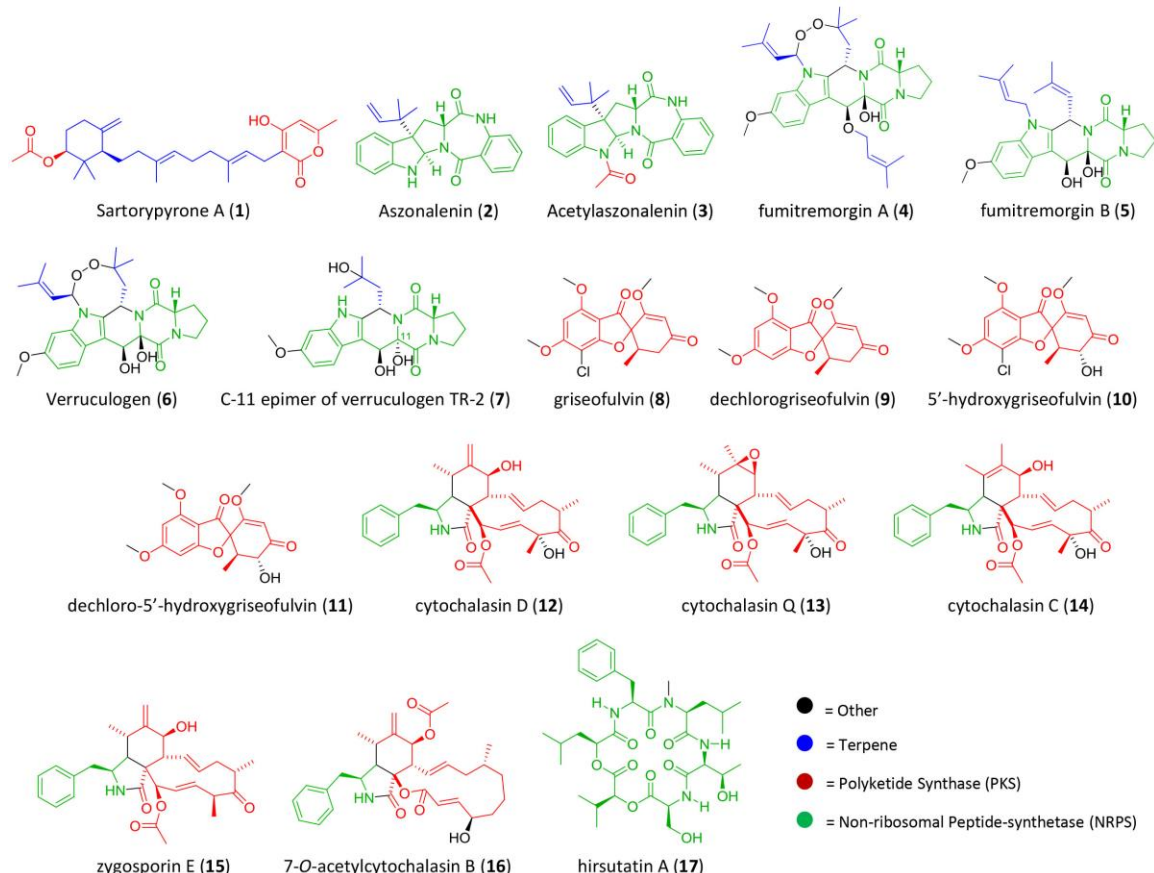


**Figure 60.** The Diversity of Secondary Metabolites Isolated from the Co-Culture of Wild Type *Aspergillus fischeri* (NRRL 181) and *Xylaria cubensis* (G536). The color of the structure indicates the different biosynthetic class of the secondary metabolites; blue = terpene, red = polyketide, green = non-ribosomal peptide, and black = other biosynthetic pathways.

**Co-culture Analysis of the Junction Between *A. fischeri* and *X. cubensis* via Droplet Probe Reveals Varied Chemical Diversity Not Present in Either Monoculture.** To obtain baseline data, the monoculture of *X. cubensis* was sampled by droplet probe, and the LC-MS base peak chromatogram only showed two peaks, which corresponded to griseofulvin (**8**) and dechlorogriseofulvin (**9**) as determined by comparison of accurate mass and retention time of a standard.<sup>188, 307</sup> Griseofulvin (**8**) and

dechlorogriseofulvin (**9**) were present in multiple spots across the mycelium, with both more concentrated at the mycelial edge. The monoculture of wild type *A. fischeri* was analyzed in an identical manner, and based on the same data analyses, sartorypyrone A (**1**), aszonalenin (**2**), acetylaszonalenin (**3**), fumitremorgin A (**4**), fumitremorgin B (**5**), verruculogen (**6**), and C-11 epimer of verruculogen TR-2 (**7**) were present (Figures 60 and 61).<sup>16</sup>

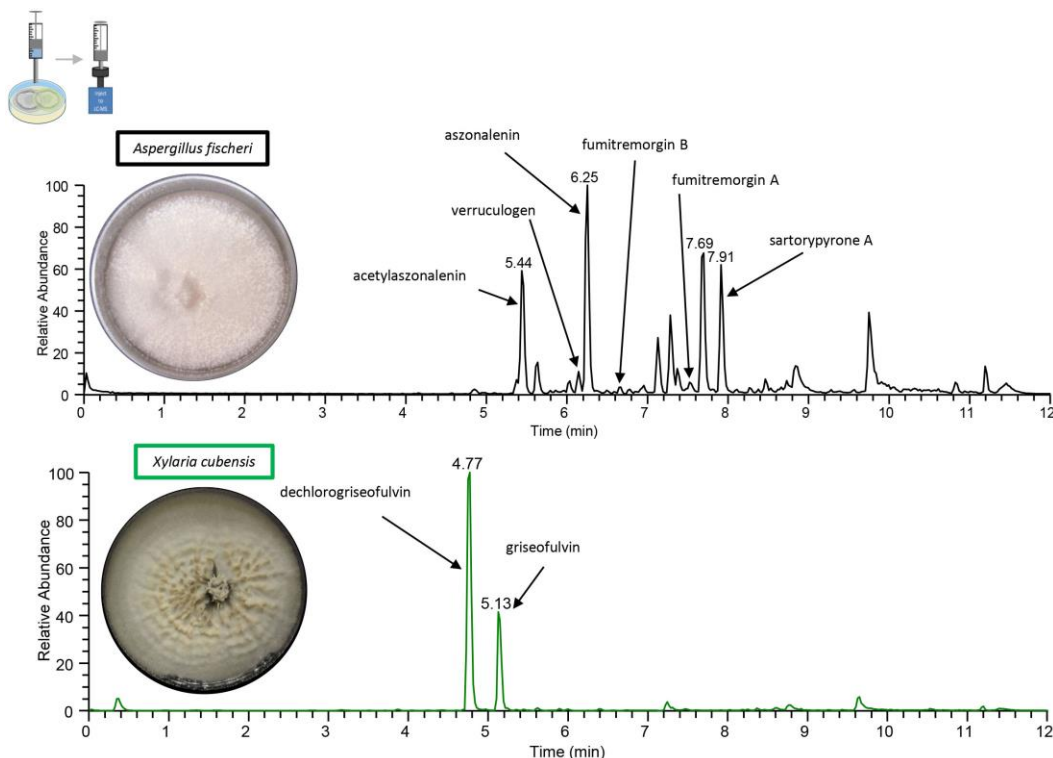


**Figure 61.** The Chromatograms from the Droplet Probe Analysis of the Monocultures, as Taken at the Mycelial Edge. Wild type *A. fischeri* (top; black) indicates the presence of sartorypyrone A (**1**), aszonalenin (**2**), acetylaszonalenin (**3**), fumitremorgin A (**4**), fumitremorgin B (**5**), and verruculogen (**6**). *X. cubensis* (bottom; green) shows dechlorogriseofulvin (**9**) and griseofulvin (**8**), which are analogues that have fungistatic ability. Only the isolated and fully characterized peaks are annotated.

**In Situ Co-Culture Analysis of *A. fischeri* and *X. cubensis* Via Droplet Probe Reveals Varied Chemical Diversity at the Junction Between the Two Fungi Not Present in the Monoculture Experiments.** A deadlock was formed in the *A. fischeri* and *X. cubensis* co-culture (Figure 62). The two fungi grew toward the middle of the plate, and at the junction where both fungal mycelia overlap, neither of the two was able to grow further. The LC-MS profile showed distinct peaks (i.e. the presence of multiple ions) in co-culture (Figure 63), some of which were absent from the monocultures.

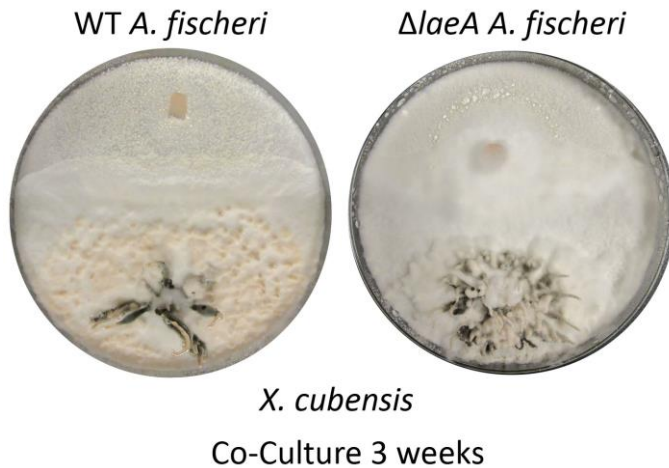


**Figure 62.** Wild Type *A. fischeri* can Form a Deadlock while  $\Delta laeA$  *A. fischeri* Gets Displaced by *X. cubensis* During the Co-Culture. The left image shows the growths of wild type *A. fischeri* and the right image shows the growths of  $\Delta laeA$  *A. fischeri* with *X. cubensis* over a three-week timeline.

Griseofulvin (**8**) and dechlorogriseofulvin (**9**) were not detected in the region of the co-culture where only *X. cubensis* mycelia were growing, however, both of these compounds were detected at the junction. Alternately, the monoculture had more accumulation of griseofulvin (**8**) and dechlorogriseofulvin (**9**) at the colony edge, but these compounds were present throughout the mycelia. The co-culture of wild type *A. fischeri* had the same secondary metabolites present as the monoculture. However,

secondary metabolite production was altered during co-culturing (Figure 63). For example, verruculogen (**6**) and fumitremorgin B (**5**) showed an average increase in production of about 2 and 2.5 orders of magnitude, respectively, relative to their production in monoculture across three biological replicates *in situ*.

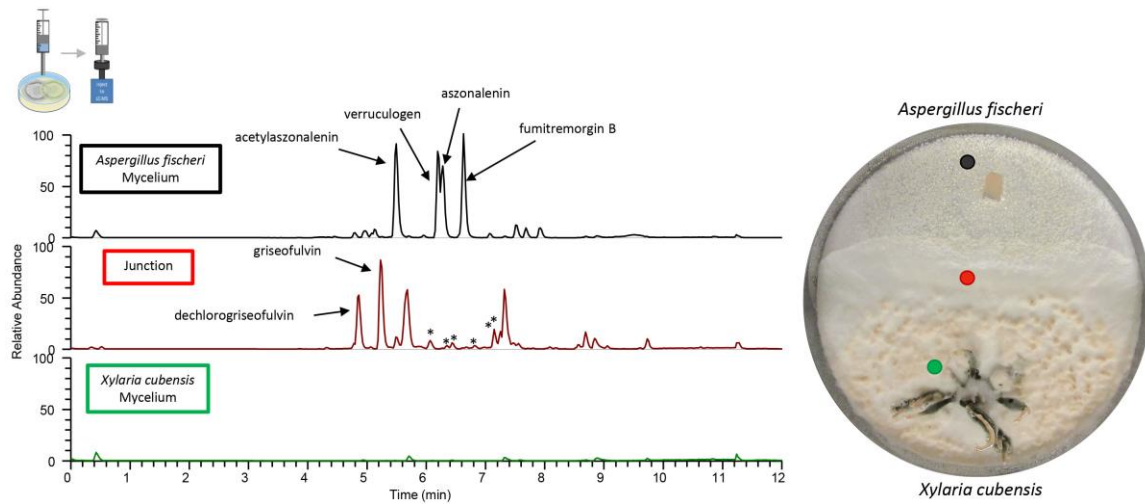


**Figure 63.** Co-Culture Produces Greater Diversity of Secondary Metabolites Over That of the Monocultures. The chromatograms from the droplet probe analysis of the co-cultures shows only three out of the eight spots examined are shown here, with the corresponding colored dot indicating the location at which the mycelium was sampled. Wild type *A. fischeri* (Top) showed the presence of the secondary metabolites as seen in monoculture (Figure 61); however, there were differences in the relative abundance of the mycotoxins such as verruculogen and fumitremorgin B during their growth in co-culture. The junction (middle) where both fungal mycelia interact revealed the presence of griseofulvin and dechlorogriseofulvin, which were not present anywhere else in the co-culture. It also indicated the presence of secondary metabolites that were not present in the monoculture growths of either of the two fungi (asterisks). *X. cubensis* (bottom) did not show the presence of the two previously present secondary metabolites (griseofulvin and dechlorogriseofulvin), nor did it show the presence of any secondary metabolites.

**Large-Scale Fermentation of Co-Culture Indicated the Activation of Previously Silent Secondary Metabolites.** To isolate and elucidate the structures of newly found secondary metabolite peaks in the junction between the two fungal species in the co-culture experiment, a large-scale fermentation of *X. cubensis* and wild type *A.*

*fischeri* as a mixed co-culture on solid media was executed. The fungal growth was extracted and purified to isolate compounds that were characterized. In the co-culture griseofulvin (**8**) and dechlorogriseofulvin (**9**),<sup>307</sup> which were present in the monoculture, were isolated, as were the two analogues 5'-hydroxygriseofulvin (**10**) and dechloro-5'-hydroxygriseofulvin (**11**),<sup>307</sup> which were not observed in monoculture (Figures 79-82). The mycotoxins cytochalasin D (**12**),<sup>312</sup> cytochalasin Q (**13**),<sup>188</sup> cytochalasin C (**14**), zygosporin E (**15**),<sup>313, 314</sup> and 7-O-acetylcytochalasin B (**16**),<sup>315</sup> (Figure 64) were observed in monoculture, albeit at extremely low concentrations that did not afford structural characterization. However, under co-culture conditions, they increased in abundance to an extent that afforded isolation and full structural characterization (Figures 83-86). Finally, hirsutatin A (**17**),<sup>316</sup> which was not detected in the monoculture, was isolated and characterized in the large-scale co-culture (Figure 87).

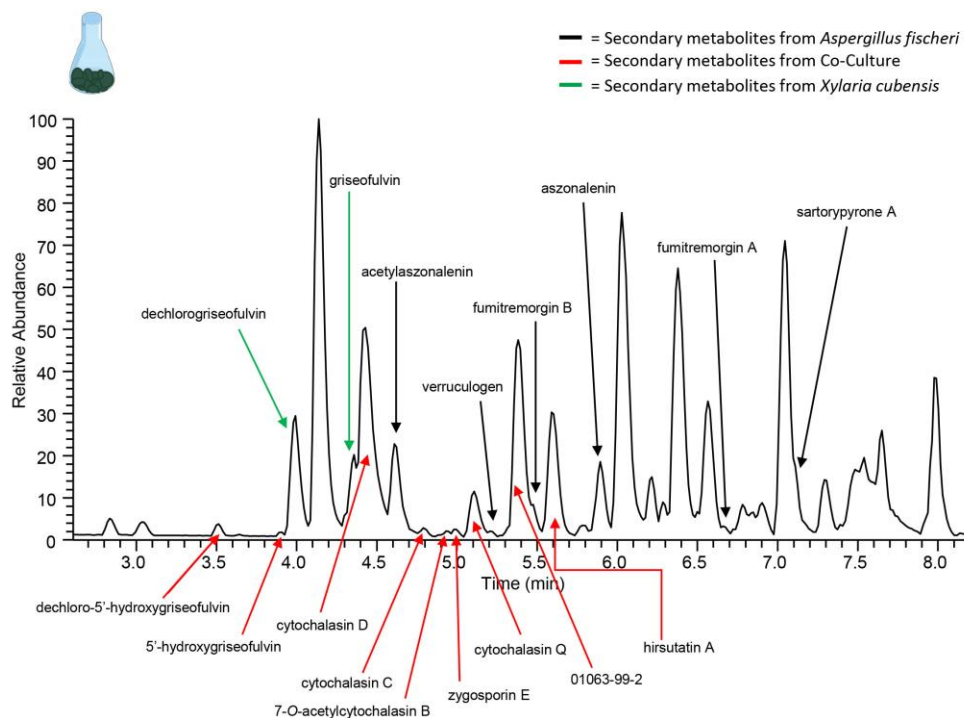


**Figure 64.** Increase in Chemical Diversity in the Co-Culture Caused the Characterization of Secondary Metabolite Not Seen in Monoculture. The chromatogram produced from the large-scale extraction of mixed co-culture. Black arrows indicate the secondary metabolites from the monoculture of wild type *A. fischeri*; green arrows indicate the secondary metabolites from the monoculture of *X. cubensis*; and red arrows indicate the secondary metabolites isolated from the co-culture of wild type *A. fischeri* and *X. cubensis*.

### Metabolomics Analyses Shows Different Chemical Entities in the

**Monoculture Versus Co-Culture.** Comparison of metabolite profiles is often achieved using multivariate statistical modeling protocols such as principal component analysis (PCA)<sup>317</sup>. To determine the degree of difference between the metabolite profiles observed during the large-scale mono or co-culture, PCA scores and loadings plots were generated (Figures 65a and 65b). Untargeted metabolomics analyses of fungal samples using LC-MS yielded 2111 features (unique *m/z*-retention time pairs) for 60 samples (five biological replicates of *X. cubensis*, *A. fischeri*, and the co-culture of the two fungal organisms, all analyzed in quadruplicate). Examination of these plots illustrated that clusters of *X. cubensis*, *A. fischeri*, and the co-culture of the two organisms were clustered distinctly in the PCA plot, which accounted for 89.9% of the variability among samples (PC1=69.4%, PC2=20.5%) (Figure 65a).

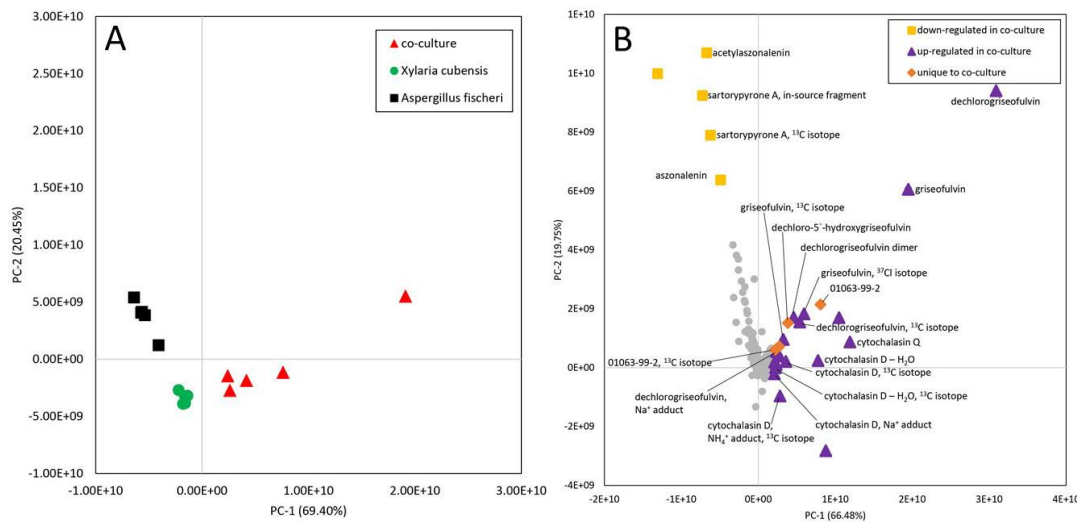


**Figure 65a.** Principal component analysis (PCA) scores plot of fungal samples shows distinct differences between the co-culture and monocultures. Five biological replicates of each sample type are plotted using peak area data for each sample that was an average of four injections (four technical replicates). Distinct clusters were observed between *X. cubensis*, *A. fischeri*, and co-cultured organisms. **Figure 65b.** Loadings plot from untargeted mass spectrometry based PCA of fungal samples shows the presence of unique and upregulated secondary metabolites in the co-culture. Metabolites with positive values along the horizontal axis were more heavily represented in co-cultures than monocultures or were unique to the co-culture entirely. Yellow squares = compounds that were detected at a lower abundance in the co-culture than in the monoculture of *Aspergillus fischeri*. Purple triangles = compounds that showed increased production in the co-culture and were produced by one or both fungi (Table 5.1). Orange diamonds = compounds that were only detected in co-culture samples. Gray circles = compounds that do not contribute to the difference between the cultures. Metabolites were identified following isolation using a combination of mass spectral and NMR data. In cases where compounds were of too low abundance to be isolated, comparisons were made against the literature using *m/z* values from high-resolution mass spectrometry data. Identifications based on mass alone, without purification, are tentative.

To evaluate which compounds contributed to the separation between groups, the PCA loadings plot was inspected (Figure 65b) using averaged data from both biological and technical replicates. Inspection of principal component loadings enables identification of variables that are responsible for the observed groupings in the PCA scores plot; the more a given variable diverges from other variables in the loadings plot, the more it contributes to the separation between groups in the scores plot. The two

components utilized for this loadings plot explained 86.2% of the variability among samples (PC1=66.5%, PC2=19.8%). In this plot, compounds were identified as those that were 1) more abundant in the co-culture, 2) less abundant in the co-culture, and 3) unique to the co-culture (Table 5.1). Metabolites with positive values along the x-axis, including griseofulvin analogues, cytochalasins, and a compound with a novel chemical scaffold (sample ID 01063-99-2) were detected in greater abundance in co-culture than in monocultures (purple triangles), or were completely unique to the co-culture (orange diamonds), and are responsible for the shift observed of the co-culture samples in the PCA scores plot.

#### **Genome Mining Implicates *X. cubensis* as the Species Producing**

**Cytochalasin During the Co-Culture.** To determine whether *A. fischeri* or *X. cubensis* produced the cytochalasin congeners isolated from the co-culture, a combination of genome mining and mass spectrometry was used. Cytochalasins are a wide structural class of mycotoxins and are very common in Xylariales species.<sup>318-321</sup> To attempt to determine which organism was producing cytochalasin D during the co-culture experiment, we searched for genes orthologous to a previously described biosynthetic gene cluster responsible for cytochalasin E production in *Aspergillus clavatus*.<sup>322</sup> A putative cytochalasin cluster was not found in *A. fischeri*, and only 4 out of 8 individual cytochalasin genes were identified in the genome and they were unclustered (Table 5.2). Potential orthologs for the Non-ribosomal Peptide Synthase-Polyketide Synthase hybrid and enoyl reductase genes were found in a biosynthetic gene cluster in *A. fischeri* that likely produces the secondary metabolite aspyridone.<sup>16</sup> Sequencing of the genome of *X. cubensis* has not been reported, and the closest evolutionary relative that has a sequenced genome is *Rosellinia necatrix*.<sup>289, 323</sup> Upon analysis of the *R. necatrix*

genome, a complete cytochalasin gene cluster was found (Table 5.2) and led us to hypothesize that *X. cubensis* was responsible for biosynthesizing the cytochalasins isolated from the batch co-culture. Furthermore, un-isolatable amounts of the cytochalasins were detected by mass spectrometry in the mono-culture of *X. cubensis*, thus supporting our hypothesis that the cytochalasins were most likely biosynthesized by *X. cubensis* during co-culture.

***In situ Analysis of a Co-Culture Between  $\Delta$ laeA A. fischeri and X. cubensis Reveals the Ecological Importance of Secondary Metabolites in Interspecies***

**Chemical Interactions.** A less diverse secondary metabolite profile was observed in  $\Delta$ laeA *A. fischeri* compared to the wild type *A. fischeri*, while the growth rates between the strains was equivalent.<sup>16</sup> Mycelial displacement was observed when  $\Delta$ laeA *A. fischeri* was grown with *X. cubensis*. Once the junction was formed (about two weeks), *X. cubensis* continued to grow and took up more territory from the  $\Delta$ laeA *A. fischeri*. After three weeks the mycelium of  $\Delta$ laeA *A. fischeri* had been covered by *X. cubensis* (Figure 62).

**Discussion**

In this study, we performed the chemical analysis of two fungi, *Aspergillus fischeri* and *Xylaria cubensis*, under both monoculture and co-culture conditions to characterize the secondary metabolites produced by these fungi using both *in situ* analysis with droplet probe as well as large-scale fermentation (Figure 66). Specifically, we found that the secondary metabolites identified by comparing the analytical profiles in monoculture were different than those observed from co-culture *in situ* (Figures 61 and 63). In co-culture, the signals for secondary metabolites present at the junction, or the region of conflict zone<sup>324</sup>, appeared to be unique and were formed as a result of the interspecies

cross talk between the two fungi (Figure 63). We also found that when wild type *A. fischeri* was co-cultured with *Xylaria cubensis*, a junction or conflict zone was formed. However, when  $\Delta$ laeA *A. fischeri* was co-cultured with *X. cubensis*, the conflict zone was disturbed and  $\Delta$ laeA *A. fischeri* was displaced by *X. cubensis* (Figure 62). When *X. cubensis* and wild type *A. fischeri* were co-cultured in large-scale, so as to isolate and characterize the compounds, we showed an increase in chemical diversity, including a putative novel scaffold, suggesting the co-culture stimulated cryptic biosynthesis in one or both fungi (Figure 64).

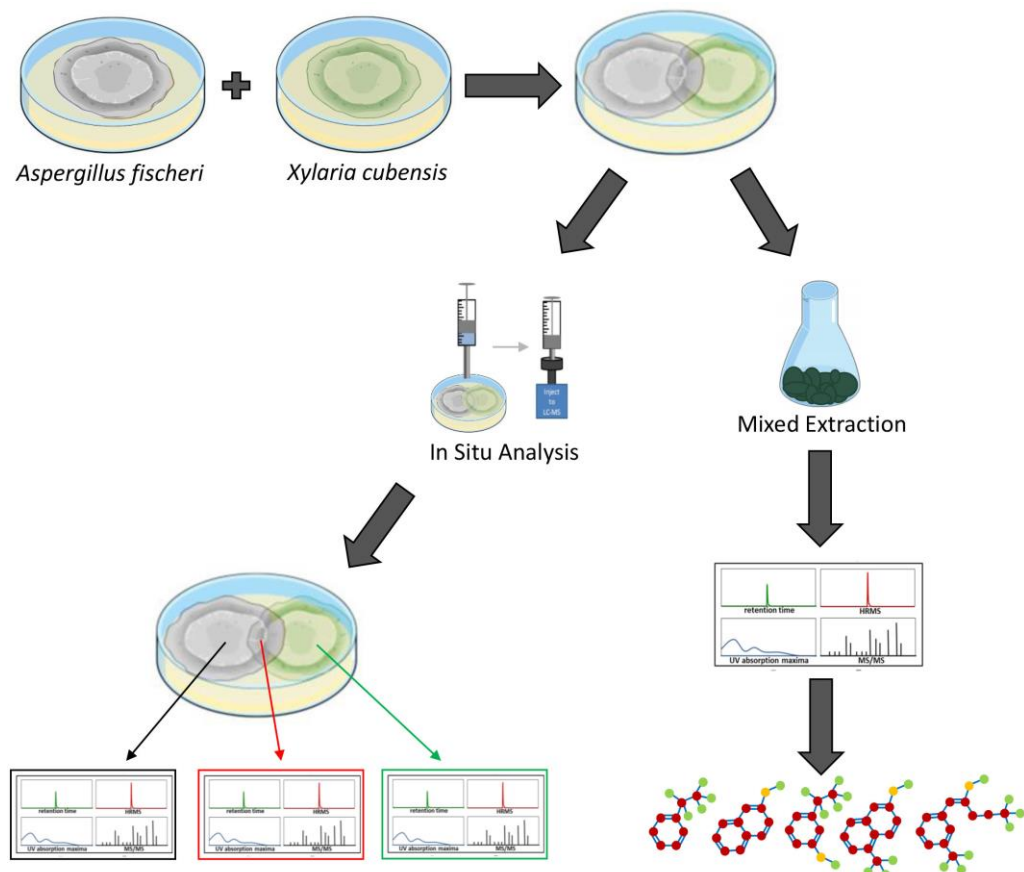


**Figure 66.** Overview of How the Secondary Metabolites Biosynthesized During the Monoculture and Co-Culture Were Analyzed. *Aspergillus fischeri* (NRRL 181) and *Xylaria cubensis* (G536) were grown as monocultures in separate Petri plates before they were co-cultured. The co-culture and monocultures are then analyzed (left) via *in*

*situ* microextractions where spatial mapping was performed, which provides a map of how the secondary metabolites are distributed along the co-culture landscape in the Petri plate. Large-scale fermentation (mixed culture; right) where both fungi were transferred together onto solid fermentation media in 250 mL Erlenmeyer flasks and the co-culture was allowed to grow for 3-4 weeks. Subsequently the cultures were extracted with organic solvents using standard natural product extraction and characterization protocols

*In situ* analysis of co-culture between wild type *A. fischeri* and *X. cubensis* reveals that chemistry not previously observed in monocultures was produced at the junction or conflict zone in interspecies chemical interactions. Most studies of fungi-fungi co-culture or fungi-bacteria co-culture demonstrate that when two microbes are co-cultivated, new chemical compounds are biosynthesized by one or both microbes as a result of some interspecies interaction or interspecies cross talk.<sup>325</sup> Using droplet probe, we observed new chemical profiles at the junction between the two-competing species (Figure 63). A similar result was found in a co-culture study between *Aspergillus nidulans* with *Streptomyces hygroscopicus*,<sup>326</sup> which reported the physical interaction and close contact between *S. hygroscopicus* and *A. nidulans* stimulated the production of aromatic polyketides. Another recent study, which performed *in situ* mapping using MALDI-imaging-HRMS, demonstrated the increased production of prodigiosin produced by endophytic *Serratia marcescens* when grown in co-culture with endophytic fungi,<sup>290</sup> where higher amounts of prodigiosin were produced at the contact site between the fungal and bacterial cultures. Thus, by sampling fungi and their surrounding environment, *in situ* methods have the ability to map the location of fungal metabolites. The ability to map chemical diversity of secondary metabolites *in situ* provides an ability to probe biological questions directly, such as why the fungus produces such compounds and how they are spatially distributed. Determining whether a compound is

produced for defense, communication, attraction, or other purposes, can be explored via these mapping experiments.<sup>289, 298</sup>

*In situ* visualization of griseofulvin production in monoculture versus co-culture was different, due to the differential accumulation of griseofulvin (**8**), suggesting how antagonistic or combative species use allelochemicals for attack on other microbes to break through the conflict zone. Griseofulvin is an antifungal compound that can be classified as an allelochemical (allomone), which is implicated in interspecies interactions that can benefit the producing organism, but not the receiving one.<sup>289, 307, 327</sup> The question of how fungi protect themselves from such armaments is often pondered. They seem to have at least three specific mechanisms to do so, including the up regulation of efflux transporters, detoxifying enzymes, and duplicate copies of the target protein.<sup>284, 328, 329</sup>

Furthermore, our study provides a striking visualization of how fungi use secondary metabolites during interspecies interactions. We demonstrate that when *X. cubensis* is grown in monoculture and sampled via droplet probe, griseofulvin (**8**) and dechlorogriseofulvin (**9**) are present in the mycelium but mostly towards the outer edge of the growing colony (Figure 61). This was observed in three biological replicates *in situ*, indicating that *X. cubensis* may be marshaling these fungistatic allelochemicals to the front line of the “battlefield”. Similarly, previous literature also reports that when *X. cubensis* is grown in co-culture with *Penicillium restrictum*, that the majority of griseofulvin was exuded to the colony edge,<sup>289</sup> thus suggesting it makes the antifungal compound but does not keep it inside its own mycelium, perhaps protecting itself via enhancement of efflux.<sup>284, 328</sup> In the present study, we see that in fact there is no trace of antifungal compound in the mycelium of *X. cubensis* in co-culture (Figure 63). Rather,

we observe that several fungistatic antifungal compounds (griseofulvin (**8**), dechlorogriseofulvin (**9**), and two analogues 5`-hydroxygriseofulvin (**10**) and dechloro-5`-hydroxygriseofulvin (**11**)) are sent out towards the junction where the two species have formed a deadlock or conflict zone (Figures 62 and 63). Thus, the *in situ* experiments demonstrate how *X. cubensis* is using its secondary metabolite arsenal to stop the growth of wild type *A. fischeri*.

Overproduction of griseofulvin has also been reported in guttates from *X. cubensis*, when it was grown in media enriched with the antifungal compound amphotericin B.<sup>330</sup> Our spatial study of griseofulvin and its analogues using droplet probe provides experimental evidence that in more complex environments, such as co-cultures, the location and the amounts of key secondary metabolites (i.e. griseofulvin and analogues) are both up regulated as well as outwardly extruded towards the competing fungal species. In a previous study, we also found that when *Coniolariella* spp., which is known to produce the herbicidal compound mevalocidin,<sup>331</sup> were examined by droplet probe, the secondary metabolites were concentrated in the guttates and in the surrounding media.<sup>332</sup> These data confirm our observation in the present study that antagonistic compounds are extruded outwardly towards the receiving organism for maximum benefit to the producing organism. Together, our results suggest that both the amounts and spatial distributions of secondary metabolites can vary during interspecies interactions.

When wild type *A. fischeri* and *X. cubensis* were grown together, a deadlock was formed (Figure 62), where neither fungus was able to capture territory from the other.<sup>333</sup> Even though *X. cubensis* was able to biosynthesize secondary metabolites that stunt the growth of the competing fungus, *A. fischeri* was most likely able to compete due to the

presence of its secondary metabolite arsenal, such as the fumitremorgin class of alkaloids (**4-7**). Droplet probe analysis of the co-culture of wild type *A. fischeri* and *X. cubensis* *in situ* suggested that no new secondary metabolites were biosynthesized by wild type *A. fischeri* (Figure 63). However, in the three spatial locations sampled in the co-culture where there was only *A. fischeri* mycelium, there was a relative change in the relative abundance of the mycotoxins produced. For example, the relative abundance of the mycotoxins verruculogen (**6**) (on average 99-fold) and fumitremorgin B (**5**) (on average 156-fold) increased in co-culture versus monoculture, as seen by the area under the curve. This was observed across three separate biological replicates *in situ*, suggesting that *A. fischeri* increased the abundance of its mycotoxin biosynthesis to better compete with *X. cubensis*.<sup>334, 335</sup>

Manipulating global transcriptional regulators may shed light on the biosynthesis of secondary metabolites in fungi.<sup>336</sup> The deletion mutant of *laeA* provides support to the notion that secondary metabolites are akin to a fungal arsenal;<sup>11</sup> if they are no longer available to the fungus, it loses the space, and eventually the battle, during interspecies interactions. *LaeA* is an important regulator of secondary metabolism in *Aspergillus* spp..<sup>205, 305</sup> We confirmed this observation in *A. fischeri*, when we studied the chemical profiles of  $\Delta laeA$  *A. fischeri*.<sup>16</sup> Our results found that the majority of the secondary metabolites produced by the wild type strain were produced at a lower abundance in the  $\Delta laeA$  *A. fischeri*.<sup>16</sup> Based on those findings we hypothesized that because the  $\Delta laeA$  strain has a perturbed secondary metabolite arsenal, it would be unable to compete with griseofulvin producing *X. cubensis*. When the  $\Delta laeA$  strain was co-cultured with *X. cubensis*, the conflict zone was disturbed, and  $\Delta laeA$  *A. fischeri* was displaced by outward production of griseofulvin and its analogues by *X. cubensis* (Figure 62). Our

study thus provides visual evidence using *in situ* mapping that fungi utilize secondary metabolites in order to compete ecologically with other microbes for nutrition and space. We hypothesize here that if the chemical diversity of secondary metabolites is perturbed ( $\Delta laeA$  *A. fischeri*), it could lead to loss of small molecules, the loss of territory, and defeat in the fungal battlefield during interspecies interactions.<sup>337</sup> Further studies using genetic knock outs are however, necessary to provide further support of our hypothesis.

Previously silenced secondary metabolites are expressed in co-culture during stressful conditions, likely due to the activation of silent genes.<sup>17, 325, 326, 338, 339</sup> Because Petri plates with nutrient agar produce a low yield, particularly when only a small portion of the plate has the chemistry of interest (i.e. the junction), a scale up study was conducted to enhance the amounts of secondary metabolites. The scale up allowed for characterization of the newly activated secondary metabolites (Figure 64), as well as the secondary metabolites previously present (Figure 61). It confirmed the presence of compounds **1 - 7** from *A. fischeri*, as well as compound **8** and **9** in *X. cubensis*. It also showed the activation of griseofulvin analogues (compounds **10** and **11**), all of which have fungistatic properties. Similarly, the biosynthesis of cytochalasin mycotoxins were activated in co-culture conditions, and hirsutatin A (**17**) was also isolated from the mixed co-culture.<sup>316</sup> This compound has only been reported from an insect pathogenic fungus *Hirsutella nivea* (Hypocreales, Ascomycota), but never from *A. fischeri* nor *X. cubensis*. There is no biosynthetic gene cluster linked to this metabolite, but with a trace amount being detectable in the monoculture of *X. cubensis*, we hypothesize that it may have biosynthesized this secondary metabolite. The activation of these defensive secondary metabolites during co-culturing was most likely due to the signaling and threat

assessment that occurred between the two fungi, suggesting that hirsutatin A (**17**) provides *X. cubensis* with some sort of competitive advantage.

Among the new signals present in the chromatographic profile of the large-scale co-culture, we were pleased to find an unknown peak (01063-99-2; Figure 64), which upon chemical characterization revealed a novel chemical scaffold suggesting that co-culturing of the two cultures in large-scale resulted in the stimulation of cryptic biosynthetic gene clusters in one or both fungi. The complete chemical characterization and identification of the producer strain of the unknown peak is currently ongoing. Numerous previous studies have found new chemistry in large-scale co-culture fermentations.<sup>56, 286, 340, 341</sup>

## Materials and Methods

**General Experimental Procedures.** The NMR data were collected using a JOEL ECS-400 spectrometer, which was equipped with a JOEL normal geometry broadband Royal probe, and a 24-slot autosampler, and operated at 400 MHz for <sup>1</sup>H and 100 MHz for <sup>13</sup>C, a JOEL ECA-500 spectrometer operating at 500 MHz for <sup>1</sup>H and 125 MHz for <sup>13</sup>C (Both from JOEL USA, Inc.), or an Agilent 700 MHz spectrometer (Agilent Technologies), equipped with a cryoprobe, operating at 700 MHz for <sup>1</sup>H and 175 MHz for <sup>13</sup>C. HRMS experiments utilized either a Thermo LTQ Orbitrap XL mass spectrometer or a Thermo Q Exactive Plus (Thermo Fisher Scientific); both were equipped with an electrospray ionization source. A Waters Acquity UPLC (Waters Corp.) was utilized for both mass spectrometers, using a BEH C<sub>18</sub> column (1.7 μm; 50 mm x 2.1 mm) set to a temperature of 40°C and a flow rate of 0.3 ml/min. The mobile phase consisted of a linear gradient of CH<sub>3</sub>CN-H<sub>2</sub>O (both acidified with 0.1% formic acid), starting at 15% CH<sub>3</sub>CN and increasing linearly to 100% CH<sub>3</sub>CN over 8 min, with a 1.5 min hold before

returning to the starting condition. The HPLC separations were performed with Atlantis T3 C<sub>18</sub> semi-preparative (5 µm; 10 x 250 mm) and preparative (5 µm; 19 x 250 mm) columns, at a flow rate of 4.6 ml/min and 16.9 ml/min, respectively, with a Varian Prostar HPLC system equipped with a Prostar 210 pumps and a Prostar 335 photodiode array detector (PDA), with the collection and analysis of data using Galaxie Chromatography Workstation software. Flash chromatography was performed on a Teledyne ISCO Combiflash Rf 200 and monitored by both ELSD and PDA detectors.

**Isolation and Identification of *Aspergillus fischeri* and *Xylaria cubensis*.**

*Aspergillus fischeri* strain NRRL 181 was obtained from ARS Culture Collection (NRRL).<sup>16</sup> The *A. fischeri* ΔlaeA mutant was prepared using methods outlined previously.<sup>16</sup> *Xylaria cubensis* strain G536 was isolated as an endophyte from surface sterilized twigs of *Asimina triloba* and identified using molecular methods as outlined previously.<sup>289</sup>

**Cultures of *Aspergillus fischeri* and *Xylaria cubensis* on Solid Nutrient**

**Media in Petri Plates.** *Aspergillus fischeri* and *Xylaria cubensis* were maintained on potato dextrose agar (PDA; Difco). To establish individual monocultures, an agar plug from the leading edge of the colony was cut out aseptically and transferred onto 50 mm Petri plates with oatmeal agar (OMA; Difco). Oatmeal was chosen since this condition yielded enhanced biosynthesis of secondary metabolites.<sup>16</sup> The monocultures were grown for 18 days. For co-culture, an agar plug from each of the two strains was placed approximately 40 mm apart on the Petri plate with OMA media. The Petri plates were incubated at room temperature (~22°C) for 18 days under 12-hr light/dark cycles. For both monoculture and co-culture growths, *in situ* analyses were conducted after 18 days (Figure 66).

**In situ Chemical Analysis Using Droplet Probe.** To characterize the secondary metabolic profiles of monocultures and co-cultures *in situ*, the droplet probe was used to chemically map the locations of the biosynthesized secondary metabolites. Sampling the surface of fungi *in situ* was performed using the droplet-liquid microjunction-surface sampling probe (droplet probe), using methodology detailed previously.<sup>289, 297, 299, 300, 342</sup> Briefly, it uses a CTC/LEAP HTC PAL auto-sampler (LEAP Technologies Inc.) that has been converted to an automated droplet probe system. The microextractions (~5 µl) were performed using 1:1 MeOH:H<sub>2</sub>O. The droplet was dispensed at a rate of 2 µl/s from the needle, held on the fungal surface for 2 seconds, and then withdrawn at the same rate before injecting into an LC-MS system (Figure 67). The LC-MS used a solvent system of CH<sub>3</sub>CN and H<sub>2</sub>O, with both being acidified with 0.1% formic acid. The chromatography method had a flow rate of 0.3 ml/min and a gradient of 15% to 100% CH<sub>3</sub>CN over 8 min, holding at 100% for 2 min, and returned to the starting conditions for 2 min. The surface of the fungal mycelia were sampled for secondary metabolites.

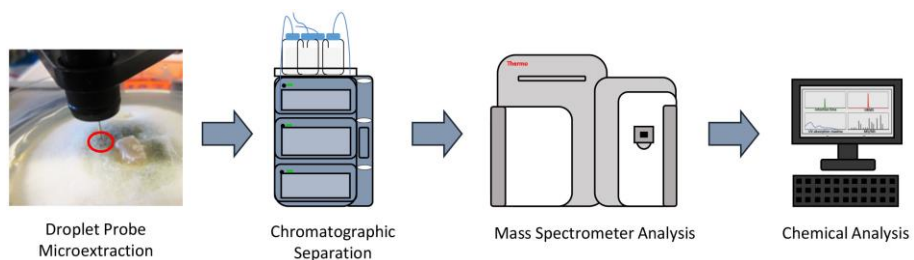


**Figure 67.** General Procedure for How the Droplet Probe Works. A microextraction using 1:1 H<sub>2</sub>O:MeOH (H<sub>2</sub>O for droplet retention and MeOH for extraction) is performed *in situ* at the desired location on the surface of the living fungal cultures. That droplet is then injected into an LC-MS system, which allows for separating and analyzing the different peaks, which correspond to different secondary metabolites.

*Xylaria cubensis* and wild type *Aspergillus fischeri* were grown side by side on OMA for 14 days. This plate was sampled spatially perpendicular to the interface of the co-culture at eight locations. Wild type *A. fischeri* was sampled in three locations. The first sampling point was the point of inoculation, and then two points were evenly spaced before the junction of the two fungal mycelia. Two spots were sampled within the junction where both fungal mycelia overlap. Two spots were sampled in the mycelium of *X. cubensis* with them being evenly distributed through the mycelium. The final location sampled was the stroma of *Xylaria cubensis* (Figure 70). This was performed on three separate Petri plates for biological replication, and the results were similar.

**Large-Scale Fermentation of *Aspergillus fischeri* and *Xylaria cubensis* Co-Cultures.** To identify the secondary metabolites that were biosynthesized during the co-culture experiment, they were grown in large-scale fermentation to isolate and characterize the secondary metabolites. To inoculate oatmeal cultures, agar plugs from *A. fischeri* and *X. cubensis* growths on PDA were cut from the edge of the cultures and transferred to separate liquid seed media that contained 10 ml YESD broth (2% soy peptone, 2% dextrose, and 1% yeast extract; 5 g of yeast extract, 10 g of soy peptone, and 10 g of D-glucose in 500 ml of deionized H<sub>2</sub>O) and cultivated at 22°C with agitation at 100 rpm for 3 (*A. fischeri*) and 5 days (*X. cubensis*). YESD seed cultures of both fungi grown individually were subsequently used to inoculate 16, 250 ml Erlenmeyer flasks that contained 10 g of autoclaved Quaker Breakfast Oatmeal each (10 g of oatmeal with 17 ml of deionized H<sub>2</sub>O and sterilized for 15–20 mins at 121°C) and grown at room temperature for 4 weeks.

**Chemical Characterization of *Aspergillus fischeri* and *Xylaria cubensis* Co-Cultures.** To characterize the secondary metabolites produced from the co-culture, the

fungal cultures underwent extraction and purification to isolate secondary metabolites. The large-scale co-culture was extracted by adding 60 ml of (1:1) MeOH–CHCl<sub>3</sub> to each 250 ml flask, chopping thoroughly with a spatula, and shaking overnight (~ 16 h) at ~ 100 rpm at 22°C. The culture was filtered *in vacuo*, and 90 ml CHCl<sub>3</sub> and 150 ml H<sub>2</sub>O were added to the filtrate. The mixture was stirred for 30 min and then transferred to a separatory funnel. The organic layer (CHCl<sub>3</sub>) was drawn off and evaporated to dryness *in vacuo*. The dried organic layer was reconstituted in 100 ml of (1:1) MeOH–CH<sub>3</sub>CN and 100 ml of hexanes, transferred to a separatory funnel, and shaken vigorously. The defatted organic layer (MeOH–CH<sub>3</sub>CN) was evaporated to dryness *in vacuo*.

The defatted extract was dissolved in CHCl<sub>3</sub>, absorbed onto Celite 545 (Acros Organics), and fractionated by normal phase flash chromatography using a gradient of hexane–CHCl<sub>3</sub>–MeOH at a 30 ml/min flow rate and 61.0 column volumes, which yielded five fractions. Fraction 1 was purified further via preparative HPLC using a gradient system 90:10 to 100:0 of CH<sub>3</sub>CN–H<sub>2</sub>O with 0.1% formic acid over 30 min at a flow rate of 16.9 ml/min to yield eight subfractions. Subfraction eight (32.74 mg), which eluted at 30 min, yielded aszonalenin (**2**) and fumitremorgin A (**4**). Fraction 2 was purified further via preparative HPLC using a gradient system 20:80 to 100:0 of CH<sub>3</sub>CN–H<sub>2</sub>O with 0.1% formic acid over 30 min at a flow rate of 16.9 ml/min to yield twelve subfractions. Subfractions 2, 3, 4, 5, 9 and 10 yielded dechloro-5'-hydroxygriseofulvin (**11**) (0.20 mg), 5'-hydroxygrisoefulvin (**10**) (0.48 mg), dechlorogriseofulvin (**9**) (0.80 mg), griseofulvin (**8**) (0.88 mg), verruculogen (**6**) (0.18 mg), and sartorypyrone A (**1**) (0.34mg), which eluted at approximately 13.4, 15.2, 15.7, 17.5, 26.1, and 30.3 min, respectively. Fraction 3 was purified further via preparative HPLC using a gradient system 40:60 to 75:25 of CH<sub>3</sub>CN–H<sub>2</sub>O with 0.1% formic acid over 30 min at a flow rate of 16.9 ml/min to yield twelve

subfractions. Subfractions 3, 4, 5, 6, 7, 8, and 12 yielded compounds cytochalasin D (**12**) (16.64 mg), acetylaszonalenin (**3**) (5.94 mg), 7-O-acetylcytochalasin B (**16**) (0.47 mg), cytochalasin C (**14**) (1.08 mg), hirsutatin A (**17**) (0.76 mg), fumitremorgin B (**5**) (0.41 mg), zygosporin E (**15**), and the C-11 epimer of verruculogen TR-2 (**7**), which eluted at approximately 13.5, 15.6, 18.5, 20.0, 24.0, 27.5, and 30.0 min, respectively. Compounds **15** and **7** co-eluted in a single fraction (18.37 mg) and were further purified via preparative HPLC using a gradient system 50:50 to 55:45 of CH<sub>3</sub>CN-H<sub>2</sub>O with 0.1% formic acid over 30 min at a flow rate of 16.9 ml/min to yield 0.65 and 1.73 mg, respectively.

**LC-MS Analysis.** To detect metabolites, LC-MS analysis was conducted in the positive ion mode. The mass spectrometer scanned across a mass range of *m/z* 200 to 2000 at a resolution of 70,000, and a spray voltage of 4,000. It was coupled to an Acquity UPLC system (Waters Corp.), which had a flow rate of 0.3 ml/min and utilized a BEH C<sub>18</sub> column (2.1 mm x 50 mm, 1.7 µm) that was operated at 40°C. The mobile phase consisted of Fisher Optima LC-MS grade CH<sub>3</sub>CN–H<sub>2</sub>O (both acidified with 0.1% formic acid). The gradient began at 15% CH<sub>3</sub>CN and linearly increased to 100% CH<sub>3</sub>CN over 8 mins. It was held at 100% CH<sub>3</sub>CN for 1.5 mins before returning to starting conditions to re-equilibrate.

**Metabolomics Analyses.** Principal component analysis (PCA) analysis was conducted on the LC-MS data obtained for the large-scale fermentations of the mono and co-cultures. Untargeted LC-MS datasets for each sample were individually aligned, filtered, and analyzed using MZmine 2.20 software (<http://mzmine.sourceforge.net/>).<sup>280</sup> Peak detection was achieved using the following parameters: noise level (absolute value), 1×10<sup>6</sup>; minimum peak duration, 0.05 min; *m/z* variation tolerance, 0.05; and *m/z*

intensity variation, 20%. Peak list filtering and retention time alignment algorithms were used to refine peak detection. The join algorithm integrated all sample profiles into a data matrix using the following parameters: *m/z* and retention time (RT) balance set at 10.0 each, *m/z* tolerance set at 0.001, and RT tolerance set at 0.5 mins. The resulting data matrix was exported to Excel (Microsoft) for analysis as a set of *m/z* – RT pairs with individual peak areas detected in quadruplicate analyses. Samples that did not possess detectable quantities of a given marker ion were assigned a peak area of zero to maintain the same number of variables for all sample sets. Ions that did not elute between 2 and 8 minutes and/or had an *m/z* ratio less than 200 or greater than 800 were removed from analysis. Final chemometric analysis, including hierarchical cluster analysis and data filtering<sup>281</sup> and PCA was conducted using Sirius version 10.0 (Pattern Recognition Systems AS).<sup>282</sup> The PCA scores and loadings plots were generated using data from five individual biological replicates of the large scale fermentations. Each biological replicate was plotted using averaged peak areas obtained across four replicate injections (technical replicates). The same number of replicate analyses were used for each monoculture and the co-culture.

**Identifying Secondary Metabolite Genes in *A. fischeri* and *X. cubensis*.** To identify which strains likely produced the secondary metabolites in co-culture we utilized the genome of *A. fischeri* and *Rosellinia necatrix*, a close evolutionary relative of *X. cubensis*.<sup>323</sup> Individual proteins from the *Aspergillus clavatus* cytochalasin E cluster were used as web-based, blastp<sup>343</sup> queries (accessed on 8-22-18) against the entire *X. cubensis* or *A. fischeri* proteomes found on the non-redundant protein sequences databases of NCBI. A Reciprocal Best BLAST approach<sup>141</sup> was performed to infer

orthology between cytochalasin cluster proteins and blast hits found in *A. fischeri* and *X. cubensis*.

## Conclusions

Fungal interactions are fascinating, but how these chemical ecology interactions occur in nature is poorly understood. This is mainly due to the frequent difficulty of measuring secondary metabolites *in situ* during fungal interactions, which hinders our understanding of what happens during chemical interaction when two fungi interact *in situ*. The droplet probe technique helped gain insight into the ecology of interspecies interactions and spatial distribution of the secondary metabolites *in situ*, information that is typically lost through a traditional extraction protocol. Our data revealed that while fungi are growing in a more complex environment (co-culture), they respond differently to interspecies interaction and alter the distribution and production of key secondary metabolites accordingly. Based on the results presented herein, we hypothesize that *ΔlaeA A. fischeri* co-culture experiments demonstrate that secondary metabolites may provide a competitive advantage to the producing fungi, and that such metabolites could play an important role in shaping interspecies chemical interactions. A total of 18 secondary metabolites were biosynthesized in large-scale co-culture. Of those metabolites, two were characterized from the monoculture of *X. cubensis* and seven were characterized from the monoculture of *A. fischeri*. Thus, nine were characterized solely from the co-culture experiment, which included a putative novel scaffold that was biosynthesized only in co-culture. If we are to understand the full extent of fungal secondary metabolites in drug discovery, and the potential role of such metabolites in structuring fungal communities in nature, *in situ* information about species interactions for a wide variety of fungi is required.

## Supplementary Data

**Table 5.1.** List of altered features in the co-culture of *X. cubensis* and *A. fischeri* analyzed by LC-MS.

Compound	Ion/retention time <sup>a</sup> (molecular formula, δ [ppm])	Adducts, fragments, and isotopes (molecular formula, δ [ppm])	Difference Among Samples	Produced by Samples
Dechlorogriseofulvin	319.118 [M+H] <sup>+</sup> /3.928 (C <sub>17</sub> H <sub>19</sub> O <sub>6</sub> <sup>+</sup> , 0.501)	320.120 [M+H] <sup>+</sup> , <sup>13</sup> C isotope (C <sub>27</sub> H <sub>19</sub> O <sub>6</sub> <sup>+</sup> , 3.124) 341.099 [M+Na] <sup>+</sup> ([C <sub>27</sub> H <sub>18</sub> O <sub>6</sub> + Na] <sup>+</sup> , 2.932) 637.228 [2M+H] <sup>+</sup> , ([2C <sub>27</sub> H <sub>18</sub> O <sub>6</sub> + H] <sup>+</sup> , 0.785)	Higher abundance in mixed co-culture	<i>X. cubensis</i> , co-culture
Unknown Metabolite A	324.209 [M+H] <sup>+</sup> /6.932 (C <sub>22</sub> H <sub>28</sub> O <sub>2</sub> <sup>+</sup> , 0.215) <sup>b</sup>		Higher abundance in mixed co-culture	<i>X. cubensis</i> , <i>A. fischeri</i> , co-culture
Unknown Metabolite B	326.305 [M+H] <sup>+</sup> /7.502 (C <sub>20</sub> H <sub>40</sub> NO <sub>2</sub> <sup>+</sup> , 0.905)		Higher abundance in mixed co-culture	<i>X. cubensis</i> , <i>A. fischeri</i> , co-culture
Dechloro-5'-hydroxygriseofulvin	335.113 [M+H] <sup>+</sup> /3.445 (C <sub>17</sub> H <sub>19</sub> O <sub>7</sub> <sup>+</sup> , 0.233)		Unique to mixed co-culture	Co-culture
Griseofulvin	353.079 [M+H] <sup>+</sup> /4.269 (C <sub>17</sub> H <sub>18</sub> ClO <sub>6</sub> <sup>+</sup> , 0.538)	354.081 [M+H] <sup>+</sup> , <sup>13</sup> C isotope (C <sub>17</sub> H <sub>18</sub> ClO <sub>6</sub> <sup>+</sup> , 4.236) 355.075 [M+H] <sup>+</sup> , <sup>37</sup> Cl isotope (C <sub>17</sub> H <sub>18</sub> ClO <sub>6</sub> <sup>+</sup> , 2.816)	Higher abundance in mixed co-culture	<i>X. cubensis</i> , co-culture
Aszonalenin	374.186 [M+H] <sup>+</sup> /5.321 (C <sub>23</sub> H <sub>24</sub> N <sub>3</sub> O <sub>2</sub> <sup>+</sup> , 2.271)		Lower abundance in mixed co-culture	<i>A. fischeri</i>
Sartorypyrone A	457.295 [M+H] <sup>+</sup> /7.054 (C <sub>28</sub> H <sub>41</sub> O <sub>5</sub> <sup>+</sup> , 1.159)	458.298 [M+H] <sup>+</sup> , <sup>13</sup> C isotope (C <sub>28</sub> H <sub>41</sub> O <sub>5</sub> <sup>+</sup> , 1.724) 397.274 [M+H-acetic acid] <sup>+</sup> ([C <sub>28</sub> H <sub>41</sub> O <sub>5</sub> -C <sub>2</sub> H <sub>4</sub> O <sub>2</sub> ] <sup>+</sup> , 0.680)	Lower abundance in mixed co-culture	<i>A. fischeri</i>
01063-99-2	413.232 [M+H] <sup>+</sup> /5.308	414.235 [M+H] <sup>+</sup> , <sup>13</sup> C isotope (C <sub>25</sub> H <sub>33</sub> O <sub>5</sub> <sup>+</sup> , 2.414)	Unique to mixed co-culture	Co-culture

	(C <sub>25</sub> H <sub>33</sub> O <sub>5</sub> <sup>+</sup> , 1.936)			
Acetylaszonalenin	416.197 [M+H] <sup>+</sup> /4.552 (C <sub>25</sub> H <sub>26</sub> N <sub>3</sub> O <sub>3</sub> <sup>+</sup> , 1.009)		Lower abundance in mixed co-culture	Co-culture, <i>A. fischeri</i>
Unknown Metabolite C	431.242 [M+H] <sup>+</sup> /5.306 (C <sub>25</sub> H <sub>35</sub> O <sub>6</sub> <sup>+</sup> , 2.226)		Unique to mixed co-culture	Co-culture
Cytochalasin D	508.269 [M+H] <sup>+</sup> /4.433 (C <sub>30</sub> H <sub>38</sub> NO <sub>6</sub> <sup>+</sup> , 1.790)	509.273 [M+H] <sup>+</sup> , <sup>13</sup> C isotope (C <sub>30</sub> H <sub>38</sub> NO <sub>6</sub> <sup>+</sup> , 0.589) 490.258 [M+H-H <sub>2</sub> O] <sup>+</sup> ([C <sub>30</sub> H <sub>38</sub> NO <sub>6</sub> -H <sub>2</sub> O] <sup>+</sup> , 2.754) 491.262 [M+H-H <sub>2</sub> O] <sup>+</sup> , <sup>13</sup> C isotope ([C <sub>30</sub> H <sub>38</sub> NO <sub>6</sub> -H <sub>2</sub> O] <sup>+</sup> , 1.486) 526.300 [M+NH <sub>4</sub> ] <sup>+</sup> , <sup>13</sup> C isotope ([C <sub>30</sub> H <sub>37</sub> NO <sub>6</sub> +NH <sub>4</sub> ] <sup>+</sup> , 0.266) 530.251 [M+Na] <sup>+</sup> ([C <sub>30</sub> H <sub>37</sub> NO <sub>6</sub> +Na] <sup>+</sup> , 1.622)	Higher abundance in mixed co-culture	<i>X. cubensis</i> , co-culture
Cytochalasin Q <sup>c</sup>	508.269 [M+H] <sup>+</sup> /5.057 (C <sub>30</sub> H <sub>38</sub> NO <sub>6</sub> <sup>+</sup> , 1.790)		Higher abundance in mixed co-culture	<i>X. cubensis</i> , co-culture
Unknown Metabolite D	508.270 [M+H] <sup>+</sup> /4.686 (C <sub>30</sub> H <sub>38</sub> NO <sub>6</sub> <sup>+</sup> , 0.177)	525.296 [M+NH <sub>4</sub> ] <sup>+</sup> , ([C <sub>30</sub> H <sub>37</sub> NO <sub>6</sub> +NH <sub>4</sub> ] <sup>+</sup> , 0.876)	Higher abundance in mixed co-culture	<i>X. cubensis</i> , co-culture
Unknown Metabolite E	496.339 [M+H] <sup>+</sup> /6.312 (C <sub>28</sub> H <sub>48</sub> O <sub>7</sub> <sup>+</sup> , 0.403)		Lower abundance in mixed co-culture	<i>A. fischeri</i>
Hirsutatin A	677.374 [M+H] <sup>+</sup> /5.514 (C <sub>34</sub> H <sub>53</sub> -N <sub>4</sub> O <sub>10</sub> <sup>+</sup> , 0.0)	694.407 [M+NH <sub>4</sub> ] <sup>+</sup>	Higher abundance in mixed co-culture	<i>X. cubensis</i> , co-culture

List of altered features in the co-culture of *X. cubensis* and *A. fischeri* analyzed by LC-MS.

<sup>a</sup> RT in minutes

<sup>b</sup> based on isotope patterns, adduct formation, and accurate mass, most likely a cytochalasin

<sup>c</sup> cytochalasin Q from in house dereplication database, which analyzes molecular weight, retention time, UV absorbance, and MS2 data.

**Table 5.2.** Putative orthologs of the cytochalasin gene cluster found in *X. cubensis* and *A. fischeri*.

<i>A. clavatus</i> Gene ID	Putative function	<i>R. necatrix</i> Protein ID	% Query Coverage	% Identity	E-value	RBBH?
ACLA_0 78640	Zn2-Cys6 Binuclear Cluster Transcription Factor	GAP 90887.2	98	38	1.00E-62	YES
ACLA_0 78650	Baeyer-Villiger monooxygenase	GAP 90886.1	94	69	0	YES
ACLA_0 78660	NRPS-PKS Hybrid	GAP 90879.1	99	64	0	YES
ACLA_0 78670	p450	GAP 90880.1	97	73	0	YES
ACLA_0 78680	a/b Hydrolase	GAP 90882.1	100	74	0	YES
ACLA_0 78690	Hypothetical Protein	GAP 90883.1	99	76	0	YES
ACLA_0 78700	Enoyl Reductase	GAP 90884.1	97	74	0	YES
ACLA_0 78710	p450	GAW 26913.1	71	58	1.00E-157	YES

**Table 5.3.** Biological replicates Area Under the Curve for Average Increase in Mycotoxins During the Co-Culture.

Sample Location	Verruculogen AUC	Fumitremorgin B AUC
Monoculture ® plate 1	4802578	3500315
Monoculture ® plate 2	1244114	364643
Average monoculture	3023346	1932479
Co-culture ® mycelium plate 1 and spot 1	271914463	96673066
Co-culture ® mycelium plate 1 and spot 2	366115822	68873847
Co-culture ® mycelium plate 1 and spot 3	71382535	26574515
Co-culture ® mycelium plate 2 and spot 1	1524267537	1693328571
Co-culture ® mycelium plate 2 and spot 2	469851785	309567783
Co-culture ® mycelium plate 2 and spot 3	345340713	64012614
Co-culture ® mycelium plate 3 and spot 1	120837062	56565051
Co-culture ® mycelium plate 3 and spot 2	590479791	78819794
Average Co-culture	470023714	299301905
Co-culture fold increase over monoculture	155.5	99.0



**Figure 68.** Wild type and  $\Delta laeA$  *Aspergillus fischeri* and *Xylaria cubensis* grown on Petri plates. **A.** Wild type *Aspergillus fischeri* (NRRL 181); **B.**  $\Delta laeA$  *Aspergillus fischeri*; **C.** *Xylaria cubensis* (G536) grown on oatmeal agar (Difco).



**Figure 69.** Co-culture growths.

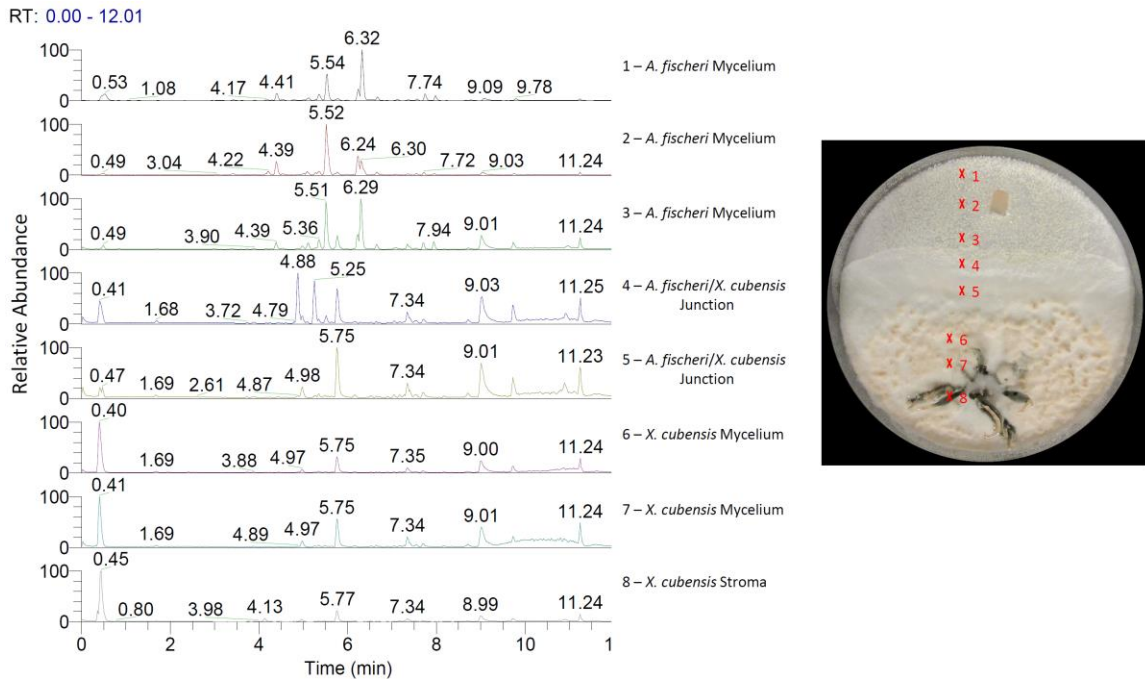


**Figure 70.** Base peak of all eight spots across the co-culture. A total of eight locations were sampled across the co-culture (three spots on *Aspergillus fischeri* mycelium, two spots at the junction, two spots on *Xylaria cubensis* mycelium, and one spot on *Xylaria cubensis* stroma). Spatial difference of secondary metabolites across the co-culture (Plate 1) is shown using stacked chromatograms.

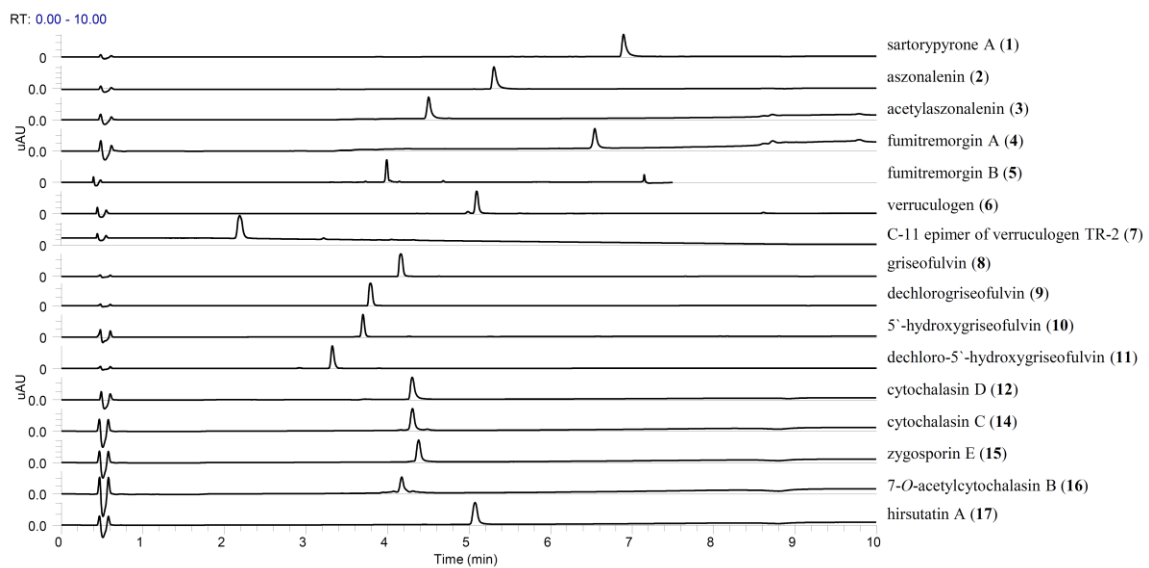


**Figure 71.** Photodiode-Array (PDA) Detector Chromatogram of secondary metabolites.

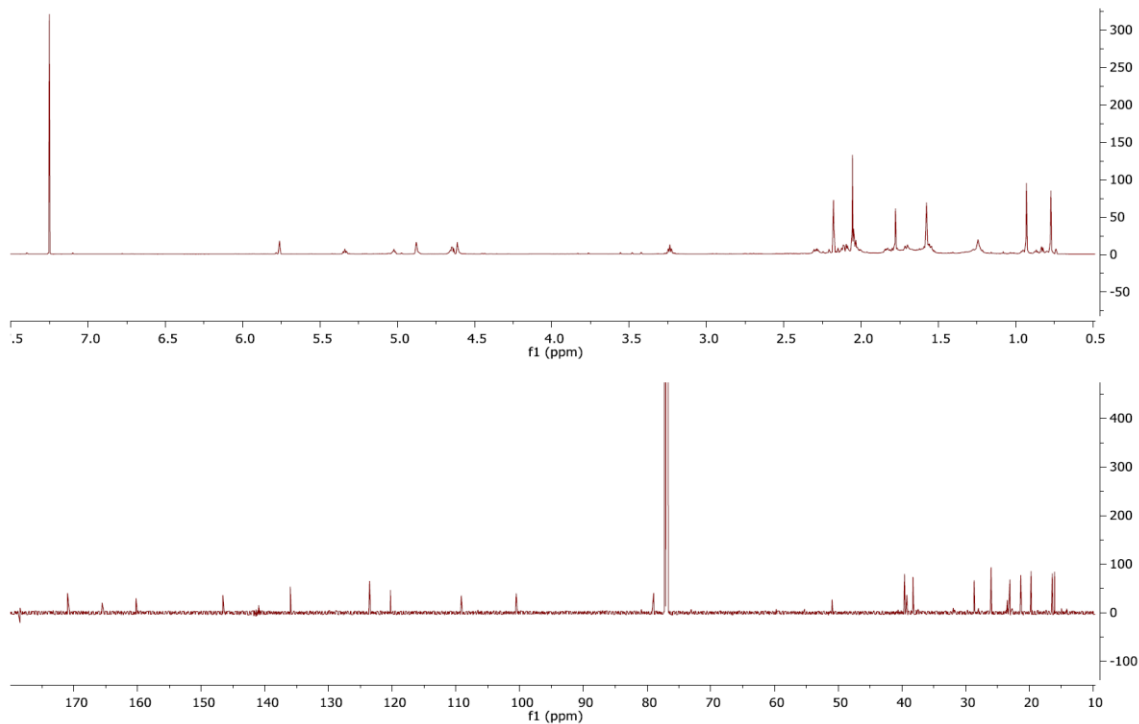


**Figure 72.**  $^1\text{H}$  NMR spectrum (700 MHz, Top) and  $^{13}\text{C}$  NMR spectrum (175 MHz, Bottom) both in  $\text{CDCl}_3$ , of sartorypyrone A (**1**).

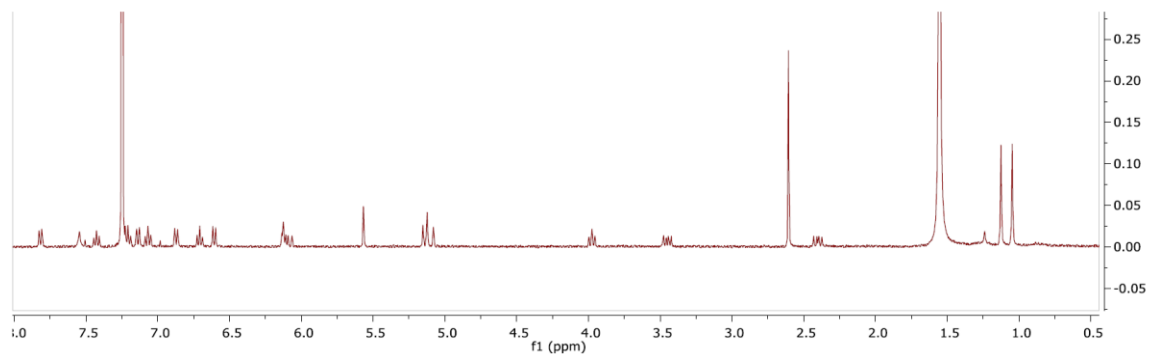


**Figure 73.**  $^1\text{H}$  NMR spectrum (400 MHz) in  $\text{CDCl}_3$ , 169cetylaszon (**2**).

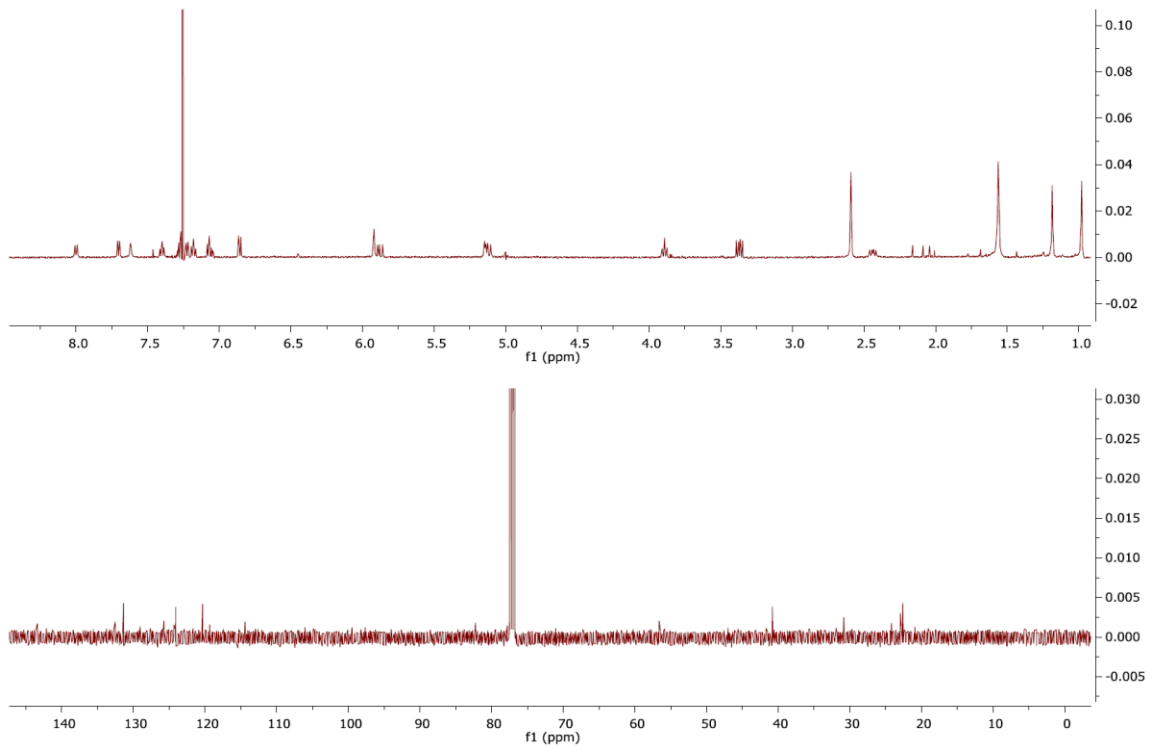


**Figure 74.**  $^1\text{H}$  NMR spectrum (500 MHz, Top) and  $^{13}\text{C}$  NMR spectrum (125 MHz, Bottom) both in  $\text{CDCl}_3$ , of 170cetylaszonalenin (**3**).

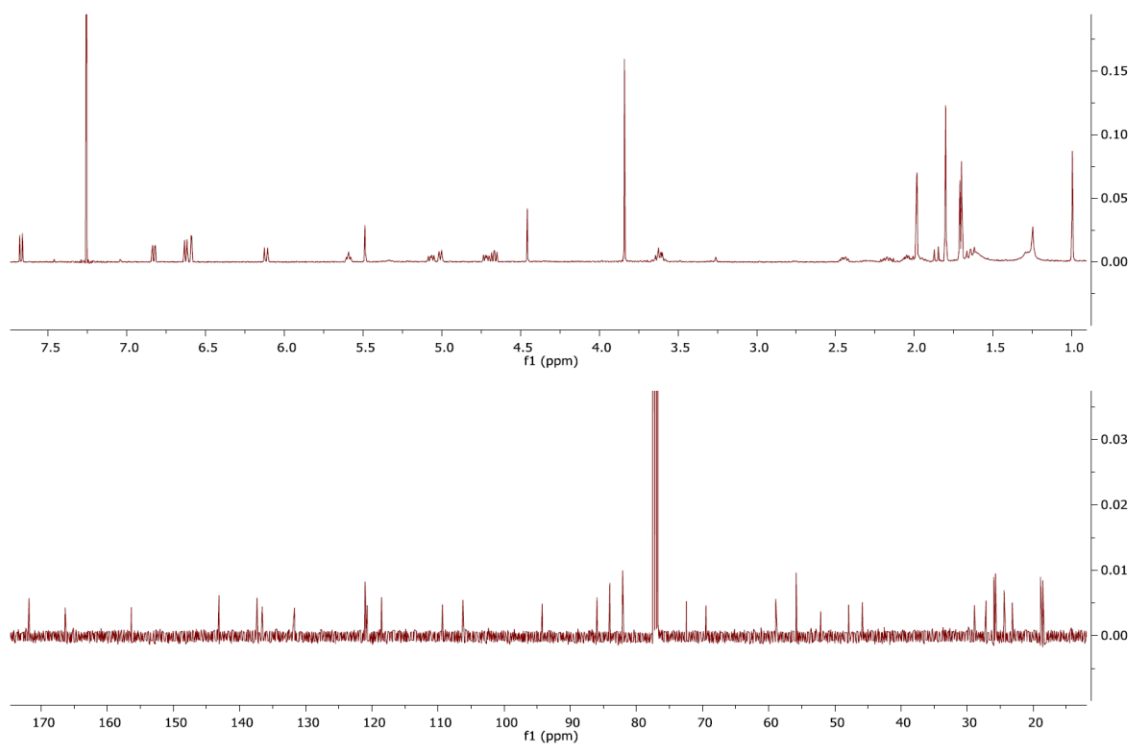


**Figure 75.**  $^1\text{H}$  NMR spectrum (500 MHz, Top) and  $^{13}\text{C}$  NMR spectrum (125 MHz, Bottom) both in  $\text{CDCl}_3$ , of fumitremorgin A (**4**).

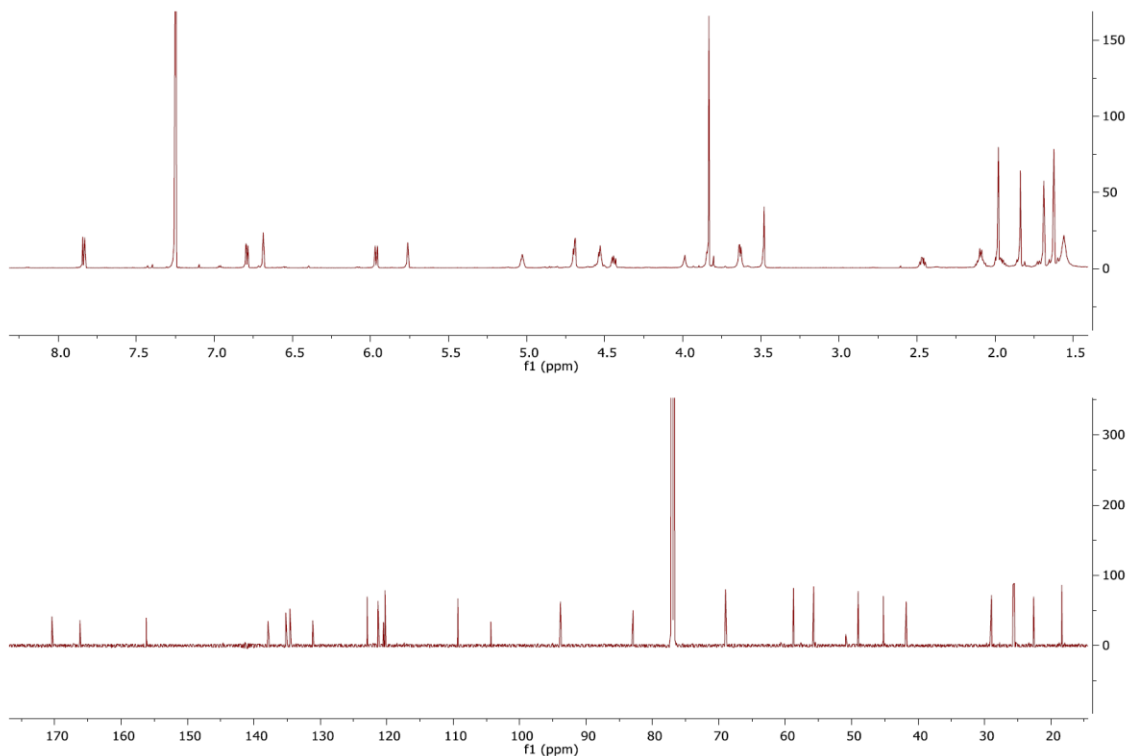


**Figure 76.**  $^1\text{H}$  NMR spectrum (700 MHz, Top) and  $^{13}\text{C}$  NMR spectrum (175 MHz, Bottom) both in  $\text{CDCl}_3$ , of fumitremorgin B (**5**).

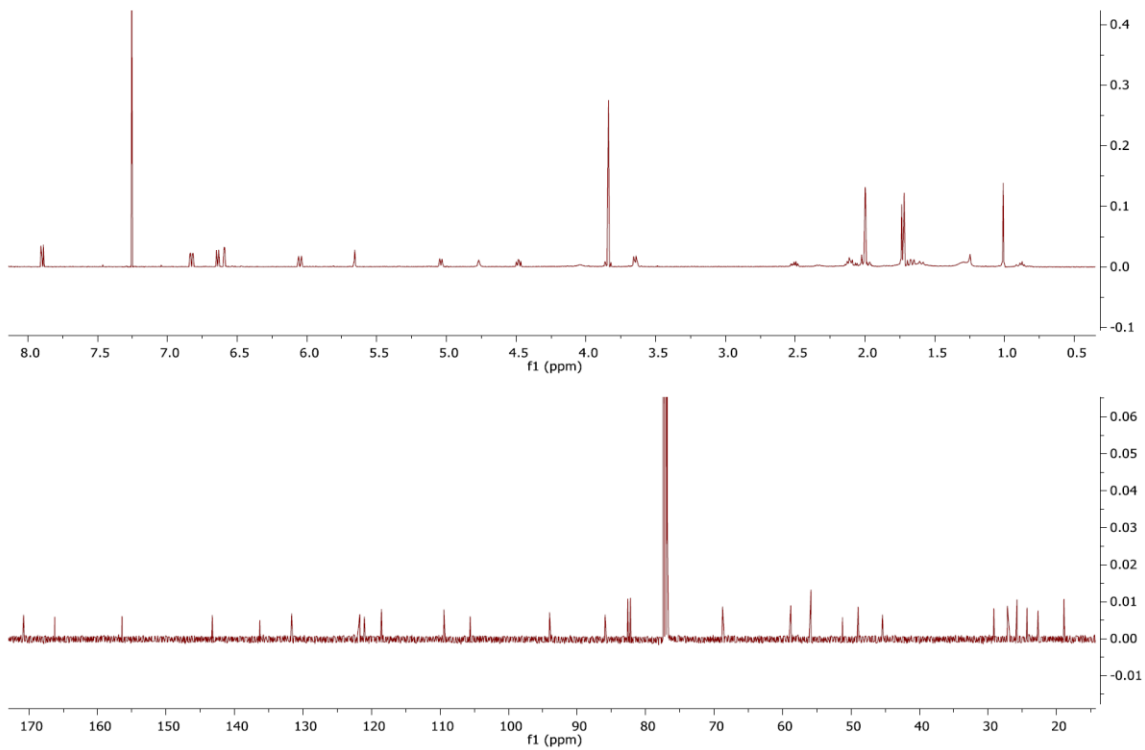


**Figure 77.**  $^1\text{H}$  NMR spectrum (500 MHz, Top) and  $^{13}\text{C}$  NMR spectrum (125 MHz, Bottom) both in  $\text{CDCl}_3$ , of verruculogen (**6**).

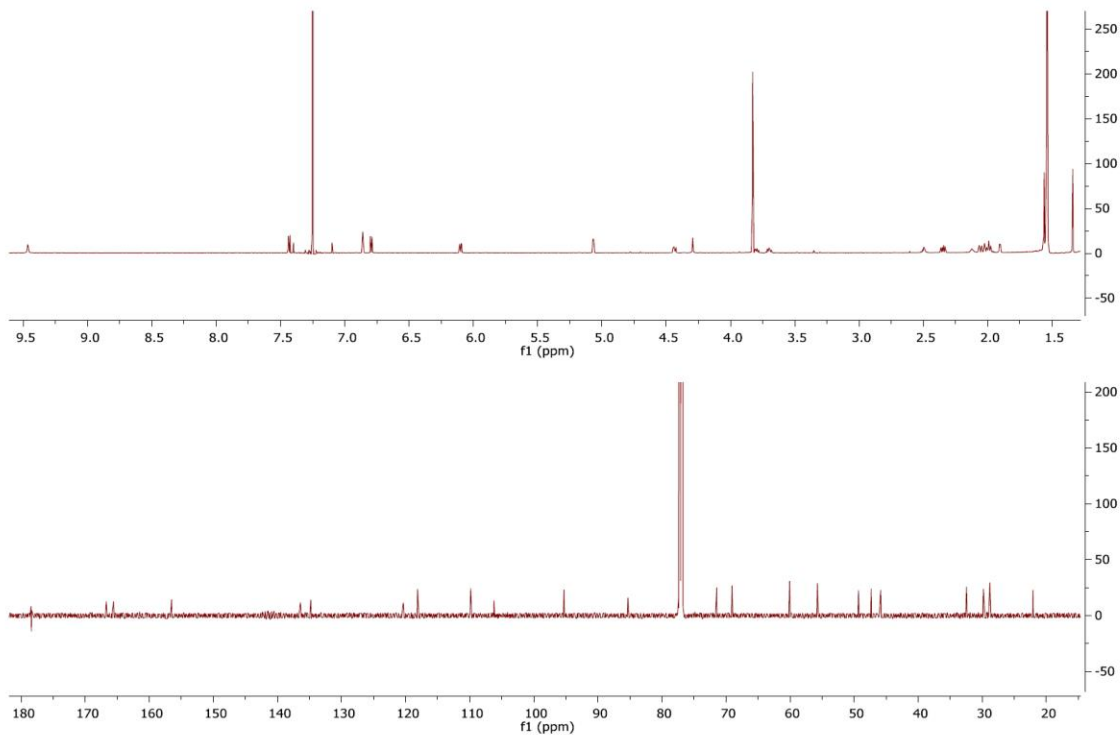


**Figure 78.**  $^1\text{H}$  NMR spectrum (700 MHz, Top) and  $^{13}\text{C}$  NMR spectrum (175 MHz, Bottom) both in  $\text{CDCl}_3$ , of C-11 epimer of verruculogen TR-2 (**7**).

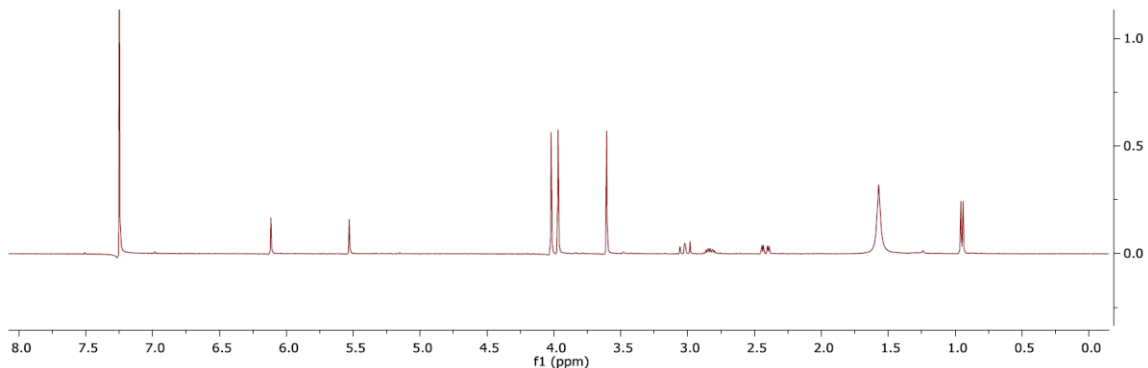


**Figure 79.**  $^1\text{H}$  NMR spectrum (400 MHz) in  $\text{CDCl}_3$ , griseofulvin (**8**).

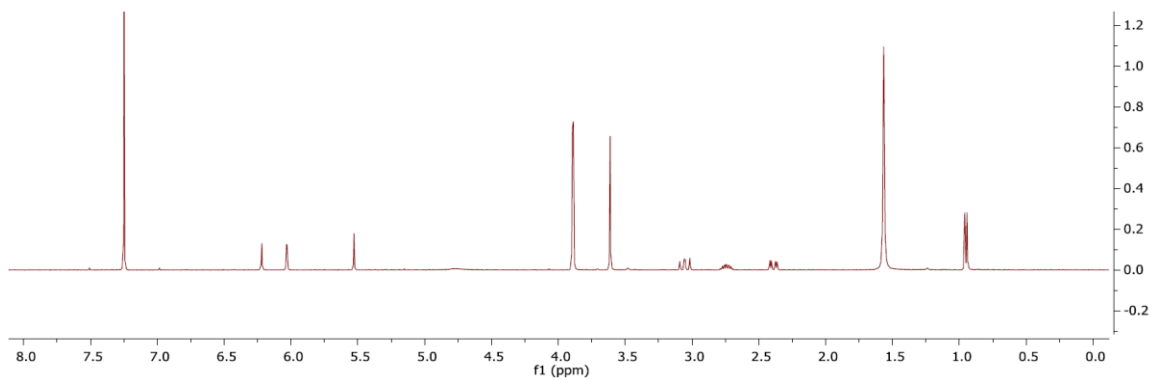


**Figure 80.**  $^1\text{H}$  NMR spectrum (400 MHz) in  $\text{CDCl}_3$ , dechlorogriseofulvin (**9**).

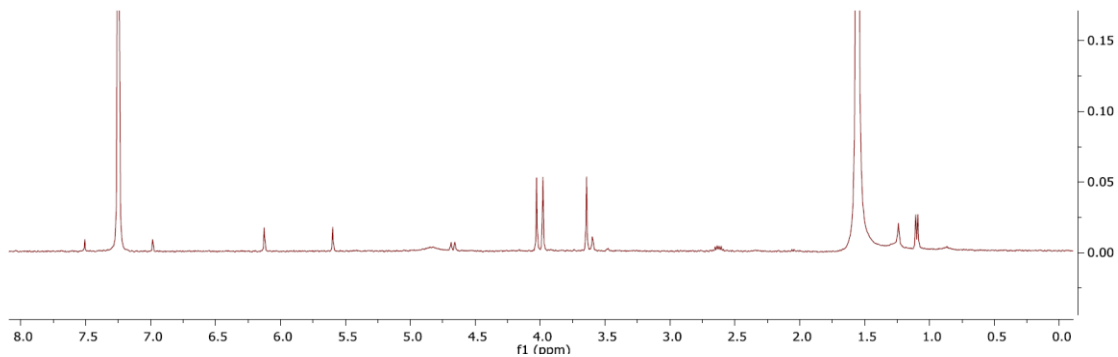


**Figure 81.**  $^1\text{H}$  NMR spectrum (400 MHz) in  $\text{CDCl}_3$ , 5'-hydroxygriseofulvin (**10**).

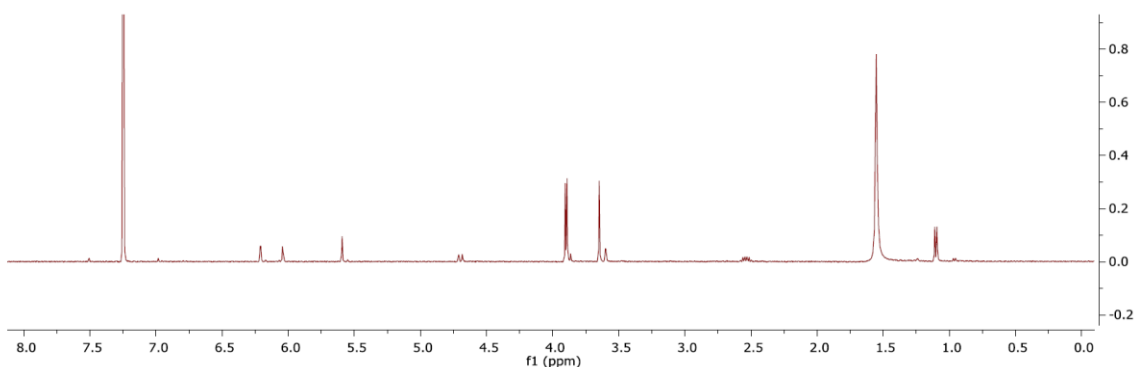


**Figure 82.**  $^1\text{H}$  NMR spectrum (400 MHz) in  $\text{CDCl}_3$ , dechloro-5'-hydroxygriseofulvin (**11**).

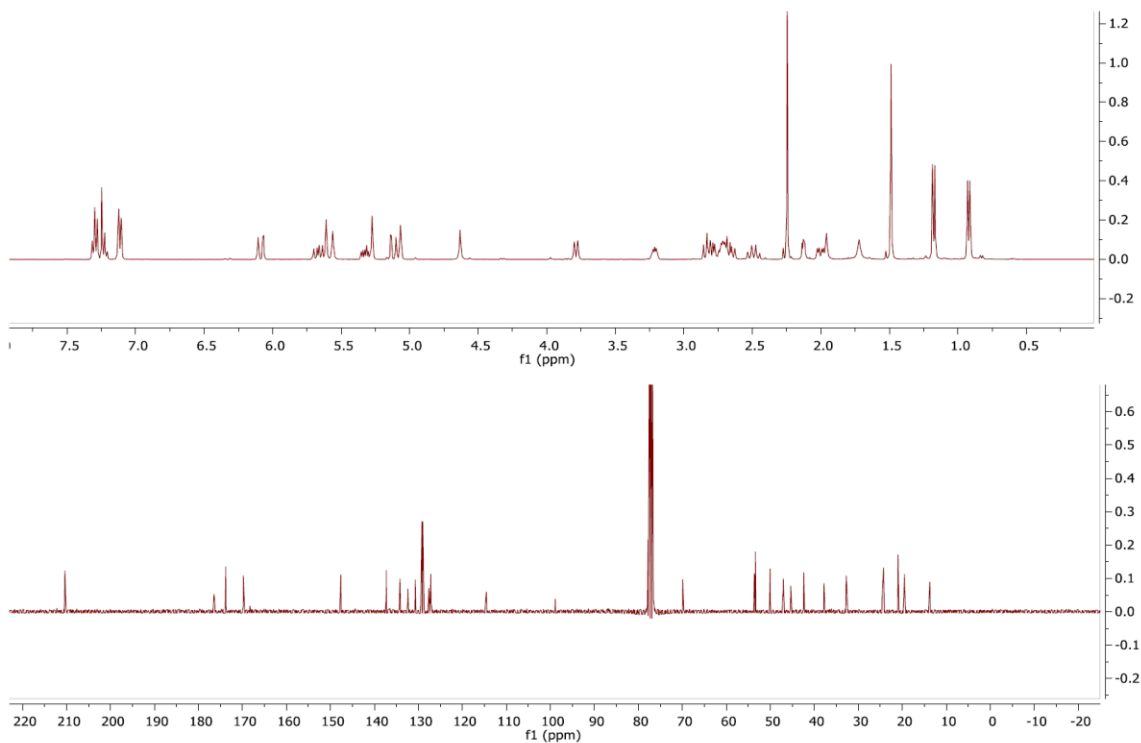


**Figure 83.**  $^1\text{H}$  NMR spectrum (400 MHz, Top) and  $^{13}\text{C}$  NMR spectrum (100 MHz, Bottom) both in  $\text{CDCl}_3$ , of cytochalasin D (**12**).

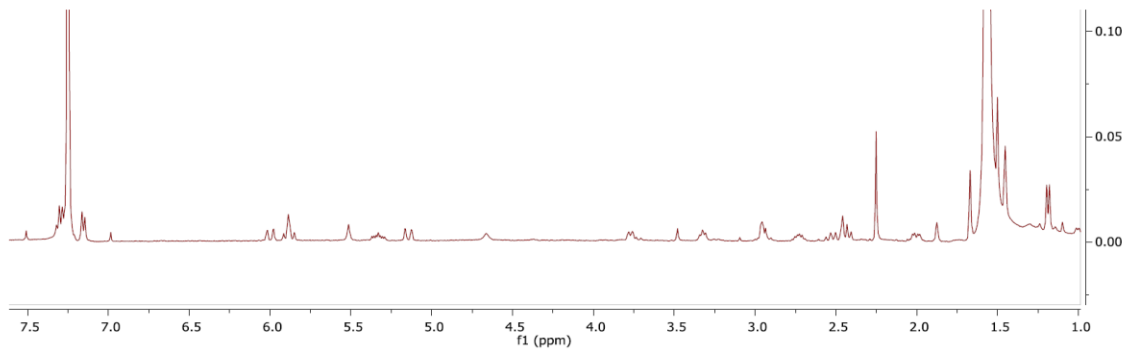


**Figure 84.**  $^1\text{H}$  NMR spectrum (400 MHz) in  $\text{CDCl}_3$ , cytochalasin C (**14**).

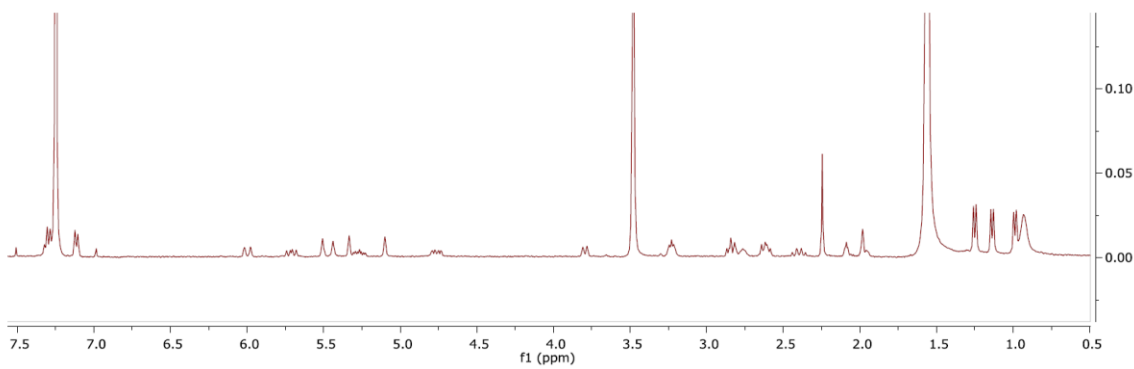


**Figure 85.**  $^1\text{H}$  NMR spectrum (400 MHz) in  $\text{CDCl}_3$ , zygosporin E (**15**).

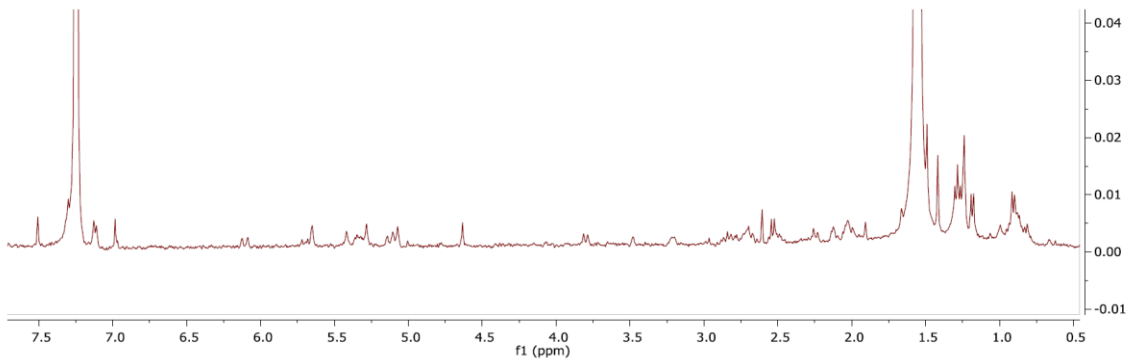


**Figure 86.**  $^1\text{H}$  NMR spectrum (400 MHz) in  $\text{CDCl}_3$ , 7-O-acetylcytochalasin B (**16**).

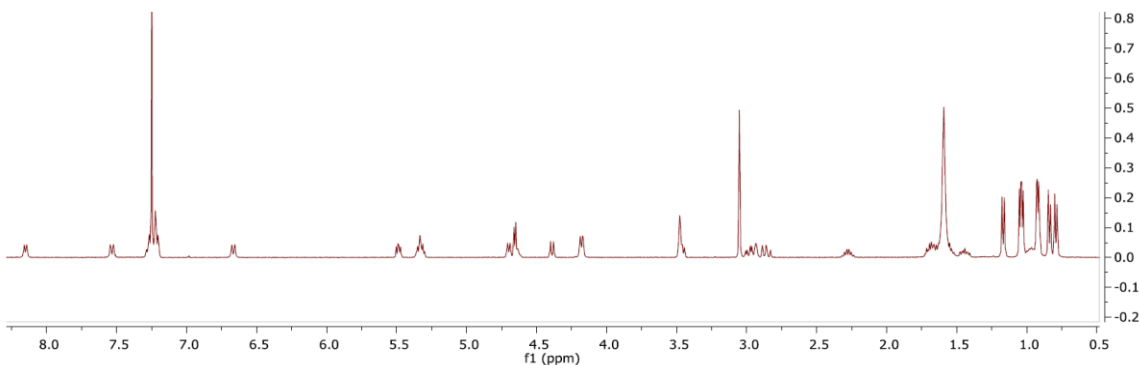


**Figure 87.**  $^1\text{H}$  NMR spectrum (400 MHz) in  $\text{CDCl}_3$ , hirsutatin A (**17**).

## CHAPTER VI

### WHELDONE: CHARACTERIZATION OF A UNIQUE SCAFFOLD FROM THE CO-CULTURE OF *ASPERGILLUS FISCHERI* AND *XYLARIA FLABELLIFORMIS*

Sonja L. Knowles, Huzefa A. Raja, Israa H. Isawi, Laura Flores-Bocanegra, Patricia H. Reggio, Cedric J. Pearce, Joanna E. Burdette, Antonis Rokas, Nicholas H. Oberlies. Org. Lett. 2020, 22, 1878-1882.

Wheldone (**1**) was isolated and elucidated from the co-culture of *Aspergillus fischeri* (NRRL 181) and *Xylaria flabelliformis* (G536), where secondary metabolite biosynthesis was stimulated by antagonism between these fungi. First observed via *in situ* analysis between these competing fungal cultures, the conditions were scaled to reproducibly generate **1**, whose novel structure was elucidated by one- and two-dimensional NMR and mass spectrometry. Compound **1** displayed cytotoxic activity against breast, ovarian, and melanoma cancer cell lines.

Fungi have been explored for new compounds for nearly 100 years, and that has led to the discovery of unique chemical diversity possessing promising biological activities, ranging from antibiotic, to immunosuppressant, to cholesterol lowering.<sup>5, 344-347</sup> In nature, fungi grow in competition for resources, and as such, they have evolved the ability to adapt to changes in their environment. One of the ways they stave off rival organisms is through the activation of biosynthetic gene clusters, thereby stocking their arsenal for chemical warfare.<sup>6, 10, 12, 29, 59</sup> Under standard lab conditions, fungi have been shown to produce only a fraction of their potential secondary metabolites.<sup>43, 348</sup> As such, co-culturing fungi, forcing them to compete for limited resources, may present a pragmatic strategy to stimulate the biosynthesis of novel chemical diversity.<sup>17, 43, 62, 341, 349</sup>

To test this, fungi with antagonistic properties were chosen to participate in co-culture experiments. The draft genome for *Xylaria flabelliformis* (strain G536; previously named *Xylaria cubensis*) was reported recently,<sup>14</sup> and this strain biosynthesizes griseofulvin, which is an FDA-approved fungistatic compound that is known to interact with a broad range of fungi.<sup>289, 307, 330</sup> Fungistatic denotes that it inhibits fungal growth, rather than killing competing fungi.<sup>350</sup> We hypothesized that griseofulvin (and co-biosynthesized analogues) would impart stress on the competing fungal culture, especially since we observed that *X. flabelliformis* exudes these compounds into its surroundings.<sup>15, 289</sup>

*Aspergillus fischeri* (strain NRRL 181) was chosen as the challenger due to its genetic tractability<sup>16</sup> and the biosynthesis of metabolite weaponry in the form of mycotoxins.<sup>15, 16, 334, 335</sup> Indeed, bioinformatic analysis of the genomes of both organisms predicted the presence of as many as 48 biosynthetic gene clusters for  $\textcircled{R}$ <sup>16</sup> and 86 biosynthetic gene clusters for *X. flabelliformis*,<sup>14</sup> yet only a relatively narrow range of secondary metabolites has been reported from either fungus. Our hypothesis was that the stress caused by the chemical warfare between these organisms would activate ‘silent’ biosynthetic gene clusters and generate unprecedented chemical diversity.<sup>57, 60, 61,</sup>

326, 349

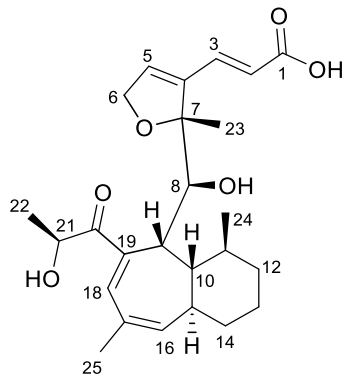


**Figure 88.** Wheldone (**1**) Was Isolated From the Co-Culture of *Aspergillus fischeri* and *Xylaria flabelliformis*.

In a previous study, we reported the biosynthesis of several compounds that were found only in the co-culture, including one putative new structure.<sup>15</sup> As reported herein, the isolation and characterization of a secondary metabolite (**1**) (Figure 88) with a novel chemical scaffold supported our postulate that co-culturing could generate new chemical diversity. This experiment was repeated several times in Petri dishes and in Erlenmeyer flasks (i.e. scaled up 5 times), demonstrating both a reproducible and scalable way to generate new fungal metabolites.

## Results

To initiate this experiment, monocultures of *X. flabelliformis* and ® were examined first *in situ* (Petri plates) by the droplet probe<sup>351</sup> to generate baseline profiles of the secondary metabolites. *X. flabelliformis* concentrates its fungistatic metabolites towards the colony edge (i.e. the youngest part of the fungal culture).<sup>289</sup> Alternatively, ® had an even distribution of secondary metabolites across its mycelium (i.e. the colony edge and the colony center had similar metabolites and relative abundances).<sup>15</sup> Next, co-cultures of *X. flabelliformis* and ® were examined by droplet probe once a clear “junction” was formed (Figure 89 and larger version in Figure 99), which is the dividing

area that is essentially the “battlefield” between the two competing fungi. The profile of compounds in the *X. flabelliformis* side of the co-culture was interesting, as secondary metabolites were primarily observed in the junction. In contrast,  $\textcircled{R}$  was able to upregulate the biosynthesis of mycotoxins, suggesting that it was responding to the fungistatic properties imparted by the other fungus.<sup>15</sup>

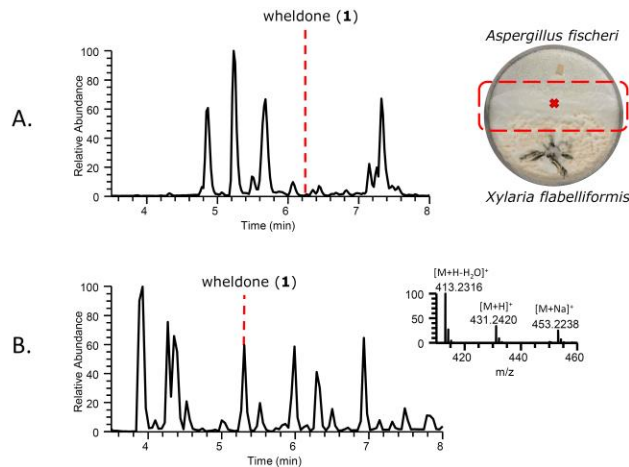


**Figure 89.** Panel A: Wheldone (**1**) was first noted as a minor component in the base peak chromatogram during *in situ* analysis<sup>15</sup> of the junction that developed between  $\textcircled{R}$  and *X. flabelliformis* (shown in the box in the co-culture Petri dish at the right). Panel B: The base peak chromatogram of the scaled-up co-culture experiment (250 ml Erlenmeyer flasks), with the insert showing the mass spectrum of **1** and its adducts. Note that the chromatographic conditions were different between panels A (*in situ* analysis) and B (UPLC-MS), which is why the retention time of **1** varies.

There were several known metabolites identified in the junction that were not observed in the monoculture, as reported recently.<sup>16, 60, 335</sup> However, there was one minor peak that did not match with any metabolites in an in house database of over 525 fungal metabolites,<sup>188</sup> could not be characterized via mass defect filtering,<sup>189</sup> and the molecular formula and spectroscopic data did not correlate to any organic compounds in the literature. Thus, this metabolite was targeted for isolation and characterization. Collectively, these data suggested that biosynthetic gene clusters, which were previously

silent, could be activated via co-culturing experiments to generate new chemical diversity.

To isolate and characterize the compound observed *in situ* in the co-culture experiments, solid-phase co-cultures of  $\textcircled{R}$  and *X. flabelliformis* were grown on oatmeal (see the supporting information). The organic extract [CHCl<sub>3</sub>–MeOH (1:1)] of the fermentation product underwent purification using normal-phase flash chromatography to afford six fractions. Upon further purification via C<sub>18</sub> preparative HPLC, fraction 2 yielded compound **1** (5.48 mg) (Figure 88). The purity (99%) of **1** was assessed via UPLC-MS (Figure 92). This process was repeated five times to isolate larger quantities of **1** (>15 mg), showing the reproducibility and scalability of co-culturing experiments.

**Table 6.1.** <sup>1</sup>H (700 MHz), <sup>13</sup>C (175 MHz), and HMBC NMR Data for **1** in CD<sub>3</sub>OD

Pos	$\delta_{\text{C}}$ , type	$\delta_{\text{H}}$ (J, Hz)	HMBC (H → C)
1	172.2, C		
2	122.6, CH	5.71 (d, 15.97)	4, 1
3	137.4, CH	7.40 (d, 16.00)	6, 2, 4, 5, 1
4	137.1, C		
5	142.8, CH	6.46 (t, 1.96)	6, 7, 3, 4
6	74.8, CH <sub>2</sub>	4.75 (dd, 12.01, 1.30) 4.81 (dd, 12.01, 1.03)	4, 5
7	95.2, C		
8	76.1, CH	3.54 (d, 10.41)	23, 9, 7, 19
9	43.0, CH	3.84 (dd, 10.45, 2.12)	15, 10, 8, 7, 17, 19
10	44.0, CH	1.96 (dt, 10.78, 3.49)	16
11	31.6, CH	1.19 (m)	
12	36.4, CH <sub>2</sub>	0.94 (dq, 12.82, 2.63) 1.56 (m)	
13	23.5, CH <sub>2</sub>	1.23 (m) 1.48 (m)	

14	32.8, CH <sub>2</sub>	1.50 (m) 1.74 (m)	
15	34.6, CH	2.88 (br s)	
16	142.9, CH	5.81 (br s)	25, 14, 10, 19
17	133.6, C		
18	121.9, CH	6.57 (s)	9, 8, 17, 19, 20
19	157.3, C		
20	208.7, C		
21	74.2, CH	4.41 (q, 7.04)	22, 20
22	20.8, CH <sub>3</sub>	1.35 (d, 7.04)	21, 20
23	19.3, CH <sub>3</sub>	1.42 (s)	8, 7, 5
24	20.5, CH <sub>3</sub>	0.78 (d, 6.47)	11, 12, 10
25	20.0, CH <sub>3</sub>	1.91 (d, 1.11)	17, 16, 19

Compound 1 was obtained as a white amorphous powder with a molecular formula of C<sub>25</sub>H<sub>34</sub>O<sub>6</sub> as determined via HRESIMS along with <sup>1</sup>H, <sup>13</sup>C, and edited-HSQC NMR data (Table 6.1), demonstrating an index of hydrogen deficiency of 9. The <sup>13</sup>C NMR data (Table 6.1) indicated the presence of 25 carbons, inclusive of two carbonyl, eight vinylic, four oxygenated, and eleven aliphatic carbons. The <sup>1</sup>H and edited-HSQC NMR data (Table 6.1) indicated four methyls, five olefinic protons, four methines, and three methylenes. The HMBC correlations from H-3 to C-1 and C-2, and from H-2 to C-1, as well as COSY cross correlations between H-3 and H-2, indicated a trans (*J*<sub>H-3/H-2</sub> = 15.97 Hz) α,β-unsaturated carboxylic acid. The COSY correlation between H-5 and H<sub>2</sub>-6, the HMBC correlations from H<sub>2</sub>-6 to C-5, H-5 to C-7 and C-4, and H<sub>3</sub>-23 to C-7 and C-5, along with the oxygenated carbons at C-6 ( $\delta$ <sub>C</sub> 74.8) and C-7 ( $\delta$ <sub>C</sub> 95.2) established the methylated 2,5-dihydrofuran ring. HMBC correlations between H-2 to C-4, and H-3 to C-5 and C-4, formed the connection between furan ring and the α,β-unsaturated carboxylic acid.

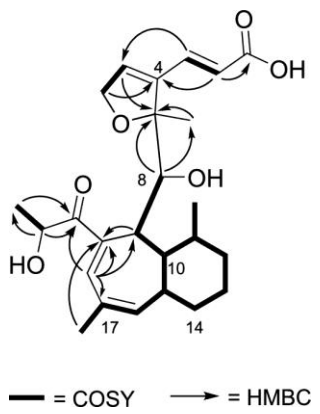
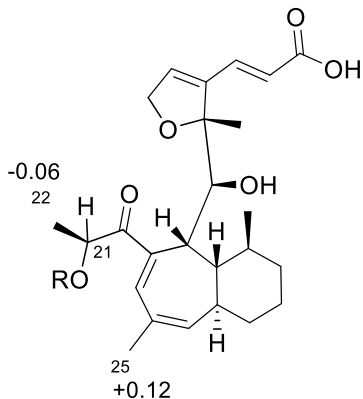


**Figure 90.** Key COSY and HMBC correlations for **1**.

The COSY NMR spectrum of **1** displayed an eleven-proton spin system ( $\text{H-8/H-9/H-10/H-11/H}_3\text{-24/H}_2\text{-12/H}_2\text{-13/H}_2\text{-14/H-15/H-16/H}_3\text{-25}$ ), which served to frame the bicyclic system (Figure 90). The seven membered-ring was discerned via HMBC correlations from  $\text{H}_3\text{-25}$  to C-19, H-9 to C-19 and C-17, and H-18 to C-9, C-17, and C-19. The  $\alpha$ -hydroxy-1-propanone side chain was elucidated through the COSY correlations of  $\text{H}_3\text{-22}$  ( $\delta_{\text{H}}/\delta_{\text{C}}$  1.35/20.8) and H-21 ( $\delta_{\text{H}}/\delta_{\text{C}}$  4.41/74.2) and the HMBC correlations to C-20 from both  $\text{H}_3\text{-22}$  and H-21; this side chain was connected to the seven-member ring via an HMBC correlation between H-18 and C-20. The bicyclic system was connected to the furan ring system via HMBC correlations from H-8 to C-7, and C-23, and  $\text{H}_3\text{-23}$  to C-8. The absolute configuration of **1** was assigned via the Mosher's esters method<sup>95</sup> and NOESY correlations (Figures 97 and 98), establishing the configuration as (7*R*,8*S*,9*R*,10*R*,11*S*,15*R*,21*S*) (Figure 91).



**1a:** R = (S)-MTPA  
**1b:** R = (R)-MTPA

**Figure 91.**  $\Delta\delta_H$  values [ $\Delta\delta$  (in ppm) =  $\delta_S - \delta_R$ ] obtained for (S)- and ®-MTPA esters of wheldone (**1**) (1a and 1b, respectively) in pyridine-*d*<sub>5</sub>.

Compound **1** was tested against a panel of tumor cell lines (Table 6.2), MDA-MB-231 (triple negative human breast cancer), OVCAR-3 (human ovarian cancer), and MDA-MB-435 (human melanoma cancer) using methods described previously.<sup>352</sup> Although taxol was more potent, these data demonstrated that the cell lines responded to both compounds in the same rank (i.e. taxol and **1** display the highest and lowest activities in the same cell lines) with the highest response seen in MDA-MB-435, followed by OVCAR3 and then MDA-MB-231.

**Table 6.2.** Activity of **1** Against Three Tumor Cell Lines

Compound	IC <sub>50</sub> (µM) <sup>a</sup>		
	MDA-MB-231	OVCAR-3	MDA-MS-435
<b>1</b>	7.6	3.8	2.4
taxol	0.17	0.0051	0.00043

<sup>a</sup>IC<sub>50</sub> values were determined as the concentration required to inhibit growth to 50% of control with a 72 h incubation.

Using the co-culturing of ® and *X. flabelliformis*, one novel compound (**1**) with cytotoxic activity was isolated and characterized. Our strategy employed the droplet probe<sup>351</sup> to first pilot the co-culture conditions in a Petri dish, essentially scouting for changes in secondary metabolite profile at the intersection of the fungal cultures.<sup>15</sup> Then, the co-cultures were scaled to reproducibly generate **1** on the mg scale, biosynthesizing enough material for further chemical and biological evaluation. Importantly, the scaled growths imparted a much higher concentration of **1** as compared to the Petri plates, likely because the antagonistic fungi were in close contact throughout the Erlenmeyer flask, as opposed to when they grow into each other in a Petri dish, which gives a visual indication of the battlefield (Figures 89 and 99), but is likely less efficient than constant interaction.

During the peer review of this manuscript, we started co-culturing *X. flabelliformis* with another ascomycete fungus (strain MSX79272). Natural products studies on strain MSX79272 will be reported in more detail in the future; however, based on DNA barcoding,<sup>353</sup> we know that it is not an *Aspergillus* sp. We were encouraged when we observed a peak in the extract from a co-culture experiment of these fungi that aligned with the retention time and HRMS data for **1** (Figure 100). The peak was isolated via HPLC, and a comparison between the <sup>1</sup>H NMR data for **1** from both co-culture experiments were in concordance (Figure 100). Since **1** was generated when *X. flabelliformis* was used in co-culture experiments with two different fungal strains, we hypothesize biosynthesis by this organism. Of the limited fungal-fungal co-culture experiments in the literature (~40),<sup>52</sup> this is the first example of using an alternate fungus to narrow down the biosynthetic source for the new chemical entity. Given that the genomes of both fungal strains used in this study have been sequenced, and putative

biosynthetic gene clusters have been predicted,<sup>14, 16</sup> future studies will take advantage of the development of improved heterologous gene expression platforms for targeted production of fungal secondary metabolites<sup>354</sup> and to identify the biosynthetic gene cluster responsible for the biosynthesis of wheldone.

## Materials and Methods

**General Experimental Procedures.** Optical rotation data were obtained using a Rudolph Research Autopol III polarimeter, and UV spectra were measured with a Varian Cary 100 Bio UV-vis spectrophotometer. The NMR data were collected using an Agilent 700 MHz spectrometer (Agilent Technologies), equipped with a cryoprobe, operating at 700 MHz for <sup>1</sup>H and 175 MHz for <sup>13</sup>C. HRMS experiments utilized either a Thermo LTQ Orbitrap XL mass spectrometer or a Thermo Q Exactive Plus (Thermo Fisher Scientific); both were equipped with an electrospray ionization source. A Waters Acquity UPLC (Waters Corp.) was utilized for both mass spectrometers, using a BEH C<sub>18</sub> column (1.7 μm; 50 mm x 2.1 mm) set to a temperature of 40°C and a flow rate of 0.3 mL/min. The mobile phase consisted of a linear gradient of CH<sub>3</sub>CN-H<sub>2</sub>O (both acidified with 0.1% formic acid), starting at 15% CH<sub>3</sub>CN and increasing linearly to 100% CH<sub>3</sub>CN over 8 min, with a 1.5 min hold before returning to the starting condition. The HPLC separations were performed with Atlantis T3 C<sub>18</sub> preparative (5 μm; 19 x 250 mm) column, with a Varian Prostar HPLC system equipped with a Prostar 210 pumps and a Prostar 335 photodiode array detector (PDA), with the collection and analysis of data using Galaxie Chromatography Workstation software. Flash chromatography was performed on a Teledyne ISCO CombiFlash Rf 200 and monitored by both ELSD and PDA detectors.

**Fungal Strain Isolation and Identification.** *Aspergillus fischeri* strain NRRL 181 was obtained from ARS Culture Collection (NRRL).<sup>16</sup> *Xylaria flabelliformis* (formally

*Xylaria cubensis*) strain G536 was isolated as an endophyte from surface sterilized twigs of *Asimina triloba* and identified using molecular methods as outlined previously.<sup>289</sup> The genome for *X. flabelliformis* was reported recently.<sup>14</sup>

**Fermentation, Extraction, and Isolation.** Storage, fermentation, and extraction conditions were reported previously.<sup>15</sup> Briefly,  $\circledR$  and *X. flabelliformis* were grown separately in 10 mL of YESD broth (2% soy peptone, 2% dextrose, and 1% yeast extract; 5 g of yeast extract, 10 g of soy peptone, and 10 g of D-glucose in 500 mL of deionized H<sub>2</sub>O) and cultivated at 22°C with agitation at 100 rpm for 3 ( $\circledR$ ) and 5 days (*X. flabelliformis*). YESD seed cultures of both fungi grown individually were subsequently used to inoculate 16, 250 mL Erlenmeyer flasks that contained 10 g of autoclaved Quaker Breakfast Oatmeal each (10 g of oatmeal with 17 mL of deionized H<sub>2</sub>O and sterilized for 15–20 mins at 121°C). Following incubation at room temperature for 3 weeks, each solid culture was extracted by adding 60 mL of 1:1 MeOH-CHCl<sub>3</sub>. Subsequently, each culture was chopped with a spatula and left to shake overnight (~16 hrs) at ~100 rpm at room temperature. The cultures (16 flasks) were combined and filtered *in vacuo*, and 1500 mL CHCl<sub>3</sub> and 2400 mL H<sub>2</sub>O were added to the filtrate. The mixture was stirred for 30 min and then transferred to a separatory funnel. The organic layer (CHCl<sub>3</sub>) was drawn off and evaporated to dryness *in vacuo*. The dried organic layer was reconstituted in 300 mL of (1:1) MeOH-CH<sub>3</sub>CN and 300 mL of hexanes, transferred to a separatory funnel, and shaken vigorously. The defatted organic layer (MeOH-CH<sub>3</sub>CN) was evaporated to dryness *in vacuo*. The organic layer (1.28 g) was dissolved in CHCl<sub>3</sub>, absorbed onto Celite 545 (Acros Organics), and fractionated by normal phase flash chromatography using a gradient of hexane-CHCl<sub>3</sub>-MeOH at a 30 mL/min flow rate and 61.0 column volumes, which yielded six fractions. Fraction two (239.22 mg) was

further purified via preparative HPLC using a gradient system 50:50 to 90:10 of CH<sub>3</sub>CN-H<sub>2</sub>O with 0.1% formic acid over 30 min at a flow rate of 16.9 mL/min to yield 14 subfractions. Subfraction four (5.48 mg), which eluted at 14.0 min, yielded wheldone (**1**). This process has been repeated several times to isolate larger quantities of **1**, showing the reproducibility of co-culturing *R* and *X. flabelliformis*.

**Preparation of the *R*- and (S)-MTPA Ester Derivatives of wheldone.** To 0.25 mg of compound **1** were added 450  $\mu$ L of pyridine-*d*5, and the solution was transferred into an NMR tube. To initiate the reaction, 20  $\mu$ L of *R*-(*-*)- $\alpha$ -methoxy- $\alpha$ -(trifluoromethyl)phenylacetyl (MTPA) chloride were added with careful shaking and then monitored immediately by <sup>1</sup>H NMR at the following time points: 0, 5, 10, and 15 min. The reaction was found to be complete in 5 min, yielding the mono (S)-MTPA ester derivative (**1a**). <sup>1</sup>H NMR data of **1a** (500 MHz, pyridine-*d*5):  $\delta$ H 1.55 (3H, H<sub>3</sub>-22), 1.88 (3H, H<sub>3</sub>-25). In an analogous manner, 0.25 mg of compound **1** dissolved in 400  $\mu$ L pyridine-*d*5 was reacted in a second NMR tube with 20  $\mu$ L of S-(+)- $\alpha$ -methoxy- $\alpha$ -(trifluoromethyl)phenylacetyl (MTPA) chloride for the same time points, to afford the mono *R*-MTPA ester derivative (**1b**). <sup>1</sup>H NMR data of **1b** (500 MHz, pyridine-*d*5):  $\delta$ H 1.61 (3H, H<sub>3</sub>-22), 1.76 (3H, H<sub>3</sub>-25).

**Wheldone (**1**)**. White, amorphous powder;  $[\alpha]_D^{20} = +182$  (c 0.10, MeOH); UV (MeOH)  $\lambda_{\text{max}}$  (log  $\epsilon$ ) 262 (3.74), 217 (3.70) nm; <sup>1</sup>H NMR (CD<sub>3</sub>OD, 700 MHz) and <sup>13</sup>C (CD<sub>3</sub>OD, 175 MHz) (See Table 1); HRESIMS *m/z* 431.2423 [M+H]<sup>+</sup> (calcd. For C<sub>25</sub>H<sub>35</sub>O<sub>6</sub>, 431.2433).

**Cytotoxicity Assay.** Human melanoma cancer cells MDA-MB-435, human breast cancer cells MDA-MB-231 and human ovarian cancer cells OVCAR3 were purchased from the American Type Culture Collection (Manassas, VA). The cell line was propagated at 37°C in 5% CO<sub>2</sub> in RPMI 1640 medium, supplemented with fetal bovine

serum (10%), penicillin (100 units/mL), and streptomycin (100 µg/mL). Cells in log phase growth were harvested by trypsinization followed by two washing to remove all traces of enzyme. A total of 5,000 cells were seeded per well of a 96-well clear, flat-bottom plate (Microtest 96®, Falcon) and incubated overnight (37°C in 5% CO<sub>2</sub>). Samples dissolved in DMSO were then diluted and added to the appropriate wells. The cells were incubated in the presence of test substance for 72 h at 37°C and evaluated for viability with a commercial absorbance assay (CellTiter-Blue Cell Viability Assay, Promega Corp, Madison, WI) that measured viable cells. IC<sub>50</sub> values are expressed in µM relative to the solvent (DMSO) control.

## Supplementary Data

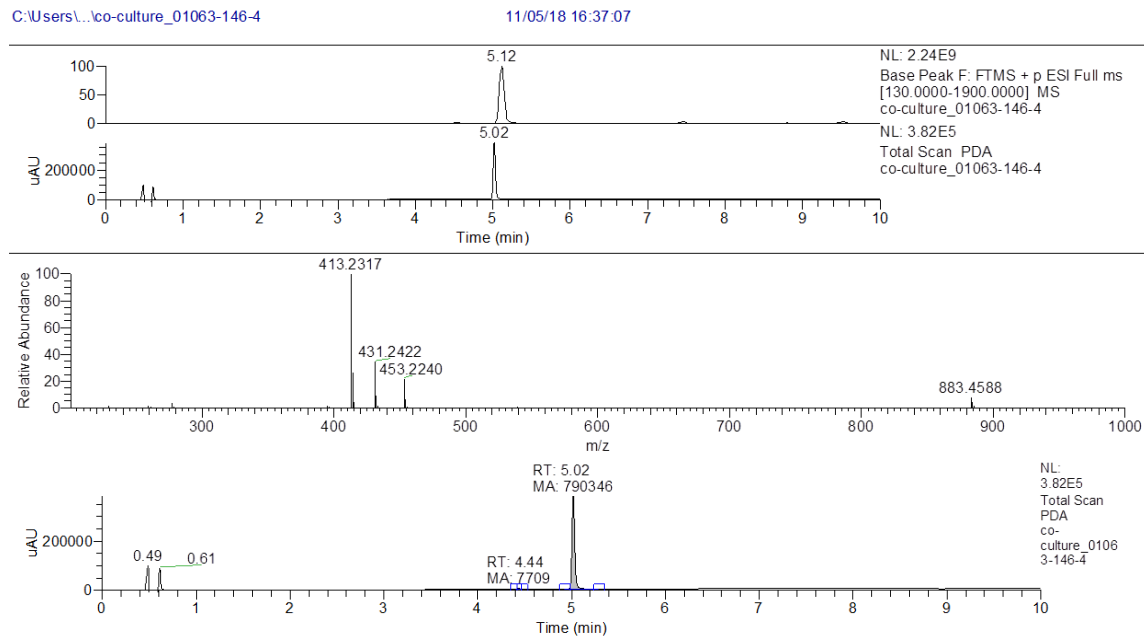


**Figure 92.** LC-MS chromatogram, (+)-HRESIMS spectrum, and purity of compound 1.

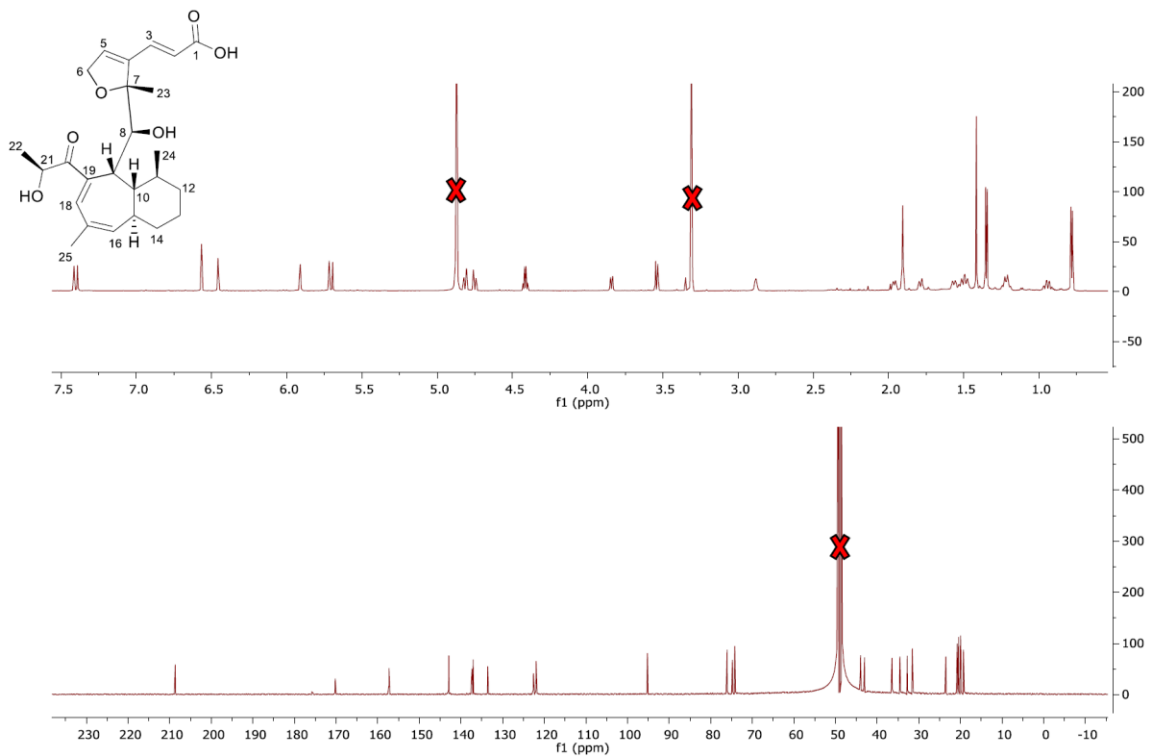


**Figure 93.**  $^1\text{H}$  (700 MHz) and  $^{13}\text{C}$  (175 MHz) NMR data for wheldone (**1**) in  $\text{CD}_3\text{OD}$ .

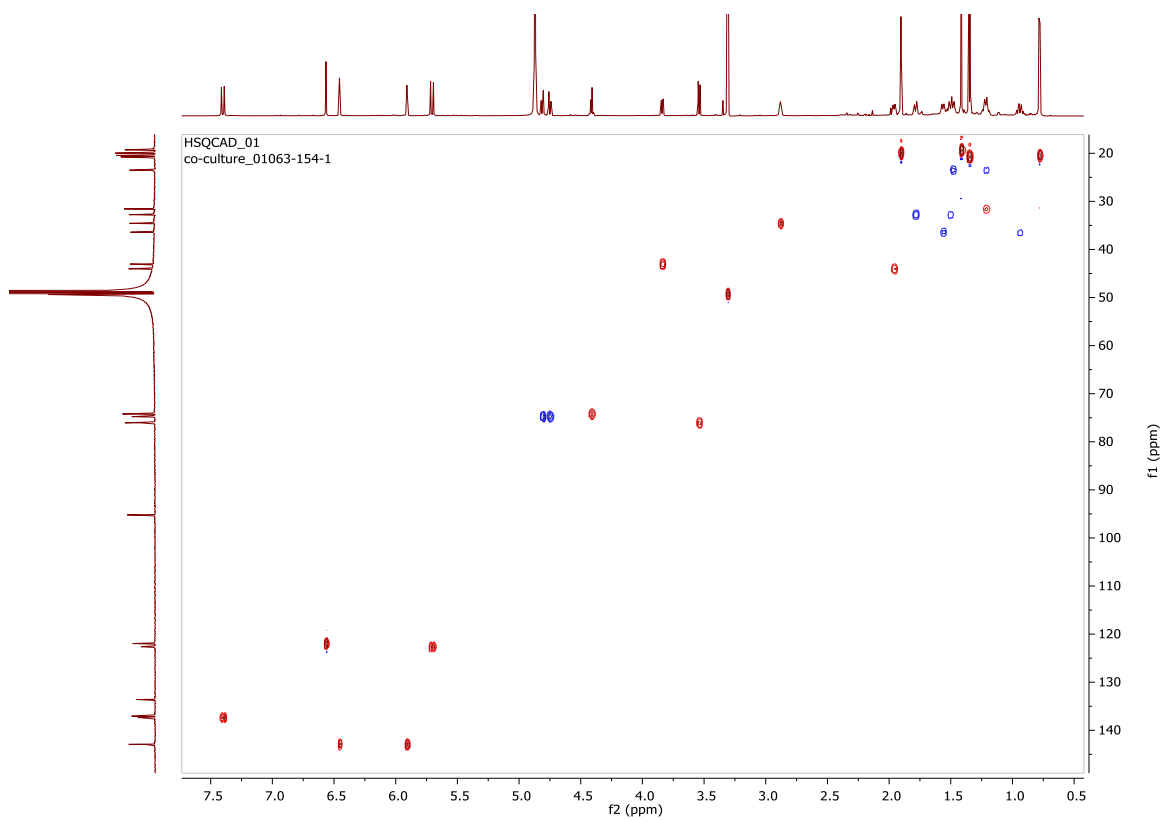


**Figure 94.** HSQC NMR spectrum of compound **1** (700 MHz,  $\text{CD}_3\text{OD}$ ).

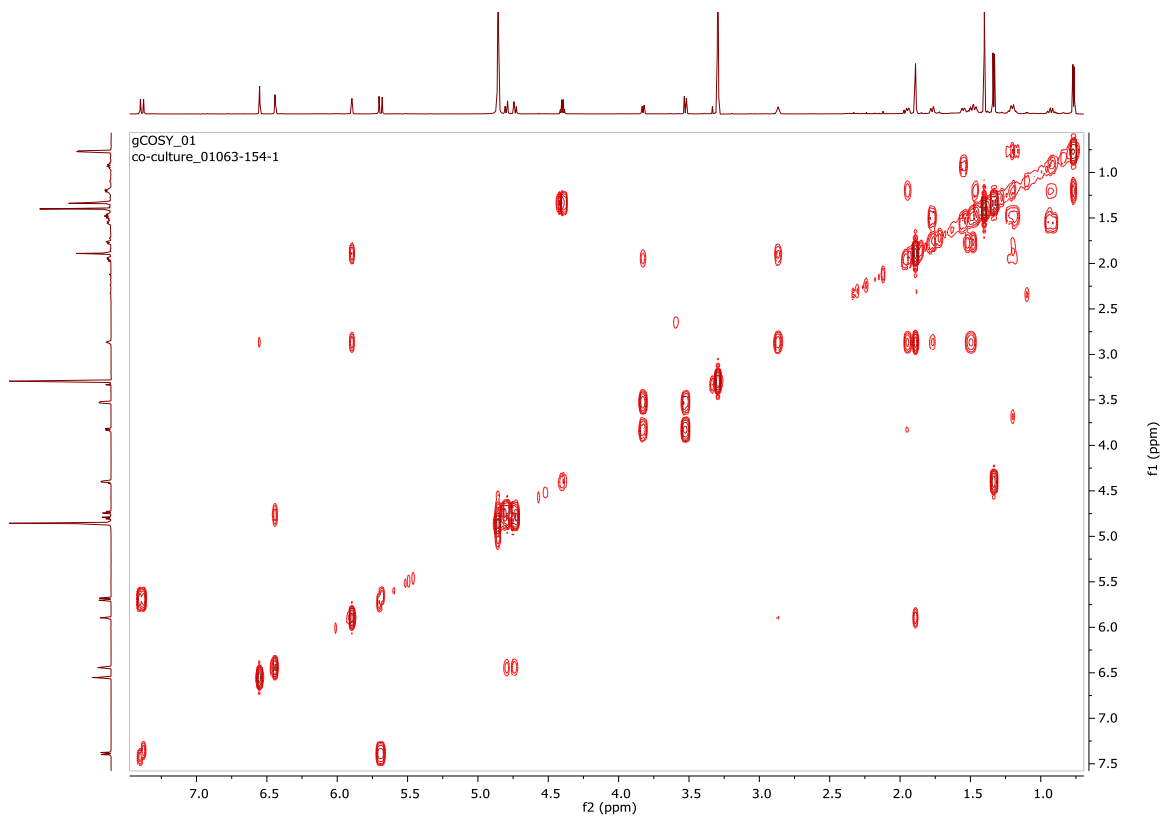


**Figure 95.** COSY NMR spectrum of compound **1** (700 MHz,  $\text{CD}_3\text{OD}$ ).

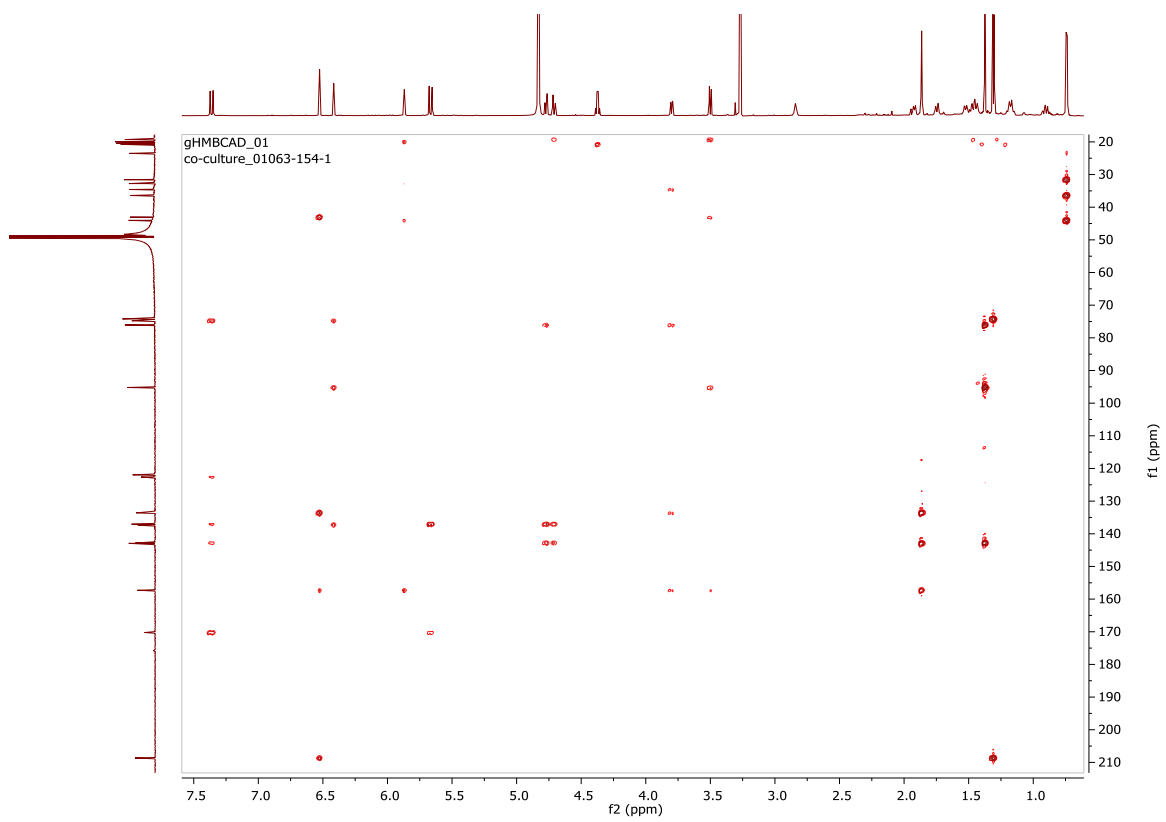


**Figure 96.** HMBC NMR spectrum of compound **1** (700 MHz, CD<sub>3</sub>OD).

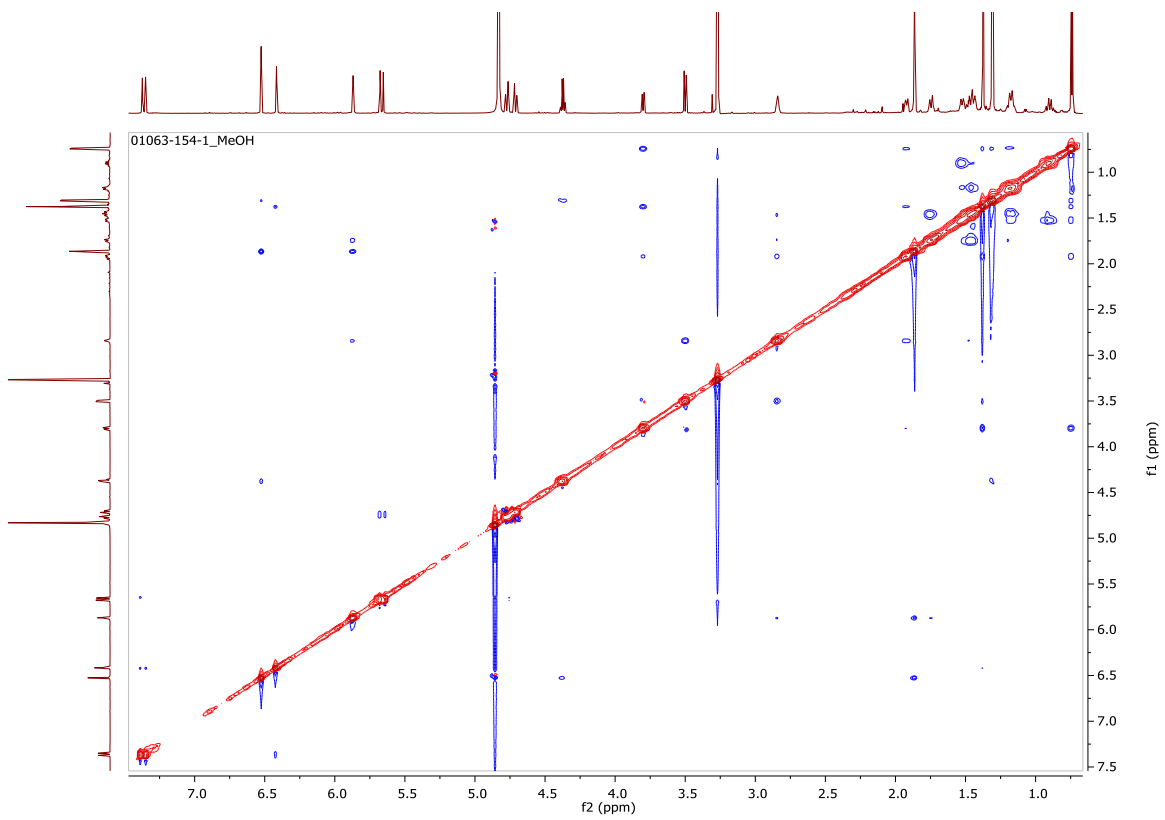


**Figure 97.** NOESY NMR spectrum of compound **1** (400 MHz, CD<sub>3</sub>OD).

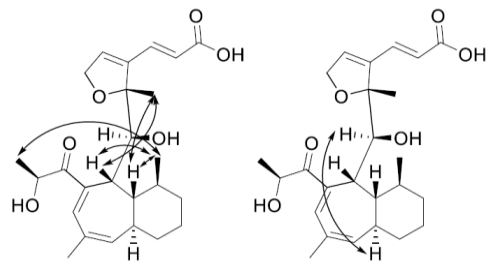


**Figure 98.** Key NOESY correlations for compound 1. The structure is presented twice, so that it is easier to see the key correlations for each face of the molecule.

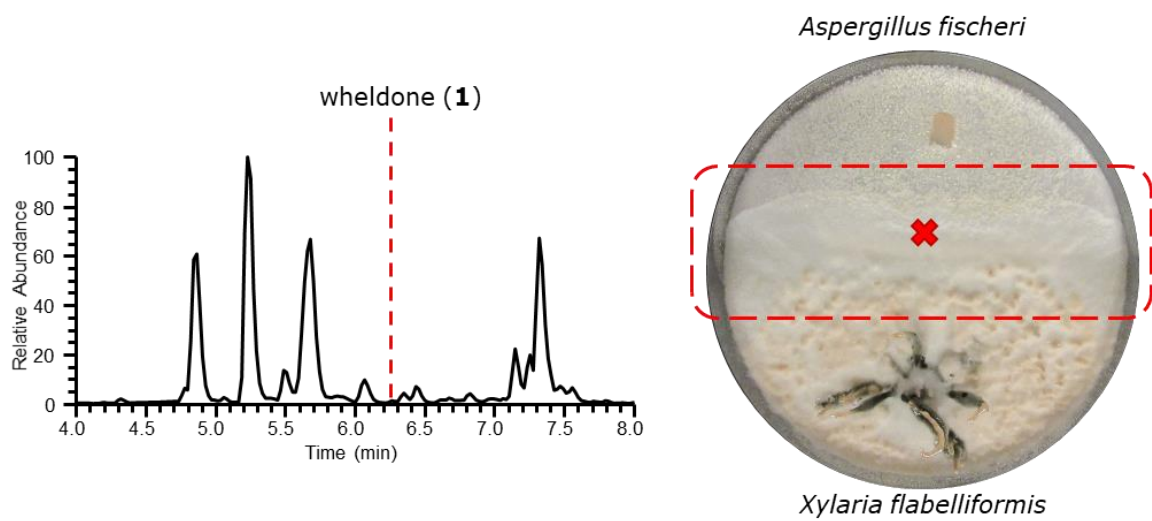


**Figure 99.** A larger version of Figure 89 Panel A.

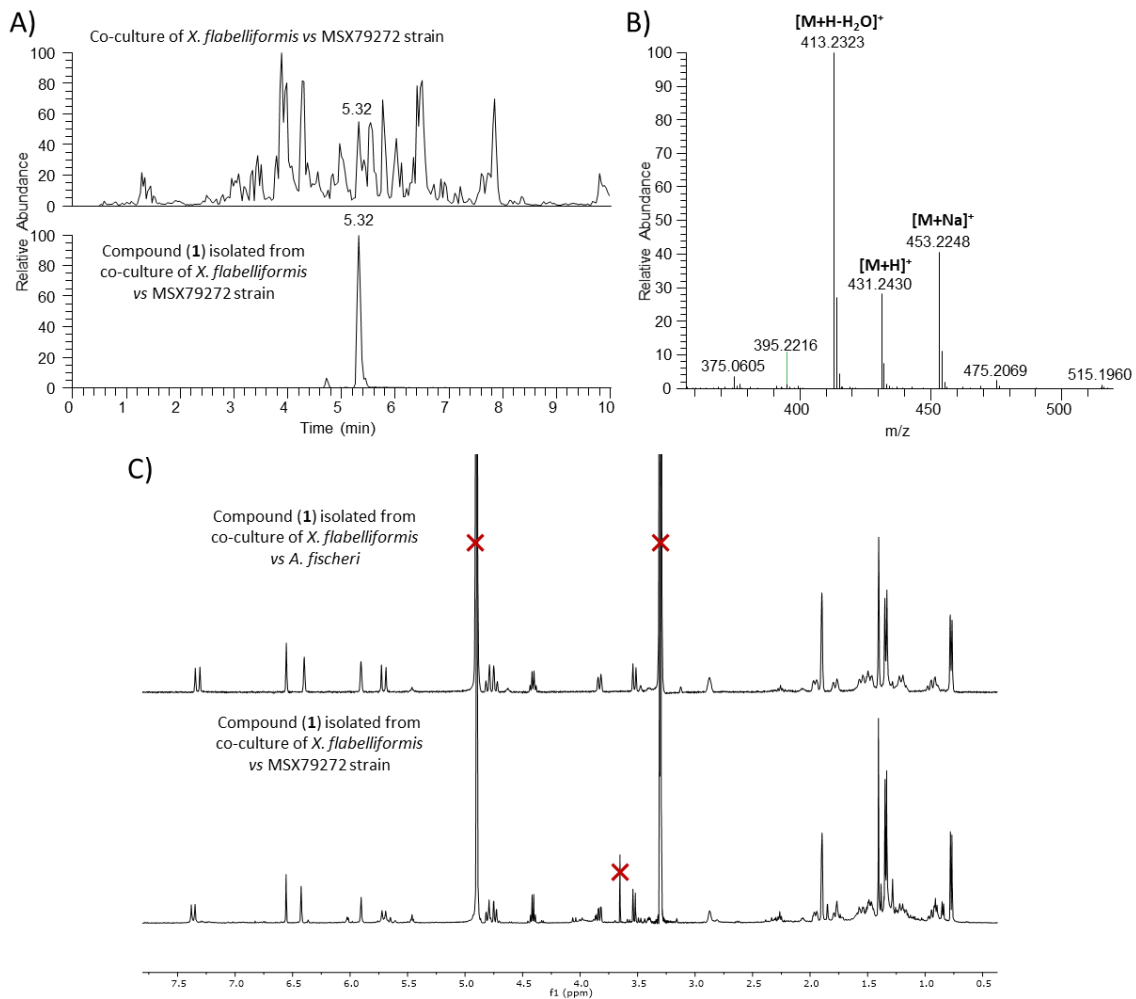


**Figure 100.** Data confirming the biosynthesis of **1** from a co-culture of *X. flabelliformis* vs. fungal strain MSX76272. Confirming the biosynthesis of **1** from a co-culture of *X. flabelliformis* vs. fungal strain MSX76272. A) UPLC-MS chromatogram (base peak of extract; top and **1**; bottom) for the co-culture of *X. flabelliformis* vs strain MSX76272. B) Mass spectrum data of **1** isolated from *X. flabelliformis* vs. MSX76272. C)  $^1\text{H}$  NMR data comparison between **1** isolated from the two separate co-culture experiments.

## CHAPTER VII

### ORTHOGONAL METHOD FOR DOUBLE BOND PLACEMENT VIA OZONE-INDUCED DISSOCIATION MASS SPECTROMETRY (OZID-MS)

Sonja L. Knowles, Ngoc Vu, Daniel A. Todd, Huzefa A. Raja, Antonis Rokas, Qibin Zhang, and Nicholas H. Oberlies. *Journal of Natural Products* 2019, 82, 3421-3431.

Most often, the structures of secondary metabolites are solved using a suite of NMR techniques. However, there are times when it can be challenging to position double bonds, particularly those that are fully substituted or when there are multiple double bonds in similar chemical environments. Ozone-Induced Dissociation Mass Spectrometry (OzID-MS) serves as an orthogonal structure elucidation tool, using predictable fragmentation patterns that are generated after ozonolysis across a carbon-carbon double bond. This technique is finding growing use in the lipidomics community, suggestive of its potential value for secondary metabolites. This methodology was validated by confirming the double bond positions in five fungal secondary metabolites, specifically: ent-sartorypyrone E (**1**), sartorypyrone A (**2**), sorbicillin (**3**), trichodermic acid A (**4**), and AA03390 (**5**). This demonstrated its potential with a variety of chemotypes, ranging from polyketides to terpenoids, and including those in both conjugated and non-conjugated polyenes. In addition, the potential of using this methodology in the context of a mixture was piloted by studying *Aspergillus fischeri*, first examining a traditional extract and then sampling a live fungal culture *in situ*. While the intensity of signals varied from pure compound to extract to *in situ*, the utility of the technique was preserved.

The structures of many organic compounds, particularly natural products, are typically elucidated by interpretation of a suite of NMR experiments.<sup>63-68</sup> However, there are times when derivatization is required to finalize a structure. In the lore of drug discovery, camptothecin and taxol (paclitaxel) are two prominent examples,<sup>355-357</sup> although there are certainly scores of others. While NMR instrumentation and pulse sequences continue to evolve,<sup>358-360</sup> some derivatizations are used fairly often in structure elucidation, such as reductions/oxidations,<sup>361-363</sup> reactions to assign absolute configuration, either via installing heavy atoms for X-ray crystallography or the use of Mosher's esters,<sup>92, 93, 95, 96, 156</sup> and peptide hydrolysis/Marfey's analysis.<sup>364-366</sup> In short, the reactions of organic chemistry remain beneficial for structural analysis.

Challenges can arise when striving to position double bonds in structurally complex natural products via NMR, particularly for fully substituted double bonds and compounds with multiple double bonds in similar chemical environments.<sup>72-74</sup> During the initial steps of structure elucidation of secondary metabolites, many factors can lead to the assignment of an incorrect structure,<sup>69-71</sup> and common examples include endocyclic vs. exocyclic double bonds<sup>75, 76</sup> and a change in functional groups.<sup>77, 78</sup> As new techniques are developed, this often leads to structural re-assignments.<sup>363, 367-369</sup> Again, even with the latest advancements in NMR, there is room for orthogonal techniques that serve to either assign, or at least verify, the *de novo* structure elucidation of natural products. In addition, with the growing popularity of metabolomics, where structures may be inferred solely from hyphenated mass spectrometry data, a tool that could position carbon-carbon double bonds could be valuable, particularly for discerning the structures of isobars.<sup>80</sup>

In a molecule containing carbon-carbon double bonds, low energy collision-induced dissociation (CID) cannot be used readily for their positioning in a polyene motif due to their high stability. To overcome this challenge, alternative approaches were introduced to derivatize such bonds, with the aim of inducing diagnostic fragment ions under CID. There are many selective reactions, and some of them were coupled with mass spectrometry to pinpoint the double bond location in a molecule, such as: dimethyl disulfate reaction,<sup>370</sup> Paternò-Büchi reaction,<sup>371, 372</sup> ozonolysis, and meta chloroperoxybenzoic acid (m-CPBA)<sup>373</sup> epoxidation reaction. The common requirement between these methods (with the exception of ozonolysis) is that the reaction was performed in solution phase prior to the ionization, which leads to the loss of information about the accurate mass of the intact molecule and the need to use CID to induce subsequent diagnostic product ions. Hence, when using collision energy to fragment the desired bond, additional fragments would be generated from neighboring bonds, leading to a complicated spectrum, and as a result, such data were time consuming to interpret.<sup>374</sup>

Ozonolysis, which uses ozone to cleave alkene double bonds, is a well-known reaction that is covered in nearly all introductory organic chemistry classes.<sup>375</sup> In the past, ozone ( $O_3$ ) gas was employed to study the carbon-carbon double bonds of lipids in solution and at the ionization source of the mass spectrometer (a technique termed OzESI). Every unsaturated molecule would interact with ozone at the ionization source, to produce the molozonide, and this would subsequently cleave to the Criegee and carbonyl product ions (discussed further below). However, the detected ions would be the combination of the ozonolysis products and ESI products (i.e. electrospray ionization). Hence, a full scan mass spectrum of a complex sample under such

conditions would be convoluted with information of precursor ions and product ions in the same scan. Moreover, one cannot assign the product ion to the original parent ions. As a result, OzESI experiments were not recommended for complex samples, and as expected, the resulting data from an OzESI experiment were both complicated and lacked intact structural characterization information.<sup>376, 377</sup>

To circumvent the aforementioned challenges, ozone-induced dissociation mass spectrometry (OzID-MS) was introduced in 2008,<sup>79</sup> which implements the ozonolysis reaction in the gas phase inside the mass spectrometer. This approach provided the mass selection option for intact structure elucidation of double bond positional isomers of lipids before the targeted ion reacted with ozone in the trap chamber.<sup>80-85</sup> The mechanism of OzID-MS is based on the fundamentals of ozonolysis, which selectively cleaves carbon-carbon double bonds, particularly those on the acyl chains of lipids. This results in unique product ions, aldehyde or ketone, depending on the double bond substitution before the cleavage, and a Criegee ion, which is a carbonyl oxide zwitterion (Figure 102).<sup>86</sup> This mechanism has the advantages of being both reliable and predictable, thereby facilitating downstream data analysis. Recently, OzID-MS has become a prominent technique for pinpointing the location of double bonds in the fatty acyl chains of lipids exactly because of the predictable cleavage patterns and unique fragments.<sup>79, 80, 82, 85</sup>

Given the promise of OzID-MS for facilitating double bond placement in lipids, it is somewhat surprising that this technique has rarely been used in natural products, with most examples being of compounds similar to fatty acids but with various head groups.<sup>378-380</sup> For example, it aided in the elucidation of double bond locations in several bisresorcinol and hexadecenoylanthranilic acid isomers.<sup>379, 380</sup> While it is not possible to

replace the tools and value of NMR characterization, OzID-MS can serve as an orthogonal structure elucidation tool. Essentially, initiation of ozonolysis across a carbon-carbon double bond in a mass spectrometer provides valuable data that complement those derived from NMR experiments. Since OzID-MS is effectively a tandem mass spectrometry technique, it has the further advantage of not requiring pure compounds, which means the technique can be applied to a complex sample matrix. With the goal of expanding the utility of this technique, we piloted its use with a range of fungal metabolites as pure compounds, in the context of an extract, and *in situ*.

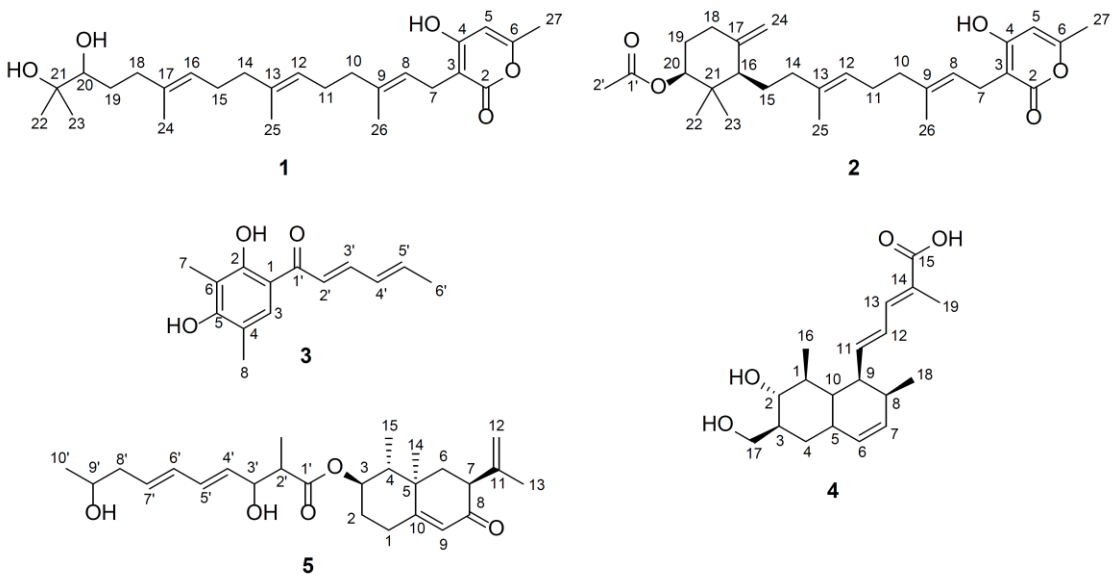


**Figure 101.** Compounds 1-5.

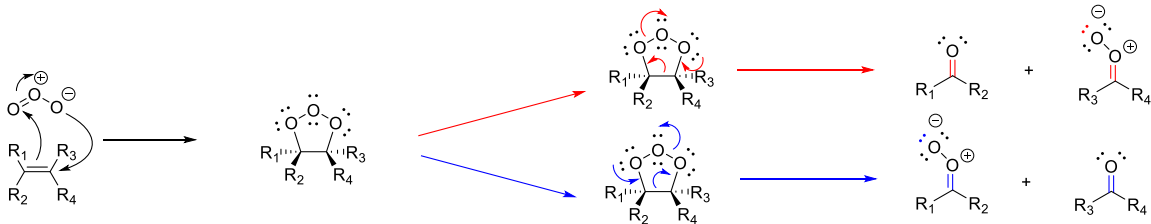


**Figure 102.** In ozonolysis carbon-carbon double bonds react with ozone via a 1,3-dipolar cycloaddition. Two products are formed via the subsequent retro 1,3-dipolar cycloaddition, resulting in a ketone/aldehyde and a Criegee intermediate. The red arrows (top) and blue arrows (bottom) represent the two routes in which the molozonide can undergo the retro 1,3-dipolar cycloaddition

## Results

### Structure Elucidation by Traditional NMR and Mass Spectrometry

**Techniques.** In ongoing studies of the genetic and secondary metabolite profiles of *Aspergillus fischeri*, which is of interest due to its close evolutionary relationship with the human pathogen *Aspergillus fumigatus*, we have characterized a series of fungal metabolites, including seven known compounds, one new natural product, and two new compounds.<sup>16</sup> The structure of one of the latter, which was assigned the trivial name ent-sartorypyrone E (**1**), was elucidated by traditional spectroscopic and spectrometric techniques, and all of those data are discussed in the Supporting Information. Mosher's esters analysis<sup>95</sup> was attempted to assign the absolute configuration of position 20, but unfortunately, those data were inconclusive. This was supported by the literature, which showed that this methodology does not work well for vicinal diols.<sup>381</sup> Instead, the Snatzke method would need to be implemented, but due to the paucity of sample, this was not conducted.<sup>382-384</sup> During the final drafting of this manuscript, the structure of sartorypyrone E was published by Bang et al.,<sup>385</sup> and our NMR data were in agreement. However, those authors reported performing Mosher's ester analysis, establishing the hydroxy in the S configuration. Since the measured  $[\alpha]_{D}^{20}$  value for **1** was opposite in

sign, although of greater magnitude, to the value reported for sartorypyrone E,<sup>385</sup> we hypothesized position 20 as *R*, as suggested by the trivial name ent-sartorypyrone E (**1**).

When the structure of **1** was solved via NMR data, the double bond locations were assigned through HMBC and COSY correlations (Figure 103). The double bond between positions 8 and 9 was identified by the COSY correlation of H-26 to H-8 and the HMBC correlations of H-10 to C-8, C-9, and C-26 and H-8 to C-3, C-10, and C-26. The double bond between positions 12 and 13 was identified by the COSY correlations of H-25 to H-12 and the HMBC correlations of H-14 to C-12, C-13, and C-25 and H-12 to C-10, C-14, and C-15. The double bond between positions 16 and 17 was identified by the COSY correlation of H-24 to H-16 and the HMBC correlations of H-18 to C-16, C-17, and C-24 and H-16 to C-14, C-18, and C-24. Thus, 2D NMR data were instrumental for positioning the double bonds.

### Structure Elucidation by Traditional NMR and Mass Spectrometry

**Techniques. For Compound 1.** Ent-sartorypyrone E (**1**) was obtained as a white solid with a molecular formula of  $C_{26}H_{40}O_5$  as determined via HRESIMS along with  $^1H$ ,  $^{13}C$ , and edited-HSQC NMR data (Table 7.2), demonstrating an index of hydrogen deficiency of 7. Inspection of the MS and NMR data suggested **1** as an analogue of sartorypyrone A (**2**).<sup>162</sup> For example, **1** showed a trisubstituted unsaturated  $\delta$ -lactone moiety, as noted by two conjugated double bonds ( $\delta_C$  100.6, 165.5, 100.5, and 160.3 for C-3, C-4, C-5, and C-6 respectfully) containing one olefinic proton ( $\delta_H$  5.75 for H-5), both of which were conjugated with an ester ( $\delta_C$  165.6 for C-2). Additional similarities included NMR signals characteristic of two sequential isoprene units, which were connected to the  $\alpha$ -position ( $\delta_C$  100.6 for C-3) of the  $\delta$ -lactone moiety. Key differences between compound **2**<sup>162</sup> and **1** were in the terminal part of the terpenoid side chain. Specifically, compound **1** lacked the

terminal cyclohexane moiety along with the acetyl group seen in **2**, which were replaced by a dihydroxy unsaturated isoprene unit, as indicated by NMR data characteristic of two methyls ( $\delta_H/\delta_C$  1.2/26.4; 1.2/23.2 for  $\text{CH}_3$ -22 and  $\text{CH}_3$ -23, respectively), two methylenes ( $\delta_H/\delta_C$  2.22/2.06/26.8; 1.40/1.59/29.5 for  $\text{CH}_2$ -18 and  $\text{CH}_2$ -19, respectively), one oxymethylene ( $\delta_H/\delta_C$  3.36/78.3, for CH-20), and a quaternary oxygenated carbon ( $\delta_C$  73.1 for C-21) (Figures 110 and 111). These data, along with further analysis of the 2D-NMR data, including COSY and HMBC experiments (Figure 103), yielded the structure of compound **1** (Figures 112-114).

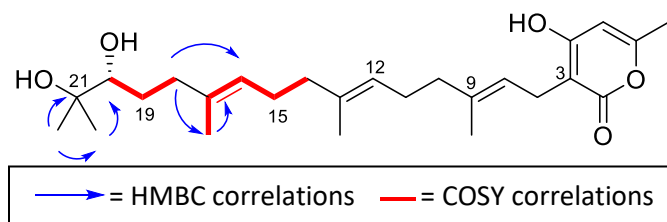


**Figure 103.** Key COSY and HMBC correlations for compound **1**

**Analysis of Double Bond Positions in Pure Compounds by OzID-MS.** The OzID-MS technique was tested on the fungal metabolites ent-sartorypyrone E (**1**), sartorypyrone A (**2**), sorbicillin (**3**),<sup>386, 387</sup> trichodermic acid A (**4**),<sup>388</sup> and AA03390 (**5**),<sup>389</sup> where the observed accurate masses corresponding to the carbonyl/Criegee product ions confirmed the placement of double bonds in these molecules. Infusion of sodium acetate into the mass spectrometry system (see Experimental) was used to increase the abundance of sodiated adducts, which are needed to effect fragmentation in the OzID-MS experiment.<sup>80, 81, 390</sup>

When performing OzID-MS on compound **1**, the sodium ion can associate with the hydroxy moieties at the end of the isoprene chain (left side of molecule) or the

oxygens in the lactone ring (right side of molecule), which is why all the theoretically possible carbonyl and Criegee ions were observed from both ends of the molecule. Regardless of where sodium associated with **1** (i.e.  $[M + Na]^+$ ), the targeted parent ion was observed at  $m/z$  455.2772. When sodium associated with the hydroxys at the ends of the isoprene chain, the double bonds were cleaved into ketones (previously di-substituted) and Criegee ions (Figure 104A). The ketones were observed at positions C-9 ( $m/z$  319.2248), C-13 ( $m/z$  251.1634), and C-17 ( $m/z$  183.0992), and the Criegee ions were observed at positions C-9 ( $m/z$  335.2202), C-13 ( $m/z$  267.1579), and C-17 ( $m/z$  199.0954) (Table 7.3). When sodium associated with the lactone ring, the double bonds were cleaved into aldehydes (previously mono-substituted) and Criegee ions (Figure 104). The aldehydes were observed at positions C-8 ( $m/z$  191.0332), C-12 ( $m/z$  259.0954), and C-16 ( $m/z$  327.1578), and the Criegee ions were observed at positions C-8 ( $m/z$  207.0287), C-12 ( $m/z$  275.0902) and C-16 ( $m/z$  343.1526) (Table 7.3). To verify the unique product ions of OzID-MS, **1** was re-analyzed under the identical parameter settings, but with argon in replacement of ozone (Figure 104B); as expected, the OzID fragmentation patterns were not observed under these conditions.

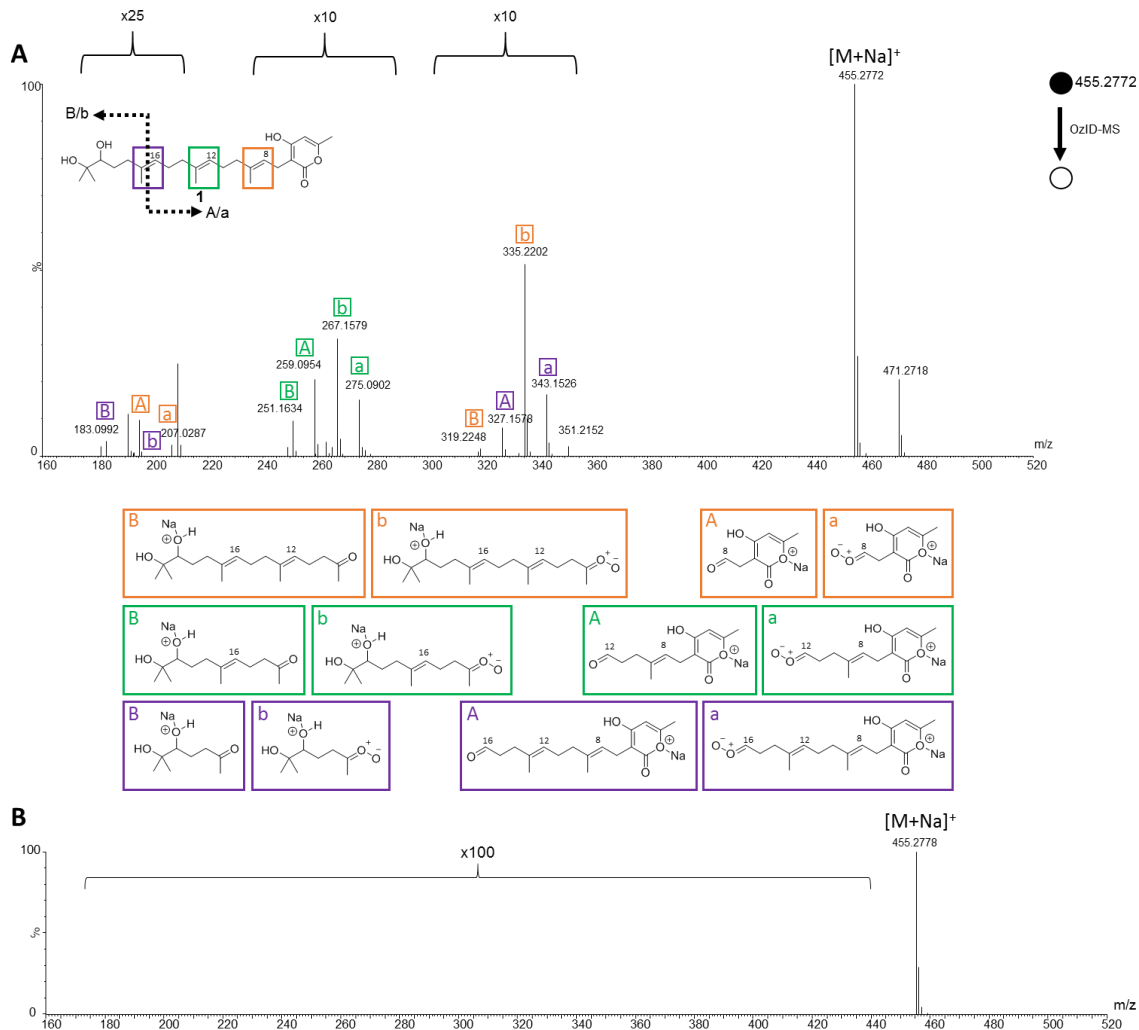


**Figure 104.** **A:** The OzID-MS spectrum of ent-sartorypyrone E (**1**) after targeted OzID fragmentation. The structure of **1** is shown on the top left. The purple, green, and orange boxes around the diterpene double bonds indicate positions where ozonolysis occurred. The informative OzID fragments are labeled with the colors corresponding to the structure. The capital letters represent the ketone fragments, and the lower-case letters represent the Criegee ion fragments. The A/a corresponds to the sodium ion associating with the lactone ring (right side of the molecule), whereas the B/b corresponds to the sodium ion associating with hydroxys at the end of the isoprene chain (left side of the molecule). The OzID-MS products (shown under spectrum) are color and letter coded to represent the cleaved double bond, and these data are tabulated in Supporting Information Table 7.3. **B:** Compound **1** being analyzed in argon, to demonstrate that the fragments in A are unique to OzID-MS

A known metabolite, sartorypyrone A (**2**), was also isolated from *I*, and it was subjected to OzID-MS to validate the technique, illustrating its use as an orthogonal tool for pinpointing the location of double bonds within a chain. Given their structural similarities, sodium associated with compound **2** in a manner largely analogous to what was observed with **1**. For instance, regardless of where sodium associated with the molecule (i.e.  $[M + Na]^+$ ), the targeted parent ion was observed at *m/z* 479.2784. When the sodium associated with lactone ring, there were two pairs of OzID product ions, corresponding to double bonds at C-12 (*m/z* 259.0984 and 275.0936) and C-8 (*m/z* 191.0335 and 207.0283), recognized as aldehyde (previously mono-substituted) and Criegee ions, respectively, in each pair. However, when sodium associated with the ester, only a pair of ozonolysis product ions were observed, representing those induced at C-8 and recorded at *m/z* 343.1948 and 359.2246, corresponding to the ketone and Criegee ions, respectively (Figure 105 and Table 7.6). While this was slightly different than what was observed with **1**, since C-12 was not cleaved, we were not surprised by these results. OzID-MS is known to be a charged-induced reaction, and as such, the distance and interaction between where the sodium adduct was formed, relative to the double bond, can hinder the efficiency of ozonolysis.<sup>390</sup> An example of this phenomenon is sphingomyelin, where OzID-MS was able to characterize the double bonds in the fatty acyl chains, but not the double bond on the long chain base.<sup>391</sup> This is an important distinction for OzID-MS, as the distance of the double bond(s) from where the sodium associates to form the adduct is important. Even though it was not possible to obtain product ions from ozonolysis at the C-12 position when sodium associated with the left side of molecule, the data from the OzID products from when sodium associated with the lactone ring confirmed the position of this carbon-carbon double bond.

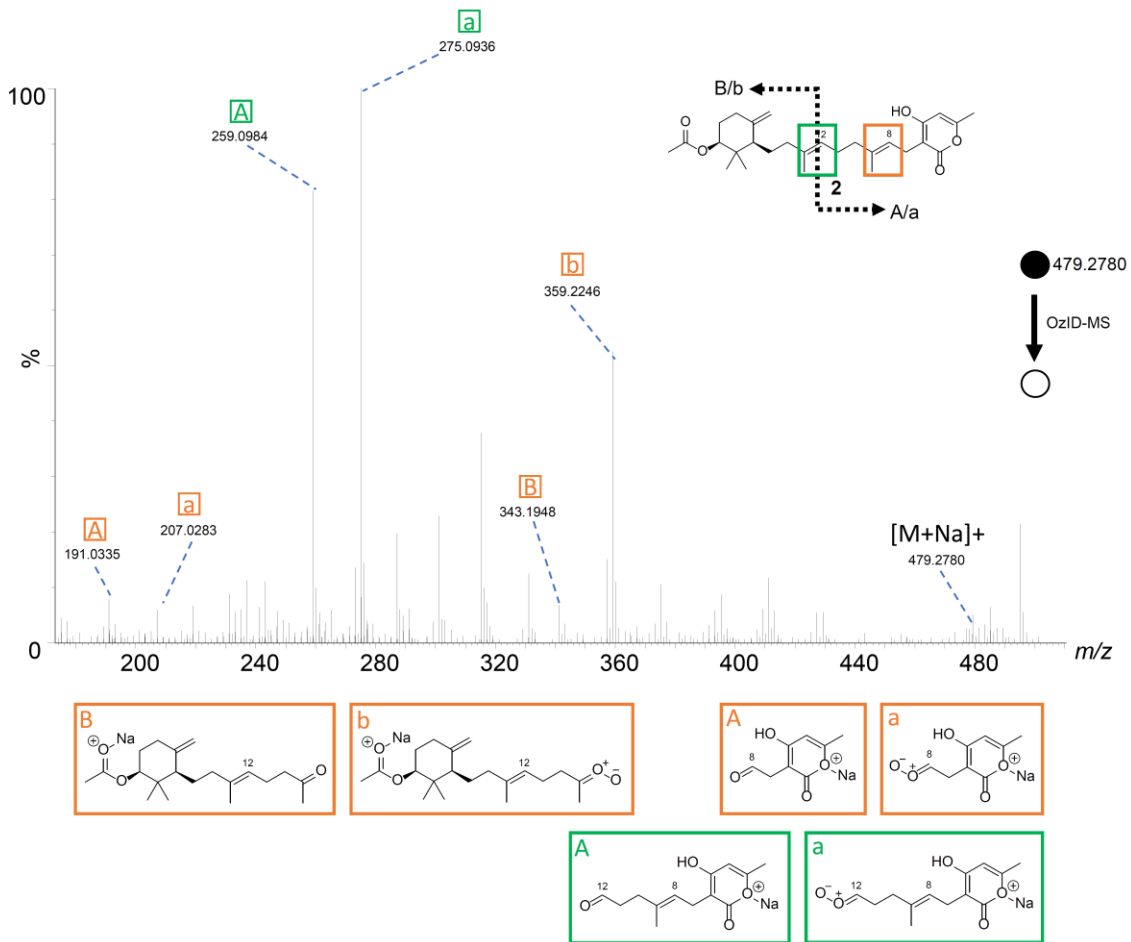


**Figure 105.** The OzID-MS spectrum of **2** after targeted OzID fragmentation. The structure of **2** is shown on the top left. The green and orange boxes around the double bonds indicate positions where the ozonolysis occurred. The informative OzID fragments are labeled with the colors corresponding to the structure, analogous to those in Figure 104. The OzID-MS products (shown under spectrum) are color and letter coded to represent the double bond that was cleaved, and these data are tabulated in Table 7.6

Next, a selection of other fungal metabolites from our compound library were examined, such as the polyketide **3**, which has conjugated double bonds and was first described from *Penicillium notatum*.<sup>386, 387</sup> In a conjugated system, in addition to the aldehyde/ketone and Criegee ion fragments, a diagnostic epoxide is observed.<sup>80</sup> In this example, sodium can associate with the hydroxys or ketone to form a singly charged  $[M + Na]^+$  species observed at  $m/z$  255.1053. The double bonds at positions C-2' ( $m/z$  209

217.0475) and C-4' (*m/z* 243.0625) were cleaved into aldehydes, confirming their positions (Figure 106 and Table 7.7). A highlight of this structure was the unique formation of the epoxide ring  $[M+Na+16]^+$  caused by the loss of dioxygen and a hydrocarbon radical from a conjugated double bond.<sup>392</sup> This observation indicated conjugated double bonds, which was confirmed by the product ion of an epoxide ring between positions C-4' and C-5' (*m/z* 271.0966), which has been observed previously with the use of this technique to discern conjugated double bonds in fatty acids.<sup>80</sup>

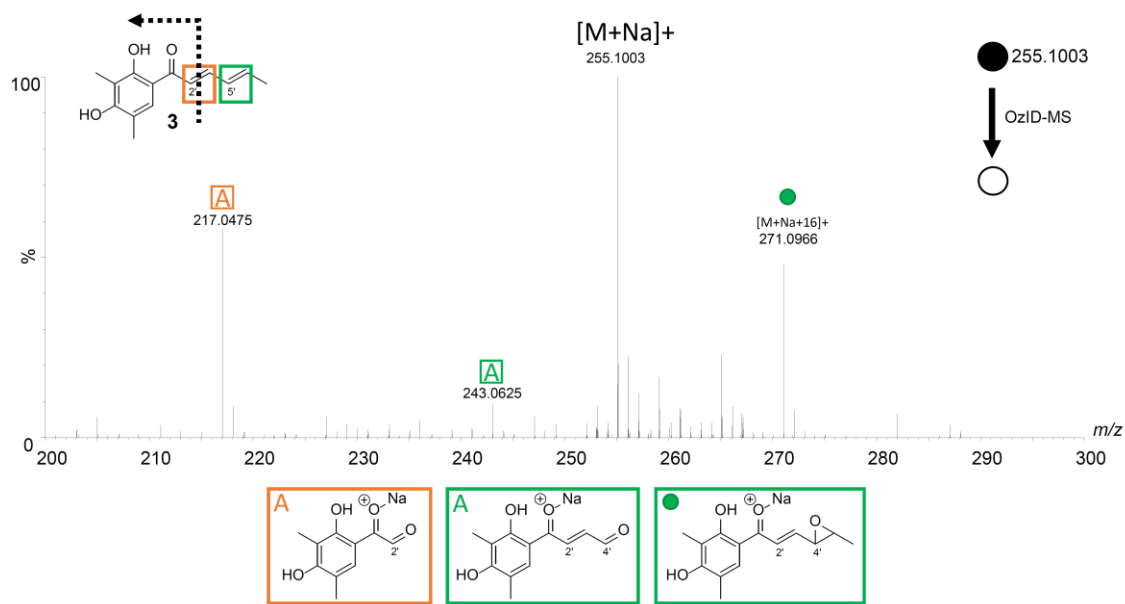
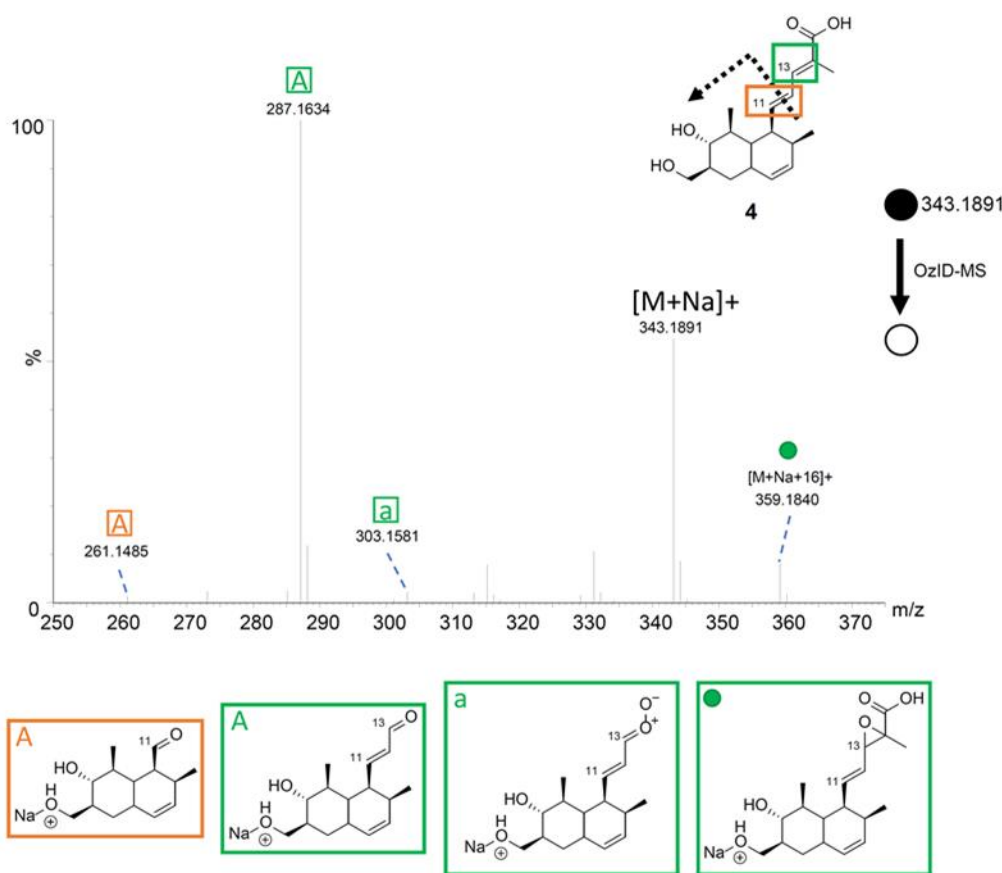


**Figure 106.** The OzID-MS spectrum of **3** after targeted OzID fragmentation. The structure of **3** is shown on the top left. The green and orange boxes around the double bonds indicate positions where ozonolysis occurred. The informative OzID fragments are labeled with the colors corresponding to the structure, analogous to those in Figure 104. The OzID-MS products (shown under spectrum) are color and letter coded to represent the double bond that was cleaved, and these data are tabulated in Table 7.7

Compound **4** is a terpenoid with conjugated double bonds that was described originally from the endophytic fungus *Trichoderma spirale*.<sup>388</sup> The sodiated adduct of this compound was found to favor the hydroxy moieties on the ring based on the recorded

OzID-MS product ions. Besides the expected ozonolysis product ions observed at  $m/z$  261.1485, 287.1632, and 303.1581, a product ion of  $[M+Na+16]^+$  was also obtained at  $m/z$  359.1840, analogous to **3** and as expected for a conjugated system (Figure 107 and Table 7.8).



With compound **5** (a meroterpenoid originally described from the deep-sea fungus *Phomopsis lithocarpus*),<sup>389</sup> the diagnostic ion  $[M+Na+16]^+$  was observed at  $m/z$  469.2548 due to conjugation. In addition, the expected OzID-MS products, specifically the aldehyde ( $m/z$  371.1844 and 397.1985) and Criegee ions ( $m/z$  387.1808 and 413.2004) were observed (Figure 108 and Table 7.9).

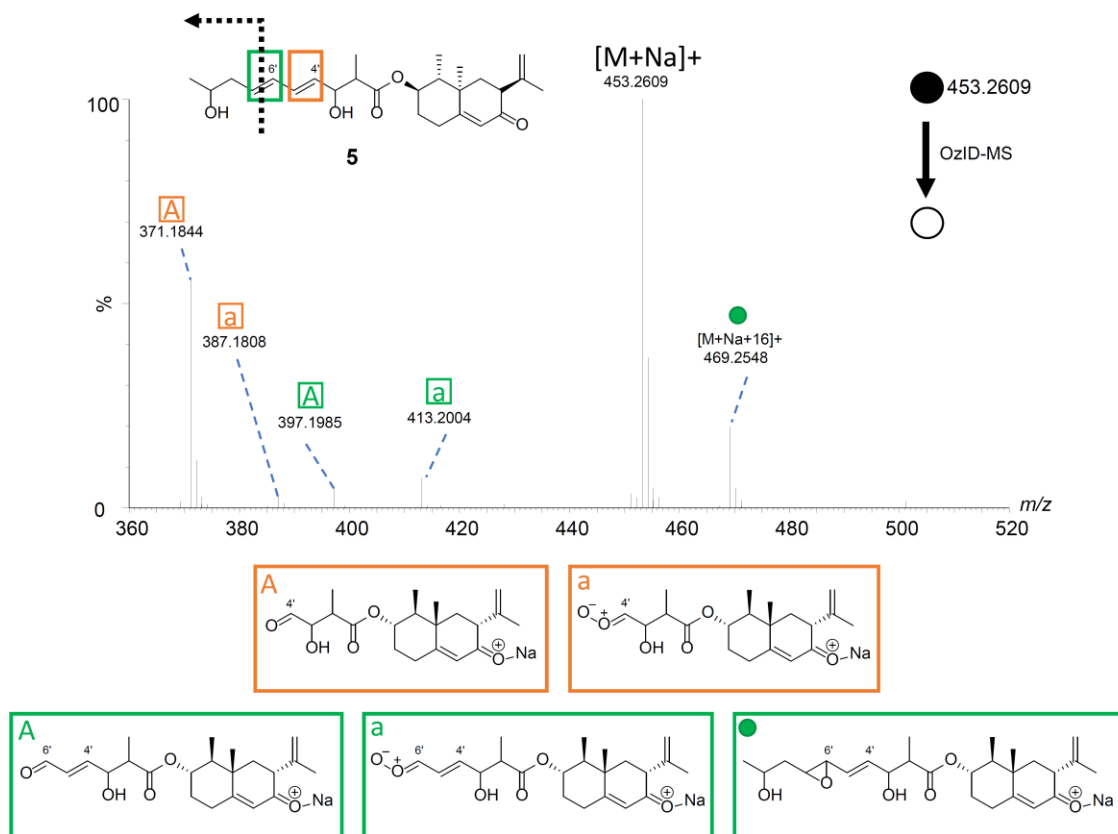


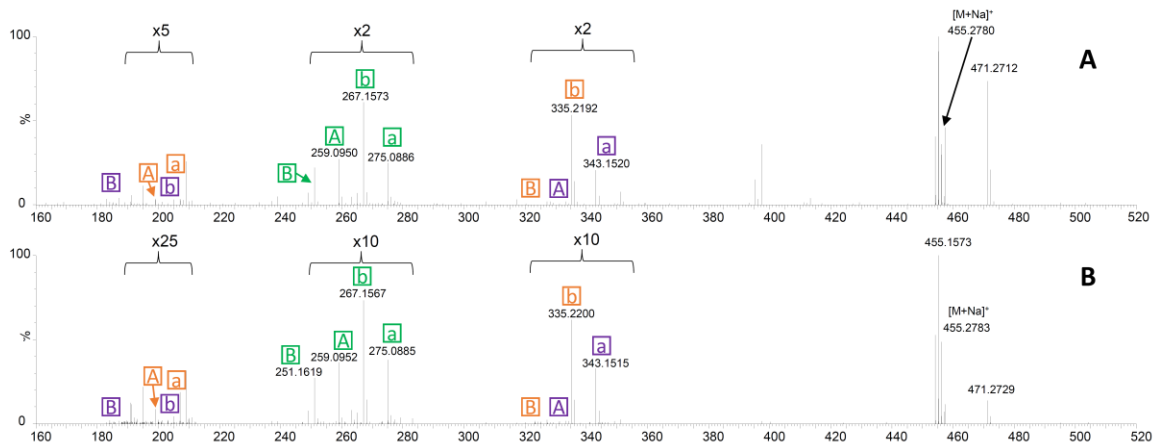
**Figure 108.** The OzID-MS spectrum of **5** after targeted OzID fragmentation. The structure of **5** is shown on the top left. The green and orange boxes around the double bonds indicate positions where the ozonolysis occurred. The informative OzID fragments are labeled with the colors corresponding to the structure, analogous to those in Figure 104. The OzID-MS products (shown under spectrum) are color and letter coded to represent the double bond that was cleaved, and these data are tabulated in Table 7.9

As could be seen from data generated by analyzing compounds **1-5**, OzID-MS can be used to verify the position of carbon-carbon double bonds in secondary metabolites. Since ozonolysis is sensitive and results in predictable fragmentation patterns, the expected product ions can be calculated and matched with the acquired data. This represents an efficient and orthogonal approach to confirm the assignment of double bond positions. In addition, the signal of  $[M+Na+16]^+$  can be used as a diagnostic ion to confirm the presence of conjugated double bonds. In total, OzID-MS confirmed the locations of the double bonds in a series of structurally diverse fungal secondary metabolites, serving as orthogonal confirmation of double bond positioning based on NMR experiments.

**Structural Confirmation from Extract and *in situ* by Direct Infusion OzID-MS.** To test whether this technique could work in the context of a multi-component mixture, the organic extract of a fermentation of *Aspergillus fischeri* was subjected to OzID-MS. The precursor ion was targeted, and then OzID-MS was performed. The fragment ions from this experiment were identical to those observed with the pure compound (**1**) (Figures 104 and 109). While the intensity of the signals was not as robust, we could confidently assign the positions of the double bonds. This was of particular relevance, since **1** was only a minor component of the extract (Figure 115).

In addition, there is growing interest in studying the chemistry of nature *in situ* via a variety of techniques.<sup>393, 394</sup> As such we tested if double bond placement could be elucidated by coupling OzID-MS with the droplet probe.<sup>297, 351</sup> We envisaged this could be powerful for co-culture studies, where interspecific interactions may stimulate the biosynthesis of unique metabolites.<sup>15, 17, 341</sup> A Petri dish of *l* was analyzed via this technique, and the sodiated precursor ion of compound **1** was observed in the full scan

spectrum. Subsequently, OzID-MS was performed through the targeted analysis of the precursor ion. The product ions that were present in the complex and *in situ* extracts mirrored those of the pure compound (Figures 104 and 109). These data confirmed that OzID-MS can also aid as an orthogonal structure elucidation tool for a compound within the context of an extract and/or *in situ*, albeit at a lower concentration (Figure 109, Tables 7.4 and 7.5). In addition, these results demonstrated the sensitivity of approach, regardless of the low abundance of the targeted compound in the extract or *in situ*.

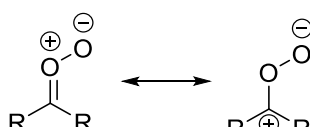


**Figure 109.** The OzID-MS studies of *Aspergillus fischeri* showing the analysis of compound 1 in the context of an extract (panel A) and from *in situ* sampling of a Petri dish of a life culture (panel B). The fragmentation patterns in both cases are analogous to those in Figure 104, and these data are tabulated in Tables 7.4 and 7.5

In summary, OzID-MS shows promise as a methodology that can be used to support the positioning of double bonds in secondary metabolites. The most straight forward approach may be to first use NMR experiments to elucidate a structure, and then employ OzID-MS fragment ions to confirm and/or pinpoint the location of carbon-carbon double bonds. While only a limited set of fungal metabolites were analyzed, we do not expect unforeseen challenges with other natural products, particularly since its

application in the lipidomics community continues to grow. The predictable nature of the fragmentation patterns expected in an OzID-MS experiment may lead to emerging tools, such as artificial intelligence,<sup>395, 396</sup> and again, the omics community may take the lead in this regard, but the results should benefit natural products research too. In addition, it is very tantalizing to add this technique to the growing spectrum of tools that are being used to study natural products *in situ*, particularly since the sensitivity of mass spectrometry can be capitalized upon to select for ions of interest for OzID-MS analysis, even those in low abundance. Key considerations for implementing this technique have been summarized (Table 7.1), and it is worth noting that this system was assembled using commercially available components that has been detailed previously.<sup>80, 81</sup>

**Table 7.1.** Key considerations for performing OzID-MS analysis.

Observation	Diagnostics
Why infuse salt adducts such as Na <sup>+</sup> ?	The counter ion aids in OzID fragmentation. Essentially, the increased intensity of the ozonide ions leads to an increase in the ozonolysis efficiency. <sup>390</sup> Other salts could be used, such as those that produce Li <sup>+</sup> ions.
What differentiates the observation of aldehyde vs. ketone peaks?	This is based on the double bond substitution before OzID fragmentation occurs. If the carbon was di-substituted, then it becomes a ketone. Alternatively, if it was mono-substituted it becomes an aldehyde.
What is the Criegee ion?	A Criegee ion is a carbonyl oxide zwitterion. 

Why is OzID-MS observed to occur from both sides of a molecule?	The counter ion (i.e. Na <sup>+</sup> ) typically associates with oxygenation, and if two spots are available on either side of the metabolite, then both the theoretical carbonyl/Criegee ions pairs are observed.
Why are not all of the “potential” fragments produced for every double bond?	The distance between where the adduct associates and the double bond affects reactivity. <sup>80, 391</sup>
Why is [M+Na+16] <sup>+</sup> a diagnostic observation?	This ion confirms that the metabolite has conjugated double bonds due to the formation of an epoxide. <sup>80, 392</sup>

## Materials and Methods

**General Experimental Procedures.** Optical rotation data were obtained using a Rudolph Research Autopol III polarimeter, and UV spectra were measured with a Varian Cary 100 Bio UV-vis spectrophotometer. The NMR data were collected using a JOEL ECS-400 spectrometer, which was equipped with a JOEL normal geometry broadband Royal probe, and a 24-slot autosampler, and operated at 400 MHz for <sup>1</sup>H, a JOEL ECA-500 spectrometer operating at 500 MHz for <sup>1</sup>H, or an Agilent 700 MHz spectrometer, equipped with a cryoprobe, operating at 700 MHz for <sup>1</sup>H and 175 MHz for <sup>13</sup>C. HRMS experiments utilized either a Thermo LTQ Orbitrap XL mass spectrometer or a Thermo Q Exactive Plus; both were equipped with an electrospray ionization source. A Waters Acquity UPLC was utilized for both mass spectrometers, using a BEH C<sub>18</sub> column (1.7 µm; 50 mm x 2.1 mm) set to a column temperature of 40°C and a flow rate of 0.3 mL/min. The mobile phase consisted of a linear gradient of CH<sub>3</sub>CN-H<sub>2</sub>O (acidified with 0.1% formic acid), starting at 15% CH<sub>3</sub>CN and increasing linearly to 100% CH<sub>3</sub>CN over 8 min, with a 1.5 min hold before returning to the starting conditions. OzID-MS data were collected using a Waters Synapt G2 HDMS. The HPLC separations were performed with

an Atlantis T3 C<sub>18</sub> semi-preparative (5 µm; 10 x 250 mm) and preparative (5 µm; 19 x 250 mm) columns, at a flow rate of 4.6 mL/min and 16.9 mL/min, respectively, with a Varian Prostar HPLC system equipped with a Prostar 210 pumps and a Prostar 335 photodiode array detector (PDA), with the collection and analysis of data using Galaxie Chromatography Workstation software. Flash chromatography was performed on a Teledyne ISCO Combiflash Rf 200 and monitored by both ELSD and PDA detectors.

**Fungal Material.** *Aspergillus fischeri* strain NRRL 181 was obtained from ARS Culture Collection (NRRL), and as described previously,<sup>15, 16</sup> the large-scale fermentation was grown on solid breakfast oatmeal (Old-fashioned breakfast Quaker oats). This was prepared by adding 10 g oatmeal to a 250 mL Erlenmeyer flask with 16 mL of DI-H<sub>2</sub>O, which was autoclaved at 121°C for 30 min. After inoculation, the culture was grown for 14 days at room temperature.

**Extraction and Isolation.** To each of the solid fermentation cultures (10 flasks) of *I*, 60 mL of CHCl<sub>3</sub>-MeOH (1:1, v/v) were added, and the cultures were chopped using a spatula followed by shaking overnight (~ 16 hrs.). The resulting slurries were vacuum filtered, and 90 mL of CHCl<sub>3</sub> and 150 mL of DI H<sub>2</sub>O were added to the filtrate. This 4:1:5 CHCl<sub>3</sub>:MeOH:H<sub>2</sub>O mixture was partitioned in a separatory funnel, and the organic layer was drawn off and evaporated to dryness *in vacuo*. This sample was then reconstituted and partitioned with 100 mL CH<sub>3</sub>CN:MeOH (1:1, v/v) and 100 mL of hexanes. The organic layer was then evaporated to dryness to generate 440mg of the organic extract. The sample was then dissolved in CHCl<sub>3</sub>, absorbed onto celite 545 (Acros Organics, celite 545), and fractioned by normal phase flash chromatography using a gradient of hexane-CHCl<sub>3</sub>-CH<sub>3</sub>OH at an 18 mL/min flow rate and 90.0 column volumes over 24.0 min to produce five fractions. Fraction 1 was purified further via preparative HPLC using

a gradient system 20:80 to 100:0 of CH<sub>3</sub>CN-H<sub>2</sub>O (with 0.1% formic acid) over 30 min at a flow rate of 16.9 mL/min to yield seven subfractions. Subfraction 4 yielded **2** (2.88 mg), which eluted at approximately 17.0 min. Fraction 3 was purified further via preparative HPLC using the same gradient system to yield ten subfractions. Subfraction 4 yielded **1** (1.17 mg), which eluted at approximately 17.2 min.

*ent-sartorypyrone E (1)*: white solid;  $[\alpha]_D^{20} = +10$  (*c* 0.02, MeOH); UV (MeOH)  $\lambda_{\text{max}}$  (log  $\epsilon$ ) 286 (2.85), 239 (2.83) nm; <sup>1</sup>H and <sup>13</sup>C NMR data, Table 7.2; HRESIMS [M + H]<sup>+</sup> 433.2941 (calculated for C<sub>26</sub>H<sub>41</sub>O<sub>5</sub>, 433.2948).

**General Procedure for OzID-MS.** The OzID-MS experiment was performed on the modified Waters Synapt G2 HDMS as reported previously in detail.<sup>80, 81</sup> A commercially available O<sub>3</sub> generator [O<sub>3</sub> MEGA (MKS Inc.)] was used to convert O<sub>2</sub> to O<sub>3</sub> (6%), and it was plumbed to the trap and transfer cell in the TRIWAVE region through a t-valve, essentially replacing the commonly used collision gas (argon) (Figure 119). Previously, we developed a method, coined "ion dam," to enhance the ozonolysis efficiency of unsaturated molecules with ozone inside the high-resolution Traveling wave MS.<sup>81</sup> This works by having ions indirectly prolonged in the trap cell to extend their reaction time with ozone. O<sub>3</sub> was introduced to the system at 4 mL/min, creating a pressure of 1.32x10<sup>-2</sup> mbar in the trap cell, which is the reaction chamber for the ozonolysis gas phase reaction. The excess or unused O<sub>3</sub> is delivered to the converting chamber, creating O<sub>2</sub>, which is sent to the exhaust system. A commonly voiced concern is that O<sub>3</sub> can be highly corrosive due to its oxidative properties; however, in over five years of operation, such damage has not been observed on this system, likely because only a small amount of O<sub>3</sub> is needed to induce ozonolysis. Similar experiments have

been reported in the literature using several different mass spectrometry platforms and/or vendors.<sup>79, 392, 397, 398</sup>

**Pure Compound and Extract Analysis via Direct Infusion of OzID-MS.** The Synapt G2 HDMS was directly infused with 10 mmol sodium acetate at 8 µL/min using an automated syringe pump at the beginning of every injection series to increase the relative abundance of sodium ions. Pure compounds were prepared at a concentration of 0.05 mg/mL and the organic extract at 2.0 mg/mL, both in MeOH, and kept at -20°C until analyzed. Pure compounds and an organic extract were directly infused at 8 µL/min using an automated syringe pump in the positive mode; due to the system being flushed with sodium acetate the predominant ions were sodiated adducts.

The ESI source conditions were finalized as: spray voltage, 3.0 kV; sampling cone, 45 V; extraction cone, 6 V; source temperature, 100 °C; desolvation temperature, 200 °C; cone gas flow, 50 L/h; desolvation gas flow, 500 L/h. Isolation of precursor ions was carried out in the quadrupole at ~1Th isolation width (LM=16, HM =15). All spectra were acquired for 30s at 0.5s/scan. For pure compound OzID-MS, the traveling wave in the trap was optimized and operated accordingly to the “ion dam” setting,<sup>81</sup> i.e. trap entrance, 5.0V; bias, 2.0V; trap dc, 0.1V; exit, 0V; trap wave velocity, 8m/s; wave height, 0.2V; for extract, same parameters were applied except trap entrance was set to 3V and dc to -0.5V to increase signal intensity. Default instrument settings for all the remaining parameters were applied. The instrument was calibrated daily in Resolution mode using sodium iodide following manufacturer’s instructions obtaining less than 5 ppm RMS residual mass. Both the full scan and MS/MS levels were mass-corrected traceable to the reference lock mass using MassLynx v4.1 instrument control software (Waters Corp.).

**In situ OzID-MS.** Sampling of the surface of the fungus *in situ* was performed by a CTC/LEAP HTC PAL auto-sampler (LEAP Technologies Inc.) that was converted to an automated droplet probe system, as detailed previously.<sup>297, 351</sup> Briefly, the microextractions (5 µL) were performed by using MeOH:H<sub>2</sub>O (1:1, v/v), with water being for droplet retention and MeOH for the microextraction, on the surface of the fungus. The droplet was dispensed at a rate of 2 µL/s from the needle, held on the surface for 2 s, then withdrawn at the same rate with each droplet extraction performed thrice to concentrate the sample. Traditionally, the droplet probe is connected to a UPLC-MS system, which is how the droplet is then analyzed.<sup>156, 342, 399, 400</sup> However, currently software is not available to monitor the CTC/LEAP HTC PAL autosampler with the Synapt G2 HDMS. Thus, after conducting the microextraction via droplet probe, the solution was loaded into an offline 20 µL sample loop. A solvent system MeOH:H<sub>2</sub>O (1:1, v/v) controlled by the Synapt G2 HDMS was connected to the sample loop to carry the sample to the ESI source at 5 µL/min. The OzID-MS analysis instrument settings were the same as described above for analysis of extract.

## Supplementary Data

**Table 7.2.** NMR table of ent-sartorypyrone E (**1**)

Position	$\delta_{\text{H}}$	$\delta_{\text{C}}$	Mult (J in Hz)
2		165.6	
3		100.6	
4		165.5	
5	5.75	100.5	d (1.1)
6		160.3	
7	3.23	23.0	d (7.4)
8	5.31	120.6	m
9		140.9	
10	2.10	39.5	m
11	2.12	25.8	m
12	5.04	123.6	m
13		135.6	
14	1.99	39.4	m
15	2.08	26.1	m
16	5.15	125.1	m
17		134.7	
18	2.22	26.8	m
	2.06		m
19	1.40	29.5	dddd (14.0, 10.6, 8.4, 5.7)
	1.59		m
20	3.36	78.3	dd (10.6, 1.9)
21		73.1	
22	1.15	23.2	s
23	1.20	26.4	s
24	1.60	15.8	s
25	1.58	16.0	s
26	1.77	16.3	s
27	2.18	19.7	s

**Table 7.3.** Table of accurate masses for the OzID products of compound **1**

OzID-MS Products	Molecular Formula	Measured Value	Calculated Value	Accuracy (in ppm)
Parent Mass	$C_{26}H_{40}NaO_5^+$	455.2772	455.2773	0.2
B	$C_{18}H_{32}NaO_3^+$	319.2248	319.2249	0.3
a	$C_8H_8NaO_5^+$	207.0287	207.0269	8.7
b	$C_{18}H_{32}NaO_4^+$	335.2202	335.2198	1.2
A	$C_8H_8NaO_4^+$	191.0332	191.0320	6.3
B	$C_{13}H_{24}NaO_3^+$	251.1634	251.1623	4.4
a	$C_{13}H_{16}NaO_5^+$	275.0902	275.0895	2.5
b	$C_{13}H_{24}NaO_4^+$	267.1579	267.1573	2.2
A	$C_{13}H_{16}NaO_4^+$	259.0954	259.0946	3.1
B	$C_8H_{16}NaO_3^+$	183.0992	183.0997	2.7
a	$C_{18}H_{24}NaO_5^+$	343.1526	343.1522	1.2
b	$C_8H_{16}NaO_4^+$	199.0954	199.0946	4.0
A	$C_{18}H_{24}NaO_4^+$	327.1578	327.1573	1.5

**Table 7.4.** Table of accurate masses for the OzID products of compound **1** in an extract

OzID-MS Products	Molecular Formula	Measured Value	Calculated Value	Accuracy (in ppm)
Parent Mass	C <sub>26</sub> H <sub>40</sub> NaO <sub>5</sub> <sup>+</sup>	455.2780	455.2773	1.5
B	C <sub>18</sub> H <sub>32</sub> NaO <sub>3</sub> <sup>+</sup>	319.2239	319.2249	3.1
a	C <sub>8</sub> H <sub>8</sub> NaO <sub>5</sub> <sup>+</sup>	-	207.0269	-
b	C <sub>18</sub> H <sub>32</sub> NaO <sub>4</sub> <sup>+</sup>	335.2192	335.2198	1.8
A	C <sub>8</sub> H <sub>8</sub> NaO <sub>4</sub> <sup>+</sup>	191.0329	191.0320	4.7
B	C <sub>13</sub> H <sub>24</sub> NaO <sub>3</sub> <sup>+</sup>	251.1616	251.1623	2.8
a	C <sub>13</sub> H <sub>16</sub> NaO <sub>5</sub> <sup>+</sup>	275.0886	275.0895	3.3
b	C <sub>13</sub> H <sub>24</sub> NaO <sub>4</sub> <sup>+</sup>	267.1573	267.1573	0.0
A	C <sub>13</sub> H <sub>16</sub> NaO <sub>4</sub> <sup>+</sup>	259.0950	259.0946	1.5
B	C <sub>8</sub> H <sub>16</sub> NaO <sub>3</sub> <sup>+</sup>	183.0983	183.0997	7.6
a	C <sub>18</sub> H <sub>24</sub> NaO <sub>5</sub> <sup>+</sup>	343.1520	343.1522	0.6
b	C <sub>8</sub> H <sub>16</sub> NaO <sub>4</sub> <sup>+</sup>	199.0937	199.0946	4.5
A	C <sub>18</sub> H <sub>24</sub> NaO <sub>4</sub> <sup>+</sup>	327.1567	327.1573	1.8

**Table 7.5.** Table of accurate masses for the OzID products of compound **1** *in situ*

OzID-MS Products	Molecular Formula	Measured Value	Calculated Value	Accuracy (in ppm)
Parent Mass	$C_{26}H_{40}NaO_5^+$	455.2783	455.2773	2.2
B	$C_{18}H_{32}NaO_3^+$	319.2241	319.2249	2.5
a	$C_8H_8NaO_5^+$	-	207.0269	-
b	$C_{18}H_{32}NaO_4^+$	335.2200	335.2198	0.6
A	$C_8H_8NaO_4^+$	191.0332	191.0320	6.3
B	$C_{13}H_{24}NaO_3^+$	251.1619	251.1623	1.6
a	$C_{13}H_{16}NaO_5^+$	275.0885	275.0895	3.6
b	$C_{13}H_{24}NaO_4^+$	267.1567	267.1573	2.2
A	$C_{13}H_{16}NaO_4^+$	259.0952	259.0946	2.3
B	$C_8H_{16}NaO_3^+$	183.1024	183.0997	14.7*
a	$C_{18}H_{24}NaO_5^+$	343.1515	343.1522	2.0
b	$C_8H_{16}NaO_4^+$	199.0919	199.0946	13.6*
A	$C_{18}H_{24}NaO_4^+$	327.1583	327.1573	3.1

\* The measured value was close to the noise level which caused the ppm shift to be out of the 10 ppm range.

**Table 7.6.** Table of accurate masses for the OzID products of compound 2

OzID-MS Products	Molecular Formula	Measured Value	Calculated Value	Accuracy (in ppm)
Parent Mass	C <sub>28</sub> H <sub>40</sub> O <sub>5</sub> Na <sup>+</sup>	479.2784	479.2773	2.3
B	C <sub>20</sub> H <sub>32</sub> O <sub>3</sub> Na <sup>+</sup>	343.1948	343.2249	87.7
a	C <sub>8</sub> H <sub>8</sub> O <sub>5</sub> Na <sup>+</sup>	207.0283	207.0269	6.8
b	C <sub>20</sub> H <sub>32</sub> O <sub>4</sub> Na <sup>+</sup>	359.2246	359.2198	13.3
A	C <sub>8</sub> H <sub>8</sub> O <sub>4</sub> Na <sup>+</sup>	191.0335	191.0320	7.9
a	C <sub>13</sub> H <sub>16</sub> O <sub>5</sub> Na <sup>+</sup>	275.0936	275.0895	14.9
A	C <sub>13</sub> H <sub>16</sub> O <sub>4</sub> Na <sup>+</sup>	259.0984	259.0949	13.5

**Table 7.7.** Table of accurate masses for the OzID products of compound 3

OzID-MS Products	Molecular Formula	Measured Value	Calculated Value	Accuracy (in ppm)
Parent Mass	C <sub>14</sub> H <sub>16</sub> O <sub>3</sub> Na <sup>+</sup>	255.1003	255.0997	2.4
A	C <sub>10</sub> H <sub>10</sub> O <sub>4</sub> Na <sup>+</sup>	217.0475	217.0477	0.9
A	C <sub>12</sub> H <sub>12</sub> O <sub>4</sub> Na <sup>+</sup>	243.0625	243.0634	3.7
●	C <sub>14</sub> H <sub>16</sub> O <sub>4</sub> Na <sup>+</sup>	271.0966	271.0946	7.4

**Table 7.8.** Table of accurate masses for the OzID products of compound 4

OzID-MS Products	Molecular Formula	Measured Value	Calculated Value	Accuracy (in ppm)
Parent Mass	$C_{19}H_{28}O_4Na^+$	343.1891	343.1886	1.5
A	$C_{14}H_{22}O_3Na^+$	261.1485	261.1467	6.9
A	$C_{16}H_{24}O_3Na^+$	287.1632	287.1624	2.8
●	$C_{19}H_{28}O_5Na^+$	359.1840	359.1835	1.4
a	$C_{16}H_{24}O_4Na^+$	303.1581	303.1567	4.6

**Table 7.9.** Table of accurate masses for the OzID products of compound 5

OzID-MS Products	Molecular Formula	Measured Value	Calculated Value	Accuracy (in ppm)
Parent Mass	$C_{26}H_{38}O_5Na^+$	453.2609	453.2617	1.8
a	$C_{20}H_{28}O_6Na^+$	387.1808	387.1784	6.2
A	$C_{20}H_{28}O_5Na^+$	371.1844	371.1835	2.4
a	$C_{22}H_{30}O_6Na^+$	413.2004	413.1940	15.5
A	$C_{22}H_{30}O_5Na^+$	397.1985	397.1991	1.5
●	$C_{26}H_{38}O_6Na^+$	469.2548	469.2566	3.8

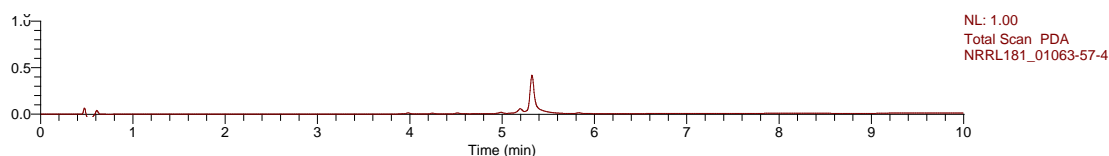


**Figure 110.** UPLC-PDA detector chromatogram of ent-sartorypyrone E (1)

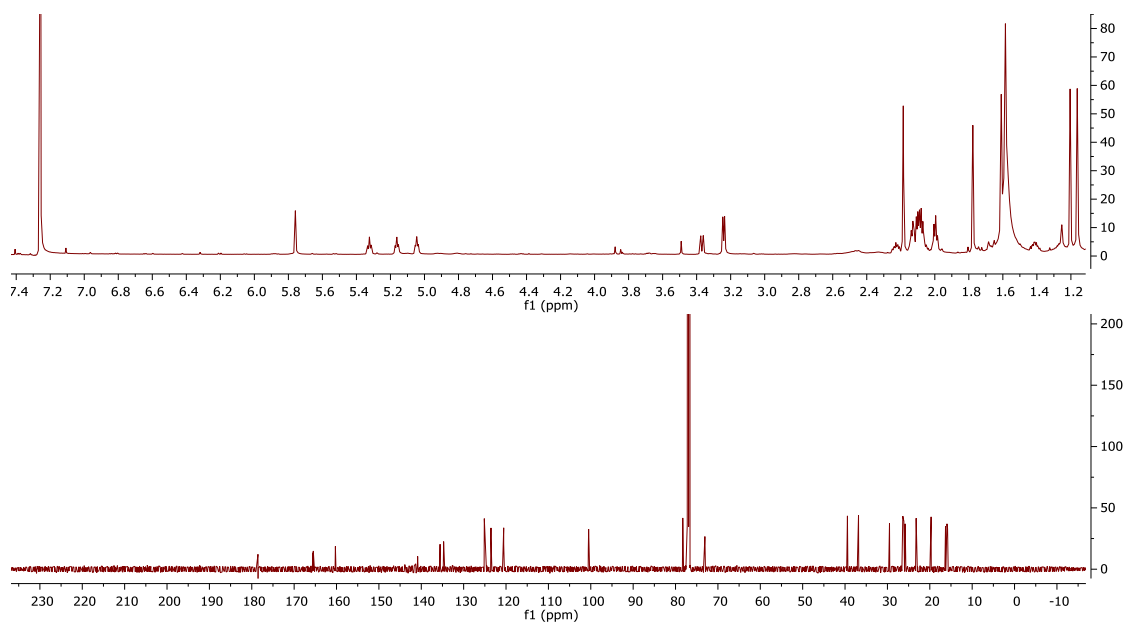


**Figure 111.**  $^1\text{H}$  NMR spectrum (700 MHz, Top) and  $^{13}\text{C}$  NMR spectrum (175 MHz, Bottom) both in  $\text{CDCl}_3$ , of ent-sartorypyrone E (**1**)

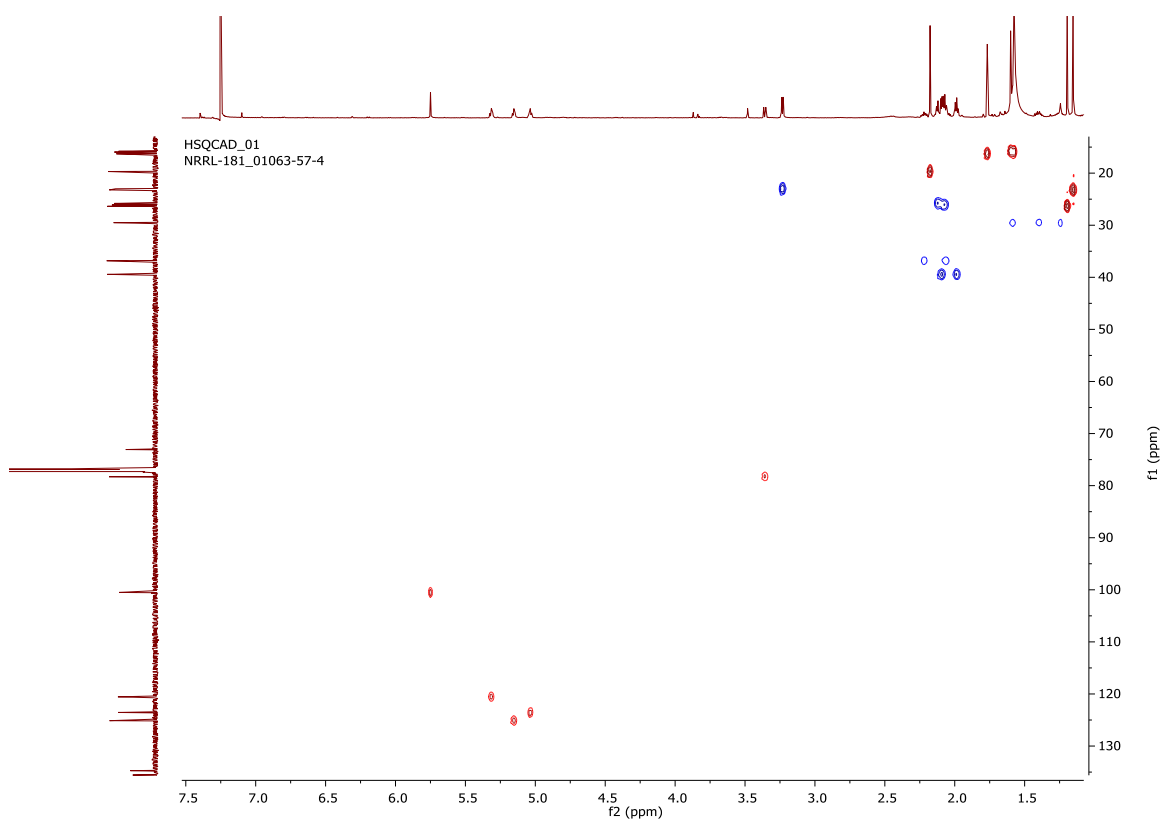


**Figure 112.** HSQC spectrum of ent-sartorypyrone E (**1**),  $\text{CDCl}_3$ , 700 MHz

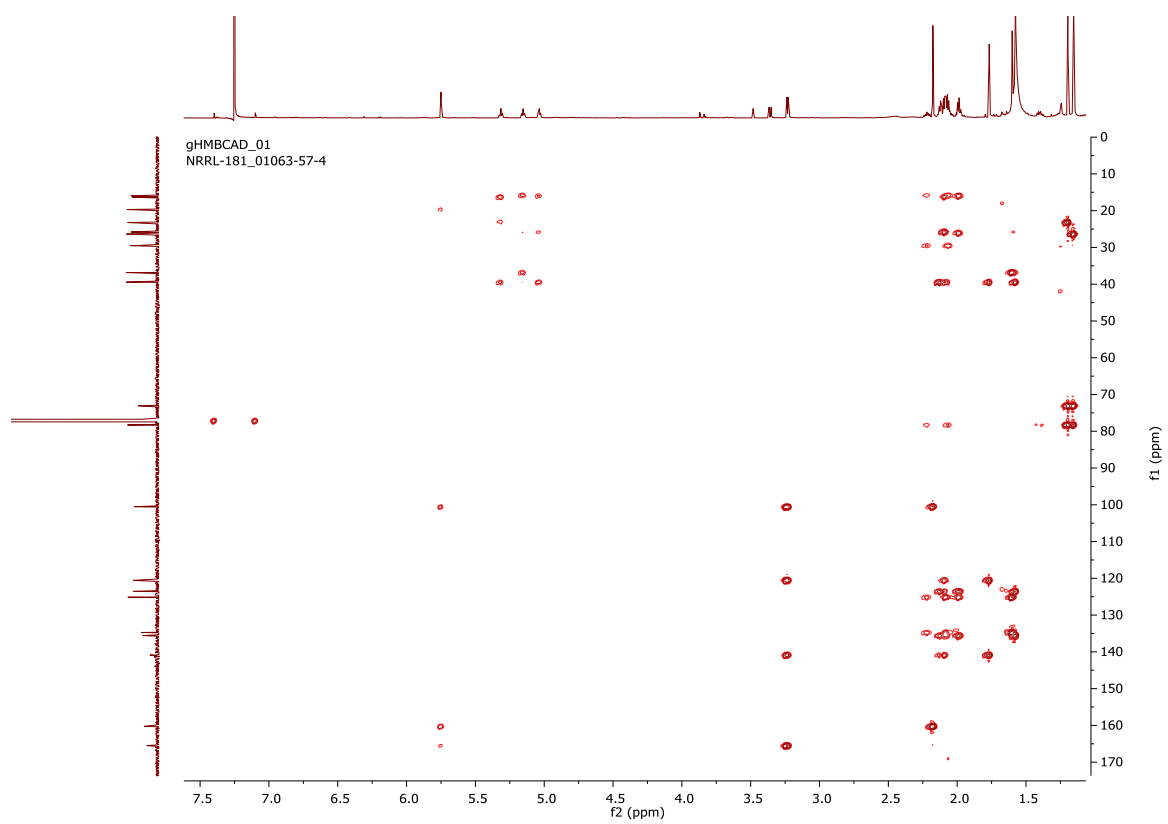


**Figure 113.** HMBC spectrum of ent-sartorypyrone E (**1**), CDCl<sub>3</sub>, 700 MHz

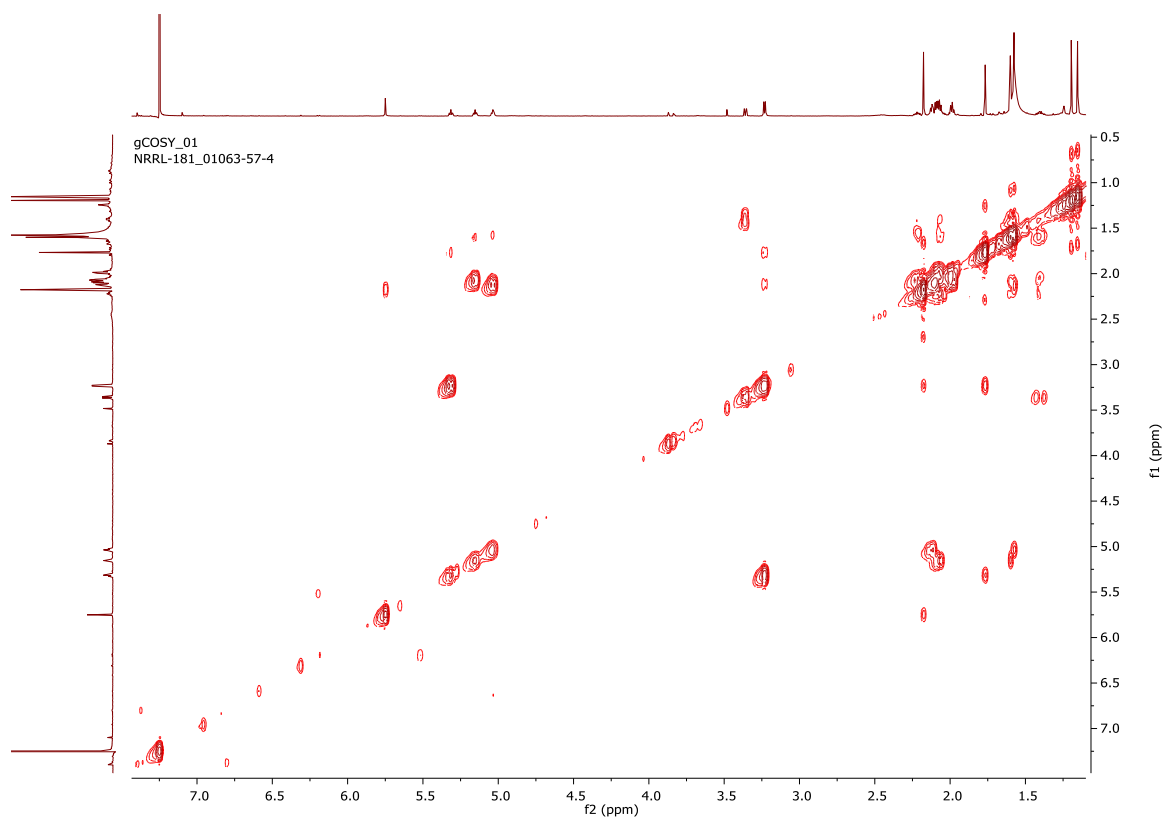


**Figure 114.** <sup>1</sup>H COSY spectrum of ent-sartorypyrone E (**1**), CDCl<sub>3</sub>, 700 MHz

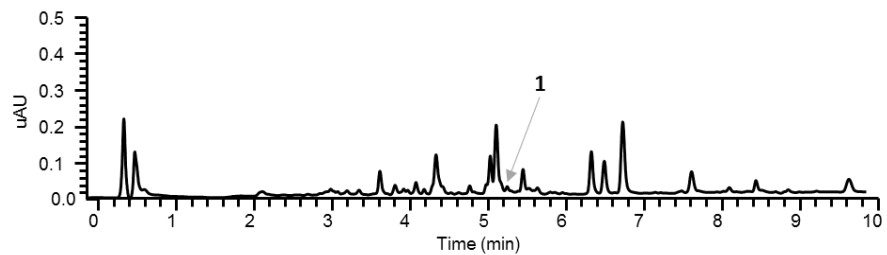


**Figure 115.** UPLC-PDA detector chromatogram of an extract of *A. fischeri* grown on solid oatmeal media

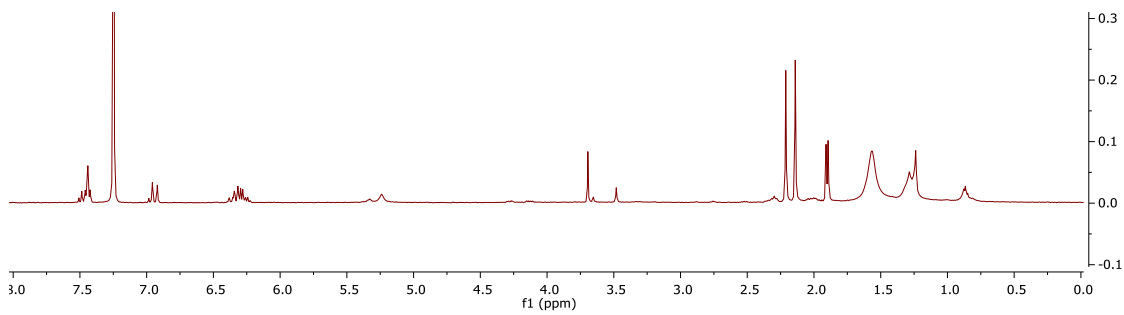


**Figure 116.** <sup>1</sup>H NMR spectrum (400 MHz) in  $\text{CDCl}_3$ , of sorbicillin (3)

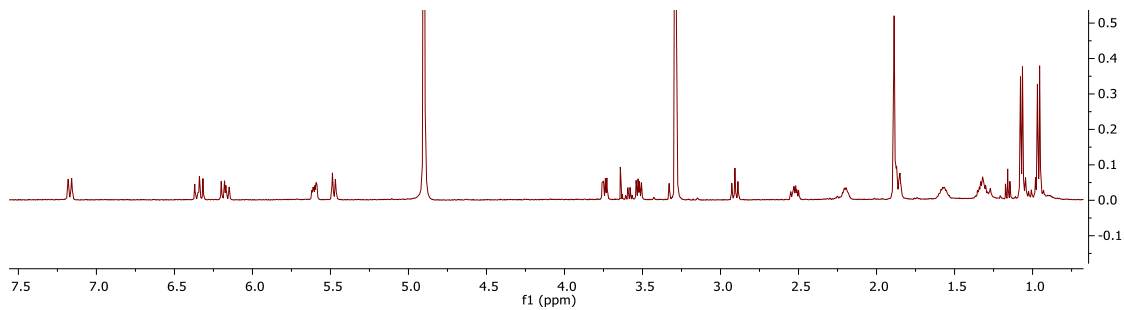


**Figure 117.** <sup>1</sup>H NMR spectrum (500 MHz) in  $\text{MeOD}$ , of trichodermic acid A (4)

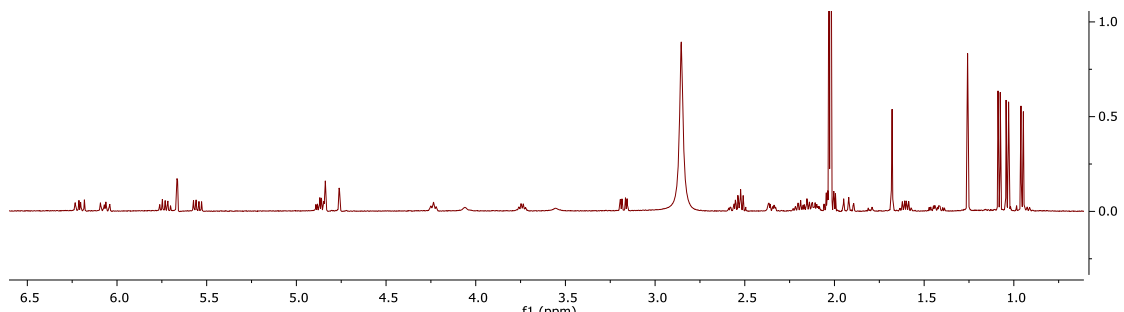


**Figure 118.** <sup>1</sup>H NMR spectrum (500 MHz) in  $(\text{CD}_3)_2\text{CO}$ , of AA03390 (5)

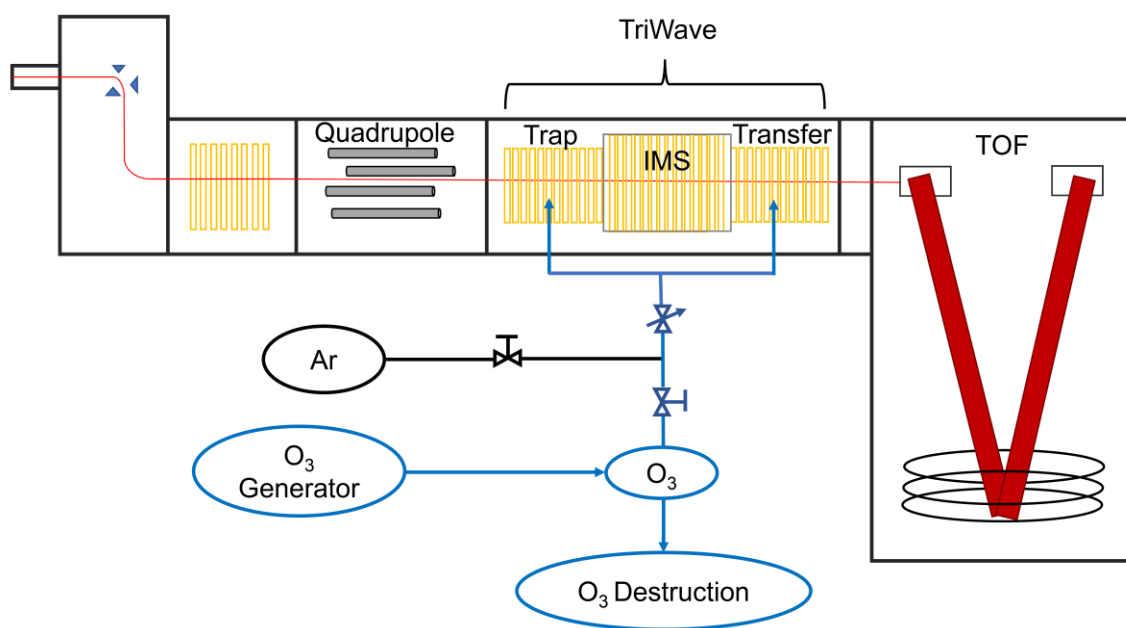


**Figure 119.** Schematic of the Waters Synapt G2 HDMS modified to allow ozone in the trap and transfer cells to perform OzID-MS. Adapted from Vu et al.<sup>81</sup>

CHAPTER VIII

OPPORTUNITIES AND LIMITATIONS FOR ASSIGNING RELATIVE  
CONFIGURATIONS OF ANTIBACTERIAL BISLACTONES USING GIAO NMR SHIFT  
CALCULATIONS

Sonja L. Knowles, Christopher D. Roberts, Mario Augustinović, Laura Flores-Bocanegra, Huzeфа A. Raja, Kimberly N. Heath-Borrero, Joanna E. Burdette, Joseph O. Falkingham III, Cedric J. Pearce, and Nicholas H. Oberlies. *J. Nat. Prod.* 2021,  
[doi.org/10.1021/acs.jnatprod.0c01309](https://doi.org/10.1021/acs.jnatprod.0c01309)

Four new bislactones, dihydroacremonol (**1**), clonostachyone (**2**), acremodiol B (**3**), and acremodiol C (**4**), along with one known compound, hymeglusin (**5**), were isolated from cultures of two fungal strains (MSX59876 and MSX59260). Both strains were identified based on phylogenetic analysis of molecular data as *Clonostachys* spp., yet they biosynthesized a suite of related, but different, secondary metabolites. Given the challenges associated with elucidating the structures and configurations of bislactones, gauge-independent atomic orbital (GIAO) NMR calculations were tested as a complement to traditional NMR and HRESIMS experiments. Fortuitously, the enantiomer of the new natural product (**4**) was known as a synthetic compound, and the predicted configuration from GIAO NMR calculations (i.e., for the relative configuration) and optical rotation calculations (i.e., for the absolute configuration) matched those of the synthesis product. These results engendered confidence in using similar procedures, particularly the mixture of GIAO NMR shift calculations coupled with an orthogonal technique, to predict the configuration of **1-3**; however, there were important limitations, which are discussed for each of these. The metabolites displayed antimicrobial activities,

with compounds **1** and **4** being the most potent against *Staphylococcus aureus* with MICs of 1 µg/mL and 4 µg/mL, respectively.

Macrolides are well known antibiotics that have been used since the early 1950s, when the first, and most well studied macrolide antibiotic, erythromycin, was marketed.<sup>401, 402</sup> Bislactones are a subgroup of macrolides and some of them have been investigated for their antibacterial properties.<sup>88-90, 403</sup> However, assigning either the relative or absolute configuration of this class of compounds can be challenging. For instance, the bislactone, acremodiol, first described in 2002,<sup>404</sup> was assigned a relative configuration as 5*R*,6*R*,11*R*,14*R* based on NOESY correlations. Nevertheless, the 5*R*,6*R*,11*R*,14*R* and 5*R*,6*R*,11*S*,14*R* acremodiol analogues were both synthesized, but the spectroscopic data from neither of these matched those in the original paper,<sup>90</sup> and as such, both the relative and absolute configuration of acremodiol remains uncertain. Another example of challenges with bislactones is 4-keto-clonostachydiol, which was first determined as 5*R*,10*R*,13*R*<sup>405</sup> and was later reassigned based on synthesis and specific rotation as 5*S*,10*S*,13*S*.<sup>88, 89</sup> In summary, determining the absolute, and sometimes even the relative, configurations of the bislactones remains problematic.

There are several ways to probe either/both the relative and/or absolute configuration of natural products. In addition to total synthesis, the gold standard for absolute configuration is X-ray crystallography,<sup>91</sup> often including the incorporation of a heavy atom,<sup>92, 93</sup> and this is essentially a snapshot of the molecule in three dimensional space.<sup>94</sup> Countless studies have also used Mosher's ester method or Marfey's reagent.<sup>95-98</sup> While the former is used largely for molecules with secondary alcohols and the latter for molecules that incorporate amino acid building blocks, what they have in common is the requirement of semi-synthetic modification or degradation of the parent

natural product.<sup>95, 97, 98</sup> Another method, electronic circular dichroism (ECD), is finding growing use, especially with the ability to compare calculated vs measured spectra, although this works best with metabolites that have a UV chromophore in the vicinity of the stereogenic element.<sup>99, 100</sup> While NMR is very popular for structure elucidation, NOESY/ROESY 2D NMR experiments allow one to only assign the relative configuration of a molecule, unless those experiments are coupled with orthogonal data.<sup>64</sup>

The use of GIAO NMR calculations for structure elucidation was reported by Bifulco and colleagues in 2002<sup>101, 102</sup> and has been gaining popularity.<sup>103-107</sup> This technique has been used more frequently in the ensuing years (Figure 122) and has aided in assigning the relative configuration or reassignment of several natural products.<sup>102, 105, 108-110</sup> As noted previously, the configuration of bislactones has been challenging, resulting in several reassessments. Thus, GIAO NMR calculations were evaluated on this subgroup of macrolides, confirming and/or assigning the relative configuration of four metabolites isolated from two *Clonostachys* spp. (strains MSX59876 and MSX59260).

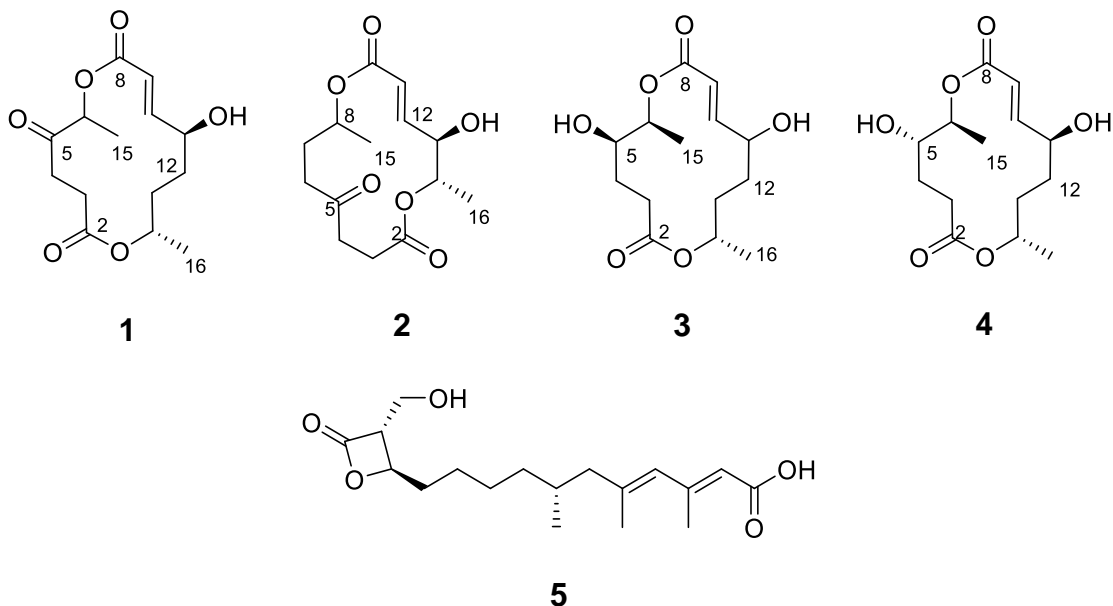


**Figure 120.** Structures of compounds 1-5.

## Results

In pursuit of structurally diverse metabolites with biological activity from fungi,<sup>406-</sup><sup>408</sup> two fungal strains from the Mycosynthetix library were flagged for further study, as they biosynthesized metabolites that did not match an inhouse database of over 625 fungal metabolites.<sup>188, 189</sup> Based on phylogenetic analysis of molecular data,<sup>353</sup> the strains were identified as *Clonostachys* spp.; however, each biosynthesized a similar, albeit, non-identical suite of polyketides (Figure 123; strain MSX59876 produced **1** and **3-5** and strain MSX59260 produced **2**). Of these, the data for **5** matched the literature for hymeglusin, which is also termed antibiotic 1233A.<sup>409, 410</sup>

Compound **4** was obtained as a white, amorphous powder with a molecular formula of C<sub>14</sub>H<sub>22</sub>O<sub>6</sub> as determined by HRESIMS data along with <sup>1</sup>H, <sup>13</sup>C, and edited-HSQC NMR data (Table 8.1). The <sup>1</sup>H NMR data matched the literature values for 5*R*,6*R*,11*R*,14*R* acremodiol, which was generated via total synthesis (Figure 144);<sup>90</sup>

however the specific rotation of **4** ( $[\alpha]_D^{20} +25$ ) was opposite to that of synthesized *5R,6R,11R,14R* acremodiol ( $[\alpha]_D^{20} -35.3$ );<sup>90</sup> both of these values were obtained in  $\text{CHCl}_3$ , and **4** was also analyzed in  $\text{MeOH}$  so as to compare with those measured for **1-3** (Table 8.16). These data suggested that compound **4** was the enantiomer of *5R,6R,11R,14R* acremodiol, and thus, had an absolute configuration of *5S,6S,11S,14S*. This observation was used as a test case for the GIAO NMR calculations (Tables 8.12-8.14), to explore its accuracy for this subgroup of macrolides. In brief, all the minimized conformers of the possible structures were obtained (Figure 147). The NMR shielding constants were calculated from these conformers, converted into chemical shifts (ppm), and then the final chemical shift values were calculated (Tables 8.12-8.13).<sup>106, 107</sup> The calculated  $^1\text{H}$  and  $^{13}\text{C}$  NMR shifts were scaled empirically (i.e., corrected mean absolute error) to remove system errors (Tables 8.12 and 8.13), which has proven to be common practice when working with these calculations.<sup>104, 105, 109</sup> Then, two different NMR calculation methods were used to assess the relative configuration. First, the individual correlation coefficients for each isomer was calculated, followed by the geometric mean of the  $^1\text{H}$  and  $^{13}\text{C}$  NMR correlation coefficients (Table 8.14).<sup>104, 105</sup> This gives a correlation coefficient for every possible isomer, and the isomer with a value closest to 1 is considered the most likely relative configuration,<sup>104</sup> which in this case was either *5S,6S,11S,14S* or *5R,6R,11R,14R*. Secondly, DP4+ (combined  $^1\text{H}$  and  $^{13}\text{C}$ ) calculations for each isomer was calculated (Table 8.17), which gives the probability for every possible isomer, and the isomer with the highest probability is most likely the relative configuration.<sup>411</sup> In this case it was either *5S,6S,11S,14S* or *5R,6R,11R,14R*. Thus, both methods were in agreement with each other. Again, given the specific rotation value of **4** being opposite to the literature data for *5R,6R,11R,14R* acremodiol,<sup>90</sup> we hypothesize

the absolute configuration of **4** as 5S,6S,11S,14S. In addition, the optical rotation of **4** was calculated (i.e., **4a** in Table 8.16), further confirming the configuration as 5S,6S,11S,14S, and ascribed the trivial name acremodiol C.

Compound **1** was obtained as a white/yellow, amorphous powder with a molecular formula of  $C_{14}H_{20}O_6$  as determined by HRESIMS data along with  $^1H$ ,  $^{13}C$ , and edited-HSQC NMR data (Table 8.1), demonstrating an index of hydrogen deficiency of 5. The  $^{13}C$  NMR data (Table 8.1) indicated 14 carbons, including three carbonyl, two vinylic, three oxygenated, and six aliphatic carbons. The  $^1H$  and edited-HSQC NMR data (Table 8.1) indicated two methyls, two olefinic protons, three methines, and four methylenes. The HMBC correlations from H-10 to C-9 and C-8 and from H-9 to C-10 and C-8, as well as the COSY correlations between H-10 and H-9, indicated a trans ( $J_{H_3/H_2} = 15.8$  Hz)  $\alpha,\beta$ -unsaturated ester (Figure 121). This half of the bislactone was formed through a seven-proton spin system (H-9/H-10/H-11/H<sub>2</sub>-12/H<sub>2</sub>-13/H-14/H<sub>3</sub>-16), as noted via COSY correlations. The other half of the bislactone was formed through HMBC and COSY correlations, focusing on correlations across two spin systems (i.e., H<sub>2</sub>-3/H<sub>2</sub>-4 and H-6/H<sub>3</sub>-15). HMBC correlations from H-6 and H<sub>3</sub>-15 to the keto group at C-5 ( $\delta_C$  208.0), and H<sub>2</sub>-3 and H<sub>2</sub>-4 to both C-5 and the ester carbonyl at C-2 ( $\delta_C$  171.5), formed the other side of the bislactone. These halves were connected to form the macrolide through the HMBC correlations of H-14 to C-2 and H-6 to C-8 coupled with the obvious oxygenation of H-14 ( $\delta_H/\delta_C$  4.93/71.1) and H-6 ( $\delta_H/\delta_C$  5.41/75.1). To probe the configuration of the stereogenic centers in **1**, we first attempted Mosher's ester analysis, but unfortunately, no reaction was observed (data not shown). This line of inquiry was abandoned and instead, NMR calculations were performed. Utilizing the correlation coefficient method, the configuration of **1** was assigned as either 6S,11R,14R or 6R,11S,14S (Table 8.5).

Then, calculation of the optical rotations for these two possibilities were used to distinguish between enantiomers. The specific of **1** agreed in sign with the calculated value for *6R,11S,14S* (i.e.,  $[\alpha]_D^{20} +166$  vs  $[\alpha]_D^{20} +51$  (*c* 0.10, MeOH); Table 8.16). Interestingly, the DP4+ method indicates that the configuration of **1** was either *6R,11R,14R* or *6S,11S,14S* (Table 8.17), and again, using the specific rotation data, the configuration was assigned as *6S,11S,14S* (Table 8.16). The benefit of testing both approaches is the confluence of data for the *11S* and *14S* assignments. However, there was discordance for the *6* position, so this position remains unassigned. As a tentative assignment based on biosynthesis, position *6* could be the *S* configuration, since it is derived from the same biosynthetic pathway as compounds **3** and **4**. The methods used to obtain this configuration were as described for **4** (Tables 8.3-8.5), and this compound was termed dihydroacremonol.

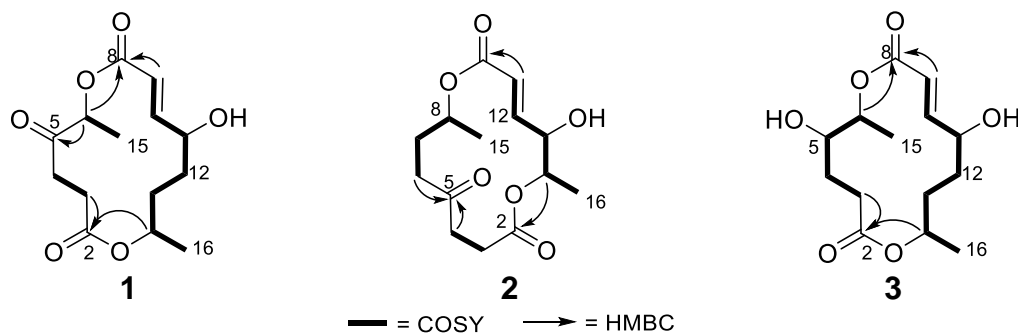


**Figure 121.** Key HMBC and COSY Correlations of Compounds **1-3**.

Compound **2** was obtained as a white, amorphous powder with a molecular formula of  $C_{14}H_{20}O_6$  as determined by HRESIMS data along with  $^1H$ ,  $^{13}C$ , and edited-HSQC NMR data (Table 8.1), demonstrating an index of hydrogen deficiency of 5. The NMR data indicated that **2** was a constitutional isomer of **1**. The HMBC correlations from H-12 to C-11 and C-10 and from H-11 to C-12 and C-10, coupled with the COSY

correlations between H-12 and H-10, indicated a trans ( $J_{H_3/H_2} = 15.8$  Hz)  $\alpha,\beta$ -unsaturated ester (Figure 121). This portion of the bislactone was formed through a five-proton spin system (H-11/H-12/H-13/H-14/H<sub>3</sub>-16) as noted via COSY correlations (Figure 121). Similar to **1**, the other portion of the bislactone was formed through HMBC and COSY correlations via two spin systems (H<sub>2</sub>-3/H<sub>2</sub>-4) and (H<sub>2</sub>-6/H<sub>2</sub>-7/H-8/H<sub>3</sub>-15). HMBC correlations from H<sub>2</sub>-7 and H<sub>2</sub>-6 to C-5 and H<sub>2</sub>-4 and H<sub>2</sub>-3 to C-5 and C-2 formed the other portion of the bislactone. These sections were connected through the HMBC correlations of H-14 to C-2 and H-8 to C-10, along with the oxygenation of H-8 ( $\delta_H/\delta_C$  4.90/71.2) and H-14 ( $\delta_H/\delta_C$  4.77/75.1). The configuration of **2**, which was assigned the trivial name clonostachyone, was assigned through GIAO NMR calculations and optical rotation calculations. The correlation coefficient method assigned the configuration of **2** to be either 8S,13S,14R or 8R,13R,14S (Table 8.8), with optical rotation calculations indicating it was 8R,13R,14S (Table 8.16). The DP4+ method predicted the configuration to be either 8R,13S,14R or 8S,13R,14S (Table 8.17), with specific rotation data suggesting 8S,13R,14S (Table 8.16). Based on the discrepancies between the two methods at position 8, and similar to the discussion for compound **1** at position 6, the configuration of **2** was established 13R,14S, with the configuration of position 8 being ambiguous and assigned as 8S\*. The methods used to carry out these calculations were as described for **4** (Tables 8.6-8.8).

Compound **3** was obtained as a white, amorphous powder with a molecular formula of C<sub>14</sub>H<sub>22</sub>O<sub>6</sub> as determined by HRESIMS data along with <sup>1</sup>H, <sup>13</sup>C, and edited-HSQC NMR data (Table 8.1). As determined by spectroscopic data, compound **3** had the same planar structure as acremodiol and **4**.<sup>90, 404</sup> For example, the spin systems via COSY and HMBC were highly similar between compounds **3** and **4**. However, because

the  $^1\text{H}$  NMR data displayed shift differences with **4** (Figures 144 and 145), GIAO NMR and optical rotation calculations were performed to ascertain the differences between these compounds. The correlation coefficient method suggested the configuration of **3** to be either  $5R,6S,11R,14S$  or  $5S,6R,11S,14R$  (Table 8.11), with optical rotation calculations indicating it was  $5R,6S,11R,14S$  (Table 8.16). The DP4+ method predicated the configuration to be either  $5S,6R,11R,14R$  or  $5R,6S,11S,14S$  (Table 8.17), with the addition of optical rotation calculations suggesting the  $5R,6S,11S,14S$  enantiomer. Based on the discrepancies between the two methods at position 11, the configuration of **3** was established as,  $5R,6S,14S$ , with the configuration of position 11 being ambiguous. As a tentative assignment based on biosynthesis, position 11 could be the S configuration, since it is derived from the same biosynthetic pathway as compounds **1** and **4**. Compound **3** was ascribed the trivial name acremodiol B, and the methods used to carry out these calculations were as described for **4** (Tables 8.9-8.11).

**Table 8.1.**  $^1\text{H}$  and  $^{13}\text{C}$  NMR Data of Compound 1-4

Pos	<b>1<sup>a</sup></b>		<b>2<sup>a</sup></b>		<b>3<sup>b</sup></b>		<b>4<sup>b</sup></b>	
	$\delta_{\text{C}}$ , type	$\delta_{\text{H}}$ (J in Hz)	$\delta_{\text{C}}$ , type	$\delta_{\text{H}}$ (J in Hz)	$\delta_{\text{C}}$ , type	$\delta_{\text{H}}$ (J in Hz)	$\delta_{\text{C}}$ , type	$\delta_{\text{H}}$ (J in Hz)
2	171.5, C		173.1, C		175.0, C		172.4, C	
3	34.9, CH <sub>2</sub>	2.74, m	28.6, CH <sub>2</sub>	2.34, m	32.2, CH <sub>2</sub>	2.59, ddd (18.6, 5.7, 3.6)	28.5, CH <sub>2</sub>	2.36, ddd (18.2, 7.3, 3.1)
				2.78, m		2.89, ddd (18.4, 11.8, 3.4)		2.72, ddd (18.2, 11.1, 2.8)
4	29.9, CH <sub>2</sub>	2.56, m	38.1, CH <sub>2</sub>	2.62, m 2.87, m	26.4, CH <sub>2</sub>	1.97, m 2.15, ddt (15.3, 11.7, 3.8)	26.8, CH <sub>2</sub>	1.81, m 2.07, ddt (14.6, 11.1, 3.5)
5	208.0, C		206.9, C		72.8, CH	3.75, dd (7.5, 4.0)	69.4, CH	4.05, ddd (8.2, 3.8, 2.6)
6	75.1, CH	5.43, q (6.9)	38.4, CH <sub>2</sub>	2.40, m 2.62, m	73.7, CH	5.33, dt (11.1, 5.6)	73.1, CH	5.04, qd (6.6, 2.5)
7			27.6, CH <sub>2</sub>	2.08, m 1.95, m				
8	164.4, C		71.2, CH	4.90, dtt (10.9, 5.9, 3.0)	165.0, C		164.6, C	
9	119.4, CH	6.10, dd (15.8, 2.1)			120.8, CH	6.03, dd (15.9, 1.9)	119.6, CH	5.97, dd (15.9, 2.2)
10	151.7, CH	7.0, dd (15.8, 2.6)	165.3, C		149.2, CH	6.71, dd (15.9, 2.3)	150.5, CH	6.82, dd (15.9, 2.8)
11	69.7, CH	4.63, br s	121.5, CH	5.97, dd (15.9, 2.0)	69.4, CH	4.65, br s	69.2, CH	4.62, dq (6.8, 2.3)
12	29.0, CH <sub>2</sub>	1.88, m	146.5, CH	6.72, dd (15.8, 3.8)	28.3, CH <sub>2</sub>	1.79, m 1.95, m	28.7, CH <sub>2</sub>	1.88, m
13	27.5, CH <sub>2</sub>	1.55, m 1.83, m	73.9, CH	4.17, m	27.0, CH <sub>2</sub>	1.63, m 1.86, m	27.8, CH <sub>2</sub>	1.54, m 1.81, m
14	71.1, CH	4.95, pd (6.3, 2.9)	75.1, CH	4.77, p (6.4)	70.8, CH	4.96, q (5.9)	69.4, CH	4.84, m
15	16.7, CH <sub>3</sub>	1.42, d (6.9)	20.0, CH <sub>3</sub>	1.29, d (6.3)	16.9, CH <sub>3</sub>	1.25, d (6.7)	14.4, CH <sub>3</sub>	1.31, d (6.6)
16	19.2, CH <sub>3</sub>	1.19, d (6.4)	18.4, CH <sub>3</sub>	1.43, d (6.5)	19.4, CH <sub>3</sub>	1.19 d (6.4)	19.8, CH <sub>3</sub>	1.15, d (6.3)

5-OH						4.34, d (7.7)		
11-OH		1.98, m						
13-OH				2.50, d (6.9)				
<sup>a</sup> CDCl <sub>3</sub> ( <sup>1</sup> H NMR 400 MHz, <sup>13</sup> C NMR 100 MHz). <sup>b</sup> CDCl <sub>3</sub> ( <sup>1</sup> H NMR 700 MHz, <sup>13</sup> C NMR 175 MHz).								

Antimicrobial activities of compounds **1**, **4**, and **5** were measured against *Pseudomonas aeruginosa*, *Escherichia coli*, *Staphylococcus aureus*, Methicillin-resistant *S. aureus*, and *Bacillus anthracis*. Compounds **1** and **4** had significant activity against *S. aureus*, with MICs of 1 µg/mL and 4 µg/mL, respectively (Table 8.2). Compound **1** was evaluated for cytotoxicity, as bislactones with a keto group have been active in leukemia cell lines;<sup>405</sup> **1** was inactive against MDA-MB-231 (triple negative human breast cancer), OVCAR-3 (human ovarian cancer), and MDA-MB-435 (human melanoma cancer) cell lines at >25 µM. Compound **1** warrants further investigation due to the promising antimicrobial activity coupled with the lack of cytotoxicity to mammalian cells.

In summary, four new bislactones (**1-4**) and one known secondary metabolite (**5**) were isolated from two *Clonostachys* spp. Notably, compounds **1** and **4** showed significant activity against *S. aureus*. Owing to the fact that there have been many challenges in assigning the configuration of bislactones in the literature,<sup>88-90, 404, 405, 412</sup> GIAO NMR calculations were used to assign the relative configurations of these metabolites and optical rotation calculations were used to assign the absolute configuration. The assignment of the absolute configuration of **4** is a noteworthy example, as few, if any, literature examples exist where the configuration of an isolated secondary metabolite was assigned using GIAO NMR calculations coupled with specific rotation data from a

synthesized enantiomer.<sup>90, 404</sup> This suggests that GIAO NMR calculations could be a credible tool for assigning the relative configuration of this subgroup of macrolides.

**Table 8.2.** Antimicrobial Activity of Compounds **1**, **4**, and **5** Against a Panel of Bacteria

Compounds	<i>P. aeruginosa</i>	<i>E. coli</i>	<i>S. aureus</i>	<i>MRSA</i>	<i>B. anthracis</i>
Minimal Inhibitory Concentrations in µg/mL					
<b>1</b>	125	125	1	125	62.5
<b>4</b>	125	125	4	125	125
<b>5</b>	125	> 250	125	125	> 250
penicillin <sup>a</sup>	> 250	16	0.25	0.50	0.25
streptomycin <sup>a</sup>	1	0.25	0.25	0.25	0.25
erythromycin <sup>a</sup>	62.5	16	0.50	0.25	0.25
rifampin <sup>a</sup>	62.5	4	0.25	0.25	0.25
clarithromycin <sup>a</sup>	125	16	0.25	> 250	0.25

<sup>a</sup>Positive controls

## Materials and Methods

**General Experimental Procedures.** Optical rotation data were obtained using a Rudolph Research Autopol III polarimeter, and UV spectra were measured with a Varian Cary 100 Bio UV-vis spectrophotometer. The NMR data were collected using either a JEOL ECS-400 spectrometer, which was equipped with a JEOL normal geometry broadband Royal probe, and a 24-slot autosampler, and operated at 400 MHz for <sup>1</sup>H and 100 MHz for <sup>13</sup>C, or a JEOL ECS-500 spectrometer operating at 500 MHz for <sup>1</sup>H and 125 MHz for <sup>13</sup>C or an Agilent 700 MHz spectrometer, equipped with a cryoprobe, operating at 700 MHz for <sup>1</sup>H and 175 MHz for <sup>13</sup>C. The NMR shifts were referenced to either CDCl<sub>3</sub> (<sup>1</sup>H 7.26 ppm and <sup>13</sup>C 77.2 ppm) or DMSO-d<sub>6</sub> (<sup>1</sup>H 2.50 ppm). HRESIMS experiments

utilized either a Thermo LTQ Orbitrap XL mass spectrometer or a Thermo Q Exactive Plus; both were equipped with an electrospray ionization source. A Waters Acuity UPLC was utilized for both mass spectrometers, using a BEH C<sub>18</sub> column (1.7 µm; 50 mm x 2.1 mm) set to a temperature of 40 °C and a flow rate of 0.3 mL/min. The mobile phase consisted of a linear gradient of CH<sub>3</sub>CN-H<sub>2</sub>O (both acidified with 0.1% formic acid), starting at 15% CH<sub>3</sub>CN and increasing linearly to 100% CH<sub>3</sub>CN over 8 min, with a 1.5 min hold before returning to the starting condition. The HPLC separations were performed on a Varian Prostar HPLC system equipped with a Prostar 210 pumps and a Prostar 335 photodiode array detector (PDA), with the collection and analysis of data using Galaxie Chromatography Workstation software. The columns used for separations were either an Gemini C<sub>18</sub> preparative (5 µm; 21.2 x 250 mm) column at a flow rate of 21.2 mL/min, or an Atlantis T3 C<sub>18</sub> preparative (5 µm; 19 x 250 mm) column at a flow rate of 16.9 mL/min. Flash chromatography was performed on a Teledyne ISCO Combiflash Rf 200 and monitored by both ELSD and PDA detectors.

**Fungal Identification.** The fungal ITS region (ITS1–5.8S-ITS2) of the nuclear ribosomal operon was sequenced using primer combination ITS1F and ITS4.<sup>413 414</sup> This region has been designated as the fungal barcoding marker.<sup>415</sup> Detailed methods for DNA extraction, PCR amplification, and Sanger sequencing of these strains followed procedures outlined by Raja et al.<sup>353</sup> A BLAST search with strains MSX59260 and MSX59876 revealed that both showed highest affinities with members of *Clonostachys* (Ascomycota, Hypocreales, Bionectriaceae). Subsequently, all authentic *Clonostachys* spp. sequence data with taxon sampling were downloaded from a recent study by Lechat et al.<sup>416</sup> followed by phylogenetic analysis using Maximum likelihood analysis using RAxML<sup>417, 418</sup> on the CIPRES server<sup>419</sup>. Briefly, an alignment was constructed in

MAFFT<sup>256</sup> using Geneious 9.1.8 (<https://www.geneious.com>) and analyzed using RAxML with the General time reversible model and 1000 fast bootstrap searches using The CIPRES Science Gateway V. 3.3. This revealed that strains MSX59260 and MSX59876 displayed phylogenetic affinities with *Clonostachys rogersoniana*<sup>420</sup> strain CBS 582.89 ( $\geq 90\%$  RAxML bootstrap support). Previous studies by our team on *C. rogersoniana* resulted in the identification of verticillin analogues.<sup>399</sup> Since strains MSX59260 and MSX59876 biosynthesized a different suite of metabolites, we suggest a more conservative approach to their identification, noting them both as *Clonostachys* sp., and their sequence data were deposited in GenBank (accession numbers: MSX59876: MW275356, MW275357; and MSX59260: MW275358, MW275359, respectively).

**Fermentation, Extraction, and Isolation.** Strains MSX59876 and MSX59260 were grown in two separate 2.8 L Fernback flasks containing 150 g of autoclaved rice prepared by adding twice the amount of distilled H<sub>2</sub>O. A seed culture grown in YESD (2% soy peptone, 2% dextrose, and 1% yeast extract; 5 g of yeast extract, 10 g of soy peptone, and 10 g of D-glucose in 500 mL of deionized H<sub>2</sub>O) medium was used as the inoculum. The rice-based culture was incubated at room temperature (~23 °C). Strain MSX59876 was extracted by adding 500 mL of 1:1 MeOH-CHCl<sub>3</sub>. Subsequently, the culture was chopped with a spatula and left to shake overnight (~16 hrs) at ~100 rpm at room temperature. The culture was combined and filtered *in vacuo*, and 450 mL CHCl<sub>3</sub> and 750 mL H<sub>2</sub>O were added to the filtrate. The mixture was then transferred to a separatory funnel. The organic layer was drawn off and evaporated to dryness *in vacuo*, reconstituted in 300 mL of 1:1 MeOH-CH<sub>3</sub>CN and 300 mL of hexanes, transferred to a separatory funnel, and shaken vigorously. This defatted organic layer was evaporated to dryness *in vacuo*. The organic layer (636 mg) was then dissolved in CHCl<sub>3</sub>, absorbed

onto Celite 545 (Acros Organics) and was separated by normal phase flash chromatography using a gradient of hexane to CHCl<sub>3</sub> to MeOH at a 30 mL/min flow rate and 61.0 column volumes, which yielded four fractions. Fraction two (50.2 mg) was further purified using preparative-HPLC using a gradient of 20:80 to 100:0 of CH<sub>3</sub>CN: H<sub>2</sub>O acidified with 0.1% formic acid over 30 min yielding four subfractions. Subfraction one, which eluted at 11.0 min, yielded dihydroacremonol (**1**; 10.9 mg). Fraction three (110.5 mg) was further purified by preparative-HPLC using a gradient of 20:80 to 60:40 for 30 minutes then 60:40 to 80:20 for 15 min with CH<sub>3</sub>CN:H<sub>2</sub>O acidified with 0.1% formic acid yielding eight subfractions. Subfractions four and six yielded acremodiol C (**4**; 2.4 mg) and hymeglusin (**5**; 7.9 mg), at 9.3 min and 28.5 min, respectively. Subfraction two underwent a further preparative-HPLC step with a gradient of 20:80 to 100:0 of CH<sub>3</sub>CN: H<sub>2</sub>O acidified with 0.1% formic acid over 30 min, yielding six subfractions. Subfraction one, which eluted at 10.3 min, yielded acremodiol B (**3**; 0.8 mg).

In an analogous manner, strain MSX59260 was extracted, and the de-fatted organic extract (1004 mg) was absorbed onto Celite 545 and was separated by normal phase flash chromatography using a gradient of hexane to CHCl<sub>3</sub> to MeOH at a 35 mL/min flow rate and 61.0 column volumes, which yielded four fractions. Fraction two (110.5 mg) was purified using preparative- HPLC using a gradient of 20:80 to 60:40 of CH<sub>3</sub>CN: H<sub>2</sub>O acidified with 0.1% formic acid over 30 min yielding six subfractions. Subfraction two (7.8 mg) was further purified using preparative-HPLC using a gradient of 20:80 to 100:0 of CH<sub>3</sub>CN: H<sub>2</sub>O acidified with 0.1% formic acid over 30 minutes yielding five subfractions. Subfraction two yielded clonostachyone (**2**; 0.8 mg), which eluted at 10.0 min.

*Dihydroacremonol (1)*: White/yellow, amorphous powder;  $[\alpha]_D^{20} = +51$  (c 0.10, MeOH); UV (MeOH)  $\lambda_{\max}$  (log  $\epsilon$ ) 283 (1.83), 226 (2.87) nm; IR  $\nu_{\max}$  3408, 1715, 1688, 1646 cm<sup>-1</sup>; <sup>1</sup>H NMR (CDCl<sub>3</sub>, 400 MHz) and <sup>13</sup>C (CDCl<sub>3</sub>, 100 MHz) (See Table 8.1); HRESIMS *m/z* 285.1329 [M+H]<sup>+</sup> (calcd. For C<sub>14</sub>H<sub>20</sub>O<sub>6</sub>, 285.1338).

*Clonostachyone (2)*: White, amorphous powder;  $[\alpha]_D^{20} = +36$  (c 0.10, MeOH); UV (MeOH)  $\lambda_{\max}$  (log  $\epsilon$ ) 274 (1.76), 223 (2.83) nm; <sup>1</sup>H NMR (CDCl<sub>3</sub>, 400 MHz) and <sup>13</sup>C (CDCl<sub>3</sub>, 100 MHz) (See Table 8.1); HRESIMS *m/z* 285.1326 [M+H]<sup>+</sup> (calcd. For C<sub>14</sub>H<sub>20</sub>O<sub>6</sub>, 285.1338).

*Acremodiol B (3)*: White, amorphous powder;  $[\alpha]_D^{250} = +75$  (c 0.10, MeOH); UV (MeOH)  $\lambda_{\max}$  (log  $\epsilon$ ) 225 (2.84) nm; <sup>1</sup>H NMR (CDCl<sub>3</sub>, 700 MHz) and <sup>13</sup>C (CDCl<sub>3</sub>, 175 MHz) (See Table 8.1); HRESIMS *m/z* 287.1484 [M+H]<sup>+</sup> (calcd. For C<sub>14</sub>H<sub>22</sub>O<sub>6</sub>, 287.1494).

*Acremodiol C (4)*: White, amorphous powder;  $[\alpha]_D^{20} = +22$  (c 0.10, MeOH),  $[\alpha]_D^{20} = +25$  (c 0.04, CHCl<sub>3</sub>); UV (MeOH)  $\lambda_{\max}$  (log  $\epsilon$ ) 213 (3.47) nm; <sup>1</sup>H NMR (CDCl<sub>3</sub>, 700 MHz) and <sup>13</sup>C (CDCl<sub>3</sub>, 175 MHz) (See Table 8.1); HRESIMS *m/z* 287.1487 [M+H]<sup>+</sup> (calcd. For C<sub>14</sub>H<sub>22</sub>O<sub>6</sub>, 287.1494).

**Cytotoxicity Assays.** Human melanoma cancer cells MDA-MB-435, human breast cancer cells MDA-MB-231 and human ovarian cancer cells OVCAR3 were purchased from the American Type Culture Collection (Manassas, VA). The cell line was propagated at 37 °C in 5% CO<sub>2</sub> in RPMI 1640 medium, supplemented with fetal bovine serum (10%), penicillin (100 units/mL), and streptomycin (100 µg/mL). Cells in log phase growth were harvested by trypsinization followed by two washing to remove all traces of enzyme. A total of 5,000 cells were seeded per well of a 96-well clear, flat-bottom plate (Microtest 96®, Falcon) and incubated overnight (37 °C in 5% CO<sub>2</sub>). Samples dissolved in DMSO were then diluted and added to the appropriate wells. The cells were

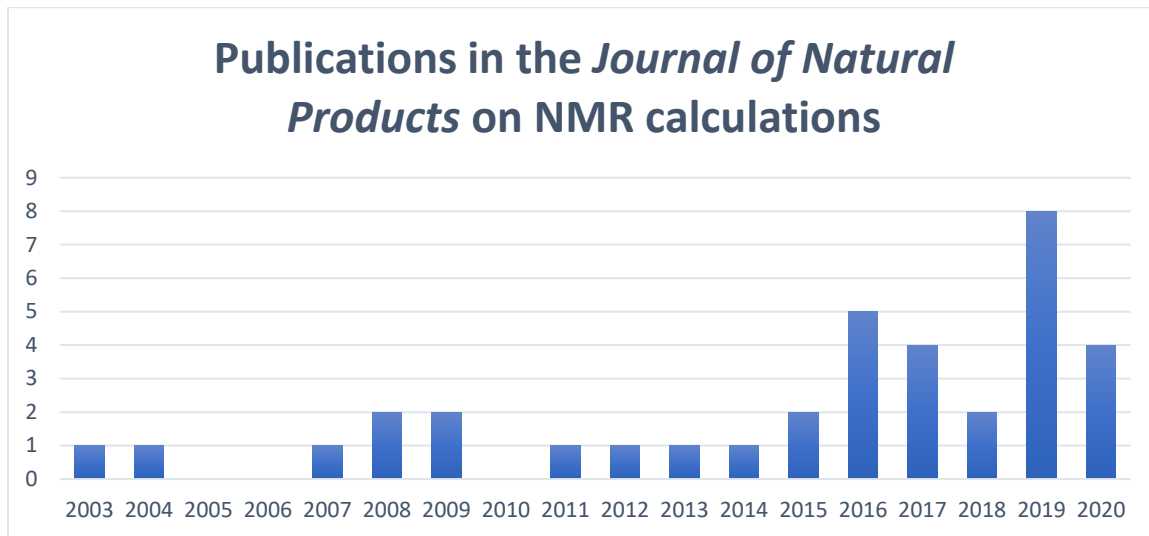
incubated in the presence of test substance for 72 h at 37 °C and evaluated for viability with a commercial absorbance assay (CellTiter-Blue Cell Viability Assay, Promega Corp, Madison, WI) that measured viable cells. IC<sub>50</sub> values are expressed in µM relative to the solvent (DMSO) control. Compound **1** was analyzed with four technical replicates and three biological replicates and was >90% pure by UPLC.

**Antimicrobial Measurement.** Minimal inhibitory concentrations of the compounds were measured by broth microdilution against the following bacteria, namely *Escherichia coli*, *Staphylococcus aureus*, *methicillin-resistant S. aureus* (MRSA), *Pseudomonas aeruginosa*, *Bacillus anthracis*, MICs were measured by broth microdilution of fresh overnight cultures according to the Clinical and Laboratory Standards Institute (CCLI) guidelines with cation-adjusted Mueller–Hinton broth and an inoculum of 10<sup>5</sup> colony-forming units (CFU)/mL. Stocks of the compounds were dissolved in Mueller–Hinton broth (Becton-Dickenson, Sparks, MD). The MIC (expressed as µg/mL) was defined as the lowest concentration of compound completely inhibiting the appearance of turbidity by eye and confirmed by absorbance 540 nm. All results represent the average of three independent measurements. Prior to testing, **1** and **4** were confirmed >90% pure by UPLC.

**Computational Details.** All molecular mechanics calculations were performed using Macromodel (Version 12.6) interface Maestro (Version 12.2) program. All conformational searches used the MMFF force field and torsional sampling Monte Carlo Multiple Minimum (MCMM) method with extended torsional sampling.<sup>106</sup> The resulting conformers were filtered checked for duplicity and minimized using a DFT forcefield at the M062X/6-31+G (d,p) level of theory. NMR shielding constants were calculated at the GIAO method at B3LYP/6-311+G (2d,p) level of theory with the IEFPCM model in

chloroform solvent. The obtained shielding constants were converted into chemical shifts (ppm) by refereeing TMS to 0 ppm. The final  $^{13}\text{C}$  and  $^1\text{H}$  NMR shifts were calculated for each conformer based on the total Boltzmann distribution and relative energies. The NMR shifts for each particular species was calculated based on the Nature Protocol by Willoughby et al.<sup>106, 107</sup> To calculate the corrected correlation coefficient ( $r$ ) for the combined  $^{13}\text{C}$  and  $^1\text{H}$  data, the calculated  $^{13}\text{C}$  and  $^1\text{H}$  NMR data was first empirically scaled ( $\delta_{\text{scaled}} = \frac{\delta_{\text{calc}} - \text{intercept}}{\text{slope}}$ ), then the individual correlation coefficients were calculated in excel (=correl(calculated, experimental)) and lastly, the geometric mean ( $r_{\text{all}} = 1 - \sqrt{(1 - r_C)(1 - r_H)}$ ) of the correlation coefficients for  $^{13}\text{C}$  and  $^1\text{H}$  was taken.<sup>104</sup>,<sup>105</sup> The DP4+ calculations were carried out by using the spreadsheet provided by the Sarotti Group.<sup>411</sup> To calculate the optical rotation values, the conformers generated for the NMR calculations were used. The optical rotations were calculated at the GIAO method at B3LYP/6-31G (d,p) level of theory in MeOH for **1-4** and in  $\text{CHCl}_3$  for **4**,<sup>111, 421</sup> based on the total Boltzmann distribution and relative energies using SpecDis..<sup>422, 423</sup>

## Supplementary Data



This graph was obtained by searching 2003 - April 2020 in SciFinder the terms: NMR calculation(s), GIAO,  $^{13}\text{C}$  calculations, and  $^1\text{H}$  calculations, with the duplicates being removed.

**Figure 122.** Publications in the *Journal of Natural Products* on NMR calculations

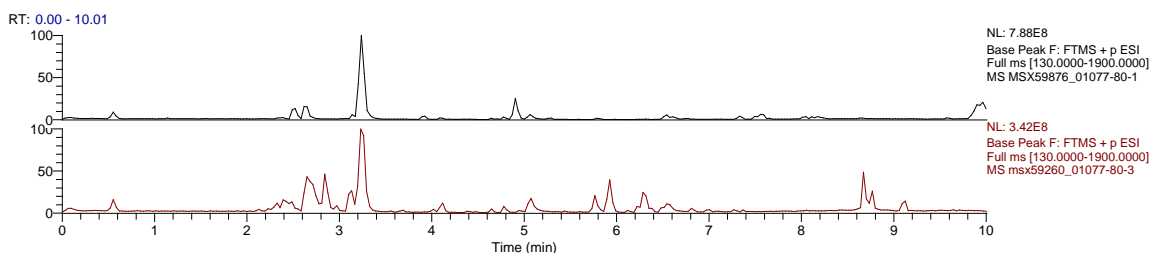


**Figure 123.** LC-MS chromatograms of MSX59876 (Top) and MSX59260 (Bottom)

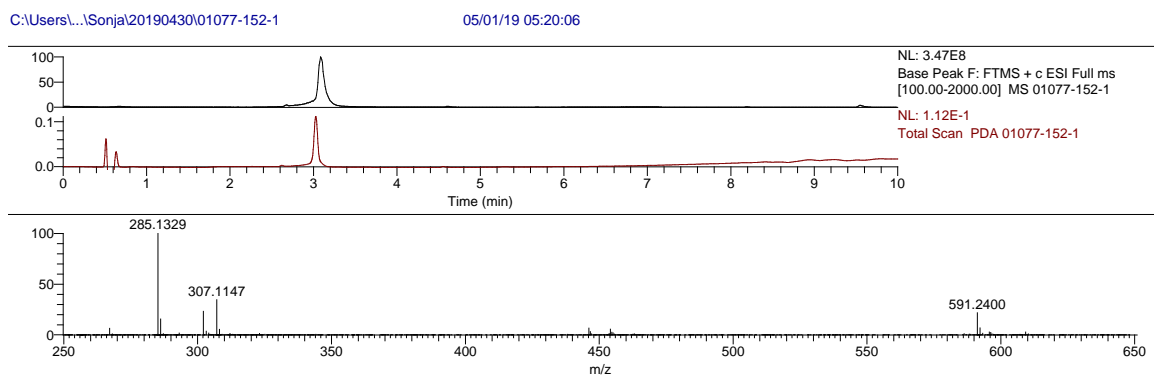


**Figure 124.** LC-MS chromatogram and (+)-HRESIMS spectrum of compound 1

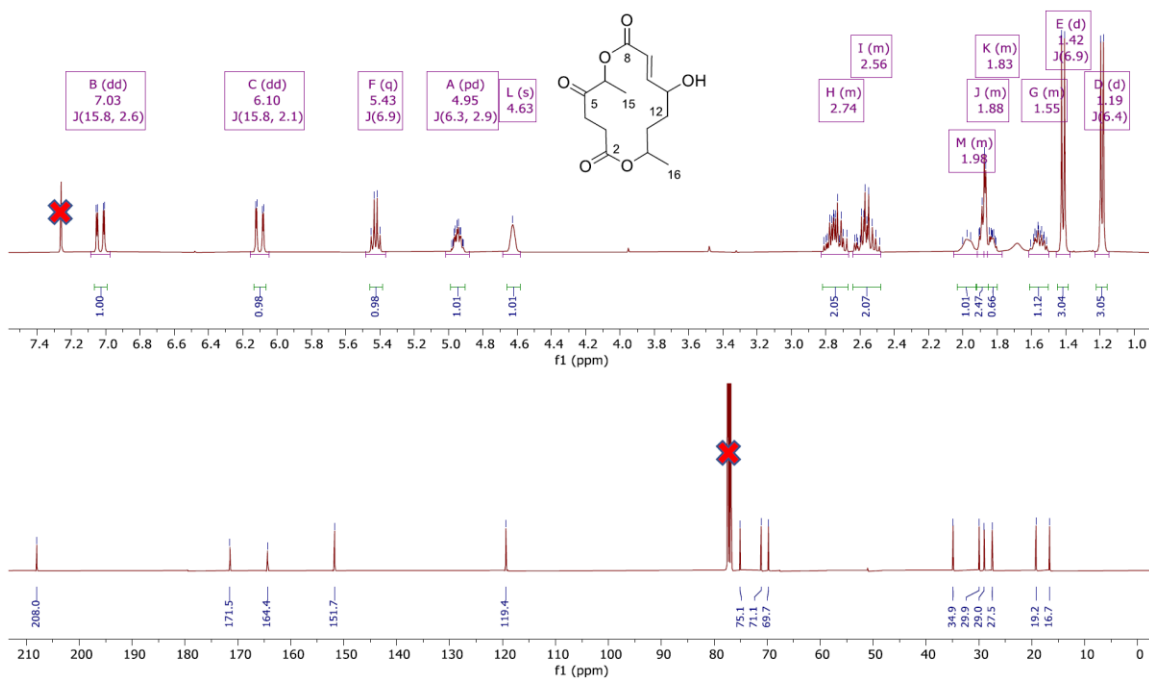


**Figure 125.** <sup>1</sup>H NMR spectrum (400 MHz, Top) and <sup>13</sup>C NMR spectrum (100 MHz, Bottom) both in CDCl<sub>3</sub>, of dihydroacremone (1)

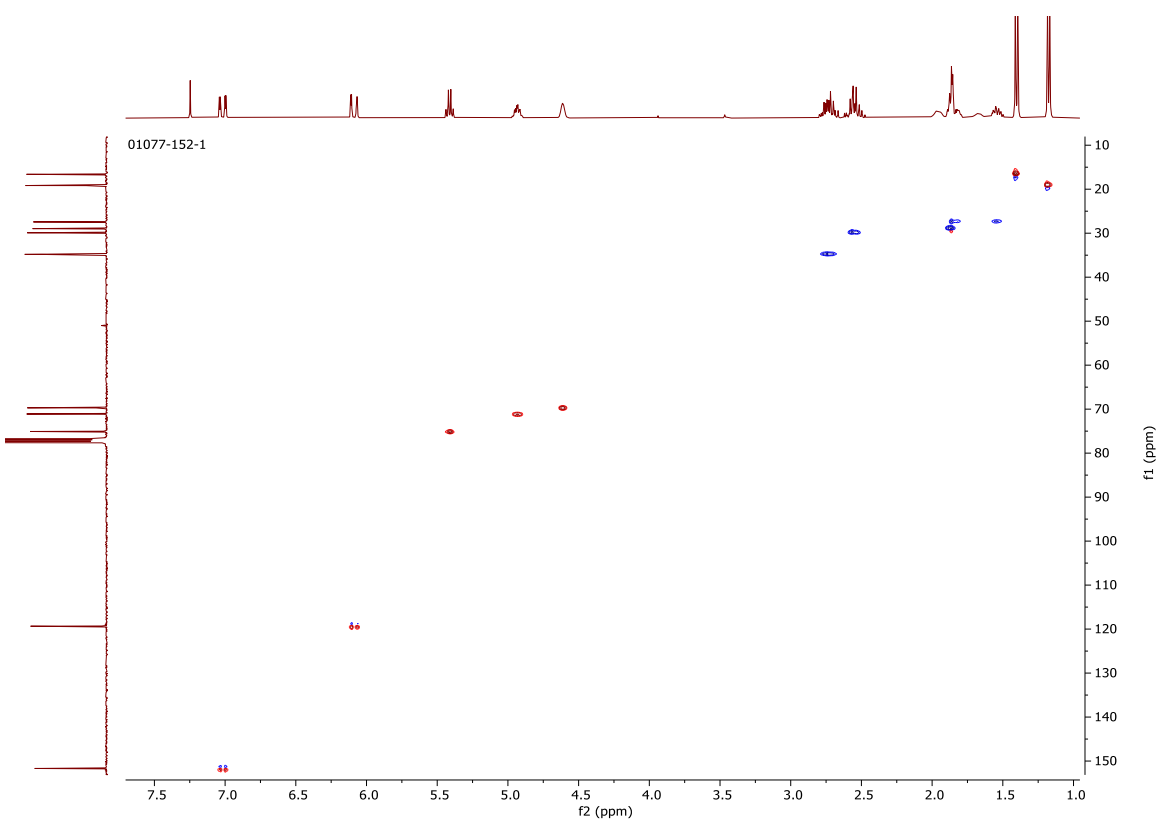


**Figure 126.** HSQC spectrum of dihydroacremonol (**1**),  $\text{CDCl}_3$ , 400 MHz

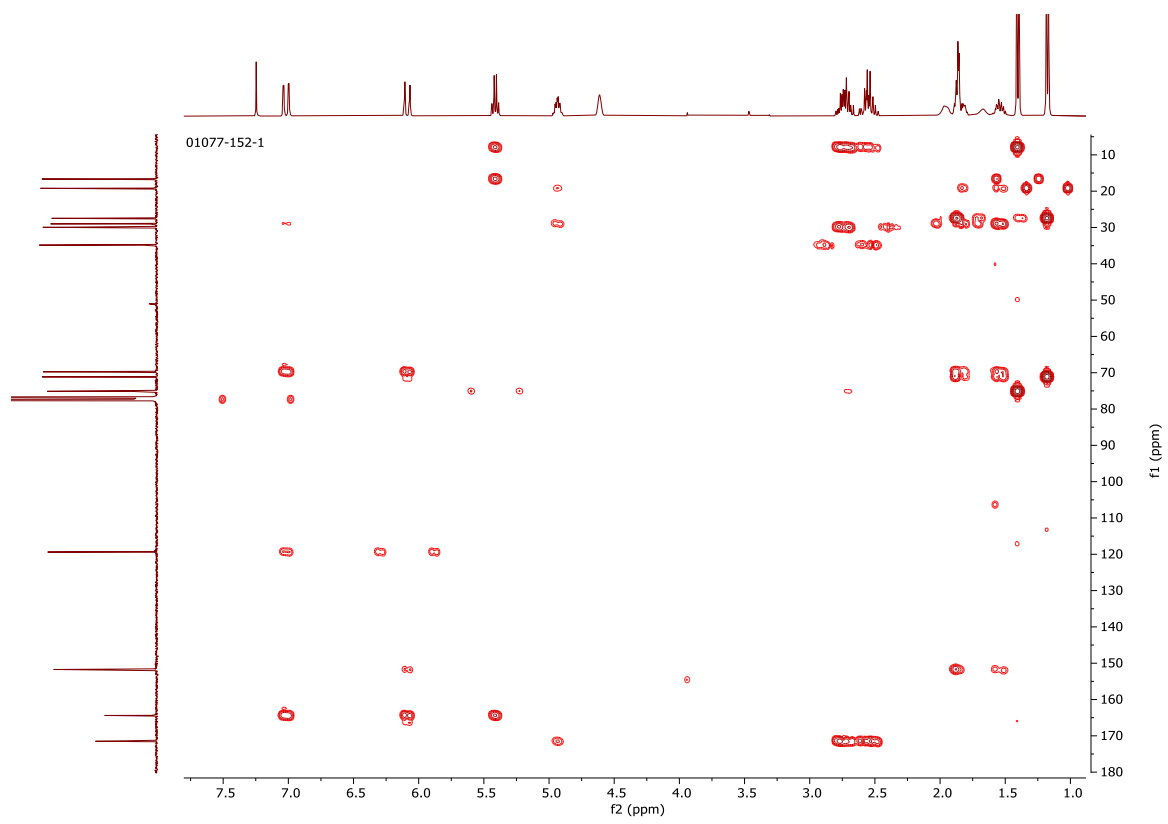


**Figure 127.** HMBC spectrum of dihydroacremonol (**1**),  $\text{CDCl}_3$ , 400 MHz

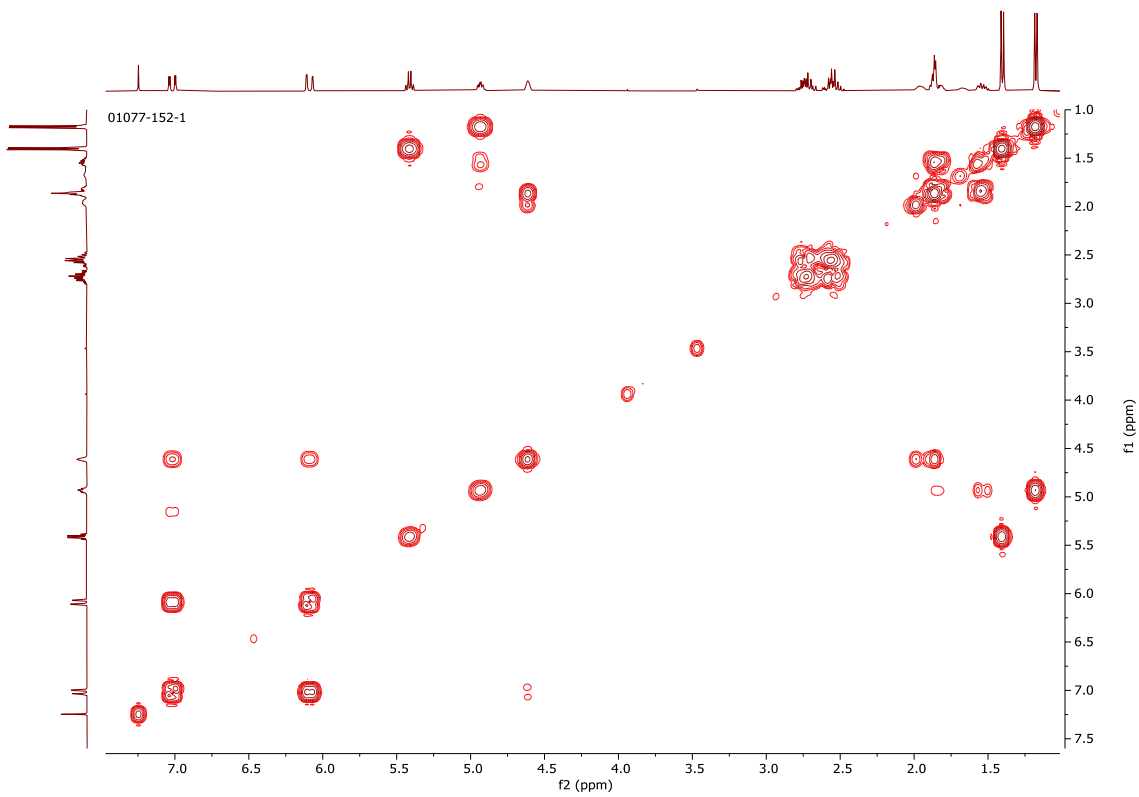


**Figure 128.**  $^1\text{H}$  COSY spectrum of dihydroacremonol (**1**),  $\text{CDCl}_3$ , 400 MHz

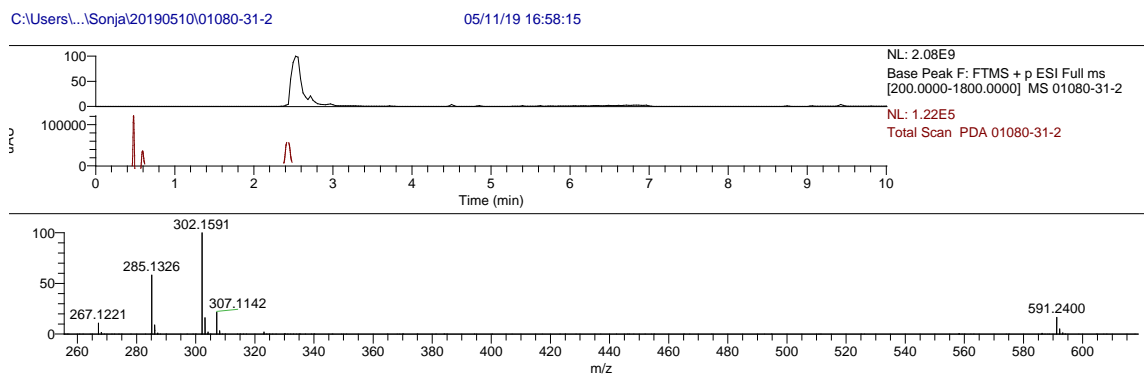


**Figure 129.** LC-MS chromatogram and (+)-HRESIMS spectrum of compound **2**

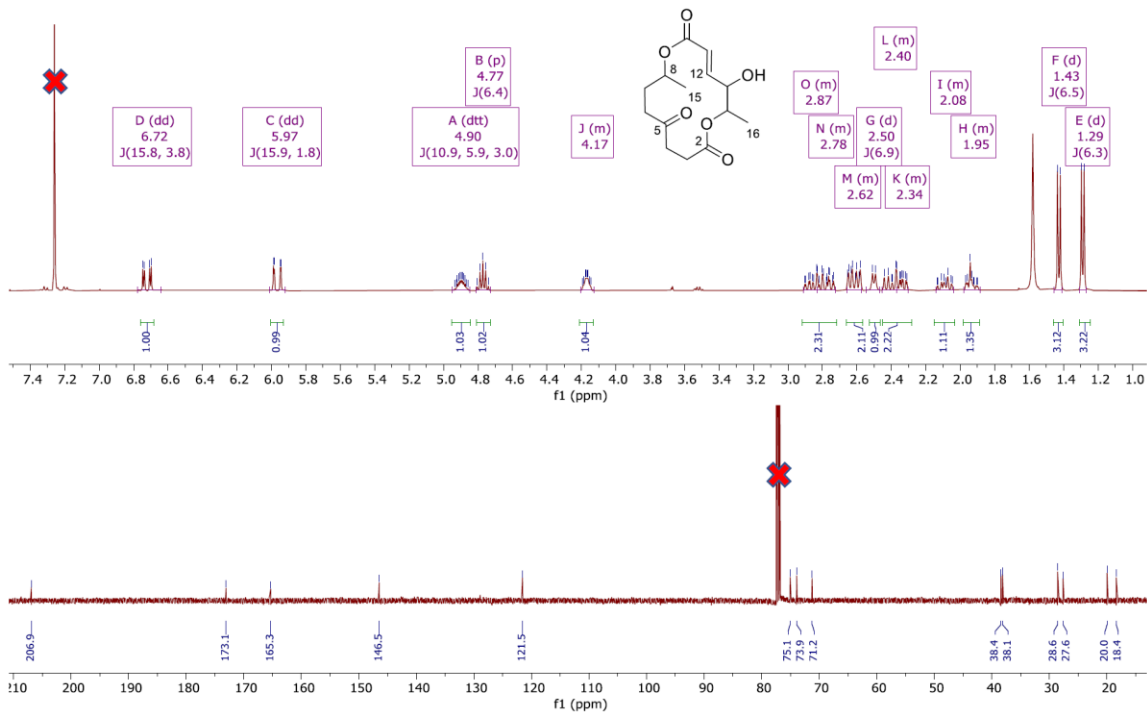


**Figure 130.** <sup>1</sup>H NMR spectrum (400 MHz, Top) and <sup>13</sup>C NMR spectrum (100 MHz, Bottom) both in CDCl<sub>3</sub>, of clonostachyone (**2**)

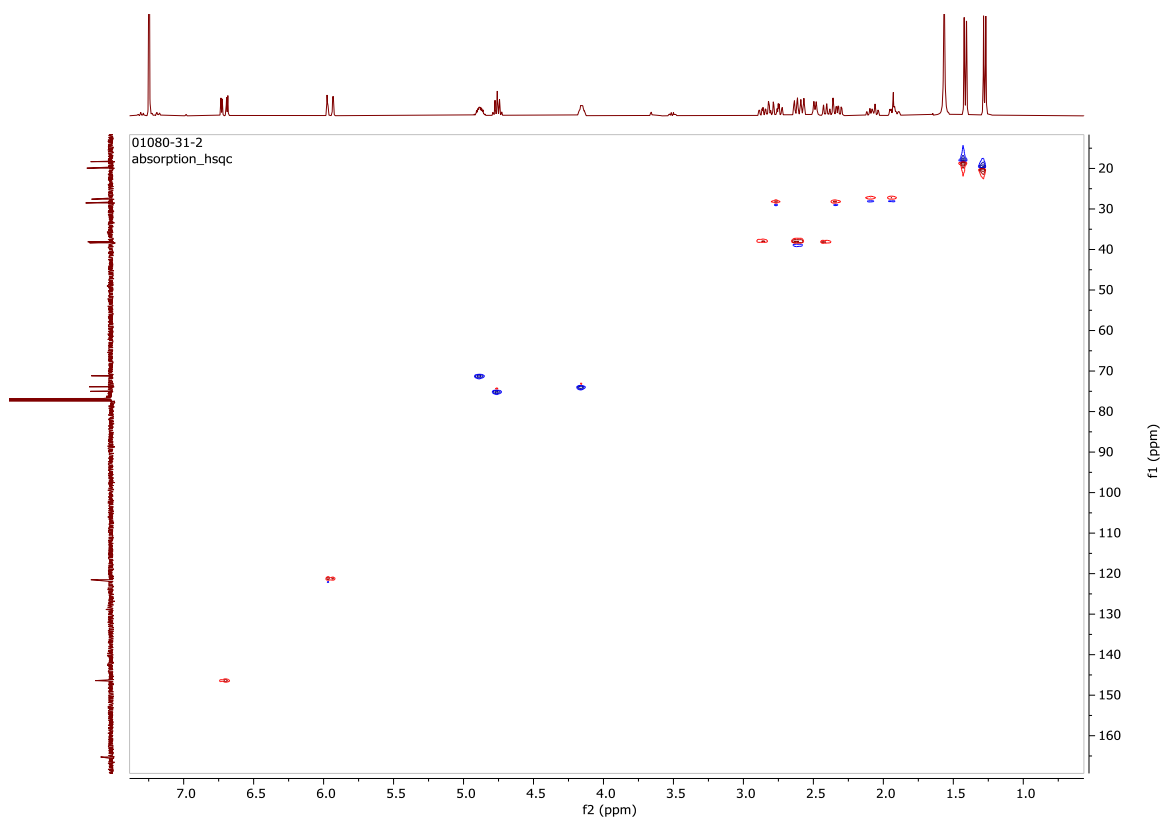


**Figure 131.** HSQC spectrum of clonostachyone (**2**), CDCl<sub>3</sub>, 400 MHz

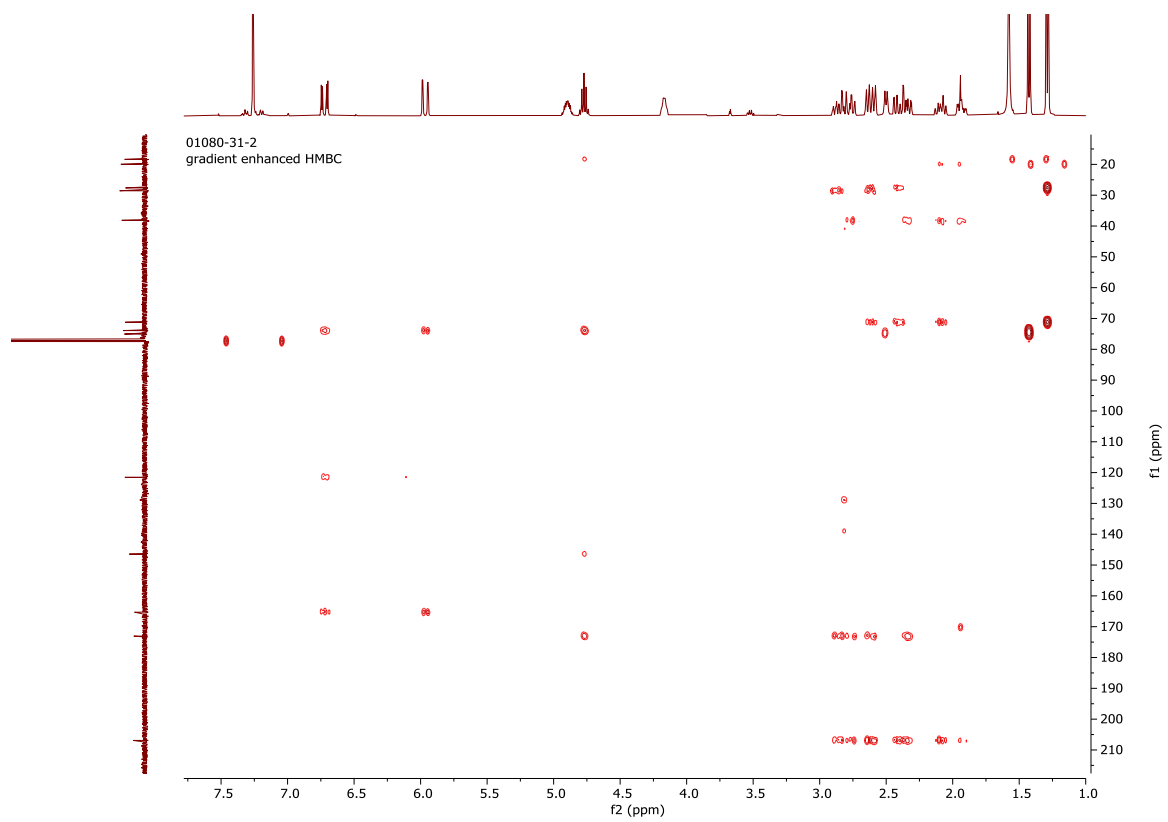


**Figure 132.** HMBC spectrum of clonostachyone (**2**),  $\text{CDCl}_3$ , 400 MHz

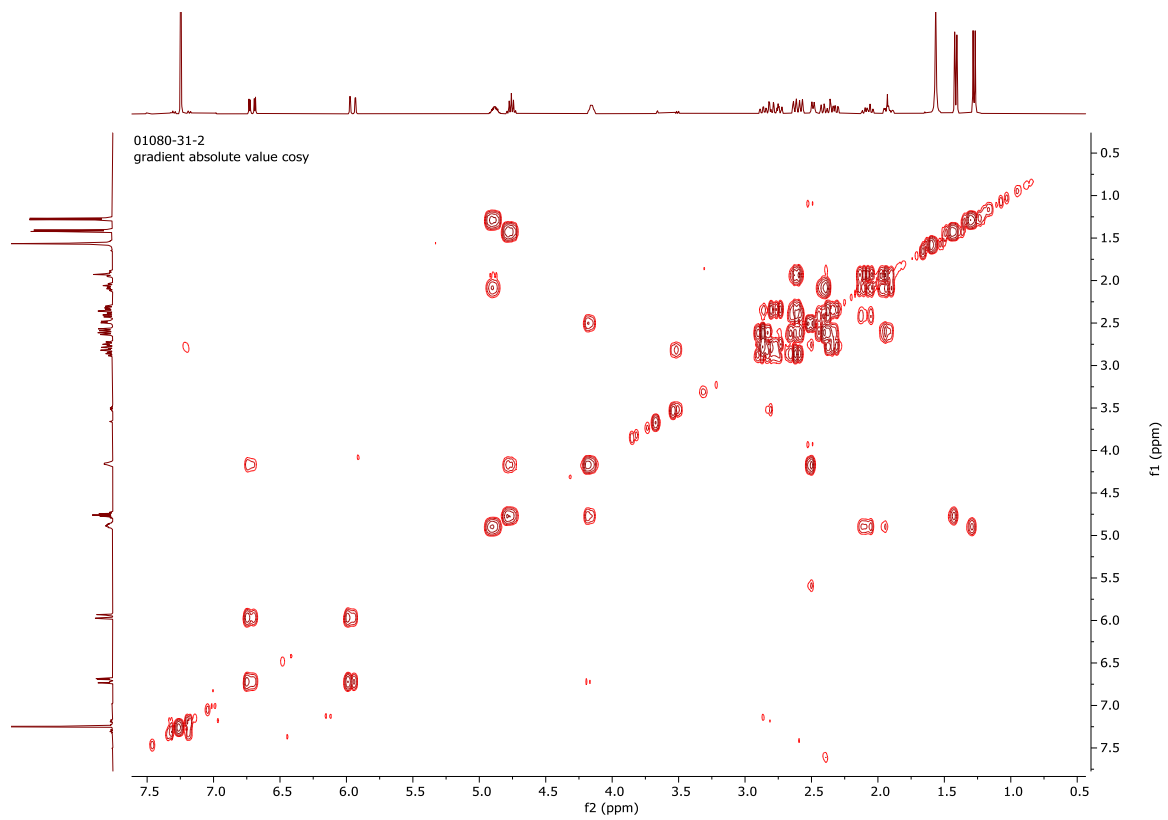


**Figure 133.**  $^1\text{H}$  COSY spectrum of clonostachyone (**2**),  $\text{CDCl}_3$ , 400 MHz

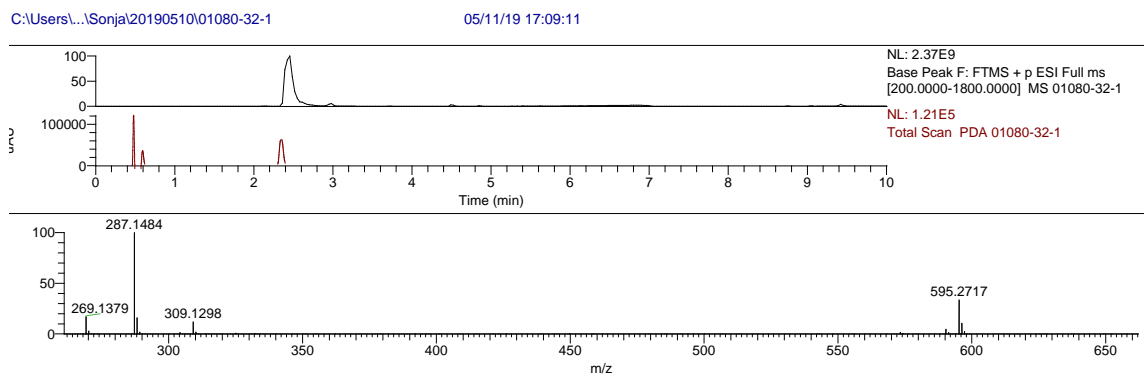


**Figure 134.** LC-MS chromatogram and (+)-HRESIMS spectrum of compound **3**

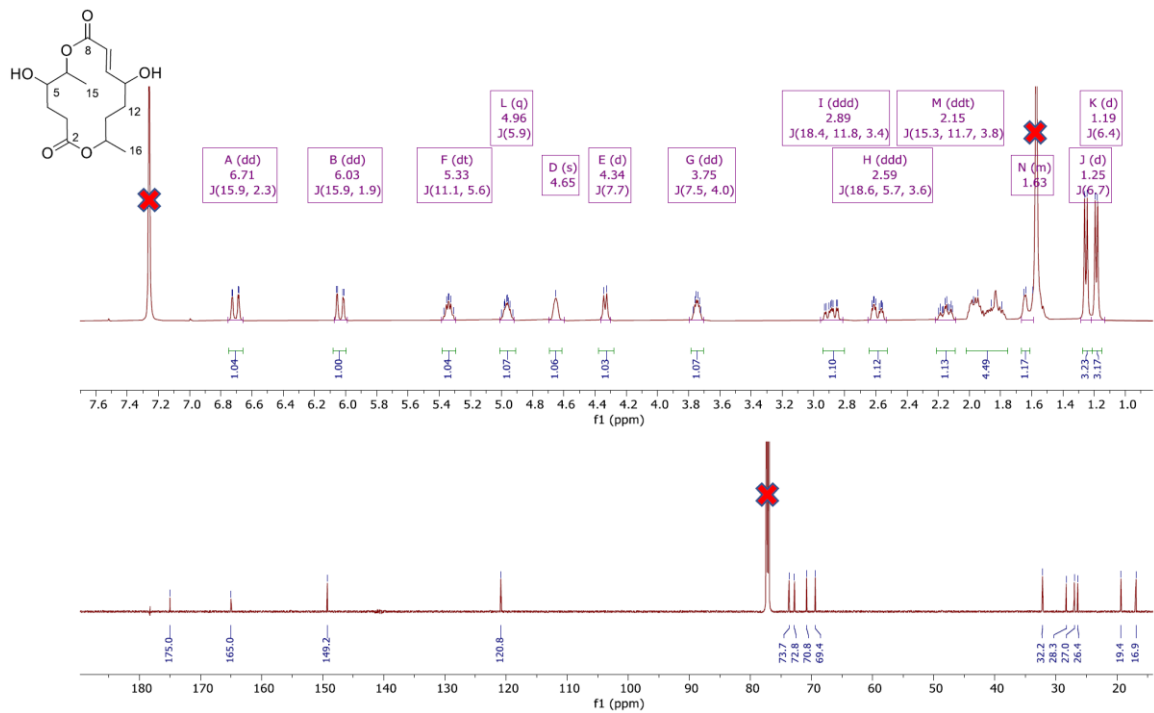


**Figure 135.** <sup>1</sup>H NMR spectrum (700 MHz, Top) and <sup>13</sup>C NMR spectrum (175 MHz, Bottom) both in CDCl<sub>3</sub>, of acremodiol B (3)

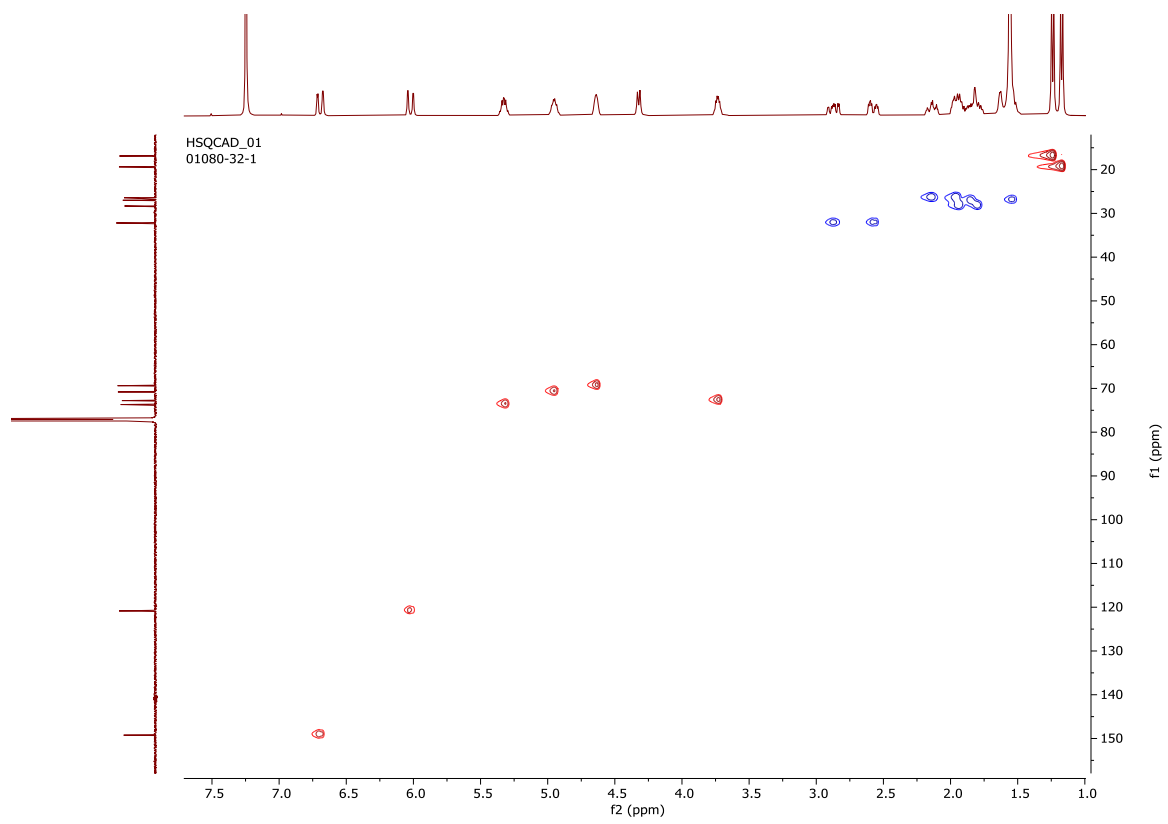


**Figure 136.** HSQC spectrum of acremodiol B (**3**),  $\text{CDCl}_3$ , 700 MHz

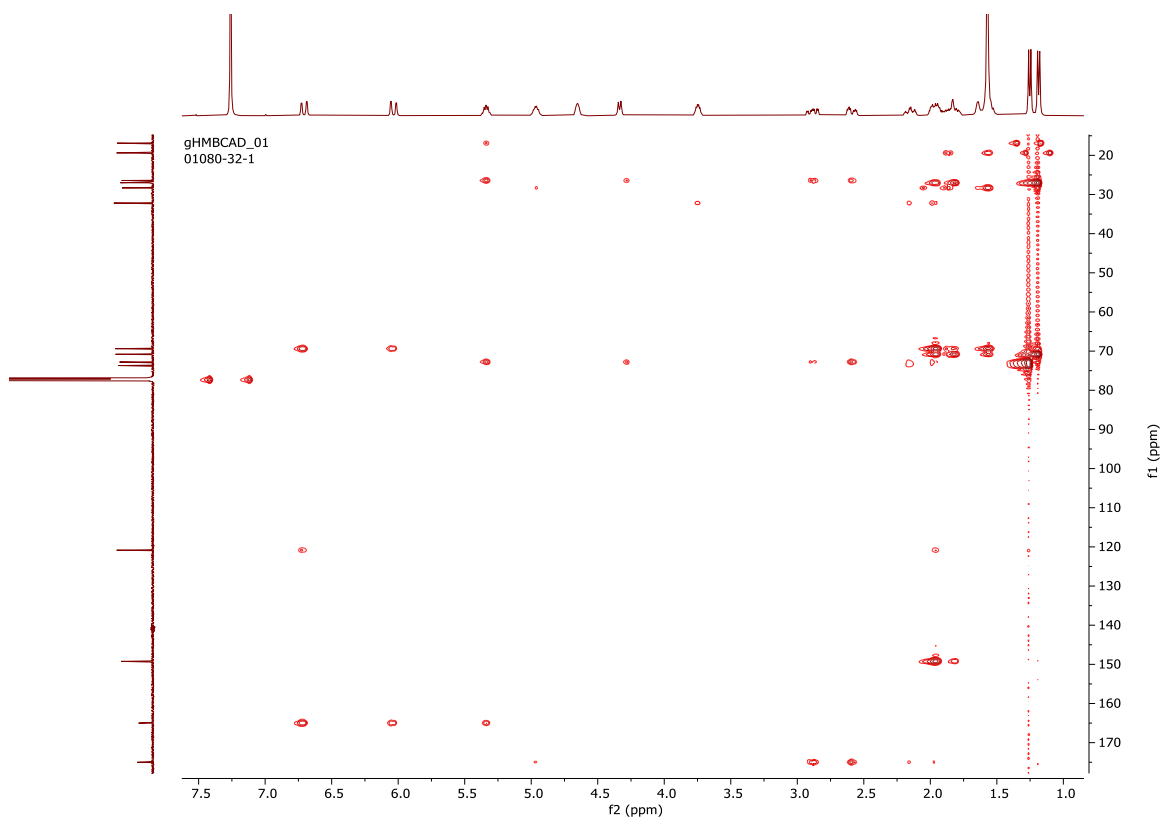


**Figure 137.** HMBC spectrum of acremodiol B (**3**),  $\text{CDCl}_3$ , 700 MHz

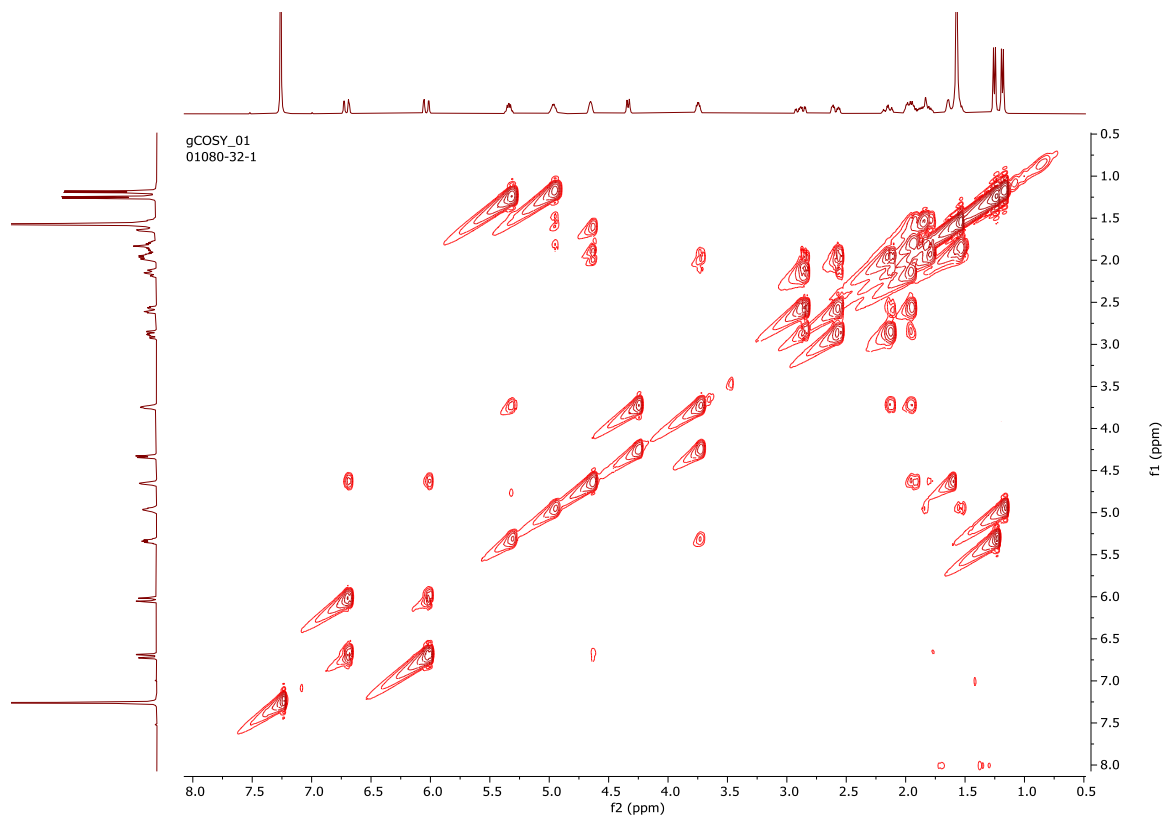


**Figure 138.**  $^1\text{H}$  COSY spectrum of acremodiol B (**3**),  $\text{CDCl}_3$ , 700 MHz

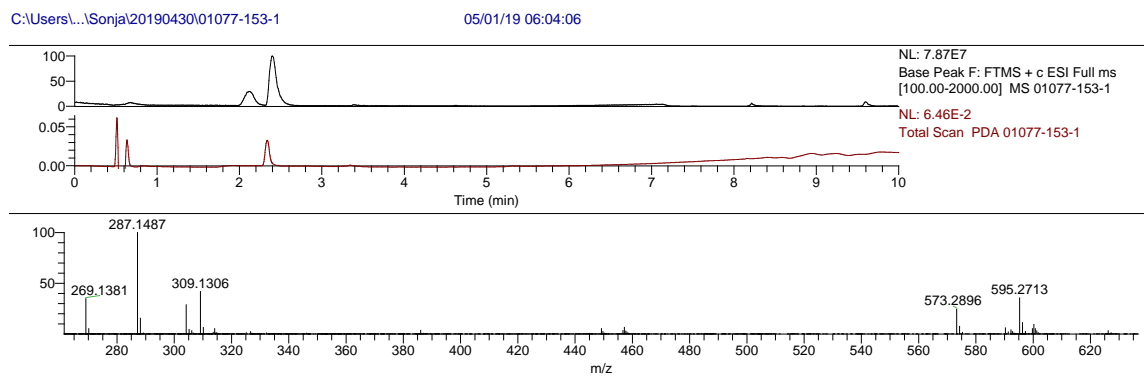


**Figure 139.** LC-MS chromatogram and (+)-HRESIMS spectrum of compound **4**

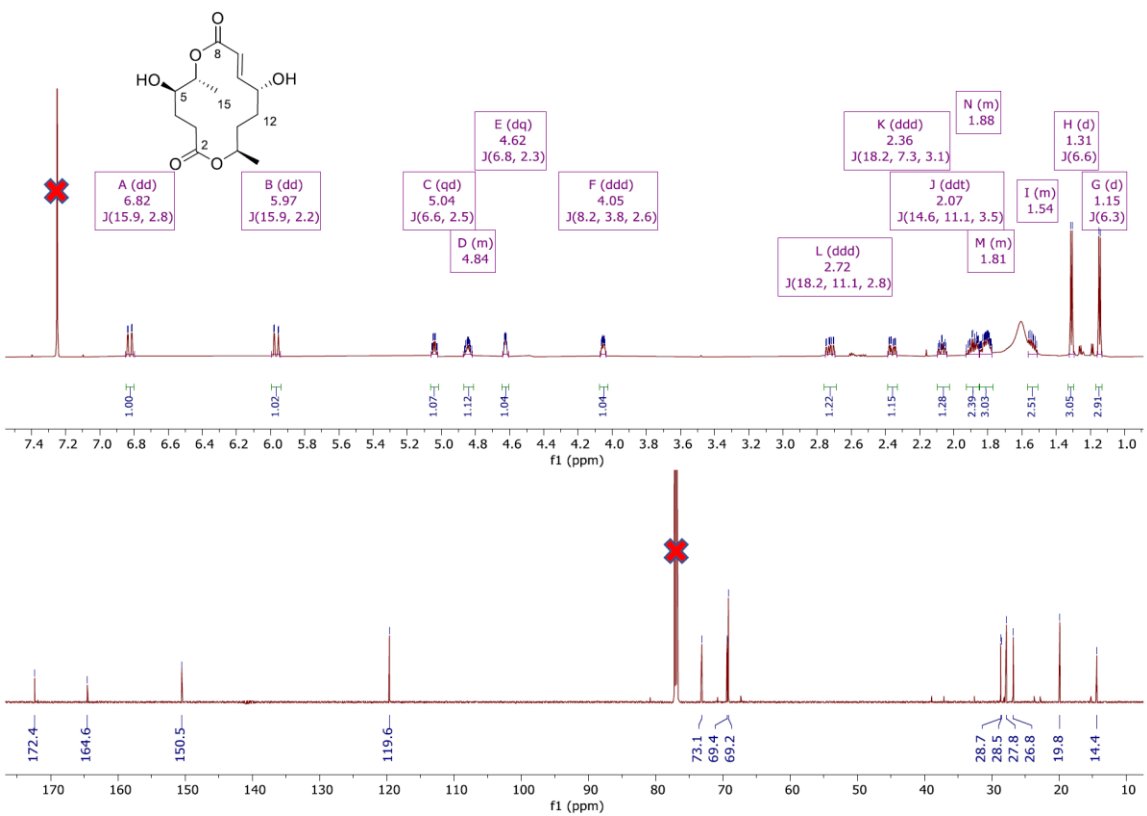


**Figure 140.** <sup>1</sup>H NMR spectrum (700 MHz, Top) and <sup>13</sup>C NMR spectrum (175 MHz, Bottom) both in CDCl<sub>3</sub>, of acremodiol C (4)

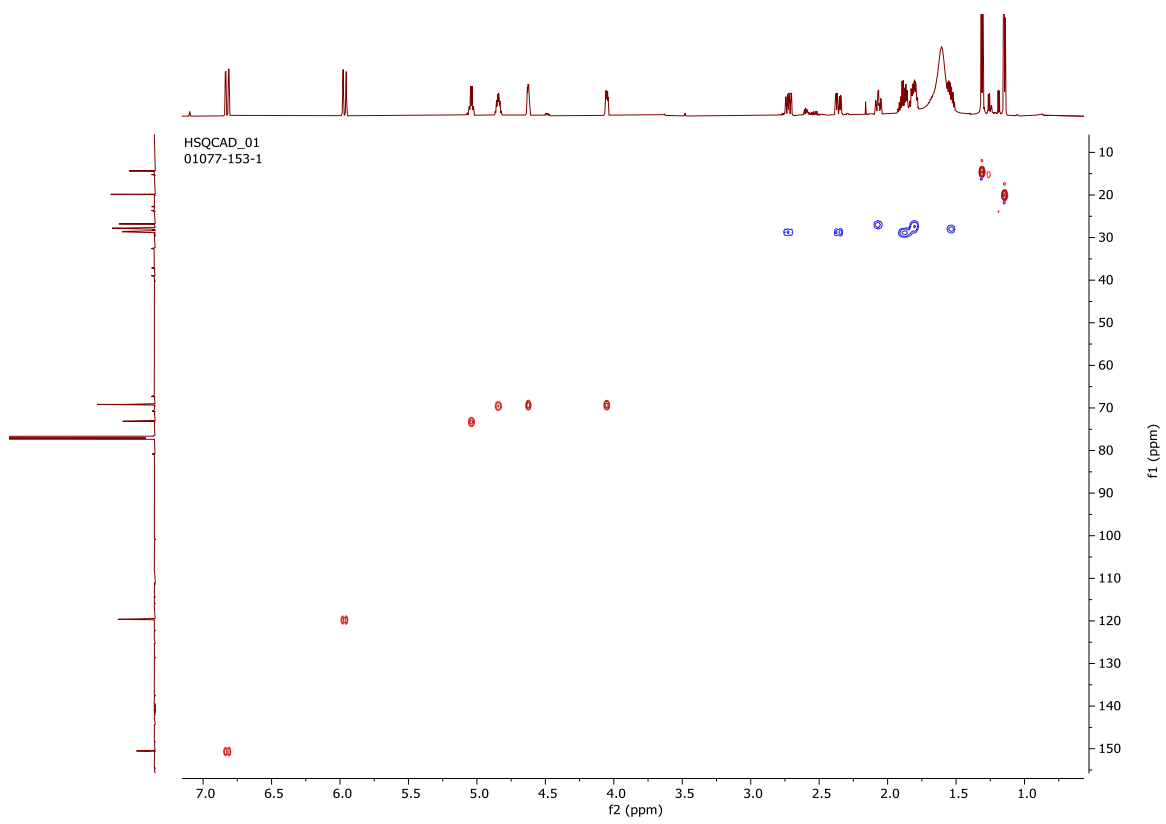


**Figure 141.** HSQC spectrum of acremodiol C (**4**),  $\text{CDCl}_3$ , 700 MHz

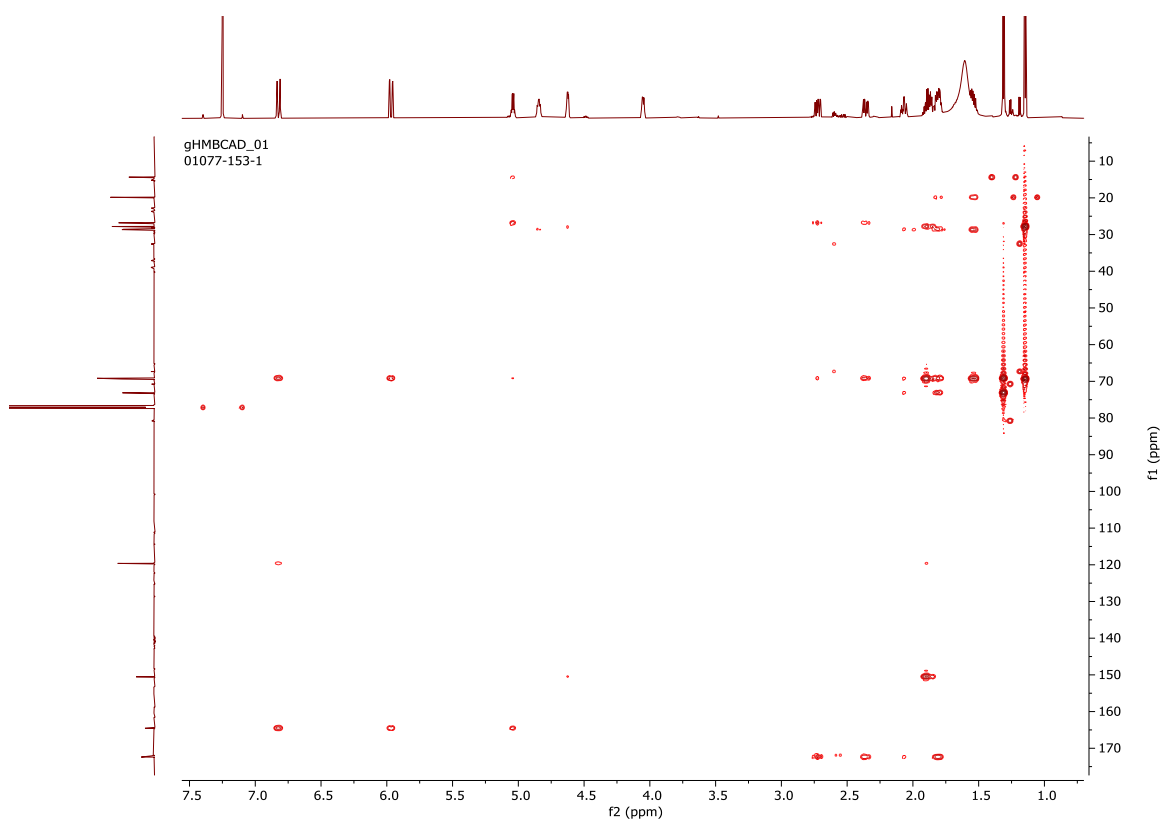


**Figure 142.** HMBC spectrum acremodiol C (**4**),  $\text{CDCl}_3$ , 700 MHz

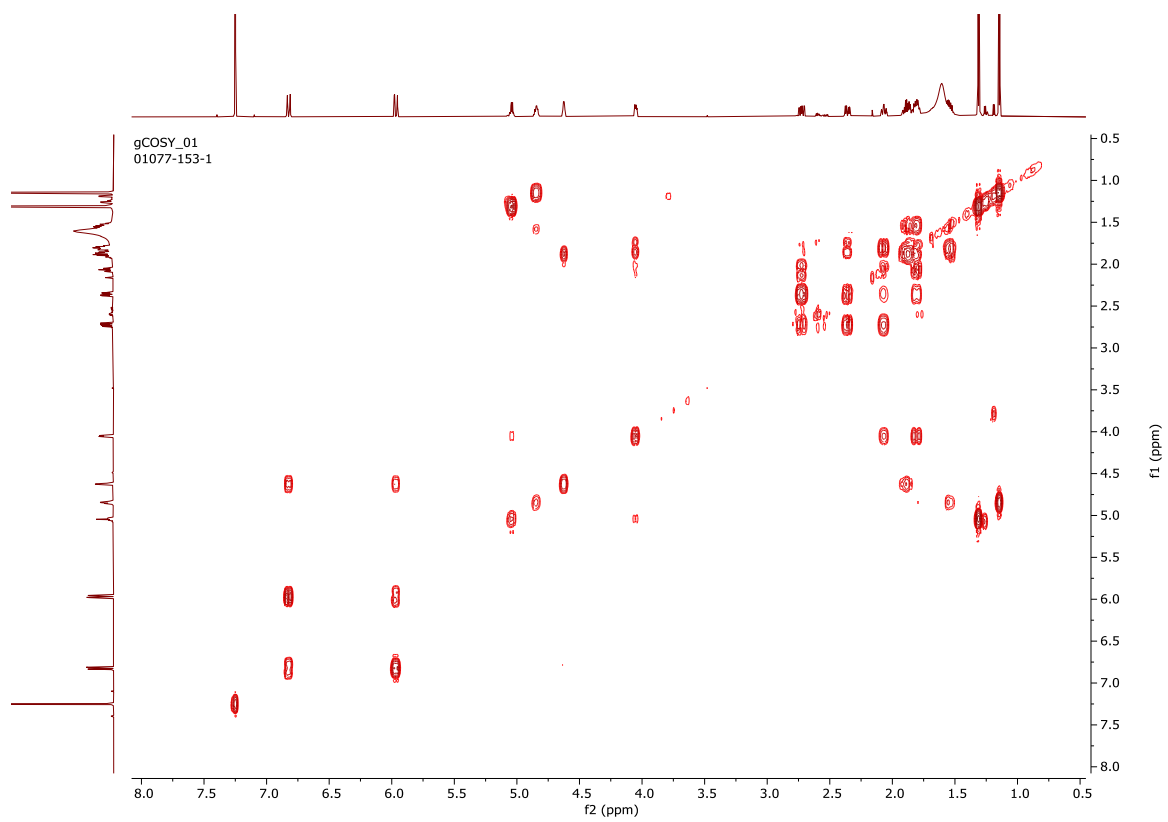


**Figure 143.** <sup>1</sup>H COSY spectrum of acremodiol C (**4**), CDCl<sub>3</sub>, 700 MHz

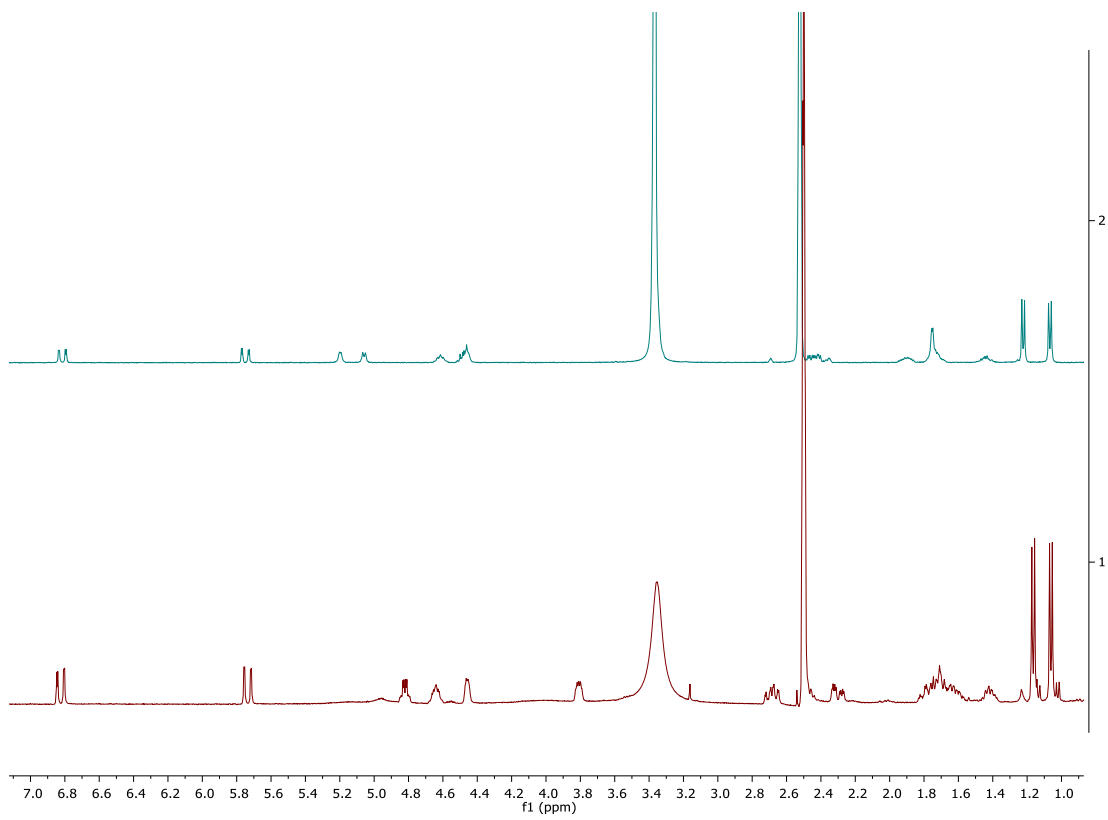


**Figure 144.** <sup>1</sup>H NMR spectrum comparison of acremodiol B (3; Top) and acremodiol C (4; Bottom), both in DMSO-*d*<sub>6</sub>, 300 MHz on the 400 MHz NMR

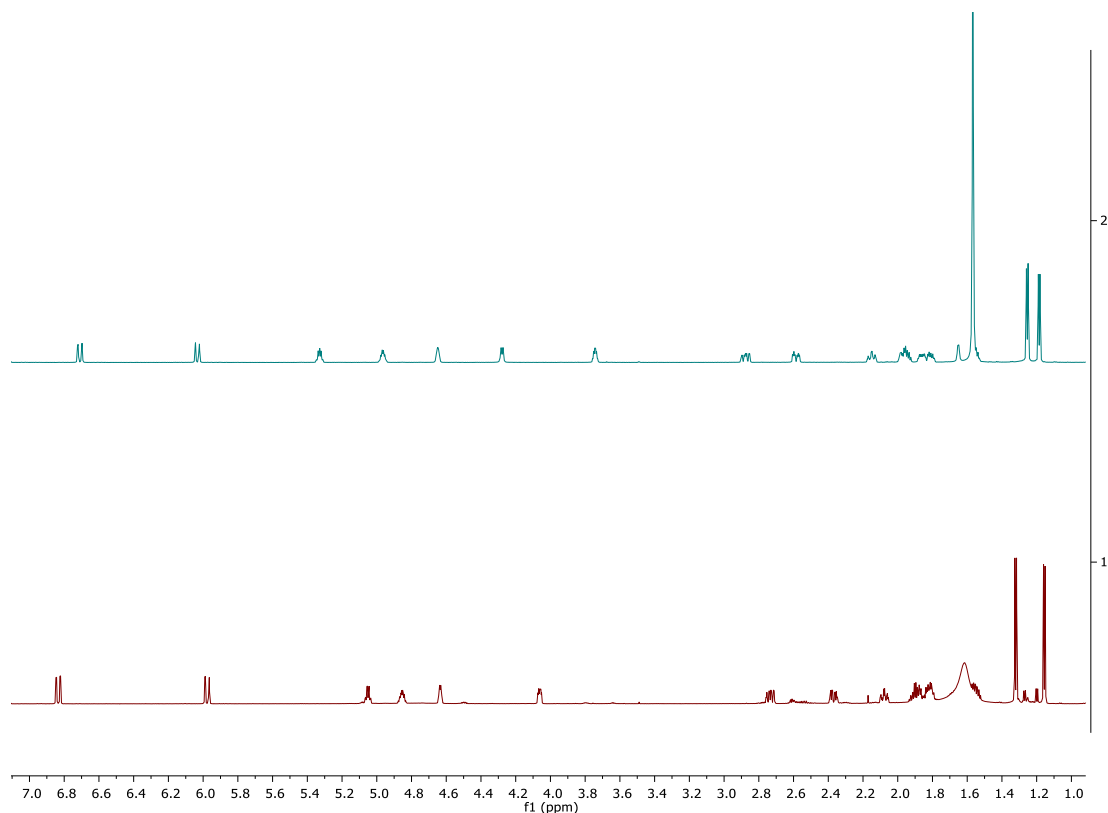


**Figure 145.** <sup>1</sup>H NMR spectrum comparison of acremodiol B (3; Top) and acremodiol C (4; Bottom), both in CDCl<sub>3</sub> on the 400 MHz NMR

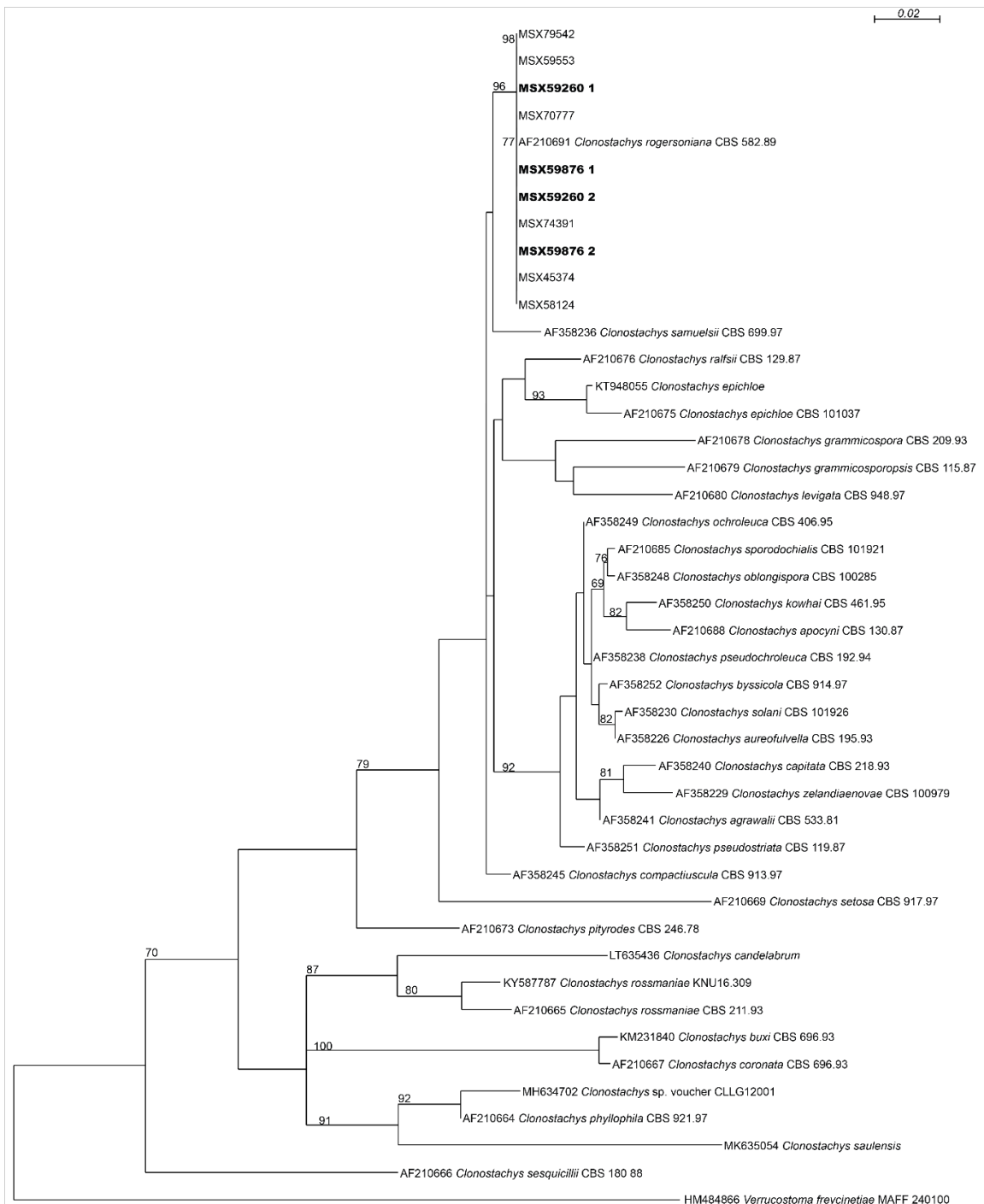


**Figure 146.** Phylogeny of MSX59260 and MSX59876. Maximum Likelihood analysis using RAxML showing the most likely tree (-lnL = 1618.89) from 44 taxa based on the ITS data (493 bp). Numbers refer to RAxML bootstrap support values  $\geq 70\%$  based on 1000 replicates. Strains MSX59260 and MSX 59876 are in bold and identified as

*Clonostachys* sp., with phylogenetic affiliations to *C. rogersiana* (Bionectriaceae, Hypocreales, Ascomycota). Bar indicates nucleotide substitutions per site.

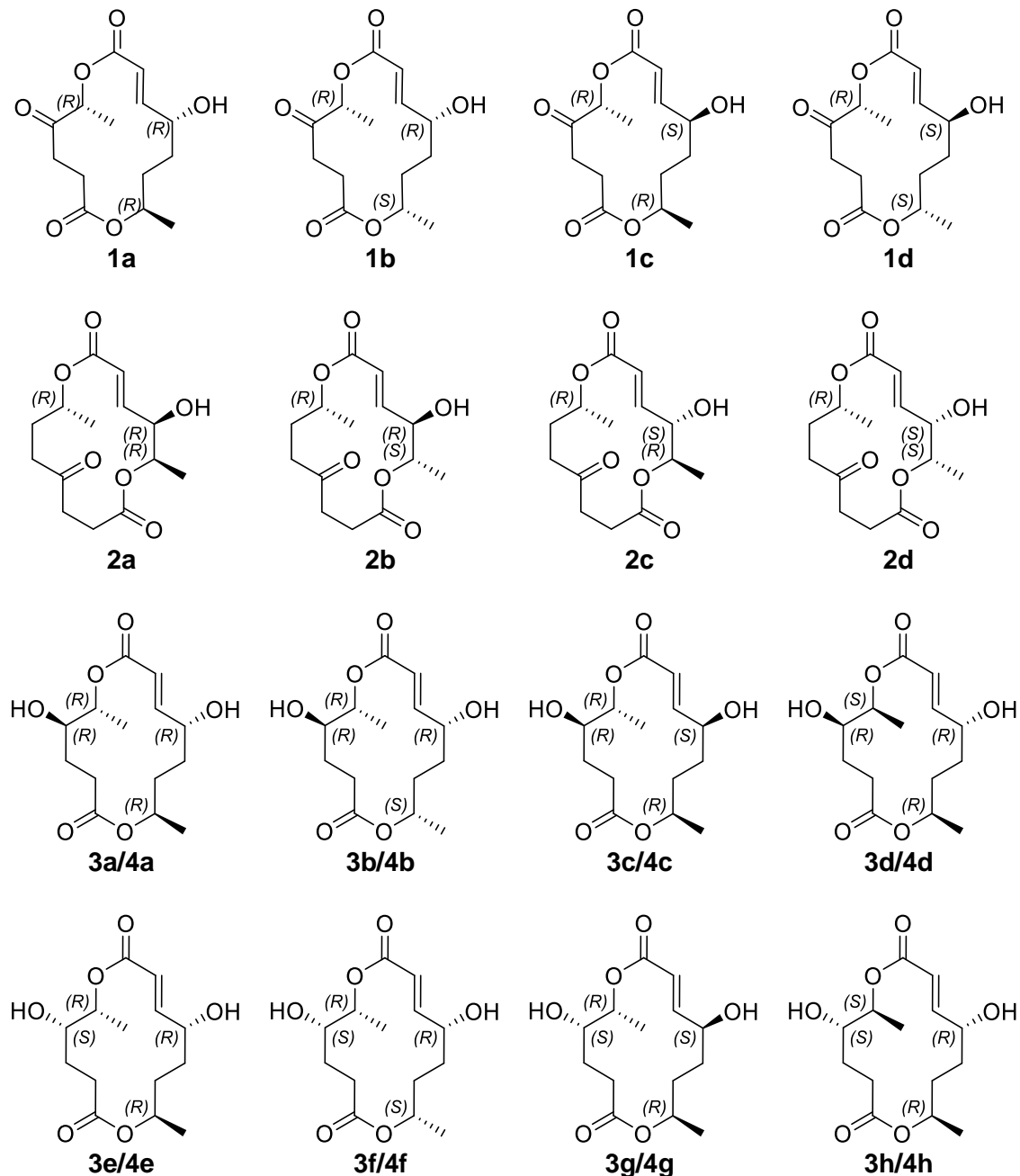


**Figure 147.** The structure used in GIAO NMR calculations. GIAO NMR calculations cannot distinguish between enantiomers, therefore, only half of all possible stereoisomers are shown for each compound

**Table 8.3.** Calculated and experimental  $^{13}\text{C}$  shifts (in ppm) for **1a-1d**

Pos	$^{13}\text{C}$ Corrected Calculated				$^{13}\text{C}$ Experimental 1
	<b>1a</b>	<b>1b</b>	<b>1c</b>	<b>1d</b>	
2	172.0426998	172.5395571	172.4469731	174.0128442	171.5
3	30.28966952	32.62059702	31.53233881	30.66707685	34.9
4	34.78250104	38.13332120	35.47345115	34.44929298	29.9
5	212.8423169	212.7458301	212.4595536	213.6713997	208.0
6	74.19171425	75.33996941	75.48626505	76.26699019	75.1
8	162.9532295	163.8774110	163.7402996	166.3803791	164.4
9	117.4768187	116.7519894	121.2598081	117.9834873	119.4
10	155.4151128	157.9855808	154.3842260	159.0400148	151.7
11	69.18461071	71.10933162	73.22123954	71.36944311	69.7
12	27.73822869	31.12906912	31.26017738	29.55367677	29.0
13	26.99576885	26.61778761	30.01647865	26.10948588	27.5
14	68.55873166	72.19325383	69.00214826	70.87892078	71.1
16	16.11940656	17.28191467	17.35213999	15.83207293	19.2
19	13.21334508	15.01896584	14.47863357	14.18479602	16.7

**Table 8.4.** Calculated and experimental  $^1\text{H}$  shifts (in ppm) for **1a-1d**

Pos	$^1\text{H}$ Corrected Calculated				$^1\text{H}$ Experimental 1
	<b>1a</b>	<b>1b</b>	<b>1c</b>	<b>1d</b>	
3a	2.548170	2.268844	2.468521	2.468823	2.73
3b	2.686907	2.762037	2.648671	2.442497	2.73
4a	3.053595	2.805082	2.819389	2.191744	2.55
4b	2.426290	2.459911	2.449257	3.105777	2.55
6	5.387993	5.358350	5.138418	4.876544	5.41
9	5.925194	6.015246	5.601510	5.853246	6.09
10	7.063152	7.383758	6.566392	7.132419	7.02
11	4.638037	4.535839	3.926989	4.440309	4.61
12a	1.906984	1.929031	1.685036	1.733795	1.86
12b	1.865961	1.519861	1.781658	1.895441	1.86
13a	1.444922	1.566922	1.621858	2.046122	1.54
13b	2.003478	1.628094	1.647885	1.433900	1.81
14	4.746854	4.557121	4.443867	4.689824	4.93
15	1.102736	1.421968	1.170226	1.402605	1.40
16	1.156638	1.129304	1.157446	1.235274	1.18

**Table 8.5.** Average values of the correlation coefficients for **1a-1d**. The “all” refers to  $^{13}\text{C}$  and  $^1\text{H}$  results combined using the geometric mean.

Compound	correlation coefficient (all)
<b>1a</b>	0.972657
<b>1b</b>	0.966325
<b>1c</b>	0.972197
<b>1d</b>	0.973266

**Table 8.6.** Calculated and experimental  $^{13}\text{C}$  shifts (in ppm) for **2a-2d**

Pos	$^{13}\text{C}$ Corrected Calculated				$^{13}\text{C}$ Experimental
	<b>2a</b>	<b>2b</b>	<b>2c</b>	<b>2d</b>	
2	173.6536931	174.9212751	175.1868321	148.9784305	173.1
3	28.27677235	28.13301049	28.48098282	26.07624936	28.5
4	36.32197009	36.28245959	37.67707866	32.90117102	38.2
5	212.6204795	212.6053341	213.1623715	183.0020226	206.9
6	37.98529357	36.18022537	39.91819758	33.59369538	38.4
7	25.68937607	24.91084298	27.98841333	22.95278146	27.6
8	69.23499463	67.47162091	71.24559867	60.26041878	71.2
10	165.3043168	164.7991334	165.3184673	141.4998486	165.3
11	119.5935266	122.3200905	119.6141590	102.9446629	121.5
12	153.0681503	149.4998930	153.9418041	133.7167530	146.5
13	73.18790739	75.66826035	74.24326563	62.66656657	73.9
14	71.37972690	72.98130337	73.81426738	62.99382748	75.1
15	15.82685101	14.67257436	16.98380860	14.05646077	20.0
16	12.54573333	14.42685008	15.86772411	10.69865207	18.4

**Table 8.7.** Calculated and experimental  $^1\text{H}$  shifts (in ppm) for **2a-2d**

Pos	$^1\text{H}$ Corrected Calculated				$^1\text{H}$ Experimental
	<b>2a</b>	<b>2b</b>	<b>2c</b>	<b>2d</b>	
3a	2.145049737	2.607784357	2.102999442	1.913060077	2.34
3b	2.657007474	2.184510764	2.807149994	1.708256947	2.80
4a	2.354019025	2.985719376	2.338051912	2.277671693	2.60
4b	2.981974657	2.306057217	2.992063798	2.070804477	2.87
6a	2.435584627	2.408635673	2.492513397	2.024482054	2.42
6b	2.761459083	2.735114306	2.589287434	1.945080287	2.60
7a	1.790071171	2.303529255	1.406881543	1.286688469	1.95
7b	1.871017620	1.474341989	2.205919631	1.776996414	2.08
8	4.641675466	4.802595023	4.493749011	3.954076885	4.90
11	5.738518574	5.688075962	5.809576441	5.151974698	5.97
12	6.899531722	6.716776755	7.029872627	6.157425266	6.72
13	4.085508982	3.858429505	4.080723027	3.626756632	4.17
14	4.936516926	4.686109929	4.549915847	4.171303763	4.77
15	1.143288857	1.101358610	1.131328667	0.822446716	1.29
16	1.269765795	1.271671428	1.333513562	1.006794775	1.43

**Table 8.8.** Average values of the correlation coefficients for **2a-2d**. The “all” refers to  $^{13}\text{C}$  and  $^1\text{H}$  results combined using the geometric mean..

Compound	correlation coefficient (all)
<b>2a</b>	0.975215
<b>2b</b>	0.981470
<b>2c</b>	0.975813
<b>2d</b>	0.967649

**Table 8.9.** Calculated and experimental  $^{13}\text{C}$  shifts (in ppm) for **3a-3h**

Pos	$^{13}\text{C}$ Corrected Calculated								$^{13}\text{C}$ Experimental
	<b>3a</b>	<b>3b</b>	<b>3c</b>	<b>3d</b>	<b>3e</b>	<b>3f</b>	<b>3g</b>	<b>3h</b>	
2	171.5197	174.6740	172.0947	173.4645	172.4039	173.7352	173.0528	175.9863	175.0
3	27.4380	32.7886	28.6026	28.3172	32.6808	28.2382	33.5399	32.6506	32.2
4	26.8323	30.3368	27.4003	26.1792	29.9742	25.4791	30.6500	28.6878	26.4
5	67.0823	70.8166	66.9625	70.9423	73.8761	71.7436	74.5763	71.0949	72.8
6	71.5408	71.2465	72.2338	73.4615	73.6996	72.2281	74.8854	72.8943	73.7
8	161.6200	163.2216	162.2793	164.5950	161.8752	164.6896	162.6564	164.7606	165.0
9	116.1348	116.7969	120.7827	118.3148	117.1511	116.7506	121.5257	119.4166	120.9
10	153.1101	153.3963	151.4339	155.8366	152.4968	156.2340	151.4299	156.6515	149.2
11	68.1747	70.3955	72.3100	70.4554	69.2621	71.0433	73.5297	71.2701	69.4
12	28.2042	31.1328	31.7023	31.0716	29.7094	34.6000	33.2739	31.4680	28.3
13	28.5209	25.8836	31.6019	28.7911	30.0210	31.6353	33.3894	28.3782	27.0
14	66.3458	70.9850	66.2665	68.8012	68.1128	68.4882	67.9026	70.5389	70.8
15	11.7923	14.7299	11.9394	13.5804	15.8978	14.0566	16.5573	13.2236	16.9
16	16.6794	16.9534	17.4828	17.3202	18.2117	17.8384	19.1795	17.3932	19.4

**Table 8.10.** Calculated and experimental  $^1\text{H}$  shifts (in ppm) for **3a-3h**

Pos	$^1\text{H}$ Corrected Calculated								$^1\text{H}$ Experimental
	<b>3a</b>	<b>3b</b>	<b>3c</b>	<b>3d</b>	<b>3e</b>	<b>3f</b>	<b>3g</b>	<b>3h</b>	
3a	2.24118	2.32356	2.21215	2.21711	2.43008	2.71651	2.37370	2.40351	2.59
3b	2.85131	2.27272	2.82266	2.74012	2.63130	2.14915	2.61124	2.39277	2.89
4a	1.58321	1.84278	1.54421	1.51062	1.69001	2.14112	1.67881	1.55331	1.97
4b	1.93602	1.56523	1.86087	2.19957	1.99269	1.47990	1.94527	2.10620	2.15
5	4.06621	3.42274	4.08286	3.89963	3.31483	3.84875	3.26179	3.51250	3.75
6	4.68910	4.58166	4.56222	4.60155	4.61615	4.82453	4.46592	4.56429	5.33
9	5.73692	5.78409	5.48174	5.63899	5.66159	5.87600	5.39268	5.60685	6.03
10	6.96738	7.20019	6.44755	6.93989	6.77516	7.08141	6.25303	6.93196	6.71
11	4.51661	4.13061	3.80385	4.40007	4.44166	4.16045	3.75160	4.38619	4.65
12a	1.79384	1.36831	1.59604	1.89223	1.78962	1.64688	1.61564	1.97798	1.61
12b	1.85621	1.64542	1.72885	1.74824	1.82915	1.70530	1.73114	1.56171	1.86
13a	1.37852	1.80335	1.51738	1.42086	1.38660	1.62702	1.54376	1.42343	1.79
13b	1.87734	1.45117	1.53458	1.92317	1.88175	1.58431	1.56331	2.01198	1.95
14	4.50477	4.57271	4.24962	4.62705	4.47158	4.52258	4.24105	4.75683	4.96
15	2.24118	2.32356	2.21215	2.21711	2.43008	2.71651	2.37370	2.40351	1.25
16	2.85131	2.27272	2.82266	2.74012	2.63130	2.14915	2.61124	2.39277	1.19

**Table 8.11.** Average values of the correlation coefficients for **3a-3h**. The “all” refers to  $^{13}\text{C}$  and  $^1\text{H}$  results combined using the geometric mean.

Compound	correlation coefficient (all)
<b>3a</b>	0.996292
<b>3b</b>	0.996195
<b>3c</b>	0.995170
<b>3d</b>	0.996190
<b>3e</b>	0.997639
<b>3f</b>	0.994274
<b>3g</b>	0.997665
<b>3h</b>	0.996217

**Table 8.12.** Calculated and experimental  $^{13}\text{C}$  shifts (in ppm) for **4a-4h**

Pos	$^{13}\text{C}$ Corrected Calculated								$^{13}\text{C}$ Experimental
	<b>4a</b>	<b>4b</b>	<b>4c</b>	<b>4d</b>	<b>4e</b>	<b>4f</b>	<b>4g</b>	<b>4h</b>	
2	172.2573	175.4740	172.8254	174.2174	173.1978	174.4660	173.8394	176.7563	172.6
3	28.1900	33.5176	29.3619	29.0701	33.3916	28.9982	34.2576	33.3917	28.7
4	27.5844	31.0646	28.1599	26.9320	30.6834	26.2397	31.3662	29.4281	27.0
5	67.8304	71.5647	67.7141	71.6952	74.6114	72.4949	75.3142	71.8438	69.4
6	72.2884	71.9947	72.9844	74.2143	74.4348	72.9794	75.6235	73.6436	73.3
8	162.3586	164.0159	163.0119	165.3478	162.6629	165.4222	163.4379	165.5283	164.7
9	116.8780	117.5679	121.5236	119.0676	117.9121	117.4929	122.2869	120.1752	119.8
10	153.8496	154.1857	152.1686	156.5895	153.2789	156.9683	152.2059	157.4176	150.7
11	68.9227	71.1433	73.0605	71.2083	69.9946	71.7948	74.2672	72.0189	69.4
12	28.9562	31.8610	32.4610	31.8244	30.4184	35.3587	33.9914	32.2089	28.8
13	29.2728	26.6092	32.3606	29.5440	30.7302	32.3947	34.1070	29.1184	28.0
14	67.0939	71.7331	67.0183	69.5540	68.8447	69.2402	68.6373	71.2877	69.6
15	12.5459	15.4499	12.7020	14.3333	16.5985	14.8195	17.2665	13.9608	14.5
16	17.4325	17.6745	18.2443	18.0730	18.9139	18.6006	19.8901	18.1312	20.0

**Table 8.13.** Calculated and experimental  $^1\text{H}$  shifts (in ppm) for **4a-4h**

Pos	$^1\text{H}$ Corrected Calculated								$^1\text{H}$ Experimental
	<b>4a</b>	<b>4b</b>	<b>4c</b>	<b>4d</b>	<b>4e</b>	<b>4f</b>	<b>4g</b>	<b>4h</b>	
3a	2.30034	2.37906	2.26870	2.27614	2.48238	2.76992	2.42321	2.45854	2.36
3b	2.90414	2.32852	2.87316	2.79356	2.68269	2.20662	2.65999	2.44789	2.72
4a	1.99834	1.62527	1.92091	2.25879	2.04696	1.54216	1.99614	2.16369	2.07
4b	1.64918	1.90116	1.60738	1.57721	1.74565	2.19865	1.73054	1.61537	1.81
5	4.10646	3.47167	4.12085	3.94065	3.36315	3.89406	3.30846	3.55836	4.05
6	4.72290	4.62364	4.59546	4.63507	4.65861	4.86287	4.50874	4.60146	5.04
9	5.75987	5.81887	5.50585	5.66140	5.69934	5.90681	5.43255	5.63540	5.97
10	6.97758	7.22649	6.46208	6.94839	6.80789	7.10360	6.29016	6.94955	6.82
11	4.55219	4.17530	3.84461	4.43574	4.48490	4.20354	3.79671	4.42483	4.62
12a	1.85763	1.42953	1.65870	1.95474	1.84480	1.70794	1.66757	2.03653	1.88
12b	1.91936	1.70499	1.79019	1.81228	1.88416	1.76595	1.78269	1.62370	1.88
13a	1.94027	1.51189	1.59785	1.98535	1.93652	1.64583	1.61540	2.07024	1.81
13b	1.44661	1.86196	1.58082	1.48841	1.44361	1.68822	1.59592	1.48656	1.54
14	4.54047	4.61475	4.28596	4.66030	4.51469	4.56307	4.28460	4.79240	4.84
15	2.30034	2.37906	2.26870	2.27614	2.48238	2.76992	2.42321	2.45854	1.31
16	2.90414	2.32852	2.87316	2.79356	2.68269	2.20662	2.65999	2.44789	1.15

**Table 8.14.** Average values of the correlation coefficients for **4a-4h**

Compound	correlation coefficient (all)
<b>4a</b>	0.998767
<b>4b</b>	0.996687
<b>4c</b>	0.997645
<b>4d</b>	0.998581
<b>4e</b>	0.997988
<b>4f</b>	0.996163
<b>4g</b>	0.997840
<b>4h</b>	0.997766

**Table 8.15.**  $^1\text{H}$  NMR spectrum comparison of literature acremodiol and compound **4** (acremodiol C)

Pos.	Literature <sup>90*</sup>	Acremodiol C <sup>#</sup>
3	2.72, 2.66 (2 dd, 1H, $J = 3.0, 11.3$ Hz) 2.34, 2.28 (2 dd, 1H, $J = 3.6, 6.7$ Hz)	2.71, 2.67 (2 dd, 1H, $J = 2.7, 11.0$ Hz) 2.33, 2.28 (2 dd, 1H, $J = 3.1, 7.2$ Hz)
4	1.78 (m, 1H) 1.64/1.43 (m, 1H)	1.79 (m, 1H) 1.65/1.43 (m, 1H)
5	3.80 (m, 1H)	3.81 (dt, 1H, $J = 3.4, 7.2$ Hz)
6	4.83 (dq, 1H, $J = 3.0, 6.7$ Hz)	4.83 (qd, 1H, $J = 2.8, 6.5$ Hz)
9	5.78 (dd, 1H, $J = 2.2, 15.8$ Hz)	5.74 (dd, 1H, $J = 2.3, 15.7$ Hz)
10	6.83 (dd, 1H, $J = 3.0, 15.8$ Hz)	6.83 (dd, 1H, $J = 2.5, 15.8$ )
11	4.47 (m, 1H)	4.46 (m, 1H)
12	1.72 (m, 2H)	1.71 (m, 2H)
13	1.64/1.43 (m, 2H)	1.65/1.43 (m, 2H)
14	4.65 (m, 1H)	4.65 (m, 1H)
15	1.17 (d, 3H, $J = 6.0$ Hz)	1.17 (d, 3H, $J = 6.6$ Hz)
16	1.07 (d, 3H, $J = 6.0$ Hz)	1.07 (d, 3H, $J = 6.4$ Hz)
* DMSO-d6 , 300 MHz		
# DMSO-d6 , 400 MHz		

**Table 8.16.** Calculated  $[\alpha]_D$  for **1a**, **1d**, **2b**, **2c**, **3a/4a**, **3e/4e**, and **3g/4g**

Compound	$[\alpha]_D$ (Calculated) MeOH	$[\alpha]_D$ (Experimental) MeOH
<b>1a</b>	RRR -85	+51
	SSS +85	
<b>1d</b>	RSS +166	+36
	SRR -166	
<b>2b</b>	RRS +28	+75
	SSR -28	
<b>2c</b>	RSR -69	+22
	SRS +69	
<b>3e</b>	SRRR -60	+25
	RSSS +60	
<b>3g</b>	SRSR -33	+25
	RSRS +33	
<b>4a</b>	RRRR -74	+22
Compound	$[\alpha]_D$ (Experimental) MeOH	$[\alpha]_D$ (Experimental) $\text{CHCl}_3$
<b>4a</b>	RRRR -71	+25

**Table 8.17.** DP4+ Analysis

	1								
DP4+ (H) DP4+ (C) DP4+ (All data)	<b>1a</b> (RRR)		<b>1b</b> (RRS)		<b>1c</b> (RSR)		<b>1d</b> (RSS)		
	95.41%		4.59%		0.00%		0.00%		
	31.83%		22.03%		44.66%		1.47%		
		96.78%		3.22%		0.00%		0.00%	
	2								
DP4+ (H) DP4+ (C) DP4+ (All data)	<b>2a</b> (RRR)		<b>2b</b> (RRS)		<b>2c</b> (RSR)		<b>2d</b> (RSS)		
	72.45%		0.02%		27.53%		0.00%		
	0.22%		0.38%		99.40%		0.00%		
		0.59%		0.00%		99.41%		0.00%	
	3								
DP4+ (H) DP4+ (C) DP4+ (All data)	<b>3a</b> (RRRR)	<b>3b</b> (RRRS)	<b>3c</b> (RRSR)	<b>3d</b> (RSRR)	<b>3e</b> (SRRR)	<b>3f</b> (SRRS)	<b>3g</b> (SRSR)	<b>3h</b> (SSRR)	
	14.26%	0.01%	0.01%	33.06%	33.23%	1.30%	0.01%	18.13%	
	0.00%	2.40%	0.00%	5.31%	62.37%	0.02%	0.15%	29.75%	
		0.00%	0%	0.00%	6.30%	74.35%	0.00%	0.00%	19.35%
	4								
DP4+ (H) DP4+ (C) DP4+ (All data)	<b>4a</b> (RRRR)	<b>4b</b> (RRRS)	<b>4c</b> (RRSR)	<b>4d</b> (RSRR)	<b>4e</b> (SRRR)	<b>4f</b> (SRRS)	<b>4g</b> (SRSR)	<b>4h</b> (SSRR)	
	88.36%	0.00%	0.00%	3.35%	7.74%	0.00%	0.00%	0.55%	
	56.06%	0.01%	1.17%	42.67%	0.06%	0.02%	0.00%	0.01%	
		97.19%	0.00%	0.00%	2.80%	0.01%	0.00%	0.00%	

## REFERENCES

- (1) Blackwell, M. *Am. J. Bot.* **2011**, *98*, 426-438.
- (2) Hawksworth, D. L.; Lücking, R. *Microbiol. Spectr.* **2017**, *5*, 79-95.
- (3) Bertrand, S.; Schumpp, O.; Bohni, N.; Bujard, A.; Azzollini, A.; Monod, M.; Gindro, K.; Wolfender, J.-L. *J. Chromatogr. A* **2013**, *1292*, 219-228.
- (4) Mueller, G. M., *Biodiversity of fungi: inventory and monitoring methods*. Elsevier 2011.
- (5) Bills, G. F.; Gloer, J. B. *Microbiol. Spectr.* **2016**, *4*, FUNK-009-2016.
- (6) Wisecaver, J. H.; Slot, J. C.; Rokas, A. *PLoS Genet.* **2014**, *10*, e1004816.
- (7) Zähner, H. *Folia Microbiol.* **1979**, *24*, 435-443.
- (8) Kinghorn, A. D.; De Blanco, E. J. C.; Lucas, D. M.; Rakotondraibe, H. L.; Orjala, J.; Soejarto, D. D.; Oberlies, N. H.; Pearce, C. J.; Wani, M. C.; Stockwell, B. R. *Anticancer Res.* **2016**, *36*, 5623-5637.
- (9) Helaly, S. E.; Thongbai, B.; Stadler, M. *Nat. Prod. Rep.* **2018**, *35*, 992-1014.
- (10) Keller, N. P. *Nat. Rev. Microbiol.* **2019**, *17*, 167-180.
- (11) Rokas, A.; Wisecaver, J. H.; Lind, A. L. *Nat. Rev. Microbiol.* **2018**, *17*, 731-744.
- (12) Rokas, A.; Mead, M. E.; Steenwyk, J. L.; Raja, H. A.; Oberlies, N. H. *Nat. Prod. Rep.* **2020**, *37*, 868-878.
- (13) Caesar, L. K.; Kelleher, N. L.; Keller, N. P. *Fungal Genet. Biol.* **2020**, 103477.

- (14) Mead, M. E.; Raja, H. A.; Steenwyk, J. L.; Knowles, S. L.; Oberlies, N. H.; Rokas, A. *Microbiol. Resour. Announc.* **2019**, *8*, e00890-19.
- (15) Knowles, S. L.; Raja, H. A.; Wright, A. J.; Lee, A. M. L.; Caesar, L. K.; Cech, N. B.; Mead, M. E.; Steenwyk, J. L.; Ries, L.; Goldman, G. H.; Rokas, A.; Oberlies, N. H. *Front. Microbiol.* **2019**, *10*, 285.
- (16) Mead, M. E.; Knowles, S. L.; Raja, H. A.; Beattie, S. R.; Kowalski, C. H.; Steenwyk, J. L.; Silva, L. P.; Chiaratto, J.; Ries, L. N.; Goldman, G. H.; Oberlies, N. H.; Rokas, A. *mSphere* **2019**, *4*, e00018-19.
- (17) Xu, X.-Y.; Shen, X.-T.; Yuan, X.-J.; Zhou, Y.-M.; Fan, H.; Zhu, L.-P.; Du, F.-Y.; Sadilek, M.; Yang, J.; Qiao, B. *Front. Microbiol.* **2018**, *8*, 2647.
- (18) Keller, N. P.; Turner, G.; Bennett, J. W. *Nat. Rev. Microbiol.* **2005**, *3*, 937-947.
- (19) Mundt, K.; Wollinsky, B.; Ruan, H. L.; Zhu, T.; Li, S. M. *ChemBioChem* **2012**, *13*, 2583-2592.
- (20) Bignell, E.; Cairns, T. C.; Throckmorton, K.; Nierman, W. C.; Keller, N. P. *Philos. Trans. R. Soc. Lond. B Biol. Sci.* **2016**, *371*, 20160023.
- (21) Vining, L. C. *Annu. Rev. Microbiol.* **1990**, *44*, 395-427.
- (22) Steenwyk, J. L.; Mead, M. E.; Knowles, S. L.; Raja, H. A.; Roberts, C. D.; Bader, O.; Houbraken, J.; Goldman, G. H.; Oberlies, N. H.; Rokas, A. *Genetics* **2020**, *216*, 481-497.
- (23) Latge, J.-P.; Chamilos, G. *Clin. Microbiol. Rev.* **2019**, *33*, e00140-18.
- (24) Ben-Ami, R.; Lewis, R. E.; Kontoyiannis, D. P. *Brit. J. Haemat.* **2010**, *150*, 406-417.
- (25) Denning, D. W.; Cadranel, J.; Beigelman-Aubry, C.; Ader, F.; Chakrabarti, A.; Blot, S.; Ullmann, A. J.; Dimopoulos, G.; Lange, C. *Eur. Respir. J.* **2016**, *47*, 45-68.
- (26) Casadevall, A. *Fungal Biol. Rev.* **2007**, *21*, 130-132.

- (27) Raffa, N.; Keller, N. P. *PLoS Pathog.* **2019**, *15*, e1007606.
- (28) Shwab, E. K.; Bok, J. W.; Tribus, M.; Galehr, J.; Graessle, S.; Keller, N. P. *Eukaryot. Cell* **2007**, *6*, 1656-1664.
- (29) Losada, L.; Ajayi, O.; Frisvad, J. C.; Yu, J.; Nierman, W. C. *Med. Mycol.* **2009**, *47*, S88-S96.
- (30) Yin, W.-B.; Baccile, J. A.; Bok, J. W.; Chen, Y.; Keller, N. P.; Schroeder, F. C. *J. Am. Chem. Soc.* **2013**, *135*, 2064-2067.
- (31) Wiemann, P.; Lechner, B. E.; Baccile, J. A.; Velk, T. A.; Yin, W.-B.; Bok, J. W.; Pakala, S.; Losada, L.; Nierman, W. C.; Schroeder, F. C. *Front. Microbiol.* **2014**, *5*, 530.
- (32) Knox, B. P.; Blachowicz, A.; Palmer, J. M.; Romsdahl, J.; Huttenlocher, A.; Wang, C. C.; Keller, N. P.; Venkateswaran, K. *mSphere* **2016**, *1*, e00227-16.
- (33) Blachowicz, A.; Raffa, N.; Bok, J. W.; Choera, T.; Knox, B.; Lim, F. Y.; Huttenlocher, A.; Wang, C. C.; Venkateswaran, K.; Keller, N. P. *mBio* **2020**, *11*, e03415-19.
- (34) Sugui, J. A.; Pardo, J.; Chang, Y. C.; Zaremba, K. A.; Nardone, G.; Galvez, E. M.; Müllbacher, A.; Gallin, J. I.; Simon, M. M.; Kwon-Chung, K. J. *Eukaryot. Cell* **2007**, *6*, 1562-1569.
- (35) Spikes, S.; Xu, R.; Nguyen, C. K.; Chamilos, G.; Kontoyiannis, D. P.; Jacobson, R. H.; Ejzykowicz, D. E.; Chiang, L. Y.; Filler, S. G.; May, G. S. *J. Infect. Dis.* **2008**, *197*, 479-486.
- (36) González-Lobato, L.; Real, R.; Prieto, J. G.; Álvarez, A. I.; Merino, G. *Eur. J. Pharmacol.* **2010**, *644*, 41-48.
- (37) Guruceaga, X.; Ezpeleta, G.; Mayayo, E.; Sueiro-Olivares, M.; Abad-Díaz-De-Cerio, A.; Aguirre Urízar, J. M.; Liu, H. G.; Wiemann, P.; Bok, J. W.; Filler, S. G. *Virulence* **2018**, *9*, 1548-1561.
- (38) Guruceaga, X.; Pérez-Cuesta, U.; Abad-Díaz de Cerio, A.; González, O.; Alonso, R. M.; Hernando, F. L.; Ramírez-García, A.; Rementeria, A. *Toxins* **2020**, *12*, 7.

- (39) Fallon, J. P.; Reeves, E. P.; Kavanagh, K. *J. Med. Microbiol.* **2010**, *59*, 625-633.
- (40) Fallon, J. P.; Reeves, E. P.; Kavanagh, K. *Microbiology* **2011**, *157*, 1481-1488.
- (41) Ishikawa, M.; Ninomiya, T.; Akabane, H.; Kushida, N.; Tsujiuchi, G.; Ohyama, M.; Gomi, S.; Shito, K.; Murata, T. *Bioorg. Med. Chem. Lett.* **2009**, *19*, 1457-1460.
- (42) Houbraken, J.; Weig, M.; Groß, U.; Meijer, M.; Bader, O. *FEMS Microbiol. Lett.* **2016**, *363*, fnv236.
- (43) Scherlach, K.; Hertweck, C. *Org. Biomol. Chem.* **2009**, *7*, 1753-1760.
- (44) Stajich, J., 1000 Fungal Genomes Project. In *1kfg Updates – Another 100 Genomes*, April 26, 2017 ed.2017.
- (45) Robey, M. T.; Caesar, L. K.; Drott, M. T.; Keller, N. P.; Kelleher, N. L. *bioRxiv* **2020**.
- (46) Galagan, J. E.; Calvo, S. E.; Cuomo, C.; Ma, L.-J.; Wortman, J. R.; Batzoglou, S.; Lee, S.-I.; Baştürkmen, M.; Spevak, C. C.; Clutterbuck, J. *Nature* **2005**, *438*, 1105-1115.
- (47) Gross, H. *Appl. Microbiol. Biotechnol.* **2007**, *75*, 267-277.
- (48) Challis, G. L. *J. Med. Chem.* **2008**, *51*, 2618-2628.
- (49) Grigoriev, I. V.; Nikitin, R.; Haridas, S.; Kuo, A.; Ohm, R.; Otillar, R.; Riley, R.; Salamov, A.; Zhao, X.; Korzeniewski, F. *Nucleic Acids Res.* **2013**, *42*, D699-D704.
- (50) Brakhage, A. A. *Nat. Rev. Microbiol.* **2013**, *11*, 21-32.
- (51) Knowles, S. L.; Raja, H. A.; Isawi, I. H.; Flores-Bocanegra, L.; Reggio, P. H.; Pearce, C. J.; Burdette, J. E.; Rokas, A.; Oberlies, N. H. *Org. Lett.* **2020**, *22*, 1878-1882.
- (52) Arora, D.; Gupta, P.; Jaglan, S.; Roullier, C.; Grovel, O.; Bertrand, S. *Biotechnol. Adv.* **2020**, 107521.

- (53) Shen, X.-T.; Mo, X.-H.; Zhu, L.-P.; Tan, L.-L.; Du, F.-Y.; Wang, Q.-W.; Zhou, Y.-M.; Yuan, X.-J.; Qiao, B.; Yang, S. *Appl. Environ. Microbiol.* **2019**, *85*, e00293-19.
- (54) Li, H.-T.; Zhou, H.; Duan, R.-T.; Li, H.-Y.; Tang, L.-H.; Yang, X.-Q.; Yang, Y.-B.; Ding, Z.-T. *J. Nat. Prod.* **2019**, *82*, 1009-1013.
- (55) Zhou, Q.-Y.; Yang, X.-Q.; Zhang, Z.-X.; Wang, B.-Y.; Hu, M.; Yang, Y.-B.; Zhou, H.; Ding, Z.-T. *Fitoterapia* **2018**, *130*, 26-30.
- (56) Wang, W.; Gong, J.; Liu, X.; Dai, C.; Wang, Y.; Li, X.-N.; Wang, J.; Luo, Z.; Zhou, Y.; Xue, Y.; Zhu, H.; Chen, C.; Zhang, Y. *J. Nat. Prod.* **2018**, *81*, 1578-1587.
- (57) Kuhar, F.; Castiglia, V.; Levin, L. *Int. Biodeterior. Biodegradation* **2015**, *104*, 238-243.
- (58) Fox, E. M.; Howlett, B. J. *Curr. Opin. Microbiol.* **2008**, *11*, 481-487.
- (59) Chatterjee, S.; Kuang, Y.; Splivallo, R.; Chatterjee, P.; Karlovsky, P. *BMC Microbiol.* **2016**, *16*, 83.
- (60) Huang, S.; Ding, W.; Li, C.; Cox, D. G. *Pharmacogn. Mag.* **2014**, *10*, 410-414.
- (61) Kettering, M.; Sterner, O.; Anke, T. *Z. Naturforsch., C, J. Biosci.* **2004**, *59*, 816-823.
- (62) Bertrand, S.; Bohni, N.; Schnee, S.; Schumpp, O.; Gindro, K.; Wolfender, J.-L. *Biotechnol. Adv.* **2014**, *32*, 1180-1204.
- (63) Martin, G. E.; Hilton, B. D.; Blinov, K. A. *J. Nat. Prod.* **2011**, *74*, 2400-2407.
- (64) Elyashberg, M. *Trends Analyt. Chem.* **2015**, *69*, 88-97.
- (65) Sauri, J.; Frédéric, M.; Tchinda, A. T.; Parella, T.; Williamson, R. T.; Martin, G. E. *J. Nat. Prod.* **2015**, *78*, 2236-2241.
- (66) Sauri, J.; Liu, Y.; Parella, T.; Williamson, R. T.; Martin, G. E. *J. Nat. Prod.* **2016**, *79*, 1400-1406.

- (67) Buevich, A. V.; Williamson, R. T.; Martin, G. E. *J. Nat. Prod.* **2014**, *77*, 1942-1947.
- (68) McAlpine, J. B.; Chen, S.-N.; Kutateladze, A.; MacMillan, J. B.; Appendino, G.; Barison, A.; Beniddir, M. A.; Biavatti, M. W.; Blumli, S.; Boufridi, A.; Butler, M. S.; Capon, R. J.; Choi, Y. H.; Coppage, D.; Crews, P.; Crimmins, M. T.; Csete, M.; Dewapriya, P.; Egan, J. M.; Garson, M. J.; Genta-Jouve, G.; Gerwick, W. H.; Gross, H.; Harper, M. K.; Hermanto, P.; Hook, J. M.; Hunter, L.; Jeannerat, D.; Ji, N.-Y.; Johnson, T. A.; Kingston, D. G. I.; Koshino, H.; Lee, H.-W.; Lewin, G.; Li, J.; Linington, R. G.; Liu, M.; McPhail, K. L.; Molinski, T. F.; Moore, B. S.; Nam, J.-W.; Neupane, R. P.; Niemitz, M.; Nuzillard, J.-M.; Oberlies, N. H.; Ocampos, F. M. M.; Pan, G.; Quinn, R. J.; Reddy, D. S.; Renault, J.-H.; Rivera-Chávez, J.; Robien, W.; Saunders, C. M.; Schmidt, T. J.; Seger, C.; Shen, B.; Steinbeck, C.; Stuppner, H.; Sturm, S.; Taglialatela-Scafati, O.; Tantillo, D. J.; Verpoorte, R.; Wang, B.-G.; Williams, C. M.; Williams, P. G.; Wist, J.; Yue, J.-M.; Zhang, C.; Xu, Z.; Simmler, C.; Larkin, D. C.; Bissona, J.; Pauli, G. F. *Nat. Prod. Rep.* **2018**, *36*, 35-107.
- (69) Suyama, T. L.; Gerwick, W. H.; McPhail, K. L. *Bioorg. Med. Chem.* **2011**, *19*, 6675-6701.
- (70) Robien, W., A Critical Evaluation of the Quality of Published <sup>13</sup>C NMR Data in Natural Product Chemistry. In *Progress in the Chemistry of Organic Natural Products 105*, Springer 2017; pp 137-215.
- (71) Brown, P. D.; Lawrence, A. L. *Nat. Prod. Rep.* **2017**, *34*, 1193-1202.
- (72) Kubo, I.; Tanis, S.; Lee, Y.; Miura, I.; Nakanishi, K.; Chapy, A. *Heterocycles* **1976**, *5*, 485-498.
- (73) Senior, M. M.; Williamson, R. T.; Martin, G. E. *J. Nat. Prod.* **2013**, *76*, 2088-2093.
- (74) Rajab, M. S.; Rugutt, J. K.; Fronczek, F. R.; Fischer, N. H. *J. Nat. Prod.* **1997**, *60*, 822-825.
- (75) Choudhary, M. I.; Hayat, S.; Khan, A. M.; Ahmed, A. *Chem. Pharm. Bull.* **2001**, *49*, 105-107.
- (76) Lin, W.; Brauers, G.; Ebel, R.; Wray, V.; Berg, A.; Sudarsono; Proksch, P. *J. Nat. Prod.* **2003**, *66*, 57-61.

- (77) Shen, Y.-C.; Lo, K.-L.; Lin, Y.-C.; Khalil, A. T.; Kuo, Y.-H.; Shih, P.-S. *Tetrahedron Lett.* **2006**, 47, 4007-4010.
- (78) Jain, S.; Laphookhieo, S.; Shi, Z.; Fu, L.-w.; Akiyama, S.-i.; Chen, Z.-S.; Youssef, D. T.; van Soest, R. W.; El Sayed, K. A. *J. Nat. Prod.* **2007**, 70, 928-931.
- (79) Thomas, M. C.; Mitchell, T. W.; Harman, D. G.; Deeley, J. M.; Nealon, J. R.; Blanksby, S. J. *Anal. Chem.* **2008**, 80, 303-311.
- (80) Barrientos, R. C.; Vu, N.; Zhang, Q. *J. Am. Soc. Mass Spectrom.* **2017**, 28, 2330-2343.
- (81) Vu, N.; Brown, J.; Giles, K.; Zhang, Q. *Rapid Commun. Mass Spectrom.* **2017**, 31, 1415-1423.
- (82) Mitchell, T. W.; Pham, H.; Thomas, M. C.; Blanksby, S. J. *J. Chromatogr. B* **2009**, 877, 2722-2735.
- (83) Poad, B. L.; Green, M. R.; Kirk, J. M.; Tomczyk, N.; Mitchell, T. W.; Blanksby, S. J. *Anal. Chem.* **2017**, 89, 4223-4229.
- (84) Poad, B. L.; Zheng, X.; Mitchell, T. W.; Smith, R. D.; Baker, E. S.; Blanksby, S. J. *Anal. Chem.* **2017**, 90, 1292-1300.
- (85) Cui, Z.; Thomas, M. J. *J. Chromatogr. B* **2009**, 877, 2709-2715.
- (86) Criegee, R. *Angew. Chem. Int. Ed. Engl.* **1975**, 14, 745-752.
- (87) Renslo, A., *The Organic Chemistry of Medicinal Agents*. McGraw Hill Professional 2015.
- (88) Han, J.; Su, Y.; Jiang, T.; Xu, Y.; Huo, X.; She, X.; Pan, X. *J. Org. Chem.* **2009**, 74, 3930-3932.
- (89) Rajaram, S.; Ramulu, U.; Ramesh, D.; Prabhakar, P.; Venkateswarlu, Y. *Helv. Chim. Acta* **2013**, 96, 2115-2123.

- (90) Sharma, G. V.; Mallesham, S.; Mouli, C. C. *Tetrahedron: Asymmetry* **2009**, *20*, 2513-2529.
- (91) Deschamps, J. R. *Life Sci.* **2010**, *86*, 585-589.
- (92) Deyrup, S. T.; Swenson, D. C.; Gloer, J. B.; Wicklow, D. T. *J. Nat. Prod.* **2006**, *69*, 608-611.
- (93) Sy-Cordero, A. A.; Day, C. S.; Oberlies, N. H. *J. Nat. Prod.* **2012**, *75*, 1879-1881.
- (94) Smyth, M.; Martin, J. *Mol. Pathol.* **2000**, *53*, 8-14.
- (95) Hoye, T. R.; Jeffrey, C. S.; Shao, F. *Nat. Protoc.* **2007**, *2*, 2451.
- (96) El-Elimat, T.; Raja, H. A.; Day, C. S.; Chen, W.-L.; Swanson, S. M.; Oberlies, N. H. *J. Nat. Prod.* **2014**, *77*, 2088-2098.
- (97) Bhushan, R.; Brückner, H. *J. Chromatogr. B* **2011**, *879*, 3148-3161.
- (98) Ayon, N. J.; Sharma, A. D.; Gutheil, W. G. *J. Am. Soc. Mass Spectrom.* **2018**, *30*, 448-458.
- (99) Li, X.-C.; Ferreira, D.; Ding, Y. *Curr. Org. Chem.* **2010**, *14*, 1678-1697.
- (100) Berova, N.; Di Bari, L.; Pescitelli, G. *Chem. Soc. Rev.* **2007**, *36*, 914-931.
- (101) Barone, G.; Duca, D.; Silvestri, A.; Gomez-Paloma, L.; Riccio, R.; Bifulco, G. *Chem. Eur. J.* **2002**, *8*, 3240-3245.
- (102) Barone, G.; Gomez-Paloma, L.; Duca, D.; Silvestri, A.; Riccio, R.; Bifulco, G. *Chem. Eur. J.* **2002**, *8*, 3233-3239.
- (103) Seco, J. M.; Quinoá, E.; Riguera, R. *Chem. Rev.* **2004**, *104*, 17-118.
- (104) Smith, S. G.; Goodman, J. M. *J. Org. Chem.* **2009**, *74*, 4597-4607.

- (105) Smith, S. G.; Goodman, J. M. *J. Am. Chem. Soc.* **2010**, *132*, 12946-12959.
- (106) Willoughby, P. H.; Jansma, M. J.; Hoye, T. R. *Nat. Protoc.* **2014**, *9*, 643-660.
- (107) Willoughby, P. H.; Jansma, M. J.; Hoye, T. R. *Nat. Protoc.* **2020**, *15*, 2277.
- (108) Bifulco, G.; Dambruoso, P.; Gomez-Paloma, L.; Riccio, R. *Chem. Rev.* **2007**, *107*, 3744-3779.
- (109) Hehre, W.; Klunzinger, P.; Deppmeier, B.; Driessen, A.; Uchida, N.; Hashimoto, M.; Fukushi, E.; Takata, Y. *J. Nat. Prod.* **2019**, *82*, 2299-2306.
- (110) Wang, B.; Dossey, A. T.; Walse, S. S.; Edison, A. S.; Merz Jr, K. M. *J. Nat. Prod.* **2009**, *72*, 709-713.
- (111) Stephens, P.; McCann, D.; Devlin, F.; Smith, A. *J. Nat. Prod.* **2006**, *69*, 1055-1064.
- (112) Lamoth, F. *Front. Microbiol.* **2016**, *7*, 683.
- (113) Tekaia, F.; Latgé, J.-P. *Curr. Opin. Microbiol.* **2005**, *8*, 385-392.
- (114) Bhabhra, R.; Miley, M. D.; Mylonakis, E.; Boettner, D.; Fortwendel, J.; Panepinto, J. C.; Postow, M.; Rhodes, J. C.; Askew, D. S. *Infect. Immun.* **2004**, *72*, 4731-4740.
- (115) Wagener, J.; Echtenacher, B.; Rohde, M.; Kotz, A.; Krappmann, S.; Heesemann, J.; Ebel, F. *Eukaryot. Cell* **2008**, *7*, 1661-1673.
- (116) Grahl, N.; Puttikamonkul, S.; Macdonald, J. M.; Gamcsik, M. P.; Ngo, L. Y.; Hohl, T. M.; Cramer, R. A. *PLoS Pathog.* **2011**, *7*, e1002145.
- (117) Willger, S. D.; Puttikamonkul, S.; Kim, K.-H.; Burritt, J. B.; Grahl, N.; Metzler, L. J.; Barbuch, R.; Bard, M.; Lawrence, C. B.; Cramer Jr, R. A. *PLoS Pathog.* **2008**, *4*, e1000200.
- (118) Sugui, J. A.; Pardo, J.; Chang, Y. C.; Müllbacher, A.; Zaremba, K. A.; Galvez, E. M.; Brinster, L.; Zerfas, P.; Gallin, J. I.; Simon, M. M. *Eukaryot. Cell* **2007**, *6*, 1552-1561.

- (119) Bok, J. W.; Balajee, S. A.; Marr, K. A.; Andes, D.; Nielsen, K. F.; Frisvad, J. C.; Keller, N. P. *Eukaryot. Cell* **2005**, *4*, 1574-1582.
- (120) Balajee, S. A.; Kano, R.; Baddley, J. W.; Moser, S. A.; Marr, K. A.; Alexander, B. D.; Andes, D.; Kontoyiannis, D. P.; Perrone, G.; Peterson, S. *J. Clin. Microbiol.* **2009**, *47*, 3138-3141.
- (121) Alastruey-Izquierdo, A.; Mellado, E.; Peláez, T.; Pemán, J.; Zapico, S.; Alvarez, M.; Rodríguez-Tudela, J.; Cuénca-Estrella, M.; Group, F. S. *Antimicrob. Agents Chemother.* **2013**, *57*, 3380-3387.
- (122) Van der Linden, J.; Arendrup, M.; Warris, A.; Lagrou, K.; Pelloux, H.; Hauser, P.; Chryssanthou, E.; Mellado, E.; Kidd, S.; Tortorano, A. *Emerg. Infect. Dis.* **2015**, *21*, 1041-4.
- (123) Fedorova, N. D.; Khaldi, N.; Joardar, V. S.; Maiti, R.; Amedeo, P.; Anderson, M. J.; Crabtree, J.; Silva, J. C.; Badger, J. H.; Albarraq, A. *PLoS Genet.* **2008**, *4*, e1000046.
- (124) Steenwyk, J. L.; Shen, X.-X.; Lind, A. L.; Goldman, G. G.; Rokas, A. *mBio* **2019**, *10*, e00925-19.
- (125) Hong, S.-B.; Kim, D.-H.; Park, I.-C.; Samson, R. A.; Shin, H.-D. *Mycobiology* **2010**, *38*, 1-6.
- (126) Frąc, M.; Jezierska-Tys, S.; Yaguchi, T., Occurrence, detection, and molecular and metabolic characterization of heat-resistant fungi in soils and plants and their risk to human health. In *Advances in Agronomy*, Elsevier2015; Vol. 132, pp 161-204.
- (127) Tong, X.; Xu, H.; Zou, L.; Cai, M.; Xu, X.; Zhao, Z.; Xiao, F.; Li, Y. *Sci. Rep.* **2017**, *7*, 1-8.
- (128) Summerbell, R. C.; De Repentigny, L.; Chartrand, C.; St Germain, G. *J. Clin. Microbiol.* **1992**, *30*, 1580-1582.
- (129) Lonial, S.; Williams, L.; Carrum, G.; Ostrowski, M.; McCarthy Jr, P. *Bone marrow transplantation* **1997**, *19*, 753-755.

- (130) Gerber, J.; Chomicki, J.; Brandsberg, J. W.; Jones, R.; Hammerman, K. J. *Am. J. Clin. Pathol.* **1973**, 60, 861-866.
- (131) Coriglione, G.; Stella, G.; Gafa, L.; Spata, G.; Oliveri, S.; Padhye, A.; Ajello, L. *Eur. J. Epidemiol.* **1990**, 6, 382-385.
- (132) Escribano, P.; Peláez, T.; Muñoz, P.; Bouza, E.; Guinea, J. *Antimicrob. Agents Chemother.* **2013**, 57, 2815-2820.
- (133) Negri, C.; Gonçalves, S.; Xafranski, H.; Bergamasco, M.; Aquino, V.; Castro, P.; Colombo, A. J. *Clin. Microbiol.* **2014**, 52, 3633-3640.
- (134) Sabino, R.; Veríssimo, C.; Parada, H.; Brandão, J.; Viegas, C.; Carolino, E.; Clemons, K. V.; Stevens, D. A. *Med. Mycol.* **2014**, 52, 519-529.
- (135) Abers, M. S.; Ghebremichael, M. S.; Timmons, A. K.; Warren, H. S.; Poznansky, M. C.; Vyas, J. M. In *A critical reappraisal of prolonged neutropenia as a risk factor for invasive pulmonary aspergillosis*, Open forum infectious diseases2016 Oxford University Press.
- (136) Beattie, S. R.; Mark, K. M.; Thammahong, A.; Ries, L. N. A.; Dhingra, S.; Caffrey-Carr, A. K.; Cheng, C.; Black, C. C.; Bowyer, P.; Bromley, M. J. *PLoS Pathog.* **2017**, 13, e1006340.
- (137) Kowalski, C. H.; Beattie, S. R.; Fuller, K. K.; McGurk, E. A.; Tang, Y.-W.; Hohl, T. M.; Obar, J. J.; Cramer, R. A. *mBio* **2016**, 7, e01515-16.
- (138) Childers, D. S.; Raziunaite, I.; Mol Avelar, G.; Mackie, J.; Budge, S.; Stead, D.; Gow, N. A.; Lenardon, M. D.; Ballou, E. R.; MacCallum, D. M. *PLoS Pathog.* **2016**, 12, e1005566.
- (139) Sandai, D.; Zhikang, Y.; Selway, L.; Stead, D.; Walker, J.; Leach, M. D.; Bohovych, I.; Ene, I. V.; Kastora, S.; Budge, S. *mBio* **2012**, 3, e00495-12.
- (140) Brown, N. A.; Goldman, G. H. *J. Microbiol.* **2016**, 54, 243-253.
- (141) Salichos, L.; Rokas, A. *PLoS ONE* **2011**, 6, e18755.

- (142) Abad, A.; Fernández-Molina, J. V.; Bikandi, J.; Ramírez, A.; Margareto, J.; Sendino, J.; Hernando, F. L.; Pontón, J.; Garaizar, J.; Rementeria, A. *Rev. Iberoam. Micol.* **2010**, 27, 155-182.
- (143) Kjærboelling, I.; Vesth, T. C.; Frisvad, J. C.; Nybo, J. L.; Theobald, S.; Kuo, A.; Bowyer, P.; Matsuda, Y.; Mondo, S.; Lyhne, E. K. *Proc. Natl. Acad. Sci. USA* **2018**, 115, E753-E761.
- (144) O'Hanlon, K. A.; Gallagher, L.; Schrettli, M.; Jöchl, C.; Kavanagh, K.; Larsen, T. O.; Doyle, S. *Appl. Environ. Microbiol.* **2012**, 78, 3166-3176.
- (145) Khaldi, N.; Seifuddin, F. T.; Turner, G.; Haft, D.; Nierman, W. C.; Wolfe, K. H.; Fedorova, N. D. *Fungal Genet. Biol.* **2010**, 47, 736-741.
- (146) Blin, K.; Wolf, T.; Chevrette, M. G.; Lu, X.; Schwalen, C. J.; Kautsar, S. A.; Suarez Duran, H. G.; de Los Santos, E. L.; Kim, H. U.; Nave, M. *Nucleic Acids Res.* **2017**, 45, W36-W41.
- (147) Lind, A. L.; Wisecaver, J. H.; Smith, T. D.; Feng, X.; Calvo, A. M.; Rokas, A. *PLoS Genet.* **2015**, 11, e1005096.
- (148) Lind, A. L.; Wisecaver, J. H.; Lameiras, C.; Wiemann, P.; Palmer, J. M.; Keller, N. P.; Rodrigues, F.; Goldman, G. H.; Rokas, A. *PLoS Biol.* **2017**, 15, e2003583.
- (149) Krzywinski, M.; Schein, J.; Birol, I.; Connors, J.; Gascoyne, R.; Horsman, D.; Jones, S. J.; Marra, M. A. *Genome Res.* **2009**, 19, 1639-1645.
- (150) Gardiner, D. M.; Howlett, B. J. *FEMS Microbiol. Lett.* **2005**, 248, 241-248.
- (151) Frisvad, J. C.; Larsen, T. O. *Front. Microbiol.* **2016**, 6, 1485.
- (152) Wiemann, P.; Guo, C.-J.; Palmer, J. M.; Sekonyela, R.; Wang, C. C.; Keller, N. P. *Proc. Natl. Acad. Sci. USA* **2013**, 110, 17065-17070.
- (153) El-Elimat, T.; Raja, H. A.; Figueroa, M.; Falkingham, J. O.; Oberlies, N. H. *Phytochemistry* **2014**, 104, 114-120.

- (154) El-Elimat, T.; Raja, H. A.; Day, C. S.; McFeeters, H.; McFeeters, R. L.; Oberlies, N. H. *Bioorg. Med. Chem.* **2017**, *25*, 795-804.
- (155) Raja, H. A.; Paguigan, N. D.; Fournier, J.; Oberlies, N. H. *Mycol. Prog.* **2017**, *16*, 535-552.
- (156) Rivera-Chávez, J.; Raja, H. A.; Graf, T. N.; Gallagher, J. M.; Metri, P.; Xue, D.; Pearce, C. J.; Oberlies, N. H. *RSC Adv.* **2017**, *7*, 45733-45741.
- (157) Sanchez, J. F.; Somoza, A. D.; Keller, N. P.; Wang, C. C. *Nat. Prod. Rep.* **2012**, *29*, 351-371.
- (158) Bode, H. B.; Bethe, B.; Höfs, R.; Zeeck, A. *ChemBioChem* **2002**, *3*, 619-627.
- (159) VanderMolen, K. M.; Raja, H. A.; El-Elimat, T.; Oberlies, N. H. *Amb Express* **2013**, *3*, 71.
- (160) Hemphill, C. F. P.; Sureechatchaiyan, P.; Kassack, M. U.; Orfali, R. S.; Lin, W.; Daletos, G.; Proksch, P. *J. Antibiot.* **2017**, *70*, 726-732.
- (161) Frisvad, J. C.; Andersen, B.; Thrane, U. *Mycol. Res.* **2008**, *112*, 231-240.
- (162) Eamvijarn, A.; Gomes, N. M.; Dethoup, T.; Buaruang, J.; Manoch, L.; Silva, A.; Pedro, M.; Marini, I.; Roussis, V.; Kijjoa, A. *Tetrahedron* **2013**, *69*, 8583-8591.
- (163) Kimura, Y.; Hamasaki, T.; Nakajima, H.; Isogai, A. *Tetrahedron Lett.* **1982**, *23*, 225-228.
- (164) Ruchti, J.; Carreira, E. M. *J. Am. Chem. Soc.* **2014**, *136*, 16756-16759.
- (165) Ellestad, G. A.; Mirando, P.; Kunstmann, M. P. *J. Org. Chem.* **1973**, *38*, 4204 - 4205.
- (166) Yamazaki, M.; Fujimoto, H.; Kawasaki, T. *Chem. Pharm. Bull.* **1980**, *28*, 245-254.

- (167) Feng, Y.; Holte, D.; Zoller, J.; Umemiya, S.; Simke, L. R.; Baran, P. S. *J. Am. Chem. Soc.* **2015**, 137, 10160-10163.
- (168) Pohland, A.; Schuller, P.; Steyn, P.; Van Egmond, H. *Pure Appl. Chem.* **1982**, 54, 2219-2284.
- (169) Afiyatullov, S. S.; Kalinovskii, A.; Pivkin, M.; Dmitrenok, P.; Kuznetsova, T. *Chem. Nat. Compd.* **2005**, 41, 236-238.
- (170) Fayos, J.; Lokensgaard, D.; Clardy, J.; Cole, R. J.; Kirksey, J. W. *J. Am. Chem. Soc.* **1974**, 96, 6785-6787.
- (171) Fill, T. P.; Asenha, H. B. R.; Marques, A. S.; Ferreira, A. G.; Rodrigues-Fo, E. *Nat. Prod. Res.* **2013**, 27, 967-974.
- (172) Wyatt, T.; Van Leeuwen, M.; Wösten, H.; Dijksterhuis, J. *Fungal Genet. Biol.* **2014**, 64, 11-24.
- (173) Latgé, J.-P. *Clin. Microbiol. Rev.* **1999**, 12, 310-350.
- (174) Dagenais, T. R.; Keller, N. P. *Clin. Microbiol. Rev.* **2009**, 22, 447-465.
- (175) Hissen, A. H.; Wan, A. N.; Warwas, M. L.; Pinto, L. J.; Moore, M. M. *Infect. Immun.* **2005**, 73, 5493-5503.
- (176) Moreno, M. Á.; Ibrahim-Granet, O.; Vicentefranqueira, R.; Amich, J.; Ave, P.; Leal, F.; Latgé, J. P.; Calera, J. A. *Mol. Microbiol.* **2007**, 64, 1182-1197.
- (177) Cramer, R. A.; Rivera, A.; Hohl, T. M. *Curr. Opin. Infect. Dis.* **2011**, 24, 315-22.
- (178) Abdolrasouli, A.; Rhodes, J.; Beale, M. A.; Hagen, F.; Rogers, T. R.; Chowdhary, A.; Meis, J. F.; Armstrong-James, D.; Fisher, M. C. *mBio* **2015**, 6, e00536.
- (179) Mellado, E.; Alcazar-Fuoli, L.; Cuenca-Estrella, M.; Rodriguez-Tudela, J. L. *Antimicrob. Agents Chemother.* **2011**, 55, 5459-5468.

- (180) Sugui, J.; Vinh, D.; Nardone, G.; Shea, Y.; Chang, Y.; Zelazny, A.; Marr, K.; Holland, S.; Kwon-Chung, K. *J. Clin. Microbiol.* **2010**, *48*, 220-228.
- (181) Hubka, V.; Barrs, V.; Dudová, Z.; Sklenář, F.; Kubátová, A.; Matsuzawa, T.; Yaguchi, T.; Horie, Y.; Nováková, A.; Frisvad, J. *Persoonia: Molecular Phylogeny and Evolution of Fungi* **2018**, *41*, 142-174.
- (182) *Nat. Microbiol.* **2017**, *2*, 17120.
- (183) Fuchs, B. B.; O'Brien, E.; El Khoury, J. B.; Mylonakis, E. *Virulence* **2010**, *1*, 475-482.
- (184) Madden, T., The BLAST sequence analysis tool. In *The NCBI Handbook [Internet]*. 2nd edition, National Center for Biotechnology Information (US)2013.
- (185) Micallef, L.; Rodgers, P. *PLoS ONE* **2014**, *9*, e101717.
- (186) Kurtz, S.; Phillippy, A.; Delcher, A. L.; Smoot, M.; Shumway, M.; Antonescu, C.; Salzberg, S. L. *Genome Biol.* **2004**, *5*, R12.
- (187) Sullivan, M. J.; Petty, N. K.; Beatson, S. A. *Bioinformatics* **2011**, *27*, 1009-1010.
- (188) El-Elimat, T.; Figueroa, M.; Ehrmann, B. M.; Cech, N. B.; Pearce, C. J.; Oberlies, N. H. *J. Nat. Prod.* **2013**, *76*, 1709-1716.
- (189) Paguigan, N. D.; El-Elimat, T.; Kao, D.; Raja, H. A.; Pearce, C. J.; Oberlies, N. H. *J. Antibiot.* **2017**, *70*, 553-56.
- (190) Wang, B.; You, J.; King, J. B.; Cai, S.; Park, E.; Powell, D. R.; Cichewicz, R. H. *J. Nat. Prod.* **2014**, *77*, 2273-2279.
- (191) Colot, H. V.; Park, G.; Turner, G. E.; Ringelberg, C.; Crew, C. M.; Litvinkova, L.; Weiss, R. L.; Borkovich, K. A.; Dunlap, J. C. *Proc. Natl. Acad. Sci. USA* **2006**, *103*, 10352-10357.

- (192) Malavazi, I.; Goldman, G. H., Gene disruption in *Aspergillus fumigatus* using a PCR-based strategy and in vivo recombination in yeast. In *Host-Fungus Interactions*, Springer 2012; pp 99-118.
- (193) Schiestl, R. H.; Gietz, R. D. *Curr. Genet.* **1989**, *16*, 339-346.
- (194) Goldman, G. H.; dos Reis Marques, E.; Ribeiro, D. C. D.; de Souza Bernardes, L. A. n.; Quiapin, A. C.; Vitorelli, P. M.; Savoldi, M.; Semighini, C. P.; de Oliveira, R. C.; Nunes, L. R. *Eukaryot. Cell* **2003**, *2*, 34-48.
- (195) Sambrook, J.; Russell, D., *Molecular cloning: A laboratory manual 3rd Ed.*; Cold Spring Harbor Laboratory Press: Plainview, NY, 2001; p 1-2344.
- (196) Yin, W.-B.; Grundmann, A.; Cheng, J.; Li, S.-M. *J. Biol. Chem.* **2009**, *284*, 100-109.
- (197) Schreitl, M.; Carberry, S.; Kavanagh, K.; Haas, H.; Jones, G. W.; O'Brien, J.; Nolan, A.; Stephens, J.; Fenelon, O.; Doyle, S. *PLoS Pathog.* **2010**, *6*, e1000952.
- (198) Dolan, S. K.; O'Keeffe, G.; Jones, G. W.; Doyle, S. *Trends in microbiology* **2015**, *23*, 419-428.
- (199) Bongomin, F.; Gago, S.; Oladele, R. O.; Denning, D. W. *J. Fungi* **2017**, *3*, 57.
- (200) Brown, G. D.; Denning, D. W.; Gow, N. A.; Levitz, S. M.; Netea, M. G.; White, T. C. *Sci. Transl. Med.* **2012**, *4*, 165rv13-165rv13.
- (201) Lewis, R. E.; Wiederhold, N. P.; Chi, J.; Han, X. Y.; Komanduri, K. V.; Kontoyiannis, D. P.; Prince, R. A. *Infect. Immun.* **2005**, *73*, 635-637.
- (202) Cramer, R. A.; Gamcsik, M. P.; Brooking, R. M.; Najvar, L. K.; Kirkpatrick, W. R.; Patterson, T. F.; Balibar, C. J.; Graybill, J. R.; Perfect, J. R.; Abraham, S. N. *Eukaryot. Cell* **2006**, *5*, 972-980.
- (203) Perrin, R. M.; Fedorova, N. D.; Bok, J. W.; Cramer Jr, R. A.; Wortman, J. R.; Kim, H. S.; Nierman, W. C.; Keller, N. P. *PLoS Pathog.* **2007**, *3*, e50.

- (204) Sugui, J. A.; Peterson, S. W.; Figat, A.; Hansen, B.; Samson, R. A.; Mellado, E.; Cuenca-Estrella, M.; Kwon-Chung, K. J. *J. Clin. Microbiol.* **2014**, *52*, 3707-3721.
- (205) Bok, J. W.; Keller, N. P. *Eukaryot. Cell* **2004**, *3*, 527-535.
- (206) Pena, G.; Monge, M.; Pereyra, M. G.; Dalcerio, A.; Rosa, C.; Chiacchiera, S.; Cavaglieri, L. *Mycotoxin Res.* **2015**, *31*, 145-150.
- (207) Belkacemi, L.; Barton, R.; Hopwood, V.; Evans, E. *Med. Mycol.* **1999**, *37*, 227-233.
- (208) Kosalec, I.; Pepelnjak, S.; Jandric, M. *Archives of Industrial Hygiene and Toxicology* **2005**, *56*, 269-273.
- (209) Reeves, E. P.; Messina, C.; Doyle, S.; Kavanagh, K. *Mycopathologia* **2004**, *158*, 73-79.
- (210) Bok, J. W.; Chung, D.; Balajee, S. A.; Marr, K. A.; Andes, D.; Nielsen, K. F.; Frisvad, J. C.; Kirby, K. A.; Keller, N. P. *Infect Immun* **2006**, *74*, 6761-8.
- (211) Nierman, W. C.; Pain, A.; Anderson, M. J.; Wortman, J. R.; Kim, H. S.; Arroyo, J.; Berriman, M.; Abe, K.; Archer, D. B.; Bermejo, C. *Nature* **2005**, *438*, 1151-1156.
- (212) Casadevall, A. *Microbe* **2006**, *1*, 359-364.
- (213) Drgona, L.; Khachatrian, A.; Stephens, J.; Charbonneau, C.; Kantecki, M.; Haider, S.; Barnes, R. *Eur. J. Clin. Microbiol. Infect. Dis.* **2014**, *33*, 7-21.
- (214) Vallabhaneni, S.; Mody, R. K.; Walker, T.; Chiller, T. *Infect. Dis. Clin.* **2016**, *30*, 1-11.
- (215) Benedict, K.; Jackson, B. R.; Chiller, T.; Beer, K. D. *Clin. Infect. Dis.* **2019**, *68*, 1791-1797.
- (216) Steenwyk, J. L.; Shen, X.-X.; Lind, A. L.; Goldman, G. H.; Rokas, A. *mBio* **2019**, *10*, e00925-19.

- (217) Rokas, A.; Mead, M. E.; Steenwyk, J. L.; Oberlies, N. H.; Goldman, G. H. *PLoS Pathog.* **2020**, *16*, e1008315.
- (218) Kamei, K.; Watanabe, A. *Med. Mycol.* **2005**, *43*, S95-S99.
- (219) Grahl, N.; Shepardson, K. M.; Chung, D.; Cramer, R. A. *Eukaryot. Cell* **2012**, *11*, 560-570.
- (220) Khoufache, K.; Puel, O.; Loiseau, N.; Delaforge, M.; Rivollet, D.; Coste, A.; Cordonnier, C.; Escudier, E.; Botterel, F.; Bretagne, S. *BMC Microbiol.* **2007**, *7*, 1-11.
- (221) Gauthier, T.; Wang, X.; Dos Santos, J. S.; Fysikopoulos, A.; Tadrist, S.; Canlet, C.; Artigot, M. P.; Loiseau, N.; Oswald, I. P.; Puel, O. *PLoS ONE* **2012**, *7*, e29906.
- (222) Mattern, D. J.; Schoeler, H.; Weber, J.; Novohradská, S.; Kraibooj, K.; Dahse, H.-M.; Hillmann, F.; Valiante, V.; Figge, M. T.; Brakhage, A. A. *Appl. Microbiol. Biotechnol.* **2015**, *99*, 10151-10161.
- (223) de Vries, R. P.; Riley, R.; Wiebenga, A.; Aguilar-Osorio, G.; Amillis, S.; Uchima, C. A.; Anderluh, G.; Asadollahi, M.; Askin, M.; Barry, K. *Genome Biol.* **2017**, *18*, 1-45.
- (224) Kjærboelling, I.; Vesth, T.; Frisvad, J. C.; Nybo, J. L.; Theobald, S.; Kildgaard, S.; Petersen, T. I.; Kuo, A.; Sato, A.; Lyhne, E. K. *Nat. Commun.* **2020**, *11*, 1-12.
- (225) Vesth, T. C.; Nybo, J. L.; Theobald, S.; Frisvad, J. C.; Larsen, T. O.; Nielsen, K. F.; Hoof, J. B.; Brandl, J.; Salamov, A.; Riley, R. *Nat. Genet.* **2018**, *50*, 1688-1695.
- (226) Knowles, S. L.; Mead, M. E.; Silva, L. P.; Raja, H. A.; Steenwyk, J. L.; Goldman, G. H.; Oberlies, N. H.; Rokas, A. *mBio* **2020**, *11*, e03361-19.
- (227) Kowalski, C. H.; Kerkaert, J. D.; Liu, K.-W.; Bond, M. C.; Hartmann, R.; Nadell, C. D.; Stajich, J. E.; Cramer, R. A. *Nat. Microbiol.* **2019**, *4*, 2430-2441.
- (228) Keller, N. P. *mBio* **2017**, *8*, e00135-17.

- (229) Ries, L. N. A.; Steenwyk, J. L.; de Castro, P. A.; de Lima, P. B. A.; Almeida, F.; de Assis, L. J.; Manfiolli, A. O.; Takahashi-Nakaguchi, A.; Kusuya, Y.; Hagiwara, D. *Front. Microbiol.* **2019**, *10*, 854.
- (230) Bastos, R. W.; Valero, C.; Silva, L. P.; Schoen, T.; Drott, M.; Brauer, V.; Silva-Rocha, R.; Lind, A.; Steenwyk, J. L.; Rokas, A. *mSphere* **2020**, *5*, e00153-20.
- (231) Drott, M.; Bastos, R.; Rokas, A.; Ries, L.; Gabaldón, T.; Goldman, G.; Keller, N.; Greco, C. *mSphere* **2020**, *5*, e00156-20.
- (232) dos Santos, R. A.; Steenwyk, J. L.; Rivero-Menendez, O.; Mead, M. E.; Silva, L. P.; Bastos, R. W.; Alastruey-Izquierdo, A.; Goldman, G. H.; Rokas, A. *Front. Genet.* **2020**, *11*, 459.
- (233) Steenwyk, J. L.; Lind, A. L.; Ries, L. N.; dos Reis, T. F.; Silva, L. P.; Almeida, F.; Bastos, R. W.; Bonato, V. L.; Pessoni, A. M.; Rodrigues, F.; Raja, H. A.; Knowles, S. L.; Oberlies, N. H.; Lagrou, K.; Goldman, G. G.; Rokas, A. *Curr. Biol.* **2020**, *30*, 2495-2507.
- (234) Yamada, A.; Kataoka, T.; Nagai, K. *Immunol. Lett.* **2000**, *71*, 27-32.
- (235) Li, X.-J.; Zhang, Q.; Zhang, A.-L.; Gao, J.-M. *J. Agric. Food Chem.* **2012**, *60*, 3424-3431.
- (236) Ito, T.; Masubuchi, M. *J. Antibiot.* **2014**, *67*, 353-360.
- (237) Hubert, J.; Nuzillard, J.-M.; Renault, J.-H. *Phytochem. Rev.* **2017**, *16*, 55-95.
- (238) Gaudêncio, S. P.; Pereira, F. *Nat. Prod. Rep.* **2015**, *32*, 779-810.
- (239) Kautsar, S. A.; Blin, K.; Shaw, S.; Navarro-Muñoz, J. C.; Terlouw, B. R.; van der Hooft, J. J.; Van Santen, J. A.; Tracanna, V.; Suarez Duran, H. G.; Pascal Andreu, V. *Nucleic Acids Res.* **2020**, *48*, D454-D458.
- (240) Dolan, S. K.; Owens, R. A.; O'Keeffe, G.; Hammel, S.; Fitzpatrick, D. A.; Jones, G. W.; Doyle, S. *Chem. Biol.* **2014**, *21*, 999-1012.

- (241) Poukka, H.; Aarnisalo, P.; Santti, H.; Jänne, O. A.; Palvimo, J. J. *J. Biol. Chem.* **2000**, *275*, 571-579.
- (242) Jackson, R. W.; Johnson, L. J.; Clarke, S. R.; Arnold, D. L. *Trends Genet.* **2011**, *27*, 32-40.
- (243) Moran, G. P.; Coleman, D. C.; Sullivan, D. J. *Eukaryot. Cell* **2011**, *10*, 34-42.
- (244) Bolger, A. M.; Lohse, M.; Usadel, B. *Bioinformatics* **2014**, *30*, 2114-2120.
- (245) Steenwyk, J.; Rokas, A. *G3 (Bethesda)* **2017**, *7*, 1475-1485.
- (246) Bankevich, A.; Nurk, S.; Antipov, D.; Gurevich, A. A.; Dvorkin, M.; Kulikov, A. S.; Lesin, V. M.; Nikolenko, S. I.; Pham, S.; Prjibelski, A. D. *J. Comput. Biol.* **2012**, *19*, 455-477.
- (247) Yandell, M.; Ence, D. *Nat. Rev. Genet.* **2012**, *13*, 329-342.
- (248) Waterhouse, R. M.; Seppey, M.; Simão, F. A.; Manni, M.; Ioannidis, P.; Klioutchnikov, G.; Kriventseva, E. V.; Zdobnov, E. M. *Mol. Biol. Evol.* **2018**, *35*, 543-548.
- (249) Waterhouse, R. M.; Tegenfeldt, F.; Li, J.; Zdobnov, E. M.; Kriventseva, E. V. *Nucleic Acids Res.* **2013**, *41*, D358-D365.
- (250) Holt, C.; Yandell, M. *BMC Bioinformatics* **2011**, *12*, 491.
- (251) Stanke, M.; Waack, S. *Bioinformatics* **2003**, *19*, ii215-25.
- (252) Zhao, S.; Latgé, J.-P.; Gibbons, J. G. *Microbiol. Resour. Announc.* **2019**, *8*.
- (253) Miao, Y.; Liu, D.; Li, G.; Li, P.; Xu, Y.; Shen, Q.; Zhang, R. *BMC genomics* **2015**, *16*, 459.
- (254) Rokas, A.; Williams, B. L.; King, N.; Carroll, S. B. *Nature* **2003**, *425*, 798-804.

- (255) Bodinaku, I.; Shaffer, J.; Connors, A. B.; Steenwyk, J. L.; Biango-Daniels, M. N.; Kastman, E. K.; Rokas, A.; Robbat, A.; Wolfe, B. E. *mBio* **2019**, *10*, e02445-19.
- (256) Katoh, K.; Standley, D. M. *Mol. Biol. Evol.* **2013**, *30*, 772-780.
- (257) Cock, P. J.; Antao, T.; Chang, J. T.; Chapman, B. A.; Cox, C. J.; Dalke, A.; Friedberg, I.; Hamelryck, T.; Kauff, F.; Wilczynski, B. *Bioinformatics* **2009**, *25*, 1422-1423.
- (258) Capella-Gutiérrez, S.; Silla-Martínez, J. M.; Gabaldón, T. *Bioinformatics* **2009**, *25*, 1972-1973.
- (259) Nguyen, L.-T.; Schmidt, H. A.; Von Haeseler, A.; Minh, B. Q. *Mol. Biol. Evol.* **2015**, *32*, 268-274.
- (260) Kalyaanamoorthy, S.; Minh, B. Q.; Wong, T. K.; von Haeseler, A.; Jermiin, L. S. *Nature methods* **2017**, *14*, 587-589.
- (261) Tavaré, S. *Lectures on mathematics in the life sciences* **1986**, *17*, 57-86.
- (262) Yang, Z. *J. Mol. Evol.* **1994**, *39*, 306-314.
- (263) Yang, Z. *Trends Ecol. Evol.* **1996**, *11*, 367-372.
- (264) Vinet, L.; Zhedanov, A. *J. Phys. A Math. Theor.* **2011**, *44*, 085201.
- (265) Hoang, D. T.; Chernomor, O.; Von Haeseler, A.; Minh, B. Q.; Vinh, L. S. *Mol. Biol. Evol.* **2018**, *35*, 518-522.
- (266) Yang, Z. *Mol. Biol. Evol.* **2007**, *24*, 1586-1591.
- (267) Raftery, A. E.; Lewis, S. M. *Practical Markov Chain Monte Carlo* **1995**, *7*, 763-773.
- (268) Emms, D. M.; Kelly, S. *Genome Biol.* **2019**, *20*, 1-14.

- (269) Camacho, C.; Coulouris, G.; Avagyan, V.; Ma, N.; Papadopoulos, J.; Bealer, K.; Madden, T. L. *BMC Bioinformatics* **2009**, *10*, 421.
- (270) Navarro-Muñoz, J. C.; Selem-Mojica, N.; Mullowney, M. W.; Kautsar, S. A.; Tryon, J. H.; Parkinson, E. I.; De Los Santos, E. L.; Yeong, M.; Cruz-Morales, P.; Abubucker, S. *Nat. Chem. Biol.* **2020**, *16*, 60-68.
- (271) Knowles, S. L.; Vu, N.; Todd, D. A.; Raja, H. A.; Rokas, A.; Zhang, Q.; Oberlies, N. H. *J. Nat. Prod.* **2019**, *82*, 3421–3431.
- (272) Li, Z.; Peng, C.; Shen, Y.; Miao, X.; Zhang, H.; Lin, H. *Biochem. Syst. Ecol.* **2008**, *36*, 230-234.
- (273) Campbell, J.; Lin, Q.; Geske, G. D.; Blackwell, H. E. *ACS Chem. Biol.* **2009**, *4*, 1051-1059.
- (274) Ma, Y.; Li, Y.; Liu, J.; Song, Y.; Tan, R. *Fitoterapia* **2004**, *75*, 451-456.
- (275) Wang, F.-Z.; Li, D.-H.; Zhu, T.-J.; Zhang, M.; Gu, Q.-Q. *Canadian Journal of Chemistry* **2011**, *89*, 72-76.
- (276) Halász, J.; Podányi, B.; Vasvári-Debreczy, L.; Szabó, A.; Hajdú, F.; Böcskei, Z.; Hegedűs-Vajda, J.; Győrbíró, A.; Hermecz, I. *Tetrahedron* **2000**, *56*, 10081-10085.
- (277) Kato, N.; Suzuki, H.; Takagi, H.; Asami, Y.; Kakeya, H.; Uramoto, M.; Usui, T.; Takahashi, S.; Sugimoto, Y.; Osada, H. *ChemBioChem* **2009**, *10*, 920-928.
- (278) Wang, F.; Fang, Y.; Zhu, T.; Zhang, M.; Lin, A.; Gu, Q.; Zhu, W. *Tetrahedron* **2008**, *64*, 7986-7991.
- (279) Zhao, J.; Mou, Y.; Shan, T.; Li, Y.; Zhou, L.; Wang, M.; Wang, J. *Molecules* **2010**, *15*, 7961-7970.
- (280) Pluskal, T.; Castillo, S.; Villar-Briones, A.; Orešič, M. *BMC Bioinformatics* **2010**, *11*, 395.
- (281) Caesar, L. K.; Kvalheim, O. M.; Cech, N. B. *Anal. Chim. Acta* **2018**, *1021*, 69-77.

- (282) Kvalheim, O. M.; Chan, H.-y.; Benzie, I. F.; Szeto, Y.-t.; Tzang, A. H.-c.; Mok, D. K.-w.; Chau, F.-t. *Chemometr. Intell. Lab. Syst.* **2011**, *107*, 98-105.
- (283) Pel, H. J.; de Winde, J. H.; Archer, D. B.; Dyer, P. S.; Hofmann, G.; Schaap, P. J.; Turner, G.; de Vries, R. P.; Albang, R.; Albermann, K.; Andersen, M. R.; Bendtsen, J. D.; Benen, J. A.; van den Berg, M.; Breestraat, S.; Caddick, M. X.; Contreras, R.; Cornell, M.; Coutinho, P. M.; Danchin, E. G.; Debets, A. J.; Dekker, P.; van Dijck, P. W.; van Dijk, A.; Dijkhuizen, L.; Driessens, A. J.; d'Enfert, C.; Geysens, S.; Goosen, C.; Groot, G. S.; de Groot, P. W.; Guillemette, T.; Henrissat, B.; Herweijer, M.; van den Hombergh, J. P.; van den Hondel, C. A.; van der Heijden, R. T.; van der Kaaij, R. M.; Klis, F. M.; Kools, H. J.; Kubicek, C. P.; van Kuyk, P. A.; Lauber, J.; Lu, X.; van der Maarel, M. J.; Meulenberg, R.; Menke, H.; Mortimer, M. A.; Nielsen, J.; Oliver, S. G.; Olsthoorn, M.; Pal, K.; van Peij, N. N.; Ram, A. F.; Rinas, U.; Roubos, J. A.; Sagt, C. M.; Schmoll, M.; Sun, J.; Ussery, D.; Varga, J.; Vervecken, W.; van de Vondervoort, P. J.; Wedler, H.; Wosten, H. A.; Zeng, A. P.; van Ooyen, A. J.; Visser, J.; Stam, H. *Nat. Biotechnol.* **2007**, *25*, 221-231.
- (284) Keller, N. P. *Nat. Rev. Microbiol.* **2018**, *1*.
- (285) Bertrand, S.; Schumpp, O.; Bohni, N.; Monod, M.; Gindro, K.; Wolfender, J.-L. *J. Nat. Prod.* **2013**, *76*, 1157-1165.
- (286) Nonaka, K.; Abe, T.; Iwatsuki, M.; Mori, M.; Yamamoto, T.; Shiomi, K.; Ômura, S.; Masuma, R. *J. Antibiot.* **2011**, *64*, 769-774.
- (287) Luo, F.; Zhong, Z.; Liu, L.; Igarashi, Y.; Xie, D.; Li, N. *Sci. Rep.* **2017**, *7*, 5265.
- (288) Mandelare, P.; Adpressa, D.; Kaweesa, E.; Zakharov, L.; Loesgen, S. *J. Nat. Prod.* **2018**, *81*, 1014-1022.
- (289) Sica, V. P.; Rees, E. R.; Tchegnon, E.; Bardsley, R. H.; Raja, H. A.; Oberlies, N. H. *Front. Microbiol.* **2016**, *7*, 544.
- (290) Eckelmann, D.; Spiteller, M.; Kusari, S. *Sci. Rep.* **2018**, *8*, 5283.
- (291) González-Menéndez, V.; Martínez, G.; Serrano, R.; Muñoz, F.; Martín, J.; Genilloud, O.; Tormo, J. R. *BMC Syst. Biol.* **2018**, *12*, 99.
- (292) Michelsen, C. F.; Khademi, S. M. H.; Johansen, H. K.; Ingmer, H.; Dorrestein, P. C.; Jelsbak, L. *ISME J.* **2016**, *10*, 1323-1336.

- (293) Wang, W.-X.; Kusari, S.; Sezgin, S.; Lamshöft, M.; Kusari, P.; Kayser, O.; Spiteller, M. *Appl. Microbiol. Biotechnol.* **2015**, *99*, 7651-7662.
- (294) Chen, P.-Y.; Hsieh, C.-Y.; Shih, C.-J.; Lin, Y.-J.; Tsao, C.-W.; Yang, Y.-L. *J. Nat. Prod.* **2018**, *81*, 1527-1533.
- (295) Bai, J.; Zhang, P.; Bao, G.; Gu, J.-G.; Han, L.; Zhang, L.-W.; Xu, Y. *Appl. Microbiol. Biotechnol.* **2018**, *102*, 8493-8500.
- (296) Tata, A.; Perez, C.; Campos, M. L.; Bayfield, M. A.; Eberlin, M. N.; Ifa, D. R. *Anal. Chem.* **2015**, *87*, 12298-12305.
- (297) Sica, V. P.; Raja, H. A.; El-Elimat, T.; Kertesz, V.; Van Berkel, G. J.; Pearce, C. J.; Oberlies, N. H. *J. Nat. Prod.* **2015**, *78*, 1926-1936.
- (298) Sica, V. P.; Raja, H. A.; El-Elimat, T.; Oberlies, N. H. *RSC Adv.* **2014**, *4*, 63221-63227.
- (299) Kertesz, V.; Van Berkel, G. J. *Anal. Chem.* **2010**, *82*, 5917-5921.
- (300) Kertesz, V.; Van Berkel, G. J. *Bioanalysis* **2013**, *5*, 819-826.
- (301) Wakefield, J.; Hassan, H. M.; Jaspars, M.; Ebel, R.; Rateb, M. E. *Front. Microbiol.* **2017**, *8*, 1284.
- (302) Abdelwahab, M. F.; Kurtán, T.; Mándi, A.; Müller, W. E.; Fouad, M. A.; Kamel, M. S.; Liu, Z.; Ebrahim, W.; Daletos, G.; Proksch, P. *Tetrahedron Lett.* **2018**, *59*, 2647-2652.
- (303) Kusari, S.; Hertweck, C.; Spiteller, M. *Chem. Biol.* **2012**, *19*, 792-798.
- (304) Spiteller, P. *Nat. Prod. Rep.* **2015**, *32*, 971-993.
- (305) Sarikaya-Bayram, Ö.; Palmer, J. M.; Keller, N.; Braus, G. H.; Bayram, Ö. *Front. Microbiol.* **2015**, *6*, 1.

- (306) Lind, A. L.; Smith, T. D.; Saterlee, T.; Calvo, A. M.; Rokas, A. *G3 (Bethesda)* **2016**, 6, 4023-4033.
- (307) Paguigan, N. D.; Al-Huniti, M. H.; Raja, H. A.; Czarnecki, A.; Burdette, J. E.; González-Medina, M.; Medina-Franco, J. L.; Polyak, S. J.; Pearce, C. J.; Croatt, M. P.; Oberlies, N. H. *Bioorg. Med. Chem.* **2017**, 25, 5238-5246.
- (308) Samson, R. A.; Hong, S.; Peterson, S.; Frisvad, J. C.; Varga, J. *Stud. Mycol.* **2007**, 59, 147-203.
- (309) Brosch, G.; Loidl, P.; Graessle, S. *FEMS Microbiol. Rev.* **2008**, 32, 409-439.
- (310) Lv, Y.; Lv, A.; Zhai, H.; Zhang, S.; Li, L.; Cai, J.; Hu, Y. *Int. J. Food Microbiol.* **2018**, 284, 11-21.
- (311) Wang, B.; Lv, Y.; Li, X.; Lin, Y.; Deng, H.; Pan, L. *Res. Microbiol.* **2018**, 169, 67-77.
- (312) Jikai, L.; Jianwen, T.; Zejun, D.; Zhihui, D.; Xianghua, W.; Peigui, L. *Helv. Chim. Acta* **2002**, 85, 1439-1442.
- (313) Vedejs, E.; Rodgers, J.; Wittenberger, S. *J. Am. Chem. Soc.* **1988**, 110, 4822-4823.
- (314) Edwards, R. L.; Maitland, D. J.; Whalley, A. J. *J. Chem. Soc. Perkin Trans. I* **1989**, 57-65.
- (315) Capasso, R.; Evidente, A.; Vurro, M. *Phytochemistry* **1991**, 30, 3945-3950.
- (316) Isaka, M.; Palasarn, S.; Sriklung, K.; Kocharin, K. *J. Nat. Prod.* **2005**, 68, 1680-1682.
- (317) Ku, K. M.; Choi, J. N.; Kim, J.; Kim, J. K.; Yoo, L. G.; Lee, S. J.; Hong, Y.-S.; Lee, C. H. *J. Agric. Food Chem.* **2009**, 58, 418-426.
- (318) Sharma, N.; Kushwaha, M.; Arora, D.; Jain, S.; Singamaneni, V.; Sharma, S.; Shankar, R.; Bhushan, S.; Gupta, P.; Jaglan, S. *J. Appl. Microbiol.* **2018**, 125, 111-120.

- (319) Wei, H.; Xu, Y.-m.; Espinosa-Artiles, P.; Liu, M. X.; Luo, J.-G.; U'Ren, J. M.; Arnold, A. E.; Gunatilaka, A. L. *Phytochemistry* **2015**, *118*, 102-108.
- (320) Chen, Z.; Huang, H.; Chen, Y.; Wang, Z.; Ma, J.; Wang, B.; Zhang, W.; Zhang, C.; Ju, J. *Helv. Chim. Acta* **2011**, *94*, 1671-1676.
- (321) Chinworrungsee, M.; Kittakoop, P.; Isaka, M.; Rungrod, A.; Tanticharoen, M.; Thebtaranonth, Y. *Bioorg. Med. Chem. Lett.* **2001**, *11*, 1965-1969.
- (322) Qiao, K.; Chooi, Y.-H.; Tang, Y. *Metab. Eng.* **2011**, *13*, 723-732.
- (323) Hsieh, H.-M.; Lin, C.-R.; Fang, M.-J.; Rogers, J. D.; Fournier, J.; Lechat, C.; Ju, Y.-M. *Mol. Phylogenetics Evol.* **2010**, *54*, 957-969.
- (324) Hautbergue, T.; Jamin, E.; Debrauwer, L.; Puel, O.; Oswald, I. *Nat. Prod. Rep.* **2018**, *35*, 147-173.
- (325) Marmann, A.; Aly, A. H.; Lin, W.; Wang, B.; Proksch, P. *Mar. Drugs* **2014**, *12*, 1043-1065.
- (326) Schroekh, V.; Scherlach, K.; Nützmann, H.-W.; Shelest, E.; Schmidt-Heck, W.; Schuemann, J.; Martin, K.; Hertweck, C.; Brakhage, A. A. *Proc. Natl. Acad. Sci. USA* **2009**, *106*, 14558-14563.
- (327) Drijfhout, F. *eLS* **2001**, 1-11.
- (328) Gilchrist, C. L.; Li, H.; Chooi, Y.-H. *Org. Biomol. Chem.* **2018**, *16*, 1620-1626.
- (329) Keller, N. P. *Nat. Chem. Biol.* **2015**, *11*, 671.
- (330) Caraballo-Rodríguez, A. M.; Mayor, C. A.; Chagas, F. O.; Pupo, M. T. *Chemoecology* **2017**, *27*, 177-185.
- (331) Gerwick, B. C.; Brewster, W. K.; Fields, S. C.; Graupner, P. R.; Hahn, D. R.; Pearce, C. J.; Schmitzer, P. R.; Webster, J. D. *J. Chem. Ecol.* **2013**, *39*, 253-261.

- (332) Sica, V. P.; Figueroa, M.; Raja, H. A.; El-Elimat, T.; Darveaux, B. A.; Pearce, C. J.; Oberlies, N. H. *J. Ind. Microbiol. Biotechnol.* **2016**, *43*, 1149-1157.
- (333) Hiscox, J.; O'Leary, J.; Boddy, L. *Stud. Mycol.* **2018**, *89*, 117-124.
- (334) Reverberi, M.; Ricelli, A.; Zjalic, S.; Fabbri, A. A.; Fanelli, C. *Appl. Microbiol. Biotechnol.* **2010**, *87*, 899-911.
- (335) Ehrlich, K. C.; Chang, P.-K.; Bhatnagar, D., Mycotoxins. April 15, 2011 ed.; John Wiley & Sons,Ltd:Chichester.: Encyclopedia of Life Sciences, 2011; pp 1-14.
- (336) Skellam, E. *Trends Biotechnol.* **2018**, *37*, 416-427.
- (337) O'Brien, J.; Wright, G. D. *Curr. Opin. Biotechnol.* **2011**, *22*, 552-558.
- (338) Pettit, R. K. *Appl. Microbiol. Biotechnol.* **2009**, *83*, 19-25.
- (339) Li, G.; Lou, H. X. *Med. Res. Rev.* **2017**, *38*, 1255-1294.
- (340) Shang, Z.; Salim, A. A.; Capon, R. J. *J. Nat. Prod.* **2017**, *80*, 1167-1172.
- (341) Adnani, N.; Chevrette, M. G.; Adibhatla, S. N.; Zhang, F.; Yu, Q.; Braun, D. R.; Nelson, J.; Simpkins, S. W.; McDonald, B. R.; Myers, C. L. *ACS Chem. Biol.* **2017**, *12*, 3093-3102.
- (342) Sica, V.; El-Elimat, T.; Oberlies, N. *Anal. Methods* **2016**, *8*, 6143-6149.
- (343) Altschul, S. F.; Gish, W.; Miller, W.; Myers, E. W.; Lipman, D. J. *J. Mol. Biol.* **1990**, *215*, 403-410.
- (344) El-Elimat, T.; Raja, H. A.; Ayers, S.; Kurina, S. J.; Burdette, J. E.; Mattes, Z.; Sabatelle, R.; Bacon, J. W.; Colby, A. H.; Grinstaff, M. W.; Pearce, C. J.; Oberlies, N. H. *Org. Lett.* **2019**, *21*, 529-534.
- (345) Li, C.-S.; Ding, Y.; Yang, B.-J.; Miklossy, G.; Yin, H.-Q.; Walker, L. A.; Turkson, J.; Cao, S. *Org. Lett.* **2015**, *17*, 3556-3559.

- (346) Vinale, F.; Sivasithamparam, K.; Ghisalberti, E.; Marra, R.; Barbetti, M.; Li, H.; Woo, S.; Lorito, M. *Physiol. Mol. Plant Pathol.* **2008**, *72*, 80-86.
- (347) Li, K.; Wang, Y.-F.; Li, X.-M.; Wang, W.-J.; Ai, X.-Z.; Li, X.; Yang, S.-Q.; Gloer, J. B.; Wang, B.-G.; Xu, T. *Org. Lett.* **2017**, *20*, 417-420.
- (348) Nützmann, H.-W.; Schroechk, V.; Brakhage, A. A., Regulatory Cross Talk And Microbial Induction Of Fungal Secondary Metabolite Gene Clusters. In *Methods in Enzymology*, Hopwood, D. A., Ed. Elsevier 2012; Vol. 517, pp 325-341.
- (349) Stierle, A. A.; Stierle, D. B.; Decato, D.; Priestley, N. D.; Alverson, J. B.; Hoody, J.; McGrath, K.; Klepacki, D. *J. Nat. Prod.* **2017**, *80*, 1150-1160.
- (350) Graybill, J.; Burgess, D.; Hardin, T. *Eur. J. Clin. Microbiol. Infect. Dis.* **1997**, *16*, 42-50.
- (351) Oberlies, N. H.; Knowles, S. L.; Amrine, C. S. M.; Kao, D.; Kertesz, V.; Raja, H. A. *Nat. Prod. Rep.* **2019**, *36*, 944-959.
- (352) Chen, W.-L.; Ren, Y.; Ren, J.; Erxleben, C.; Johnson, M. E.; Gentile, S.; Kinghorn, A. D.; Swanson, S. M.; Burdette, J. E. *J. Nat. Prod.* **2017**, *80*, 659-669.
- (353) Raja, H. A.; Miller, A. N.; Pearce, C. J.; Oberlies, N. H. *J. Nat. Prod.* **2017**, *80*, 756-770.
- (354) Greco, C.; Keller, N. P.; Rokas, A. *Curr. Opin. Microbiol.* **2019**, *51*, 22-29.
- (355) Wani, M. C.; Taylor, H. L.; Wall, M. E.; Coggon, P.; McPhail, A. T. *J. Am. Chem. Soc.* **1971**, *93*, 2325-2327.
- (356) Oberlies, N. H.; Kroll, D. J. *J. Nat. Prod.* **2004**, *67*, 129-135.
- (357) Wall, M. E.; Wani, M. C.; Cook, C.; Palmer, K. H.; McPhail, A. a.; Sim, G. *J. Am. Chem. Soc.* **1966**, *88*, 3888-3890.
- (358) Liu, Y.; Cohen, R. D.; Martin, G. E.; Williamson, R. T. *J. Magn. Reson.* **2018**, *291*, 63-72.

- (359) Saurí, J.; Bermel, W.; Parella, T.; Thomas Williamson, R.; Martin, G. E. *Magn. Reson. Chem.* **2018**, 56, 1029-1036.
- (360) Milanowski, D. J.; Oku, N.; Cartner, L. K.; Bokesch, H. R.; Williamson, R. T.; Saurí, J.; Liu, Y.; Blinov, K. A.; Ding, Y.; Li, X.-C. *Chem. Sci.* **2018**, 9, 307-314.
- (361) Ospina, C. A.; Rodríguez, A. D. *J. Nat. Prod.* **2006**, 69, 1721-1727.
- (362) Wegerski, C. J.; Sonnenschein, R. N.; Cabriales, F.; Valeriote, F. A.; Matainaho, T.; Crews, P. *Tetrahedron* **2006**, 62, 10393-10399.
- (363) Shen, Y. C.; Shih, P. S.; Lin, Y. S.; Lin, Y. C.; Kuo, Y. H.; Kuo, Y. C.; Khalil, A. T. *Helv. Chim. Acta* **2009**, 92, 2101-2110.
- (364) Kumari, G.; Serra, A.; Shin, J.; Nguyen, P. Q.; Sze, S. K.; Yoon, H. S.; Tam, J. P. *J. Nat. Prod.* **2015**, 78, 2791-2799.
- (365) Von Bargen, K. W.; Niehaus, E.-M.; Bergander, K.; Brun, R.; Tudzynski, B.; Humpf, H.-U. *J. Nat. Prod.* **2013**, 76, 2136-2140.
- (366) Bhushan, R.; Brückner, H. *Amino acids* **2004**, 27, 231-247.
- (367) Venkateswarlu, S.; Panchagnula, G. K.; Gottumukkala, A. L.; Subbaraju, G. V. *Tetrahedron* **2007**, 63, 6909-6914.
- (368) Kuramochi, K.; Saito, F.; Nakazaki, A.; Takeuchi, T.; Tsubaki, K.; Sugawara, F.; Kobayashi, S. *Biosci. Biotechnol. Biochem.* **2010**, 74, 1635-1640.
- (369) Jain, S.; Abraham, I.; Carvalho, P.; Kuang, Y.-H.; Shaala, L. A.; Youssef, D. T.; Avery, M. A.; Chen, Z.-S.; El Sayed, K. A. *J. Nat. Prod.* **2009**, 72, 1291-1298.
- (370) Carlson, D. A.; Roan, C. S.; Yost, R. A.; Hector, J. *Anal. Chem.* **1989**, 61, 1564-1571.
- (371) Ma, X.; Xia, Y. *Angew. Chem. Int. Ed. Engl.* **2014**, 53, 2592-2596.

- (372) Xie, X.; Xia, Y. *Anal. Chem.* **2019**, *91*, 7173–7180.
- (373) Feng, Y.; Chen, B.; Yu, Q.; Li, L. *Anal. Chem.* **2019**, *91*, 1791-1795.
- (374) Hancock, S. E.; Poad, B. L.; Batarseh, A.; Abbott, S. K.; Mitchell, T. W. *Anal. Biochem.* **2017**, *524*, 45-55.
- (375) Bruice, P. Y., *Organic Chemistry eighth edition*. Pearson2017.
- (376) Kishimoto, Y.; Radin, N. S. *J Lipid Res* **1963**, *4*, 437-43.
- (377) Thomas, M. C.; Mitchell, T. W.; Harman, D. G.; Deeley, J. M.; Murphy, R. C.; Blanksby, S. J. *Anal. Chem.* **2007**, *79*, 5013-22.
- (378) Auranwiwat, C.; Maccarone, A. T.; Carroll, A. W.; Rattanajak, R.; Kamchonwongpaisan, S.; Blanksby, S. J.; Pyne, S. G.; Limtharakul, T. *Tetrahedron* **2019**, *75*, 2336-2342.
- (379) Wang, H.; Leach, D. N.; Thomas, M. C.; Blanksby, S. J.; Forster, P. I.; Waterman, P. G. *Nat. Prod. Commun.* **2009**, *4*, 951-958.
- (380) Shou, Q.; Banbury, L. K.; Maccarone, A. T.; Renshaw, D. E.; Mon, H.; Griesser, S.; Griesser, H. J.; Blanksby, S. J.; Smith, J. E.; Wohlmuth, H. *Fitoterapia* **2014**, *93*, 62-66.
- (381) Shi, G.; Gu, Z.-m.; He, K.; Wood, K. V.; Zeng, L.; Ye, Q.; MacDougal, J. M.; McLaughlin, J. L. *Bioorg. Med. Chem.* **1996**, *4*, 1281-1286.
- (382) Liu, Y. X.; Ma, S. G.; Wang, X. J.; Zhao, N.; Qu, J.; Yu, S. S.; Dai, J. G.; Wang, Y. H.; Si, Y. K. *Helv. Chim. Acta* **2012**, *95*, 1401-1408.
- (383) Wang, Y.; Zheng, Z.; Liu, S.; Zhang, H.; Li, E.; Guo, L.; Che, Y. *J. Nat. Prod.* **2010**, *73*, 920-924.
- (384) Zhang, Y.; Wang, J.-S.; Wei, D.-D.; Gu, Y.-C.; Wang, X.-B.; Kong, L.-Y. *J. Nat. Prod.* **2013**, *76*, 1191-1195.

- (385) Bang, S.; Song, J. H.; Lee, D.; Lee, C.; Kim, S.; Kang, K. S.; Lee, J. H.; Shim, S. H. *J. Agric. Food Chem.* **2019**, *67*, 1831-1838.
- (386) Bigi, F.; Casiraghi, G.; Casnati, G.; Marchesi, S.; Sartori, G.; Vignali, C. *Tetrahedron* **1984**, *40*, 4081-4084.
- (387) Cram, D. J. *J. Am. Chem. Soc.* **1948**, *70*, 4240-4243.
- (388) Dong-Li, L.; Yu-Chan, C.; Mei-Hua, T.; Hao-Hua, L.; Wei-Min, Z. *Helv. Chim. Acta* **2012**, *95*, 805-809.
- (389) Jian-Lin, X.; Hong-Xin, L.; Yu-Chan, C.; Hai-Bo, T.; Heng, G.; Li-Qiong, X.; Sai-Ni, L.; Zi-Lei, H.; Hao-Hua, L.; Xiao-Xia, G.; Wei-Min, Z. *Mar. Drugs* **2018**, *16*, 329.
- (390) Barrientos, R. C.; Zhang, Q. *J. Am. Soc. Mass Spectrom.* **2019**, *30*, 1609–1620.
- (391) Marshall, D. L.; Criscuolo, A.; Young, R. S.; Poad, B. L.; Zeller, M.; Reid, G. E.; Mitchell, T. W.; Blanksby, S. J. *J. Am. Soc. Mass Spectrom.* **2019**, *1*-10.
- (392) Pham, H. T.; Maccarone, A. T.; Campbell, J. L.; Mitchell, T. W.; Blanksby, S. J. *J. Am. Soc. Mass Spectrom.* **2013**, *24*, 286-296.
- (393) Spraker, J. E.; Luu, G. T.; Sanchez, L. M. *Nat. Prod. Rep.* **2019**, *37*, 150-162.
- (394) Wu, C.; Dill, A. L.; Eberlin, L. S.; Cooks, R. G.; Ifa, D. R. *Mass Spectrom Rev* **2013**, *32*, 218-43.
- (395) Bahado-Singh, R. O.; Yilmaz, A.; Bisgin, H.; Turkoglu, O.; Kumar, P.; Sherman, E.; Mrazik, A.; Odibo, A.; Graham, S. F. *PLoS ONE* **2019**, *14*, e0214121.
- (396) Vijayan, V.; Rouillard, A. D.; Rajpal, D. K.; Agarwal, P. *Expert Opin. Drug Discov.* **2019**, *14*, 191-194.
- (397) Poad, B. L.; Pham, H. T.; Thomas, M. C.; Nealon, J. R.; Campbell, J. L.; Mitchell, T. W.; Blanksby, S. J. *J. Am. Soc. Mass Spectrom.* **2010**, *21*, 1989-1999.

- (398) Paine, M. R.; Poad, B. L.; Eijkel, G. B.; Marshall, D. L.; Blanksby, S. J.; Heeren, R. M.; Ellis, S. R. *Angew. Chem. Int. Ed. Engl.* **2018**, *57*, 10530-10534.
- (399) Amrine, C. S. M.; Raja, H. A.; Darveaux, B. A.; Pearce, C. J.; Oberlies, N. H. *J. Ind. Microbiol. Biotechnol.* **2018**, *45*, 1053-1065.
- (400) Crnkovic, C. M.; Krunic, A.; May, D. S.; Wilson, T. A.; Kao, D.; Burdette, J. E.; Fuchs, J. R.; Oberlies, N. H.; Orjala, J. *J. Nat. Prod.* **2018**, *81*, 2083-2090.
- (401) Seiple, I. B.; Zhang, Z.; Jakubec, P.; Langlois-Mercier, A.; Wright, P. M.; Hog, D. T.; Yabu, K.; Allu, S. R.; Fukuzaki, T.; Carlsen, P. N. *Nature* **2016**, *533*, 338-345.
- (402) Zuckerman, J. M.; Qamar, F.; Bono, B. R. *Med. Clin. North Am.* **2011**, *95*, 761-791.
- (403) Kauloorkar, S. V.; Kumar, P. *RSC Adv.* **2016**, *6*, 63607-63612.
- (404) Berg, A.; Notni, J.; Doerfelt, H.; Graefe, U. *J. Antibiot.* **2002**, *55*, 660-662.
- (405) Lang, G.; Mitova, M. I.; Ellis, G.; van der Sar, S.; Phipps, R. K.; Blunt, J. W.; Cummings, N. J.; Cole, A. L.; Munro, M. H. *J. Nat. Prod.* **2006**, *69*, 621-624.
- (406) González-Medina, M.; Owen, J. R.; El-Elimat, T.; Pearce, C. J.; Oberlies, N. H.; Figueroa, M.; Medina-Franco, J. L. *Front. Pharmacol.* **2017**, *8*, 180.
- (407) González-Medina, M.; Prieto-Martínez, F. D.; Naveja, J. J.; Méndez-Lucio, O.; El-Elimat, T.; Pearce, C. J.; Oberlies, N. H.; Figueroa, M.; Medina-Franco, J. L. *Future Med. Chem.* **2016**, *8*, 1399-1412.
- (408) El-Elimat, T.; Zhang, X.; Jarjoura, D.; Moy, F. J.; Orjala, J.; Kinghorn, A. D.; Pearce, C. J.; Oberlies, N. H. *ACS Med. Chem. Lett.* **2012**, *3*, 645-649.
- (409) Koseki, K.; Takahashi, Y.; Shimazaki, K.; Ebata, T.; Chuman, T.; Mori, K. *Biosci. Biotechnol. Biochem.* **1992**, *56*, 1728-1731.
- (410) Tang, X.-X.; Yan, X.; Fu, W.-H.; Yi, L.-Q.; Tang, B.-W.; Yu, L.-B.; Fang, M.-J.; Wu, Z.; Qiu, Y.-K. *J. Agric. Food Chem.* **2019**, *67*, 2877-2885.

- (411) Grimblat, N. s.; Zanardi, M. M.; Sarotti, A. M. *J. Org. Chem.* **2015**, *80*, 12526-12534.
- (412) Ojima, K.-i.; Yangchum, A.; Laksanacharoen, P.; Tasanathai, K.; Thanakitpipattana, D.; Tokuyama, H.; Isaka, M. *J. Antibiot.* **2018**, *71*, 351-358.
- (413) White, T. J.; Bruns, T.; Lee, S.; Taylor, J. *PCR protocols: a guide to methods and applications* **1990**, *18*, 315-322.
- (414) Gardes, M.; White, T. J.; Fortin, J. A.; Bruns, T. D.; Taylor, J. W. *Can. J. Bot.* **1991**, *69*, 180-190.
- (415) Schoch, C. L.; Seifert, K. A.; Huhndorf, S.; Robert, V.; Spouge, J. L.; Levesque, C. A.; Chen, W.; Consortium, F. B. *Proc. Natl. Acad. Sci. USA* **2012**, *109*, 6241-6246.
- (416) Lechat, C.; Fournier, J.; Chaduli, D.; Lesage-Meessen, L.; Favel, A. *Ascomycete.org* **2019**, *11*, 65-68.
- (417) Stamatakis, A. *Bioinformatics* **2006**, *22*, 2688-2690.
- (418) Stamatakis, A.; Hoover, P.; Rougemont, J. *Syst. Biol.* **2008**, *57*, 758-771.
- (419) Miller, M. A.; Pfeiffer, W.; Schwartz, T. In *Creating the CIPRES Science Gateway for inference of large phylogenetic trees*, 2010 gateway computing environments workshop (GCE)2010 Ieee; pp 1-8.
- (420) Schroers, H.-J., *A monograph of Bionectria (Ascomycota, Hypocreales, Bionectriaceae) and its Clonostachys anamorphs*. Centraalbureau voor Schimmelcultures Utrecht 2001.
- (421) Srebro, M.; Govind, N.; De Jong, W. A.; Autschbach, J. *J. Phys. Chem. A* **2011**, *115*, 10930-10949.
- (422) Bruhn, T.; Schaumlöffel, A.; Hemberger, Y.; Bringmann, G. *Chirality* **2013**, *25*, 243-249.
- (423) Bruhn, T.; Schaumlöffel, A.; Hemberger, Y.; Pescitelli, G. SpecDis version 1.71.